Preparation of g-C3N4 based material and analytical characterizations for environmental applications

Arianit Gashi

UNIVERSITY OF OSTRAVA, DEPARTMENT OF CHEMISTRY, OSTRAVA, CZECH REPUBLIC

&

UNIVERSITY OF HAUTE ALSACE, INSTITUT DE SCIENCE DES MATERIAUX DE MULHOUSE (IS2M), MULHOUSE, FRANCE

THESIS

To obtain the title of

Doctor of University of Ostrava

DISCIPLINE: ANALYTICAL CHEMISTRY OF HETEROGENOUS SYSTEMS

&

Doctor of University of Haute Alsace

DISCIPLINE: MATERIAL OF CHEMISTRY

To

Mgr. Arianit GASHI

PREPARATION OF g-C_3N_4 BASED MATERIAL AND ANALYTICAL CHARACTERIZATIONS FOR ENVIRONMENTAL APPLICATIONS

Supervisor: doc. RNDr. Roman MARSALEK, Ph.D.

Co-supervisor: Assoc.Prof. Julien PARMENTIER, Ph.D.

UNIVERSITÉ D'OSTRAVA, DÉPARTEMENT DE CHIMIE, OSTRAVA, RÉPUBLIQUE TCHÈQUE

&

UNIVERSITÉ DE HAUTE ALSACE, INSTITUT DE SCIENCE DES MATÉRIAUX DE MULHOUSE (IS2M), MULHOUSE, FRANCE

THÈSE

Pour obtenir le titre de

Docteur de l'Université d'Ostrava

DISCIPLINE: CHIMIE ANALYTIQUE DES SYSTÈMES HÉTÉROGÈNES

&

Docteur de l'Université de Haute Alsace

DISCIPLINE: CHIMIE DES MATÉRIAUX

Pour

Mgr. Arianit GASHI

PRÉPARATION DE MATÉRIAUX À BASE DE g-C_3N_4 ET CARACTÉRISATIONS ANALYTIQUES POUR DES APPLICATIONS ENVIRONNEMENTALES

Supervisor: doc. RNDr. Roman MARSALEK, Ph.D.

Co-supervisor: Assoc.Prof. Julien PARMENTIER, Ph.D.

Defended on 5th September, 2022 under following jury

Prof. Ing. Jiri Kucerik (Department of Chemistry Technical University of Brno, Brno, Czech Republic) **- Reviewer**

Prof. Ing. Petr Praus (Department of Chemistry Technical University of Ostrava Ostrava, Czech Republic) - **Reviewer**

Prof. RNDr. Kamila Koci, Ph.D. (Department of Chemistry Technical University of Ostrava Ostrava, Czech Republic) **– Examiner**

doc. RNDr. Vaclav Slovak, Ph.D. (Department of Chemistry University of Ostrava Ostrava, Czech Republic) **– Examiner**

Prof.Ing. Boleslav Taraba, CSc (Department of Chemistry University of Ostrava Ostrava, Czech Republic) **– Examiner**

Dr.Amane Jada, PhD (Department of Chemistry, University of Haute Alsace, IS2M, Mulhouse, France) - **Invited member**

OSTRAVSKÁ UNIVERZITA

Přírodovědecká fakulta

Akademický rok: 2021/2022

ZADÁNÍ DISERTAČNÍ PRÁCE

(projektu, uměleckého díla, uměleckého výkonu)

Jméno a příjmení:	Mgr. Arianit GASHI
Osobní číslo:	P18183
Studijní program:	P1403 Analytická chemie
Studijní obor:	Analytická chemie heterogenních systémů
Téma práce:	Příprava materiálů na bázi g-C3N4 a jejich analytická charakterizace pro environmentální aplikace
Téma práce anglicky:	Preparation of g-C3N4 based material and analytical characterization for environmental applications
Zadávající katedra:	Katedra chemie

Zásady pro vypracování

Hlavním cílem práce bude navrhnout metody pro přípravu grafitického C3N4 materiálu, který by byl vhodný pro environmentální aplikace. Budou sledovány vlivy jednotlivých parametrů přípravy na výsledné vlastnosti g-C3N4, především na vlastnosti adsorpční a fotodegradační. Poměr mezi uhlíkem a dusíkem bude modifikován vstupními prekurzory, především přídavkem karboxylových kyselin. Práce bude zaměřena také na ověření možnosti cílené úpravy materiálu g-C3N4 fluorinací za různých podmínek. Všechny připravené materiály budou charakterizovány dostupnými analytickými technikami, především SEM, TEM, FTIR, XPS, BET, TG-MS, DSC, zeta potenciál aj. Cílem je připravit materiály s vysokou adsorpční kapacitou pro odstraňování těžkých kovů a organických látek z kapalného prostředí, resp. jejich rozložení procesem fotodegradace.

Rozsah pracovní zprávy:	
Rozsah grafických prací:	
Forma zpracování disertační práce:	tištěná/elektronická
Jazyk zpracování:	Angličtina

Seznam doporučené literatury:

Dle provedené rešerše.

Školitel disertační práce: doc. RNDr. Roman Maršálek, Ph.D.
Katedra chemie

Datum zadání disertační práce: 1. října 2021
Termín odevzdání disertační práce: 31. srpna 2022

doc. RNDr. Roman Maršálek, Ph.D.
vedoucí doktorské práce

doc. RNDr. Václav Slovák, Ph.D.
vedoucí katedry

V Ostravě dne 25. května 2022

ABSTRACT

Problems with global energy and environmental pollution have led on finding the alternatives worldwide. One of the most promising solution is considered the synthesis of photocatalysts with outstanding photocatalytic activity. For this purpose graphitic carbon nitride as metal-free photocatalyst is a suitable candidate material due to its excellent properties. Despite its suitable properties, g-C_3N_4 suffers from some drawbacks, such as low specific surface area and high recombination rate of the photo-induced electron-hole pairs. These factors limit its performance on photocatalytic activity. Therefore, our objectives were focused on preparation of different composites, like C-rich-g-C_3N_4, N-rich porous carbon and F-doped-g-C_3N_4, based on g-C_3N_4 material, with possible application in photocatalysis. Then properties of such composites will be carefully detailed in fundamental point of view.

C-rich graphitic carbonitride materials (CNx) with a large range of composition have been prepared in different ratios thanks to the self-assembly of melamine (M) and a panel of polycarboxylic acid (A) such as oxalic, tartaric and citric acid (Chapter 3). This route required simple precipitation process, using water as a solvent. The thermal conversion of the formed adducts (MAy), led to CNx phases with x ranging from 0.66 to 1.4 (x =1.33 for g-C_3N_4 for comparison). The properties of these materials were followed by different techniques (XRD, Raman, TEM, TGA, XPS and DRIFT). It appears that the increase of the C content is associated to a disappearance of the long-range order of heptazine units, and to an increase of the subnanometric carbon-rich cluster size within the graphitic g-C_3N_4 structure. This trend is followed by a significant increase of the interlayer spacing and a lower proportion of the N=C-N bonds compared to C=C bonds. The thermal stability in inert atmosphere of these phases and their UV-Visible absorbance properties were also investigated.

The materials described in the Chapter 3 (calcined under inert atmosphere at 550 °C), were further pyrolized in oxidized atmosphere (air) in order to prepare N-rich porous carbon material. Thermal stability/reactivity with oxygen, of g-C_3N_4 and C-rich-g-C_3N_4 samples, with different C/N ratios was investigated under different range of temperature, (470-650 °C). The C-rich-g-C_3N_4 materials display a distinct thermal behavior in air (or inert atmosphere), compared to the basic g-C_3N_4. This behavior is explain by lower thermal stability (and decomposition) of g-C_3N_4 domains compared

to C-rich phases within the composite. Controlled oxidation at different temperature, have produced highly porous material with surface area up to 600 m^2 g^{-1}. Structural organisation of materials after oxidation was significantly changed. Disorder of materials is increased, evidenced by increase of interlayer distance and D peak. The g-C_3N_4 features were disappeared in profit of N-rich porous carbon, with different content of N and O according to the temperature used.

The highly doped g-C_3N_4 based materials were prepared via pure F_2 gas phase method, at room temperature (Chapter 5). The level of fluorine doping depends on the chemical nature and structure of materials. The C-rich-g-C_3N_4 sample has lower F content compared to g-C_3N_4, with an increase of atomic ratio from 9 at. % up to 26 at. %. All fluorinated samples have exhibited the narrowing band gap in comparision with pristine materials, from 2.66 eV to 2.57 eV, influencing photocatalytic properties. Based on electron paramagnetic resonance, visible light was efficient to produce paramagnetic species for fluorinated g-C_3N_4 samples, in contrast to C-rich-g-C_3N_4. Thereafter, materials were evaluated in photocatalytic point of view. Methyl orange solution was used as a target pollutant to perform photodegradation experiments under visible light irradiation. The results showed that all fluorinated g-C_3N_4 based photocatalysts, have enhanced the photocatalytic activites in comparision with the pristine g-C_3N_4 based samples. In case of CN-F_2_20 fluorinated sample, the degradation rate constant is increased 3.96 time higher over pristine g-C_3N_4. Whereas, for CNO-F_2_20 and CCN-F_2_20 samples the degradation rate constant was 2.29 and 2.18 time higher than corresponding CNO and CCN materials.

Key words: *graphitic carbon nitride, adducts, fluorination, photocatalysis, photodegradation, oxidation, N-rich porous carbon, methyl orange.*

DECLARATION OF HONOUR

I, the undersigned student, hereby affirm that the submitted text of my thesis in written form is identical to the text of the final thesis embedded in database DIPL2.

Ostrava . . . . . .

. . . . . .

Arianit Gashi

I hereby state that this submitted thesis is my original author work and that I elaborated it myself. I properly cite all references and other sources that I used to work up the thesis. Those references and other sources are given in the list of references.

Ostrava . . . . . .

. . . . . .

Arianit Gashi

DEDICATION

Special dedication with the love that springs from the soul and heart, I dedicate this doctoral dissertation to my late mother Melihate Gashi, who instilled in me the discipline and sense of excellence that has led me to accomplish this mission. I bow to the memory of my mother who was with me throughout my life, in difficulties or good moments. *´´Mother you left us beautiful memories, your love is our guide, although we cannot see you, you are always at our side*``. The dedication for the rest of my family, to my father who was the backbone of the family and motivated me in the path of knowledge. For my girlfriend who was with me during this period, and endless love and emotional support, my sister and my brothers growing up together in the spirit of knowledge. And finally I want a dedication to belong to my newborn nephew Akil, who adorns the moments with his smile.

ACKNOWLEDGMENT

This doctoral thesis is the result of a tireless collaboration between the University of Ostrava, Czech Republic and the Universite de Haute Alsace, Muhouse, France, based on the Cotutelle agreement. It is a privilege to be awarded the degree of Doctor of Chemistry at two European Universities.

First of all I want to thank my doctoral supervisor Mr. Roman Marsalek, Associate Professor at the University of Ostrava in Czech Republic, for the opportunity he offered me and accepted to be his student. At the same time for the motivation and the support he has given to me during these four years of studies, and the scientific contribution in the realization of the doctoral obligations.

I am also thankfull for the help provided by my co-supervisor Mr. Julien Parmentier, Associate Professor (HRD) at the University of Haute Alsace and IS2M, Mulhouse, France in the realization and fruitfull discussion of results and advancement of studies, during my stay in France also discussions were realized during my time in the Czech Republic.

The doctorate consists of teamwork, therefore I would like to thank Vaclav Slovak, Associate Professor at the University of Ostrava, for his advices on the TG-DSC analysis, Tomas Zelenka, Arjeta Kryeziu and all the members of the team in University of Ostrava.

I thank the Carbon team from IS2M institute in Mulhouse, for the contribution by the team members, Benedicte Rety and Joseph Dentzer for the help and effort of using pyrolysis, Simon for the help about Raman and FTIR techniques, Mr. Jean Marc Le Meins for productive assistance in the XRD technique, Loic Vidal for assistance in the SEM and TEM, CyrileValout for measurements in the nitrogen adsorption technique.

A special thanks goes to Mr. Pierre Bonnet and his team from Clermont Ferrand and Auvergne University, for the fruitful collaboration in the idea and experimental realization of the fluorination project, which will soon be an article and also takes place on this topic.

A thank goes to Prof. Ing Kamila Koci who gave me the opportunity to stay two months at the Technical University of Ostrava (VSB) Department of Chemistry and use their facilities to conduct some measurements in photodegradation experiments.

I am grateful and thankful to the University of Ostrava for the financial support provided to me during these four years of studies. Without this help I would not have been able to realize my stay

in France during the Cotutelle agreement. And at the end it is the family that was my motive in the path of science, so I thank them from the bottom of my heart, who have been with me in every step of this journey.

TABLE OF CONTENT

INTRODUCTION

The aim of this thesis was to develope different composite materials based on graphitic carbon nitride. Materials prepared will be investigated in terms of structural changes, with possible application as photocatalysts for organic degradation in aqueous solution. Thesis is organized into five chapters, according to individual objectives done during the study period.

The first part is focused on the theoretical general background about graphitic carbon nitride and possible informations given in the literature to modify its properties via different approaches, including composites based-g-C_3N_4, doping etc.

The second part describes the experimental procedure used to prepare the composites, photocatalysis experiments and their characterizations techniques.

Syntheis of C-rich-g-C_3N_4 materials by the melamine/poly-carboxylic adduct route, was elaborated in the third chapter. Their physico-chemical characterizations including optical and electronic properties, and possible application for H_2 generation.

Fourth part is related to the thermal oxidation of C-rich-g-C_3N_4 composites, in order to prepare N-rich porous carbon material. Here is described the thermal behavior and reactivity of materials with oxygen (in air) with different C/N ratios under different heating, and the approach used to improve the porosity.

Chemical reactivity /stability of g-C_3N_4 and C-rich-C_3N_4 materials towards the F_2 pure gas, was detailed in chapter five. Informations and explanations were given, to achieve controlled fluorination over a wide range of F content and significant improvement of many properties (e.g. electronic and photocatalytic).

SUMMARY IN FRENCH

Le carbonitrure de structure graphitique (g-C_3N_4) est un matériau prometteur pour la photocatalyse. En jouant sur l'ingénierie d'hétérojonction par un couplage avec un autre matériau de type métal ou semi-conducteur, ses propriétés peuvent être améliorées. Dans cette thèse, l'objectif est de concevoir des nanocomposites à base de g-C_3N_4 et de carbone par un procédé original permettant de contrôler les caractéristiques de ces matériaux. Ces dernières seront évaluées grâce à des méthodes physico-chimiques et photocatalytiques.

Afin d'atteindre ces objectifs, trois voies ont été choisies.

Dans la première voie, nous avons synthétisé des nanocomposites g-C_3N_4 / C avec des teneurs variables en C à partir de précurseurs originaux ayant l'avantage de présenter une distribution à l'échelle moléculaire des atomes C et N. Ces précurseurs, basés sur l'association de la mélamine et d'un acide polycarboxylique sont appelées adduits. La mélamine est la source traditionnelle de g-C_3N_4 alors que l'acide est ici la source additionnelle de C à la structure de g-C_3N_4. La carbonisation des adduits conduit à des matériaux où le C supplémentaire est distribué sous la forme de nanodomaines (ou cluster) de type graphitique au sein des plans de la structure de g-C_3N_4. Ces nanodomaines pourraient agir comme un conducteur électronique étendant la conjugaison π du carbonitrure afin d'améliorer ses propriétés photocatalytiques, par analogie avec l'hétérojonction g-C_3N_4/métal.

Dans la deuxième voie, nous avons étudié la réactivité chimique de ces nanocomposites g-C_3N_4 / C avec l'oxygène à haute température (450-650°C) et le F_2 pur à température ambiante afin de mieux comprendre leur structuration et obtenir de nouveaux matériaux aux propriétés photocatalytiques potentiellement intéressantes.

Dans la troisième voie, la stabilité thermique de ces nanocomposites g-C_3N_4 / C et des matériaux dérivés obtenus par réaction avec F_2 a été étudiée.

En parallèle, les applications photocatalytiques possibles de ces différents matériaux ont été explorées. La thèse est divisée en cinq chapitres.

CHAPTER 1

State of the art on g-C_3N_4

1.1. Introduction

Due to consumption of fossil fuels and increase of challenges in energy demands, the environmental concerns have gain attention. The concern is not just global warming but also pollution of water which leads growing awareness in the past decades. When we talk for water pollution, several categories of pollution can be highlighted. Pollution from heavy metals ions, like Pb^{2+}, Cd^{2+}, Cr^{6+}, Cu^{2+}, Co^{2+} etc. are considered with a high toxicity, and mainly discharged from industrial activities, such as, mining, metallurgy, steel industries, battery manufacturing etc. [1, 2]. On the other hand, organics (persistent) pollutants like, dyes, pharmaceuticals, herbicides, pesticides, personal care products etc. [3, 4], which are released in the environment by the processing of industry of textile, leather, paper, petroleum, pharmaceutical, agriculture etc. Last but not least, pollution from inorganic wastes, like nitrates, chlorides, phosphates are also threatens for the environment [5, 6]. Among the solutions to face these problems, photocatalysts have proven to be quite a successful, economical sustainable, non-harmful, safe and renewable technology [7, 8, 9, 10]. The principle of photocatalysis is very convenient, because solar irradiation can be used as an inexhaustible energy source. The design and synthesis of high performance photocatalysts has become an important topic. Various photocatalysts have been tested. For instance, TiO_2 is being one of the most studied photocatalyst, and it uses ultraviolet irradiation to excite its electronic structure [11]. Since ultraviolet radiation accounts for a very small fraction of the whole solar spectrum energy circa 4 % compare to visible light 43 %. Hence in this regard optimization of the properties of photocatalyst has to be performed in order to improve their performance. Efforts have then been focused on optimization of light harvesting in the visible region, electron-hole pair recombination, band gap, surface area, heterostructuration etc. [12, 13]. In non-optimized photocatalyst, the photogenerated electrons/holes pairs suffer from the high recombination rate, which may deteriorates its photocatalytic performance [14]. If a photocatalyst exhibit high surface area, it may favours the efficient photogenerated of charge separation and transfer, and also enhance the light-harvesting efficiency [15]. The photogenerated charge separation could also be improved with formation of composite-based heterojunction materials or other composites [16]. Up to date, various semiconductor were discovered and studied in the field of photocatalysis such as Fe_2O_3, SnO_2, $BiVO_4$, CdS, ZnS, Cu_2O, g-C_3N_4 etc. [17, 18, 19, 20, 21, 22 ,23].

Among organic semiconductors, graphitic carbonitride g-C_3N_4 appears as a promising candidate material. A large number of studies were carried out on its synthesis and applications. Since it is a metal-free catalyst with favourable band gap around 2.7eV [24, 25], compare to traditional catalysts like ZnO (3.37 eV) [26], TiO_2 (3.2 eV) [27]. It has got the most stable allotropic structure among carbon nitrides under normal conditions, of temperature and pressure. It is considered with high thermal and chemical stability due to the high degree of condensation of tri-s-triazine rings structure [28, 29, 30] as shown in Fig.1. Nevertheless, g-C_3N_4 has also some disadvantages. It suffers from high recombination rate of holes/electrons and low electrical conductivity [14, 31]. In order to improve these shortcomings, various strategies have been developed such as: defective engineering, doping, engineering heterojunction based on g-C_3N_4 composites etc, [32, 33]. These topics and strategies related to g-C_3N_4 will be developed in general point of view in this chapter: routes of synthesis, electronic properties of g-C_3N_4, defective engineering, non-metal doping, heterojunction engineering of g-C_3N_4 based materials, pore texture tailoring, adsorption properties and applications of g-C_3N_4.

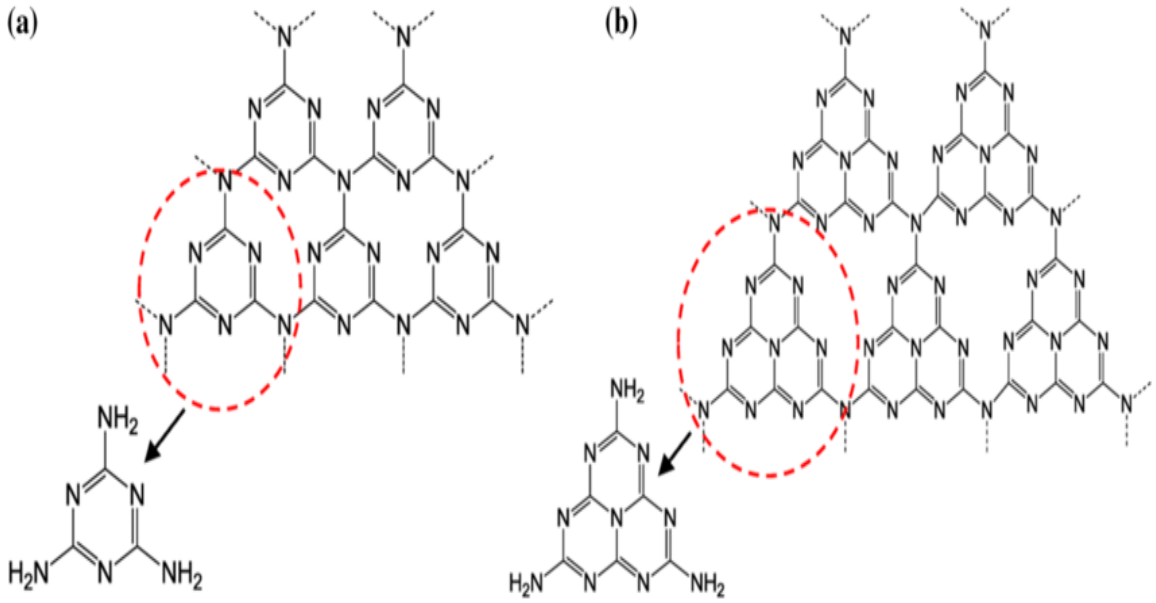

Figure 1. The two possible structures of g-C_3N_4, (a) triazine and (b) tri-s-triazine (heptazine) [34].

1.2. Routes of synthesis of g-C_3N_4

Various strategies have been used for the synthesis of g-C_3N_4, each one influencing the final properties of the material. Usually g-C_3N_4 is prepared with pyrolysis of N-rich precursors, like melamine, urea [35], thiourea [36], dicyandiamide, cyanamide [37] etc. Studies have shown that many properties of g-C_3N_4 are influenced by the precursor type as well as the preparation conditions [38]. Other routes were developed, such as solvothermal methods, Chemical Vapor Deposition (CVD), solid state reaction and so on [39, 24]. Thermal condensation of N-rich precursors is considered as the easiest route to obtain g-C_3N_4, because it requires only a furnace with or without controlled atmosphere and moderate temperature (around 550 °C). Reaction thermal pathway of g-C_3N_4 synthesis is represented in Fig. 2, starting from cyanamide precursor. This thermal process is followed by successive step. Formation of dicyanamide takes place firstly at 137 °C, then melamine or triamino-s-triazine $C_3N_3(NH_2)_3$ as a six-member ring which undergoes self-condensation by a deamination process at 350 °C, where NH_3 gaseous species are released [40, 41]. At this step, the condensation of two molecules of melamine yield to a dimer form of melamine called melam or (1,

3, 5-triazine-2, 4, 6-triamine) which takes place (Fig. 3), moreover this product is highly reactive. Within the temperature range 350-390 °C, on the closed ampoule in the gas phase is formed melamine-melem adduct, followed by a rapid formation of melem or (triamino-tri-s-triazine $C_6N_7(NH_2)_3$) which is presumed to be stable up to 500 °C during condensation process [42, 43]. The last product of condensation, before formation of polymeric g-C_3N_4 is melon compound $[(C_6N_7(NH_2)(NH)]_n$, containing infinite (*n)* units [44, 45, 46, 47, 48]. Formation of g-C_3N_4 takes place at 520 °C, exhibiting thermal instability at 600 °C which undergoes complete decomposition at 750 °C [49, 50].

Figure 2. Reaction path of the formation of g-C_3N_4, starting from cyanimide (reproduced with permission from reference) [51].

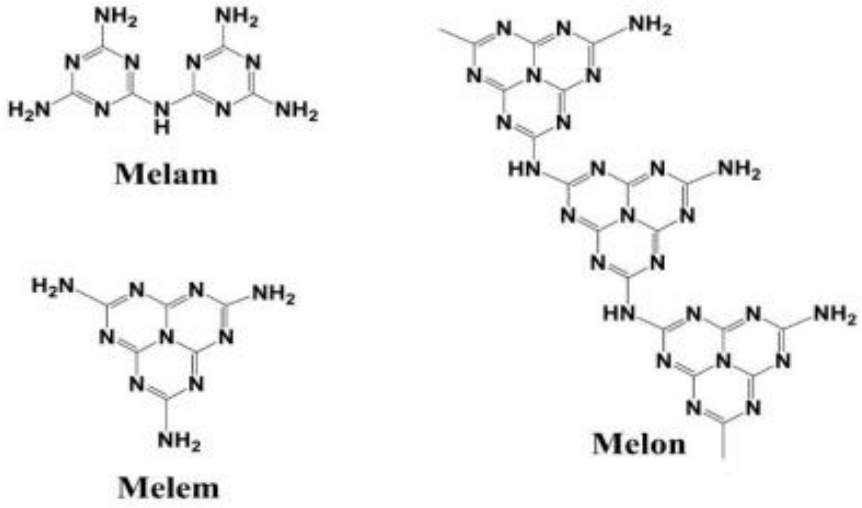

Figure 3. Structures of melam, melem, melon (reproduced with permission from reference) [52].

1.3. Electronic properties of g-C_3N_4

Benefiting from its unique tectonic structure motif, g-C_3N_4 possess special electronic properties. The lone-pair electrons from N atoms contribute to the electronic properties and particulary to the valence band. Graphitic carbon nitride exhibits the most negative conduction band (CB) edge potentials around (–1.15 eV) refered to neutral hydrogen electrode (NHE) and VB around (+1.61 eV), compared to the classical TiO_2 with a VB and CB edge potentials (+2.87 eV) and (– 0.26 eV) Fig.4 [53, 54, 55, 56, 57, 58]. g-C_3N_4 possess a medium valence band gap around (2.7 eV) compared to TiO_2 with 3.20 eV, $BiVO_4$ (2.4 eV) [59] and WO_3 (2.7 eV) [60, 51]. The g-C_3N_4 electronic structure could be tailored with the addition of chemical/structural defects, doping, heterojunction etc.

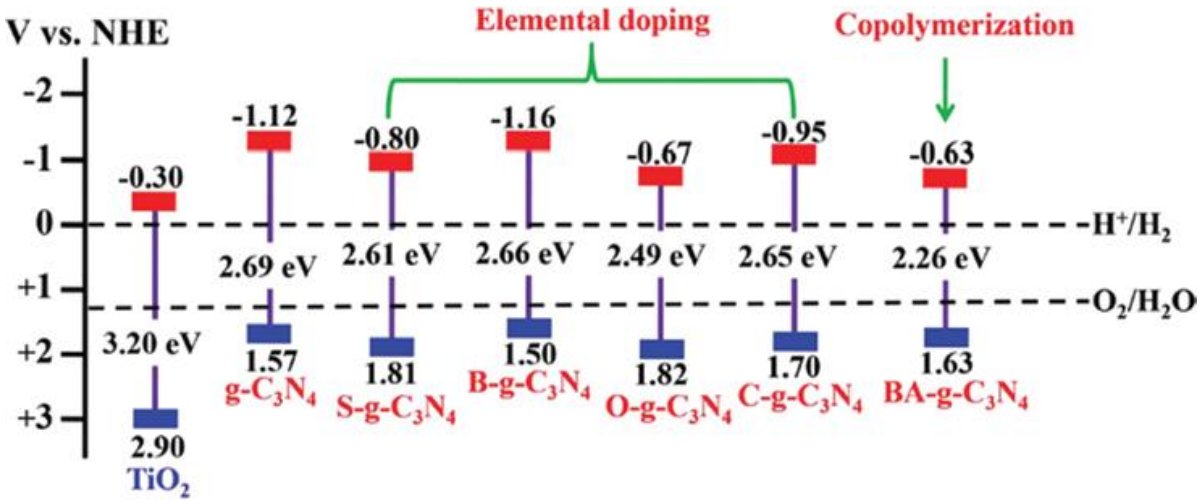

Figure 4. Schematic illustration of the band structures of typical samples of g-C_3N_4 in comparison with TiO_2 (reproduced with permission from reference) [50].

1.3.1. Defective engineering

Defective engineering has been considered with a high impact in modifying the electronic structure and band gap. Introduction of vacancies in the structure of g-C_3N_4 could be successfully done with variation of atmosphere of calcination, e.g from air to inert atmosphere and temperature. In Fig. 5 is shown the introduction of carbon vacancies on g-C_3N_4. With the aid of carbon vacancies on the structure, it is possible to hinder the recombination rate of photo-excited electron-holes [61]. Moreover they could act as a conversion centers, and could transfer the trapped photo-excited electrons to absorbed O_2, which then are generated the $^{\bullet}O_2^-$ active species. Well-known yellow g-C_3N_4 having less defects, was compare to orange g-C_3N_4 (enriched with more defects) due to two-step calcination under air and inert atmosphere, and it shows modification on the structure. Two-step calcination process, results on the breakage of some bonds and formation of distortion, while the later have exhibited a narrower band gap. As a consequence it may tailor the optical properties, thus enhancing the light in the visible range. Defectous-g-C_3N_4 has shown a good photodegradation performance toward Rhodamine B (RhB) and methyl orange (MO) [62]. For example, the synthesis of g-C_3N_4 from urea or melamine exhibits different features. g-C_3N_4 derived from urea possesses a larger specific surface area and more mesoporosity compare to melamine. The improved porous structure could increase the specific surface area, thus providing more active sites which promotes

the mass transfer during the photodegradation [63, 64]. Moreover it displays a defective structure with nitrogen vacancies acting as a trap states for the photogenerated electrons, promoting thus the separation efficiency of the photogenerated charge carriers [65, 66, 67, 68].

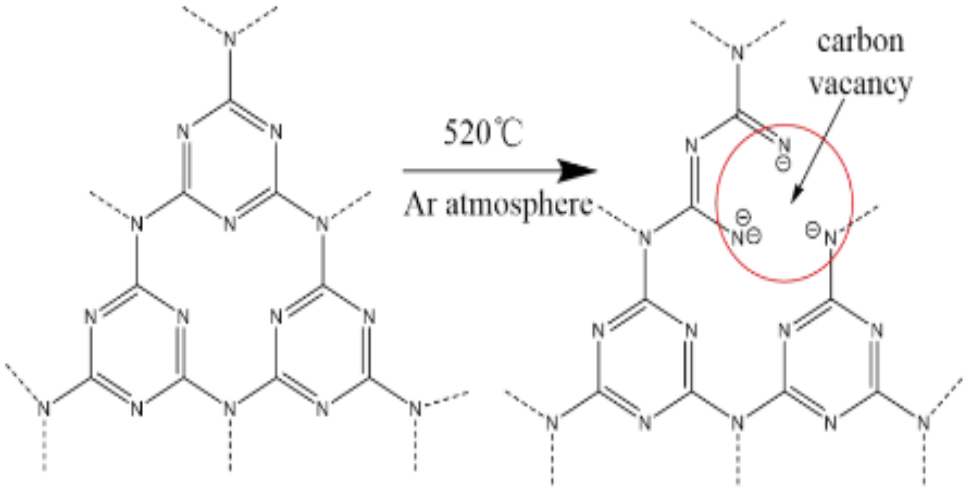

Figure 5. Carbon vacancies introduced on g-C_3N_4 framework [63].

1.3.2. Non-metal doping of g-C_3N_4

Further the doping strategy is considered with a high importance, to modify the physico-chemical properties of g-C_3N_4 while incorporating the elements into the framework (Fig. 6). This enables to tailor surface morphology, electronic and optical properties. Since bulk g-C_3N_4 absorbs in UV and near-visible region of the spectrum, this strategy allows to shift the absorption of irradiation more in visible region. It also helps to reduce the rate of recombination of photo-excited electrons and holes [69]. Different non-metallic elements doping were investigated, such as C-doping, N-doping, O-doping, S-doping, P-doping, F-doping [70, 71, 72, 73, 74, 75, 76] etc.

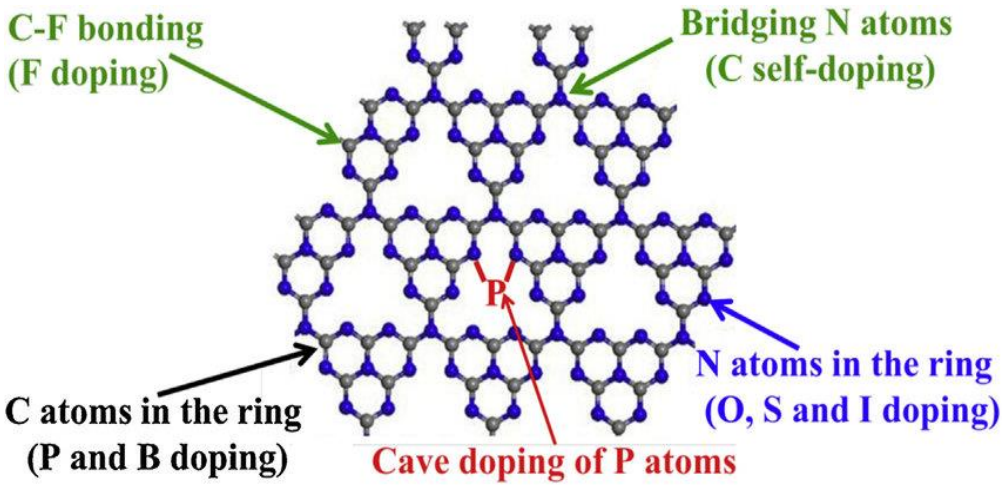

Figure 6. Possible substituted sites of non-metal doping in the single layer of g-C_3N_4 (permission from reference) [51].

Here, we have decided to focus mainly on C, O and F doping, since these strategies will be used in the upcoming Chapters. Carbon atoms could be introduced into the g-C_3N_4 structure, and replace the bridging N atoms. They can also be added as C=C chromophores and extends the π-conjugated system, thus narrowing the semiconductor bandgap and improve optical properties [77, 78, 65]. While on the hand the O-doped g-C_3N_4 can be prepared from calcination of a mixture of oxalic acid (source of O and C) and urea (source of C and N) one among of many methods [79]. This mixture has provided changes in the morphology compared to pure and dense g-C_3N_4 obtained only with urea, since it exhibits a flourishing porous structure. Apart from this advantage the O-doped g-C_3N_4 exhibit a modified electronic structure due to electron-rich O atoms. Metal-free properties of g-C_3N_4 could be modified with the strategy of non-metal doping. Among the non-metal elements, the role of halogens incorporation into the g-C_3N_4 has gain attention recently, including Cl-doped g-C_3N_4 [80], Br-doped g-C_3N_4 [81] and F-doped g-C_3N_4. The peculiarity of halogens is related to their high electronegativity which lead to covalent bond/ionic bond/metal bond formation when bonded to less electronegative element such as carbon and nitrogen. Focusing now more specifically on F-doped g-C_3N_4 material, different synthesis strategies were used for its preparation. Hydrothermal method based on NH_4F serving as a fluorine source mixed with g-C_3N_4, lead to the incorporation of F into the structure of g-C_3N_4, while forming poorly F-doped material only 6.7 at.%. It is proposed that F^- ions promotes the hydrothermal oxygenation

process by enhancing the hydrolysis and condensation progress of g-C_3N_4. In electronic point of view F-doped g-C_3N_4 sample displays a lower valence band level, and these oxygen containing groups could enhance the electron-hole separation efficiency under the light, favourable textural, optical properties and tailoring the electronic bandgap. This would improve the photocurrent response and photocatalytic activities toward organics [82, 83, 84]. Few studies were focused on increasing the F content while changing the strategy approach. Direct fluorination using dilute F_2 gas at high temperature was recently investigated. It enables to increase of F content into g-C_3N_4 framework up to 10 at. % [85] while conventional hydrothermal strategies were able to reach up to 6.7 at. % [86]. The benefits of gas phase, consists on the formation of porous structure of F-doped g-C_3N_4 material which increases the nitrogen vacancy defects and transformation of the hybridization mode from sp^2 to sp^3 due to substitution of N with F in the lattice of g-C_3N_4. Therefore, it tunes the CB and VB position with a narrowing the band gap [86] (Fig. 7). The performance of this material for photocatalytic H_2 evolution is higher compared to pristine g-C_3N_4. An enlargement of the surface area was observed due to formation of mesoporous in the g-C_3N_4 structure. The presence of F atoms could affect also the electron transition. Benefiting from these synergic effects, the separation of photogenerated charge carriers and the visible light absorption were improved. Thus, the performance in photocatalysis is enhanced [87, 85].

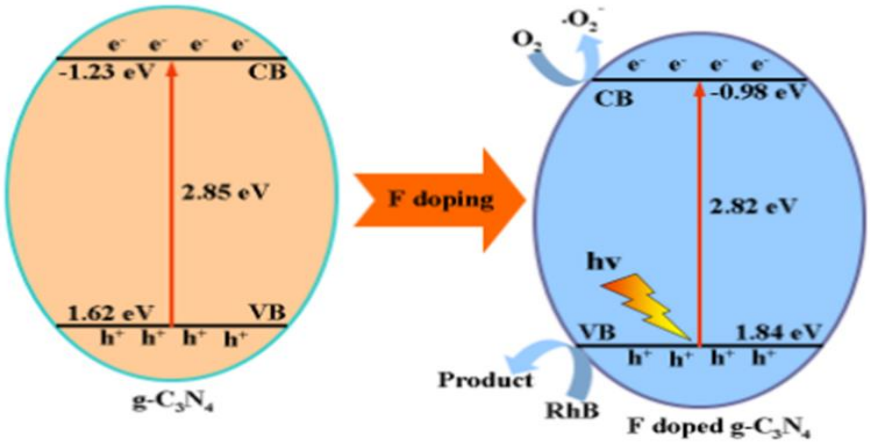

Figure 7. Mechanism for the enhanced photocatalytic activity of fluorine doped g-C_3N_4 and band gap modification [82].

1.3.3. Heterojunction engineering of g-C_3N_4 based materials

An interface between two semiconductors, where the semiconducting material possess unequal band gap compare to a homojunction, is called a heterojunction system [88]. Heterojunction engineering has been applied in the field of semiconductors for a long time, since it is a convenient way to tailor some of their electronic and photoelectronic properties.

To date, plenty of photocatalysts were developed with heterojunction, such as p-GaP/n-TiO_2, p-NiO/n-TiO_2 and p-$GaFe_2O_4$/n-$PbBi_2Nb_{1.9}W_{0.1}O_9$ or CdS/TiO_2, WO_3/TiO_2 [60], ZnO/TiO_2 and SnO_2/ZnO etc [89, 90, 91]. This trend also concerns the g-C_3N_4, since the pristine material suffers from some limitations, as mentioned previously. Therefore, in order to improve the electron/holes charge separation, plenty of g-C_3N_4 based heterojunctions were constructed, like $BiVO_4$/g-C_3N_4 [92], Cu/g-C_3N_4, TiO_2 /g-C_3N_4, ZnO/g-C_3N_4 [39, 24] .

In order to clarify how the heterojunction behaves, the g-C_3N_4/TiO_2 heterojunction system is illustrated and the mechanism of photoexcited electron-hole separation under visible light is described in Fig. 8. Firstly the visible-light irradiation excites the electronic structures of TiO_2 and g-C_3N_4 in order to produce electron-hole pairs, thanks to their narrow band gaps. Obviously CB edge potential of g-C_3N_4 is more negative compare to TiO_2 [13, 93], therefore photoexcited electrons will be easily transfer from CB of g-C_3N_4 to CB of TiO_2 through the interface of these two semiconductors. On the other hand, TiO_2 possesses a more positive VB edge potential than g-C_3N_4 which will facilitate the transfer of photo-excited holes toward VB of g-C_3N_4. Since electron and holes are accumulated on the CB and VB of TiO_2 and g-C_3N_4 respectively, then they get separated from each other, with limitation of their recombination rate [94]. Hence, the interfacial charge-transfer reaction toward the pollutant degradation will be enhanced, which leads to the improvement of photocatalytic activity of mentioned semiconductor [95, 96].

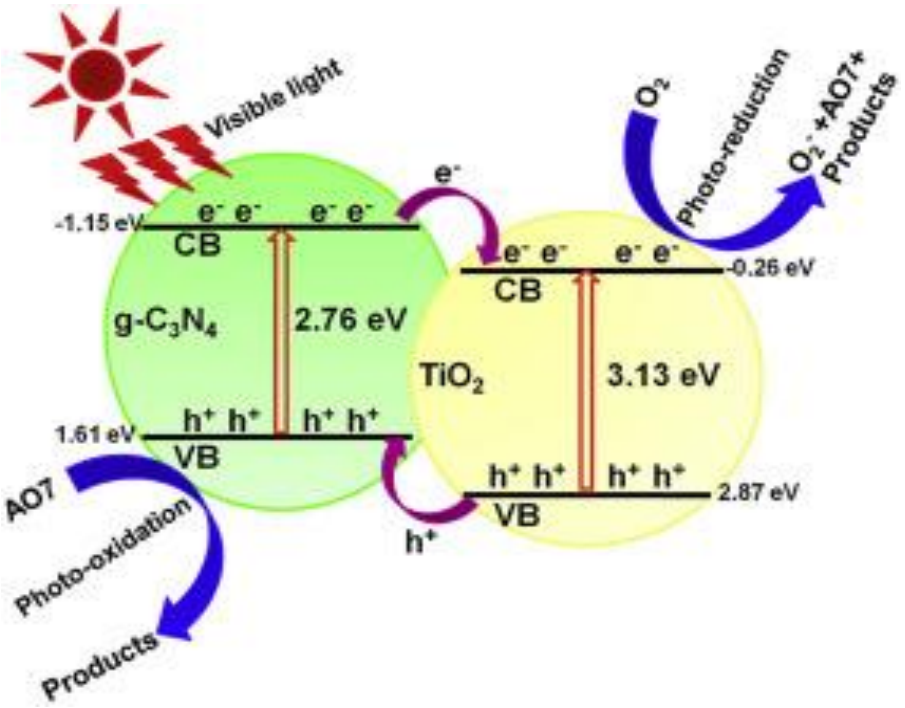

Figure 8. Mechanism for the photoexcited electron-hole separation and transport processes of AO7(pollutant) over g-C_3N_4/TiO_2 under visible-light irradiation (permission from reference) [94]. .

According to the different charge carriers separation mechanisms, g-C_3N_4 heterojunctions are classified into five types based on g-C_3N_4-metal sulphide photocatalyst model as schematized in Fig. 9. [97] named Type I, Type II heterojunction, p-n junction, Schottky junction, Z-scheme heterojunction (between the interfaces), Z-scheme heterojunction (with conductor).

Type I heterojunction, composed of semiconductor 1 (SEM 1) and semiconductor 2 (SEM 2), the VB of SEM 1 is lower than that of SEM 2, and opposite of CB, which is higher (Fig.9a). When the holes and electrons gain energy under light irradiation, photogenerated holes will be transferred from the VB of SEM 1 to the VB of SEM 2, and photo-excited electrons can be transferred from the CB of one semiconductor to another. Example of Type I heterojunctions could be mentioned SnS_2/g-C_3N_4 [98] and 2D MoS_2/g-C_3N_4 [99].

In Type II heterojunctions, two of the semiconductors are strongly bonded and build stable heterostructure. The SEM 1 and SEM 2 possess similar band potentials which are shown in Fig.9b. Generated holes in the VB of SEM 2 will be transferred to that of SEM 1, but is required that VB level of SEM 2 to be lower than that of SEM 1. Opposite behaviour is when the CB level of SEM

1 is higher than that of SEM 2, then photo-excited electrons in the CB of SEM1 will migrate to that of SEM 2. This cycle results in a spatial separation of charge carriers [100]. Therefore, electron-hole pair recombination could be hindered and the lifetime of electron could be increased. Most of the heterojunctions related to g-C_3N_4 described in the literature belong to Type II [101]. Among the Type II heterojunctions are CdS/g-C_3N_4 [102] and ZnS/g-C_3N_4 [103, 104] . Type II heterojunction appears as ideal to separate charge pairs, but it was shown to be not sufficient to overcome ultrafast electron-hole recombination [105] .

Thus, the idea was to construct p-n heterojunction (Fig.9c) which provides local extra electric field to accelerate the transfer of electron-hole pairs, while enhancing photocatalytic performance. The p-n heterojunction contains p-type semiconductor with the VB near to the Fermi level while for the n-type semiconductor, the CB is located near to the Fermi level [106]. Firstly, the holes from the p-type semiconductor will be transferred to the n-type, thus creating room for negative charge species while electrons follow the opposite way. When the Fermi level potentials reach the equilibrium, then electron and hole pairs will stop the diffusion, and at the end, at the interface between the two semiconductors, an electric field will be generated [107]. This electric field will facilitates the separation of photo-excited electron-hole pairs. In this context g-C_3N_4 is considered as n-type semiconductor due to NH/NH_2 groups acting as electron donors, while CuS is a p-type semiconductor, thus the constructing of CuS/g-C_3N_4 material is then composed of a p-n junction [108].

The Schottky junction is constructed by a semiconductor and a metal (Fig. 9d). Together, they form a space-charge separation region. The electrons are rapidly transferred from one side to another at the interface of two components [109]. An aligned of Fermi´s energy levels are formed, thus the recombination of the charge carriers is highly restricted with improvement of the photocatalytic performance. An example of Schottky junctions is NiS/g-C_3N_4 composite [110].

All the above-mentioned heterojunction photocatalysts have a significant contribution to the improvement of the electron-hole separation efficiency. Nevertheless, there are still limitations of the redox ability of composites, due to the fact that the oxidation and reduction process occur on the semiconductor which possess the lower oxidation and reduction potentials. In order to minimize these drawbacks Z-scheme heterojunction photocatalysts were constructed (Fig. 9e-f). Between the two semiconductor components, the charge transfer follow the pathway of Z-scheme (as letter Z), without addition of any electron mediators (Fig. 9e) [111, 112]. The Z-scheme

heterojunctions have gain attention, because they are enable to enhance redox potential and minimize the inefficient electron-hole pair recombination of the photocatalytic system [107]. Different g-C_3N_4 based Z-scheme heterojunctions were mentioned in the literature, including ternary photocatalysts system [113], like CdS/Au/g-C_3N_4 [114], CdS/Au/HCNS (hollow carbon nitride nanospheres) [115], g-C_3N_4/Ag/MoS_2 etc. Au and Ag are used as an electron mediator to accelerate the interparticles transfer of photogenerated electron-hole pairs [116]. Some of Z-scheme mechanisms are based on p and n type semiconductors. The p-type semiconductors include TiO_2, WO_3, $BiVO_4$, and $SrTiO_3$. They are efficient in the oxidation process to generate O_2, while n-type semiconductors $SrTiO_3$, TiO_2, ZrO_2, C_3N_4, and TaON, are efficient for reduction process to produce H_2.

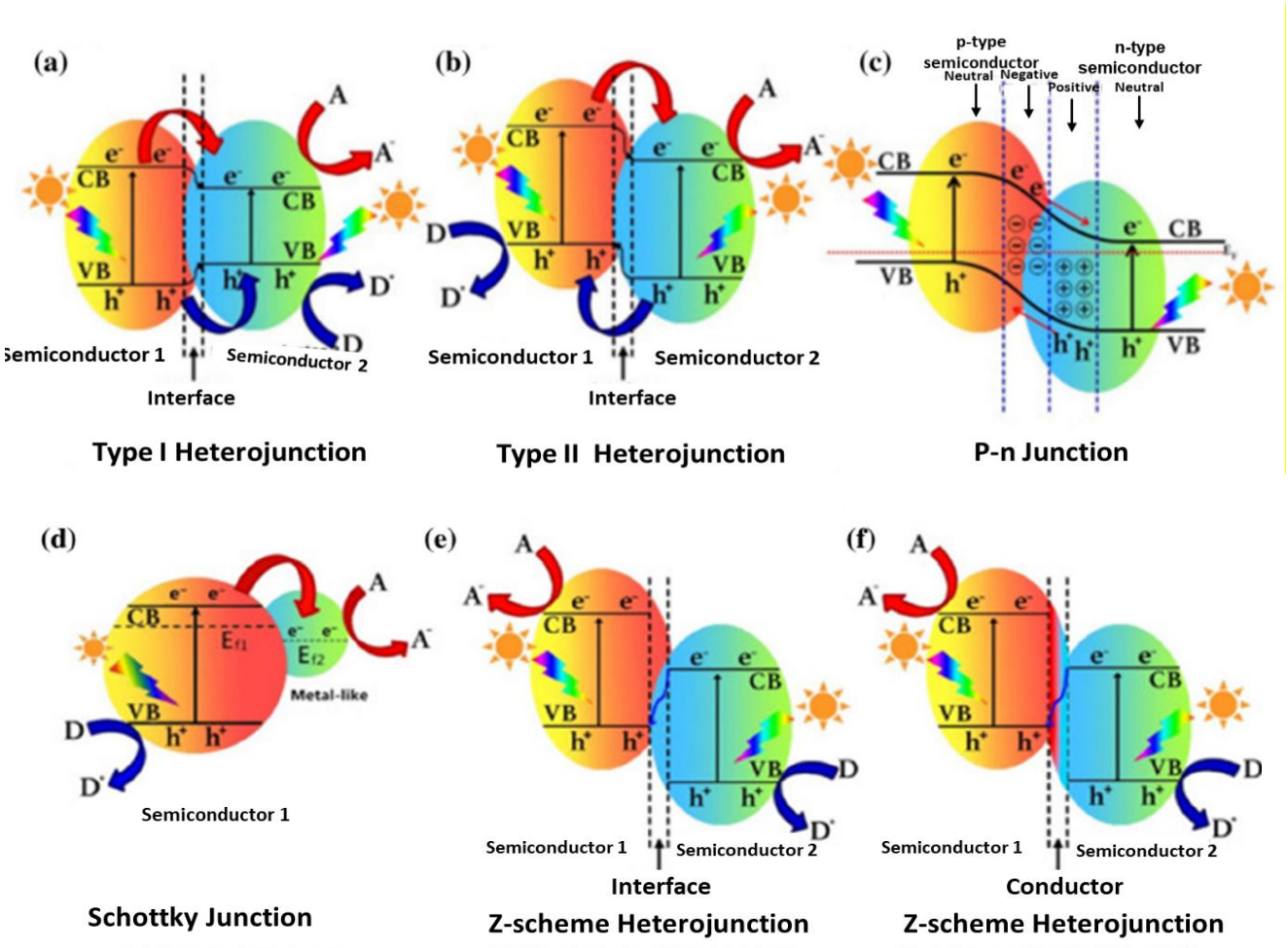

Figure 9. Different types of g-C_3N_4-based heterojunctions: a) Type I heterojunction, b) Type II heterojunction, c) p–n junction, d) Schottky junction, e) direct Z-scheme heterojunction (without an electron

mediator) and f) indirect Z-scheme (with an electron mediator). Note A, D and EF represent electron acceptor, electron donor and Fermi level respectively [117, 118].

1.3.4. Heterojunction based C/g-C_3N_4 composite

Few studies have been reported related to the construction of C/g-C_3N_4 heterojunctions. These studies have revealed that the addition of C into g-C_3N_4 could change its band gap, improve electron/hole pairs recombination, thus increasing the photocatalytic performance of water splitting [8]. The preparation of C/g-C_3N_4 heterojunctions were obtained by several routes; e.g from urea and chitin materials [119], cotton wool and urea [120] and from nanocellulose-derived C/g-C_3N_4 mixture [121]. All synthesis requires thermal or hydrothermal treatment, sonication, drying process, removing the solvent till obtaining the final product. Hence, facile method to obtain C/g-C_3N_4 heterojunctions based on the direct calcination of urea and glucose was employed recently, for the photocatalytic H_2 production under natural sunlight. Indeed, C/g-C_3N_4 heterojunction exhibits improvements compared to pristine g-C_3N_4 on following features: enhanced photocatalytic H_2 production, efficient charge carrier separation through intra Schottky junction induced by C-rich domains into g-C_3N_4, reduced the band gap, the enhancement of the optical absorption towards the visible region etc. [122]. Another route to introduce C into the g-C_3N_4 matrix could be done with melamine/agarose gel via two-step method, hydrothermal and calcination. Via this method onion-like carbon and 2D nanosheets morphology of the composite were obtained. The composite showed significant improvement in photoelectrochemical performance, with an increase in photocurrent intensity, and narrower band gap compared to bulk g-C_3N_4 [123, 124]. This indicates that separation and migration of photo-excited charges were improved, with a significant increase in porosity. The synergism effect of ultrathin 2D nanosheets structure remarkably improves the photocatalytic activity. Onion-like carbon structure enhances visible light absorption and acts as an electron receiver to facilitate charge separation and hinder the recombination, in addition the 2D nanosheets structure provides more active sites for the photocatalytic reaction [125].

1.4. Pore texture tailoring

Carbon nitride, as a metal-free material, possesses a considerable number of suitable properties for various applications. A strategy of particular importance is tailoring the porous structure. In Fig. 10 is described the endo and exo-tempalting strategies in order to synthesize porous and high-surface- area materials. For endo-templating, the templating species are occluded in the forming solid, while for exotemplating, a rigid porous solid is infiltrated with the precursor to yield another solid. The removal of endo and exotemplates from the composite led to porous and high-surface-area materials [126]. It enables an increase of the surface area by providing accessible pores and more active sites thus facilitating the molecular mass transfer, charge migration, surface reaction and light harvesting [127, 128, 129]. Photocatalytic performance is closely related to the aforementioned advantageous features, thus different pathways were used to prepare highly porous g-C_3N_4 with a variety of nanoarchitectures and morphology.

Among them, the following methods could be mentioned:

- Hard templating (nanocasting)

Using for example silica nanospheres as a template and urea as a precursor, in order to obtain sphere-like mesoporous morphology after carbonization and template removal [130].

As a matter of fact, the hard templating strategy seems to be quite effective. A facile synthesized mesoporous g-C_3N_4 photocatalyst, with a high surface area up to 550 $m^2\ g^{-1}$ [131, 132, 133] could be prepared by this route. To date, different kinds of hard templates such as $CaCO_3$ [134], mesoporous silica [135], porous anodic Al_2O_3 [136], have been used. However, the silica template method does not seem to be environmentally friendly due to the use of hazardous agents such as NH_4F or HF, which are used for the removal of silica templates. A large - scale production by the hard templating process for porous g-C_3N_4 or other porous g-C_3N_4-based composite photocatalysts is restricted to practical applications. Thus, for further development of highly porous g-C_3N_4 with different nanostructures, the focus was directed on porogen agents such as $CaCO_3$, Al_2O_3, Fe_2O_3, which enable an easy removal of the hard templates [132].

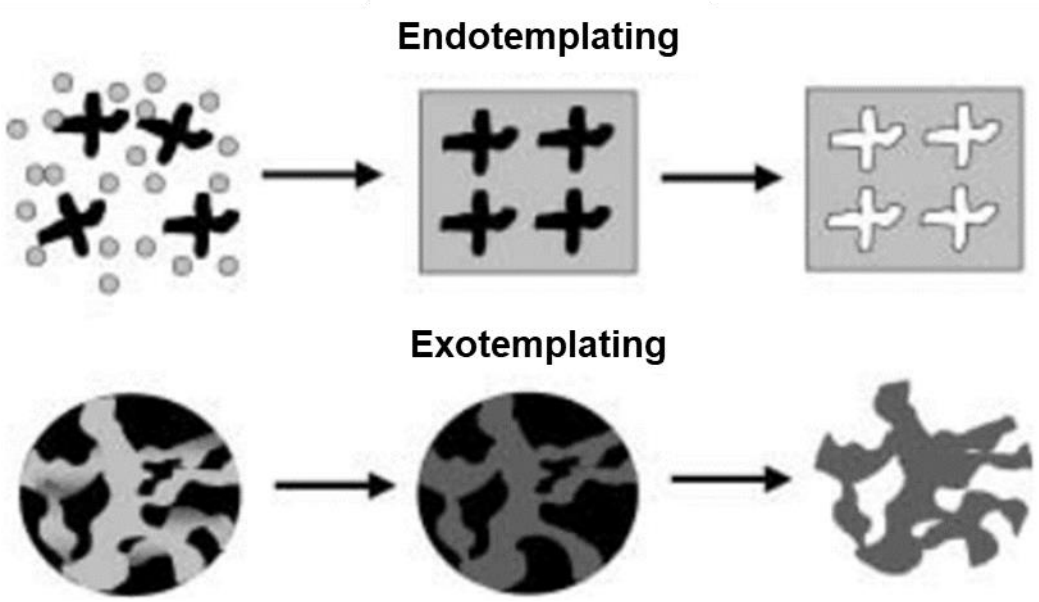

Figure 10. Illustration of endotemplating and exotemplating approaches [126].

- Self-templating or molecular cooperative assembly

The formation of supramolecular aggregates via physical interaction can strongly direct the reacting components or subunits and makes the design of assembly simple. Using the cooperative assembly between melamine and cyanuric acid (sub units) as a directing agent, particular mesostructure could be obtained. Hence, after carbonization leads to hollow spheres with mesopores, in the range of 4 to 36 nm, pore volume of 0.4 cm^{-3} g^{-1} and a surface area of 77 m^2 g^{-1} [137]. A combination of the soft templating process and thermal exfoliation during the calcination step enable to modify the texture and morphology of g-C_3N_4. For instance, the use of hexadecyl trimethyl ammonium chloride (CTAC) as the soft template promotes the formation of pores within g-C_3N_4 structure. This process occurs during the thermal condensation of melamine by CTAC decomposition and release of volatile species (Fig. 11). Here, the CTAC acts more as an organic porogen agent than a soft-template since supramolecular self-assembly with melamine and CTAC was not demonstrated.

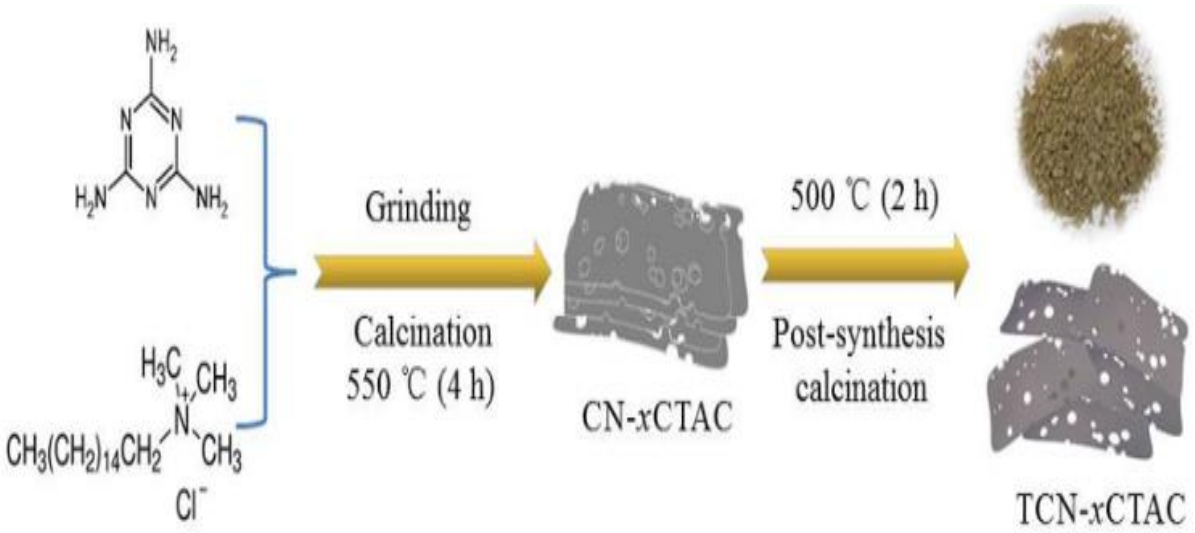

Figure 11. "Soft-templating" strategy to prepare porous g-C_3N_4 nanosheets [138].

The g-C_3N_4 nanosheets with improved textural properties typically exhibit Type IV adsorption-desorption isotherm with H3 hysteresis loop, which is mainly attributed to the presence of mesopores. In Fig. 12 is shown the nitrogen adsorption-desorption isotherm of the pure exfoliated g-C_3N_4 with its pore size distribution.

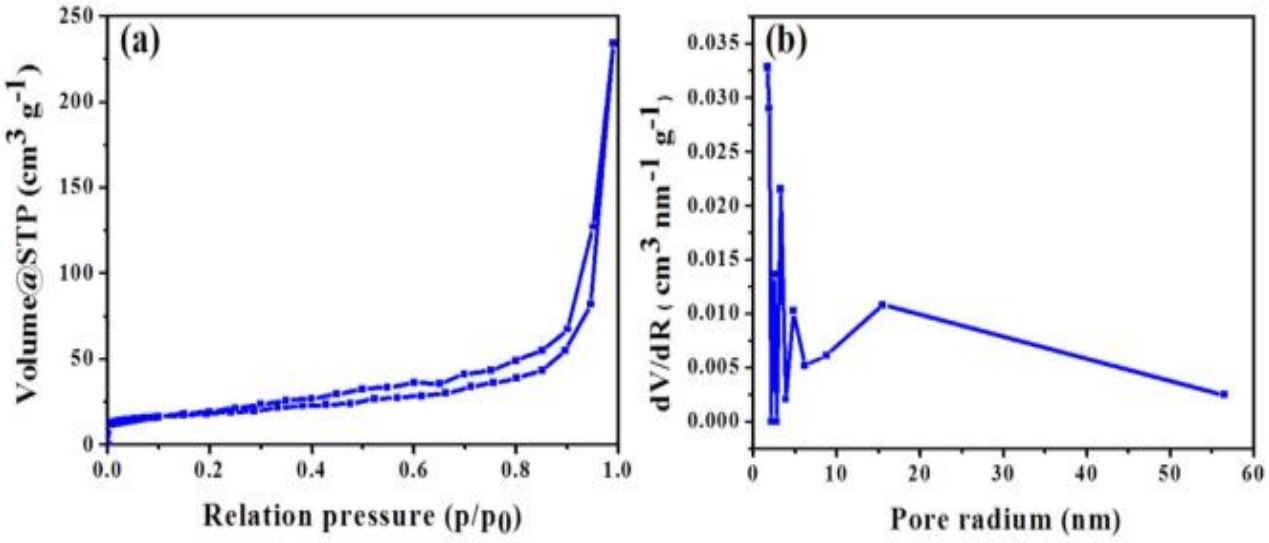

Figure 12. (a) Nitrogen adsorption-desorption isotherms of exfoliated pure g-C_3N_4 and (b) corresponding pore size distribution curves [139].

1.4.1. Adsorption properties

Porous texture and surface chemical properties are among the main features for adsorption properties of an adsorbent. Usually, the increase in the specific surface area of a photocatalyst increases the number of active sites (per g of sample). Conventional methods of preparation of g-C_3N_4 with the pyrolysis of N-rich compounds yield bulk structure with limited specific surface area and active sites with limited photocatalytic performance [140, 141, 142, 143]. Similar to the graphene or graphene oxide materials, carbon nitride possesses the ability to adsorb various adsorbates with the aid of the multiple different functional groups e.g NH_2 groups (Fig. 13). Protonation and deprotonation in an aqueous suspension also occurred for g-C_3N_4 powder. The highest efficiency of the adsorption properties is most likely related to electrostatic and chemical interactions, including interactions between hydrogen ions, hydroxyl ions, and certain groups on the g-C_3N_4 surface [144, 145, 146, 147, 148]. The pH of the system directs the degree of these chemical interactions, which results in different surface charges and zeta potentials of g-C_3N_4. It is worth mentioning that the C-N and –NH_2/–NH–/=N surface basic groups located on the g-C_3N_4 structure have a crucial role on adsorption properties of toxic molecules, especially metal ions [149, 150, 151].

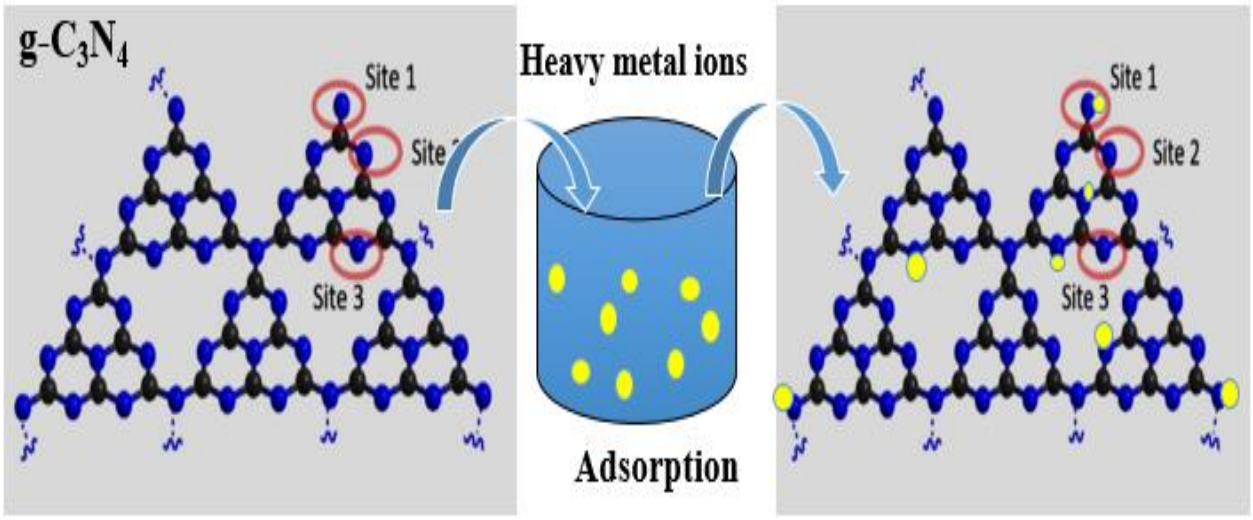

Figure 13. Adsorption of heavy metal ions onto g-C_3N_4, directed toward surface basic (=N, -NH-) groups [152].

1.5. Applications of g-C_3N_4

Graphitic carbon nitride possess a wide range of applications in various fields, including sensing, biomedical applications, wastewater and environment treatment, utilisation of sunlight and device making components [153].

1.5.1. Solar energy Utilization

From the numerous applications of g-C_3N_4, the production of the photo-electrode under visible light irradiation and the generation of photo-current is an ability of g-C_3N_4. The most challenging approach is the utilisation of solar fuel with CO_2 and water to produce clean fuels such as CO, H_2 or hydrocarbon platform molecules as a promising way using sunlight as a ‘‘smart‘‘ solution in energy demands [154, 155].

1.5.2. Wastewater and Environmental Treatment

g-C_3N_4 is best known as a potential photocatalyst for the degradation of variety of pollutants [156] [34]. The structure, synthesis, and preparation techniques of g-C_3N_4 nanosheets also determine the efficiency of the photocatalyst and its application in relation to wastewater treatment. The preparation of the materials with metal [157, 158] or non-metal doping [159] and co-doping [160] have been widely used for water and environmental treatment [24]. Unrealized application on wastewater, and the potential contamination that most photocatalysts cause in the environment, have given obstacles, as high cost, small-scale production, low-photocatalytic activity and recycling. Methyl orange as a target contaminant has been tested in the presence of many catalysts. Therefore, here is elaborated the typical mechanism of methyl orange (MO) photodegradation in the presence of g-C_3N_4/CuS heterojunction (Fig. 14). All steps were described based on principle of a heterojunction behaviour [161]. During the photodegradation process induced by light, some active species are formed, including hydroxyl radicals $^{\bullet}OH$, superoxide $HOO^{\bullet}$ and holes (h^+). The CuS semiconductor possesses a CB value higher than the redox potential of $O_2/^{\bullet}O_2^-$ (– 0.33eV),

presuming that the electrons (e^-) in the CB of CuS could not be able to reduce O_2 into $^{\bullet}O_2^-$ (Eq.1 and 2).

$O_2 + e^- \rightarrow {}^{\bullet}O_2$……(1)

$^{\bullet}O_2^- + 2H^+ + e^- \rightarrow H_2O_2$…….....(2)

$H_2O_2 + e^- \rightarrow {}^{\bullet}OH + OH^-$…….....….(3)

$MO + h^+ \rightarrow$ products $\rightarrow CO_2 + H_2O$…….....…..(4)

$MO + {}^{\bullet}OH \rightarrow$ products $\rightarrow CO_2 + H_2O$…….....…….(5)

After the H_2O_2 is activated with the existence of photo-electrons, responsible for MO degradation [162] (Eq.(3)), then $^{\bullet}OH$ species are formed. Furthermore, electron consumption could reduce the recombination probability of photogenerated electron-hole pairs, extending the lifetime of separated h^+ and e^-, and finally increasing the active species concentration. However, the potential energy of photogenerated h^+ in g-C_3N_4 was insufficient to oxidize H_2O or OH^- into the $^{\bullet}OH$ radicals ($^{\bullet}OH/H_2O$ = +2.27 eV) [163]. Therefore MO molecules could directly be oxidized and degraded by these reactive species ($^{\bullet}OH$ and h^+, etc.) efficiently (Eqs. (4) and (5)) [164, 41, 165].

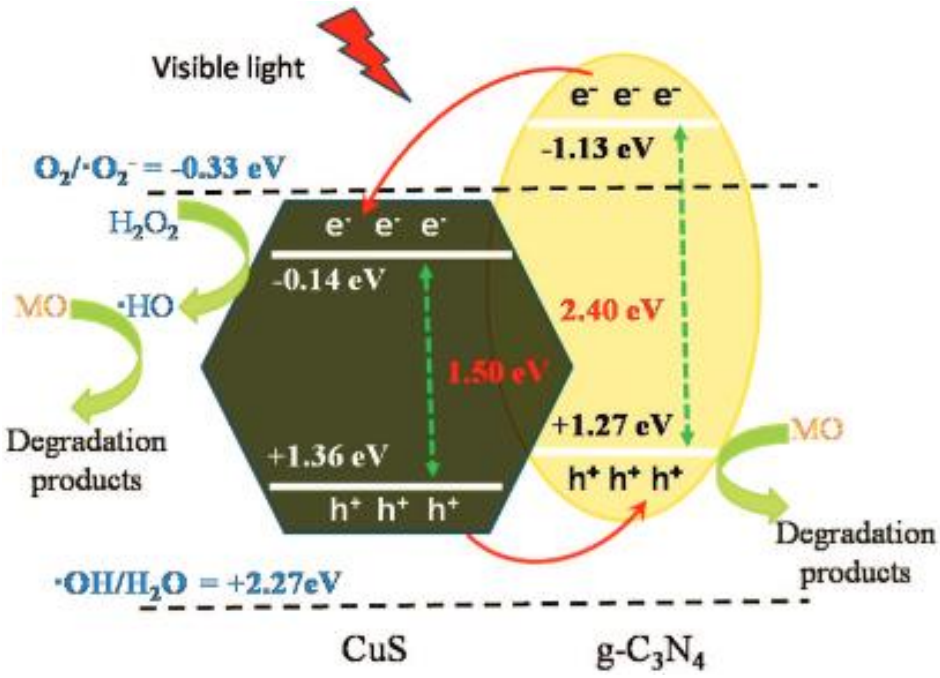

Figure 14. Schematic diagram for visible light photocatalytic mechanism of methylorange photodegradation on a g-C_3N_4/CuS composites [108] .

The water splitting approach to produce H_2 and O_2 as clean fuels using photocatalysts with sufficient potential is quite a promising strategy. The photocatalytic reactions are initiated by excitation of the semiconductor photocatalyst with light energy equal to or greater than the bandgap energy (Eg) of the material [165]. Once the semiconductor is excited by irradiation in the presence of air or without air (O_2), then separated electrons and holes follow several reaction pathways. The recombination of e^-/h^+ pairs takes place firstly, since they could recombine easily with each other on/in the semiconductor surface/volume [166]. The capacity of the photo-generated species (the e^-/h^+ pairs) could promote the redox reaction (reduction of hydrogen and oxidation of biomass). These reactions depend on the conduction and valence band positions compared to the red-ox potentials of H_2O/H_2 and O_2/H_2O respectively. In the second step, water is splited to generate H_2 and O_2 under anaerobic conditions (Fig. 15). The H^+ species are reduced by receiving the electrons to H_2 molecules, respecting the condition that the potential of E (H_2/H^+) is higher than E_{CB}, on the other hand, water is oxidized by holes to O_2 ($E_{VB} > E^o$ (O_2/H_2O) [167].

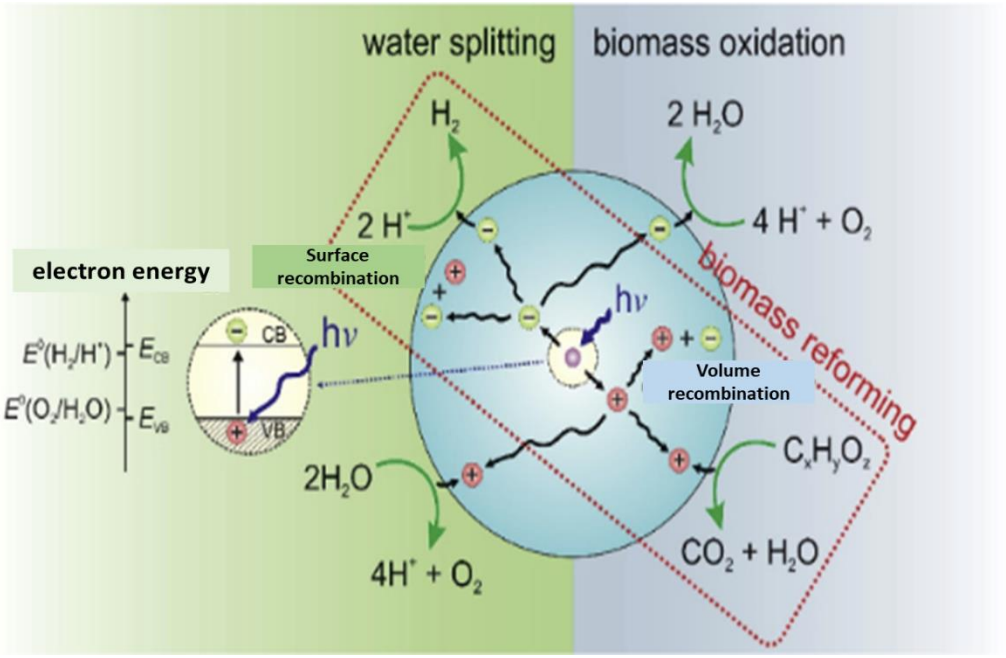

Figure 15. The schematic representation of possible reaction pathways by excitation of the semiconductor with light energy under anaerobic/aerobic conditions: water splitting (left-hand reaction), biomass oxidation (right-hand reaction), and photo-reforming (rectangular reaction) [168].

1.5.3. Biomedical and Sensing Applications

The alteration of the molecular structure of g-C_3N_4 is important in order to facilitate its handling in water. Hence, it may be relevant in applications of sensing field, biotherapy and bioimaging. Due to its light photoluminescence, highly recommended for biological related use, the g-C_3N_4 nanomaterial is a very essential candidate for biomedical and sensing applications. Ultrathin g-C_3N_4 nanosheets could be used as biomarkers for the labelling of the cell membranes. Moreover, g-C_3N_4 was considered a potential photosensitiser and pH-responsive drug nanocarrier for cancer imaging and therapy [169].

SUMMARY IN FRENCH

Un grand nombre de semi-conducteurs tels que TiO_2, WO_3, ZnO et CuO ont été testés comme photocatalyseurs pour produire de l'hydrogène par décomposition de l'eau. Cependant, ces photocatalyseurs présentent quelques limitations. Ils sont pour la plupart à base de métaux avec des ressources naturelles limitées, possèdent une surface spécifique limitée avec une bande interdite large (absorption dans l'UV principalement) et présentent une recombinaison rapide des paires électron-trou. Pour tenter de réduire la pollution et essayer de développer de nouveaux vecteurs énergétiques durables, la conception et la synthèse de photocatalyseurs efficients a suscité un intérêt scientifique croissant dans le monde de la recherche. Ces dernières années, le nitrure de carbone graphitique (g-C_3N_4) a montré de nouvelles applications potentielles dans le domaine de la photocatalyse en raison de ses propriétés uniques. Cependant, l'efficacité photocatalytique du g-C_3N_4 est aussi limitée par le taux élevé de recombinaison des paires électron-trou photo-induites et son absorption réduite dans le domaine visible. Une stratégie, peu reportée dans la littérature, est de nanostructurer le carbonitrure en présence d'un excès de C afin de présenter des sites actifs supplémentaires accessibles aux réactifs et aussi favoriser la séparation des charges des paires électron-trou.

Les principales méthodes de synthèse de g-C_3N_4 sont reportées, telles que la pyrolyse de précurseurs contenant de l'azote et du carbone (ex : mélamine, dicynamide et urée). D'autres voies de synthèse sont aussi présentées avec les différentes hétérojonctions obtenues à base de g-C_3N_4.

References

[1] G. Xiao *et al.*, 'Superior adsorption performance of graphitic carbon nitride nanosheets for both cationic and anionic heavy metals from wastewater', *Chinese Journal of Chemical Engineering*, vol. 27, no. 2, pp. 305–313, Feb. 2019, doi: 10.1016/j.cjche.2018.09.028.

[2] Q. Liao *et al.*, 'Using of g-C 3 N 4 nanosheets for the highly efficient scavenging of heavy metals at environmental relevant concentrations', *Journal of Molecular Liquids*, vol. 261, pp. 32–40, Jul. 2018, doi: 10.1016/j.molliq.2018.03.093.

[3] J. Wang and S. Wang, 'Removal of pharmaceuticals and personal care products (PPCPs) from wastewater: A review', *Journal of Environmental Management*, vol. 182, pp. 620–640, Nov. 2016, doi: 10.1016/j.jenvman.2016.07.049.

[4] Y. Pi *et al.*, 'Adsorptive and photocatalytic removal of Persistent Organic Pollutants (POPs) in water by metal-organic frameworks (MOFs)', *Chemical Engineering Journal*, vol. 337, pp. 351–371, Apr. 2018, doi: 10.1016/j.cej.2017.12.092.

[5] M. von Sperling, *Wastewater characteristics, treatment and disposal*. London: IWA Publ. [u.a.], 2007.

[6] A. Mishra, A. Mehta, S. Basu, N. P. Shetti, K. R. Reddy, and T. M. Aminabhavi, 'Graphitic carbon nitride (g–C3N4)–based metal-free photocatalysts for water splitting: A review', *Carbon*, vol. 149, pp. 693–721, Aug. 2019, doi: 10.1016/j.carbon.2019.04.104.

[7] A. Yuda and A. Kumar, 'A review of g-C3N4 based catalysts for direct methanol fuel cells', *International Journal of Hydrogen Energy*, vol. 47, no. 5, pp. 3371–3395, Jan. 2022, doi: 10.1016/j.ijhydene.2021.01.080.

[8] Y. Li *et al.*, 'Preparation of Carbon-Rich *g* -C $_3$ N $_4$ Nanosheets with Enhanced Visible Light Utilization for Efficient Photocatalytic Hydrogen Production', *Small*, vol. 13, no. 33, p. 1701552, Sep. 2017, doi: 10.1002/smll.201701552.

[9] R. Wang, X. Wang, X. Li, L. Pei, X. Gu, and Z. Zheng, 'Facile one-step synthesis of porous graphene-like g-C3N4 rich in nitrogen vacancies for enhanced H2 production from photocatalytic aqueous-phase reforming of methanol', *International Journal of Hydrogen Energy*, vol. 46, no. 1, pp. 197–208, Jan. 2021, doi: 10.1016/j.ijhydene.2020.09.156.

[10] K. Kočí *et al.*, 'Photocatalytic hydrogen production from methanol over Nd/TiO2', *Journal of Photochemistry and Photobiology A: Chemistry*, vol. 366, pp. 55–64, Nov. 2018, doi: 10.1016/j.jphotochem.2018.03.007.

[11] E. Carpio, P. Zúñiga, S. Ponce, J. Solis, J. Rodriguez, and W. Estrada, 'Photocatalytic degradation of phenol using TiO2 nanocrystals supported on activated carbon', *Journal of Molecular Catalysis A: Chemical*, vol. 228, no. 1–2, pp. 293–298, Mar. 2005, doi: 10.1016/j.molcata.2004.09.066.

[12] L. Ma *et al.*, 'Protonation of Graphitic Carbon Nitride (g-C $_3$ N $_4$) for an Electrostatically Self-Assembling Carbon@g-C $_3$ N $_4$ Core–Shell Nanostructure toward High Hydrogen Evolution', *ACS Sustainable Chem. Eng.*, vol.5, no.8, pp.7093–7103, Aug. 2017, doi: 10.1021/acssuschemeng.7b01312.

[13] F. Meng et al, 'Temperature dependent photocatalysis of g-C3N4, TiO2 and ZnO: differences in photoactive mechanism', *Journal of Colloid and Interface Science* p. 27, doi:10.1016/j.jcis.2018.07.131.

[14] A. Naseri, M. Samadi, A. Pourjavadi, A. Z. Moshfegh, and S. Ramakrishna, 'Graphitic carbon nitride (g-C $_3$ N $_4$)-based photocatalysts for solar hydrogen generation: recent advances and future development directions', *J. Mater. Chem. A*, vol. 5, no. 45, pp. 23406–23433, 2017, doi: 10.1039/C7TA05131J.

[15] Q. Han, B. Wang, J. Gao, and L. Qu, 'Graphitic Carbon Nitride/Nitrogen-Rich Carbon Nanofibers: Highly Efficient Photocatalytic Hydrogen Evolution without Cocatalysts', *Angew. Chem.*, vol. 128, no. 36, pp. 11007–11011, Aug. 2016, doi: 10.1002/ange.201605591.

[16] J. Zhang, M. Zhang, S. Lin, X. Fu, and X. Wang, 'Molecular doping of carbon nitride photocatalysts with tunable bandgap and enhanced activity', *Journal of Catalysis*, vol. 310, pp. 24–30, Feb. 2014, doi: 10.1016/j.jcat.2013.01.008.

[17] M. Mishra and D.-M. Chun, 'α-Fe 2 O 3 as a photocatalytic material: A review', *Applied Catalysis A: General*, vol. 498, pp. 126–141, Jun. 2015, doi: 10.1016/j.apcata.2015.03.023.

[18] P. A. Luque *et al.*, 'Improved photocatalytic efficiency of SnO2 nanoparticles through green synthesis', *Optik*, vol. 206, p. 164299, Mar. 2020, doi: 10.1016/j.ijleo.2020.164299.

[19] M. A., M. J., M. Ashokkumar, and P. Arunachalam, 'A review on BiVO 4 photocatalyst: Activity enhancement methods for solar photocatalytic applications', *Applied Catalysis A: General*, vol. 555, pp. 47–74, Apr. 2018, doi: 10.1016/j.apcata.2018.02.010.

[20] X. Liu *et al.*, 'Hollow CdS-based photocatalysts', *Journal of Materiomics*, vol. 7, no. 3, pp. 419–439, May 2021, doi: 10.1016/j.jmat.2020.10.010.

[21] G.-J. Lee and J. J. Wu, 'Recent developments in ZnS photocatalysts from synthesis to photocatalytic applications — A review', *Powder Technology*, vol. 318, pp. 8–22, Aug. 2017, doi: 10.1016/j.powtec.2017.05.022.

[22] M. Singh *et al.*, 'Oxygen-deficient photostable Cu $_2$ O for enhanced visible light photocatalytic activity', *Nanoscale*, vol. 10, no. 13, pp. 6039–6050, 2018, doi: 10.1039/C7NR08388B.

[23] L. Zhou *et al.*, 'Graphitic carbon nitride (g-C $_3$ N $_4$) as a sustainable heterogeneous photocatalyst for metal free and oxygen-tolerant photo-atom transfer radical polymerization (photo-ATRP)', *Green Chem.*, vol. 23, no. 23, pp. 9617–9624, 2021, doi: 10.1039/D1GC03604A.

[24] G. Dong, Y. Zhang, Q. Pan, and J. Qiu, 'A fantastic graphitic carbon nitride (g-C3N4) material: Electronic structure, photocatalytic and photoelectronic properties', *Journal of Photochemistry and Photobiology C: Photochemistry Reviews*, vol. 20, pp. 33–50, Sep. 2014, doi: 10.1016/j.jphotochemrev.2014.04.002.

[25] D. Wang *et al.*, 'Coal tar pitch derived N-doped porous carbon nanosheets by the in-situ formed g-C3N4 as a template for supercapacitor electrodes', *Electrochimica Acta*, vol. 283, pp. 132–140, Sep. 2018, doi: 10.1016/j.electacta.2018.06.151.

[26] H. M. Shanshool, M. Yahaya, W. M. M. Yunus, and I. Y. Abdullah, 'Investigation of energy band gap in polymer/ZnO nanocomposites', *J Mater Sci: Mater Electron*, vol. 27, no. 9, pp. 9804–9811, Sep. 2016, doi: 10.1007/s10854-016-5046-8.

[27] C. Dette *et al.*, 'TiO_2 Anatase with a Bandgap in the Visible Region', *Nano Lett.*, vol. 14, no. 11, pp. 6533–6538, Nov. 2014, doi: 10.1021/nl503131s.

[28] Y. Wang, X. Wang, and M. Antonietti, 'Polymeric Graphitic Carbon Nitride as a Heterogeneous Organocatalyst: From Photochemistry to Multipurpose Catalysis to Sustainable Chemistry', *Angew. Chem. Int. Ed.*, vol. 51, no. 1, pp. 68–89, Jan. 2012, doi: 10.1002/anie.201101182.

[29] X. Wang, S. Blechert, and M. Antonietti, 'Polymeric Graphitic Carbon Nitride for Heterogeneous Photocatalysis', *ACS Catal.*, vol. 2, no. 8, pp. 1596–1606, Aug. 2012, doi: 10.1021/cs300240x.

[30] X. Li *et al.*, 'Preparation and characterization of graphitic carbon nitride through pyrolysis of melamine', *Appl. Phys. A*, vol. 94, no. 2, pp. 387–392, Feb. 2009, doi: 10.1007/s00339-008-4816-4.

[31] A. Thomas *et al.*, 'Graphitic carbon nitride materials: variation of structure and morphology and their use as metal-free catalysts', *J. Mater. Chem.*, vol. 18, no. 41, p. 4893, 2008, doi: 10.1039/b800274f.

[32] P. Kumar *et al.*, 'C_3N_5 : A Low Bandgap Semiconductor Containing an Azo-Linked Carbon Nitride Framework for Photocatalytic, Photovoltaic and Adsorbent Applications', *J. Am. Chem. Soc.*, vol. 141, no. 13, pp. 5415–5436, Apr. 2019, doi: 10.1021/jacs.9b00144.

[33] K. Wang, X. Wang, H. Pan, Y. Liu, S. Xu, and S. Cao, 'In situ fabrication of CDs/g-C3N4 hybrids with enhanced interface connection via calcination of the precursors for photocatalytic H2 evolution', *International Journal of Hydrogen Energy*, vol. 43, no. 1, pp. 91–99, Jan. 2018, doi: 10.1016/j.ijhydene.2017.11.003.

[34] W.-J. Ong, L.-L. Tan, Y. H. Ng, S.-T. Yong, and S.-P. Chai, 'Graphitic Carbon Nitride ($g-C_3N_4$)-Based Photocatalysts for Artificial Photosynthesis and Environmental Remediation: Are We a Step Closer To Achieving Sustainability?', *Chem. Rev.*, vol. 116, no. 12, pp. 7159–7329, Jun. 2016, doi: 10.1021/acs.chemrev.6b00075.

[35] Y. Zheng, Z. Zhang, and C. Li, 'A comparison of graphitic carbon nitrides synthesized from different precursors through pyrolysis', *Journal of Photochemistry and Photobiology A: Chemistry*, vol. 332, pp. 32–44, Jan. 2017, doi: 10.1016/j.jphotochem.2016.08.005.

[36] Y. Hong *et al.*, 'A direct one-step synthesis of ultrathin g-C3N4 nanosheets from thiourea for boosting solar photocatalytic H2 evolution', *International Journal of Hydrogen Energy*, vol. 44, no. 14, pp. 7194–7204, Mar. 2019, doi: 10.1016/j.ijhydene.2019.01.274.

[37] G. Xin and, Y. Meng ´Pyrolysis Synthesized g-C3N4 for Photocatalytic Degradation of Methylene Blue, *Journal of Chemistry* Volume 2013, p. 5, Oct. 2012 http://dx.doi.org/10.1155/2013/187912

[38] P. Praus, 'A brief review of s-triazine graphitic carbon nitride', *Carbon Lett.*, Jan. 2022, doi: 10.1007/s42823-022-00319-9.

[39] A. Alaghmandfard and K. Ghandi, ‘A Comprehensive Review of Graphitic Carbon Nitride (g-C3N4)–Metal Oxide-Based Nanocomposites: Potential for Photocatalysis and Sensing’, *Nanomaterials*, vol. 12, no. 2, p. 294, Jan. 2022, doi: 10.3390/nano12020294.

[40] X. Wang *et al.*, ‘A metal-free polymeric photocatalyst for hydrogen production from water under visible light’, *Nature Mater*, vol. 8, no. 1, pp. 76–80, Jan. 2009, doi: 10.1038/nmat2317.

[41] S. C. Yan, Z. S. Li, and Z. G. Zou, ‘Photodegradation Performance of g-C $_3$ N $_4$ Fabricated by Directly Heating Melamine’, *Langmuir*, vol. 25, no. 17, pp. 10397–10401, Sep. 2009, doi: 10.1021/la900923z.

[42] T. Tyborski, C. Merschjann, S. Orthmann, F. Yang, M.-C. Lux-Steiner, and T. Schedel-Niedrig, ‘Crystal structure of polymeric carbon nitride and the determination of its process-temperature-induced modifications’, *J. Phys.: Condens. Matter*, vol. 25, no. 39, p. 395402, Oct. 2013, doi: 10.1088/0953-8984/25/39/395402.

[43] A. Thomas *et al.*, ‘Graphitic carbon nitride materials: variation of structure and morphology and their use as metal-free catalysts’, *J. Mater. Chem.*, vol. 18, no. 41, p. 4893, 2008, doi: 10.1039/b800274f.

[44] E. Wirnhier, M. B. Mesch, J. Senker, and W. Schnick, ‘Formation and Characterization of Melam, Melam Hydrate, and a Melam-Melem Adduct’, *Chem. Eur. J.*, vol. 19, no. 6, pp. 2041–2049, Feb. 2013, doi: 10.1002/chem.201203340.

[45] A. Sattler *et al.*, ‘Melamine–Melem Adduct Phases: Investigating the Thermal Condensation of Melamine’, *Chem. Eur. J.*, vol. 15, no. 47, pp. 13161–13170, Dec. 2009, doi: 10.1002/chem.200901518.

[46] B. Jürgens, E. Irran, J. Senker, P. Kroll, H. Müller, and W. Schnick, ‘Melem (2,5,8-Triamino-tri- *s* -triazine), an Important Intermediate during Condensation of Melamine Rings to Graphitic Carbon Nitride: Synthesis, Structure Determination by X-ray Powder Diffractometry, Solid-State NMR, and Theoretical Studies’, *J. Am. Chem. Soc.*, vol. 125, no. 34, pp. 10288–10300, Aug. 2003, doi: 10.1021/ja0357689.

[47] B. V. Lotsch and W. Schnick, ‘New Light on an Old Story: Formation of Melam during Thermal Condensation of Melamine’, *Chem. Eur. J.*, vol. 13, no. 17, pp. 4956–4968, Jun. 2007, doi: 10.1002/chem.200601291.

[48] B. V. Lotsch *et al.*, ‘Unmasking Melon by a Complementary Approach Employing Electron Diffraction, Solid-State NMR Spectroscopy, and Theoretical Calculations—Structural Characterization of a Carbon Nitride Polymer’, *Chem. Eur. J.*, vol. 13, no. 17, pp. 4969–4980, Jun. 2007, doi: 10.1002/chem.200601759.

[49] W. Wei and T. Jacob, ‘Strong excitonic effects in the optical properties of graphitic carbon nitride g -C 3 N 4 from first principles’, *Phys. Rev. B*, vol. 87, no. 8, p. 085202, Feb. 2013, doi: 10.1103/PhysRevB.87.085202.

[50] S. Cao, J. Low, J. Yu, and M. Jaroniec, ‘Polymeric Photocatalysts Based on Graphitic Carbon Nitride’, *Adv. Mater.*, vol. 27, no. 13, pp. 2150–2176, Apr. 2015, doi: 10.1002/adma.201500033.

[51] J. Wen, J. Xie, X. Chen, and X. Li, ‘A review on g-C 3 N 4 -based photocatalysts’, *Applied Surface Science*, vol. 391, pp. 72–123, Jan. 2017, doi: 10.1016/j.apsusc.2016.07.030.

[52] E. Alwin, K. Kočí, R. Wojcieszak, M. Zieliński, M. Edelmannová, and M. Pietrowski, ‘Influence of High Temperature Synthesis on the Structure of Graphitic Carbon Nitride and Its Hydrogen Generation Ability’, *Materials*, vol. 13, no. 12, p. 2756, Jun. 2020, doi: 10.3390/ma13122756.

[53] G. Fanchini, A. Tagliaferro, N. M. J. Conway, and C. Godet, ‘Role of lone-pair interactions and local disorder in determining the interdependency of optical constants of a − C N : H thin films’, *Phys. Rev. B*, vol. 66, no. 19, p. 195415, Nov. 2002, doi: 10.1103/PhysRevB.66.195415.

[54] Y. Zheng, Z. Zhang, and C. Li, ‘A comparison of graphitic carbon nitrides synthesized from different precursors through pyrolysis’, *Journal of Photochemistry and Photobiology A: Chemistry*, vol. 332, pp. 32–44, Jan. 2017, doi: 10.1016/j.jphotochem.2016.08.005.

[55] L. Chen, D. Huang, S. Ren, T. Dong, Y. Chi, and G. Chen, ‘Preparation of graphite-like carbon nitride nanoflake film with strong fluorescent and electrochemiluminescent activity’, *Nanoscale*, vol. 5, no. 1, pp. 225–230, 2013, doi: 10.1039/C2NR32248J.

[56] J. Zhu, P. Xiao, H. Li, and S. A. C. Carabineiro, ‘Graphitic Carbon Nitride: Synthesis, Properties, and Applications in Catalysis’, *ACS Appl. Mater. Interfaces*, vol. 6, no. 19, pp. 16449–16465, Oct. 2014, doi: 10.1021/am502925j.

[57] Y. Zhang *et al.*, ‘Synthesis and luminescence mechanism of multicolor-emitting g-C3N4 nanopowders by low temperature thermal condensation of melamine’, *Sci Rep*, vol. 3, no. 1, p. 1943, Dec. 2013, doi: 10.1038/srep01943.

[58] F. H. Abd El-kader, M. A. Moharram, M. G. Khafagia, and F. Mamdouh, ‘Influence of the nitrogen content on the optical properties of CNx films’, *Spectrochimica Acta Part A: Molecular and Biomolecular Spectroscopy*, vol. 97, pp. 1115–1119, Nov. 2012, doi: 10.1016/j.saa.2012.07.126.

[59] K. T. Drisya *et al.*, ‘Electronic and optical competence of TiO2/BiVO4 nanocomposites in the photocatalytic processes’, *Sci Rep*, vol. 10, no. 1, p. 13507, Dec. 2020, doi: 10.1038/s41598-020-69032-9.

[60] S. Y. Chai, Y. J. Kim, and W. I. Lee, ‘Photocatalytic WO3/TiO2 nanoparticles working under visible light’, *J Electroceram*, vol. 17, no. 2–4, pp. 909–912, Dec. 2006, doi: 10.1007/s10832-006-9073-3.

[61] F. Ge *et al.*, ‘Surface amorphous carbon doping of carbon nitride for efficient acceleration of electron transfer to boost photocatalytic activities’, *Applied Surface Science*, vol. 507, p. 145145, Mar. 2020, doi: 10.1016/j.apsusc.2019.145145.

[62] J. Chen *et al.*, ‘Porous g-C3N4 with defects for the efficient dye photodegradation under visible light’, *Water Science and Technology*, vol. 84, no. 6, pp. 1354–1365, Sep. 2021, doi: 10.2166/wst.2021.313.

[63] X. Liang, G. Wang, X. Dong, G. Wang, H. Ma, and X. Zhang, ‘Graphitic Carbon Nitride with Carbon Vacancies for Photocatalytic Degradation of Bisphenol A’, *ACS Appl. Nano Mater.*, vol. 2, no. 1, pp. 517–524, Jan. 2019, doi: 10.1021/acsanm.8b02089.

[64] Q. Liang, Z. Li, Z.-H. Huang, F. Kang, and Q.-H. Yang, 'Holey Graphitic Carbon Nitride Nanosheets with Carbon Vacancies for Highly Improved Photocatalytic Hydrogen Production', *Adv. Funct. Mater.*, vol. 25, no. 44, pp. 6885–6892, Nov. 2015, doi: 10.1002/adfm.201503221.

[65] S. Gao, X. Wang, C. Song, S. Zhou, F. Yang, and Y. Kong, 'Engineering carbon-defects on ultrathin g-C3N4 allows one-pot output and dramatically boosts photoredox catalytic activity', *Applied Catalysis B: Environmental*, vol. 295, p. 120272, Oct. 2021, doi: 10.1016/j.apcatb.2021.120272.

[66] D. Ruan, S. Kim, M. Fujitsuka, and T. Majima, 'Defects rich g-C3N4 with mesoporous structure for efficient photocatalytic H2 production under visible light irradiation', *Applied Catalysis B: Environmental*, vol. 238, pp. 638–646, Dec. 2018, doi: 10.1016/j.apcatb.2018.07.028.

[67] Y. Jiang, Z. Sun, C. Tang, Y. Zhou, L. Zeng, and L. Huang, 'Enhancement of photocatalytic hydrogen evolution activity of porous oxygen doped g-C3N4 with nitrogen defects induced by changing electron transition', *Applied Catalysis B: Environmental*, vol. 240, pp. 30–38, Jan. 2019, doi: 10.1016/j.apcatb.2018.08.059.

[68] P. Niu, G. Liu, and H.-M. Cheng, 'Nitrogen Vacancy-Promoted Photocatalytic Activity of Graphitic Carbon Nitride', *J. Phys. Chem. C*, vol. 116, no. 20, pp. 11013–11018, May 2012, doi: 10.1021/jp301026y.

[69] H. Starukh and P. Praus, 'Doping of Graphitic Carbon Nitride with Non-Metal Elements and Its Applications in Photocatalysis', *Catalysts*, vol. 10, no. 10, p. 1119, Sep. 2020, doi: 10.3390/catal10101119.

[70] P. Deng, H. Li, Z. Wang, and Y. Hou, 'Enhanced photocatalytic hydrogen evolution by carbon-doped carbon nitride synthesized via the assistance of cellulose', *Applied Surface Science*, vol. 504, p. 144454, Feb. 2020, doi: 10.1016/j.apsusc.2019.144454.

[71] J. Fang, H. Fan, M. Li, and C. Long, 'Nitrogen self-doped graphitic carbon nitride as efficient visible light photocatalyst for hydrogen evolution', *J. Mater. Chem. A*, vol. 3, no. 26, pp. 13819–13826, 2015, doi: 10.1039/C5TA02257F.

[72] N. M. Denisov, E. B. Chubenko, V. P. Bondarenko, and V. E. Borisenko, 'Synthesis of Oxygen-Doped Graphitic Carbon Nitride from Thiourea', *Tech. Phys. Lett.*, vol. 45, no. 2, pp. 108–110, Feb. 2019, doi: 10.1134/S1063785019020068.

[73] W. Wang *et al.*, 'Sulfur doped carbon quantum dots loaded hollow tubular g-C3N4 as novel photocatalyst for destruction of Escherichia coli and tetracycline degradation under visible light', *Chemical Engineering Journal*, vol. 378, p. 122132, Dec. 2019, doi: 10.1016/j.cej.2019.122132.

[74] J. Cao, H. Wang, Y. Zhao, and Y. Liu, 'Phosphorus-doped porous carbon nitride for efficient sole production of hydrogen peroxide via photocatalytic water splitting with a two-channel pathway', *J. Mater. Chem. A*, vol. 6, no. 12, pp. 1–3, 2018, doi: 10.1039/C9TA13929J.

[75] N. V. Phuc *et al.*, 'Synthesis and Photocatalytic Activity of Fluorine DOPED-g-C_3N_4', *AMM*, vol. 889, pp. 24–32, Mar. 2019, doi: 10.4028/www.scientific.net/AMM.889.24.

[76] X. Li *et al.*, 'Preparation of N-vacancy-doped g-C 3 N 4 with outstanding photocatalytic H 2 O 2 production ability by dielectric barrier discharge plasma treatment', *Chinese Journal of Catalysis*, vol. 39, no. 6, pp. 1090–1098, Jun. 2018, doi: 10.1016/S1872-2067(18)63046-3.

[77] Y. Huang, D. Li, Z. Fang, R. Chen, B. Luo, and W. Shi, 'Controlling carbon self-doping site of g-C3N4 for highly enhanced visible-light-driven hydrogen evolution', *Applied Catalysis B: Environmental*, vol. 254, pp. 128–134, Oct. 2019, doi: 10.1016/j.apcatb.2019.04.082.

[78] T. Jeong *et al.*, 'Atomic and electronic structures of graphene-decorated graphitic carbon nitride (g-C3N4) as a metal-free photocatalyst under visible-light', *Applied Catalysis B: Environmental*, vol. 256, p. 117850, Nov. 2019, doi: 10.1016/j.apcatb.2019.117850.

[79] Y. Gao, Y. Zhu, L. Lyu, Q. Zeng, X. Xing, and C. Hu, 'Electronic Structure Modulation of Graphitic Carbon Nitride by Oxygen Doping for Enhanced Catalytic Degradation of Organic Pollutants through Peroxymonosulfate Activation', *Environ. Sci. Technol.*, vol. 52, no. 24, pp. 14371–14380, Dec. 2018, doi: 10.1021/acs.est.8b05246.

[80] C. Liu *et al.*, 'Chlorine intercalation in graphitic carbon nitride for efficient photocatalysis', *Applied Catalysis B: Environmental*, vol. 203, pp. 465–474, Apr. 2017, doi: 10.1016/j.apcatb.2016.10.002.

[81] Z.-A. Lan, G. Zhang, and X. Wang, 'A facile synthesis of Br-modified g-C3N4 semiconductors for photoredox water splitting', *Applied Catalysis B: Environmental*, vol. 192, pp. 116–125, Sep. 2016, doi: 10.1016/j.apcatb.2016.03.062.

[82] M. Xu, B. Chai, J. Yan, H. Wang, Z. Ren, and K.-W. Paik, 'Facile Synthesis of Fluorine Doped Graphitic Carbon Nitride with Enhanced Visible Light Photocatalytic Activity', *NANO*, vol. 11, no. 12, p. 1650137, Dec. 2016, doi: 10.1142/S179329201650137X.

[83] L. Ming, N. Sun, L. Xu, and F. Chen, 'Fluoride ion-promoted hydrothermal synthesis of oxygenated g-C3N4 with high photocatalytic activity', *Colloids and Surfaces A: Physicochemical and Engineering Aspects*, vol. 549, pp. 67–75, Jul. 2018, doi: 10.1016/j.colsurfa.2018.04.013.

[84] L. Jiang *et al.*, 'Doping of graphitic carbon nitride for photocatalysis: A reveiw', *Applied Catalysis B: Environmental*, vol. 217, pp. 388–406, Nov. 2017, doi: 10.1016/j.apcatb.2017.06.003.

[85] L. Sun, Y. Li, and W. Feng, 'Gas-Phase Fluorination of g-C3N4 for Enhanced Photocatalytic Hydrogen Evolution', *Nanomaterials*, vol. 12, no. 1, p. 37, Dec. 2021, doi: 10.3390/nano12010037.

[86] Y. Wang, Y. Di, M. Antonietti, H. Li, X. Chen, and X. Wang, 'Excellent Visible-Light Photocatalysis of Fluorinated Polymeric Carbon Nitride Solids', *Chem. Mater.*, vol. 22, no. 18, pp. 5119–5121, Sep. 2010, doi: 10.1021/cm1019102.

[87] M. Xue *et al.*, 'Insights into the improved photocatalytic performance of fluorine surface modified mpg-C3N4 at room temperature under aqueous conditions', *Applied Catalysis A: General*, vol. 578, pp. 89–97, May 2019, doi: 10.1016/j.apcata.2019.04.004.

[88] B. J. Skromme and G. K. Sujan, ‘Semiconductor Heterojunctions ☆’, in *Reference Module in Materials Science and Materials Engineering*, Elsevier, 2018, p. B9780128035818113000. doi: 10.1016/B978-0-12-803581-8.11219-6.

[89] J. S. Jang, H. G. Kim, and J. S. Lee, ‘Heterojunction semiconductors: A strategy to develop efficient photocatalytic materials for visible light water splitting’, *Catalysis Today*, vol. 185, no. 1, pp. 270–277, May 2012, doi: 10.1016/j.cattod.2011.07.008.

[90] J. Yu, W. Wang, and B. Cheng, ‘Synthesis and Enhanced Photocatalytic Activity of a Hierarchical Porous Flowerlike p-n Junction NiO/TiO2 Photocatalyst’, *Chem. Asian J.*, vol. 5, no. 12, pp. 2499–2506, Dec. 2010, doi: 10.1002/asia.201000550.

[91] S. Selvarajan, A. Suganthi, M. Rajarajan, and K. Arunprasath, ‘Highly efficient BiVO4/WO3 nanocomposite towards superior photocatalytic performance’, *Powder Technology*, vol. 307, pp. 203–212, Feb. 2017, doi: 10.1016/j.powtec.2016.10.069.

[92] M. F. R. Samsudin, N. Bacho, S. Sufian, and Y. H. Ng, ‘Photocatalytic degradation of phenol wastewater over Z-scheme g-C3N4/CNT/BiVO4 heterostructure photocatalyst under solar light irradiation’, *Journal of Molecular Liquids*, vol. 277, pp. 977–988, Mar. 2019, doi: 10.1016/j.molliq.2018.10.160.

[93] W.-K. Jo and T. S. Natarajan, ‘Influence of TiO2 morphology on the photocatalytic efficiency of direct Z-scheme g-C3N4/TiO2 photocatalysts for isoniazid degradation’, *Chemical Engineering Journal*, vol. 281, pp. 549–565, Dec. 2015, doi: 10.1016/j.cej.2015.06.120.

[94] R. A. Senthil, J. Theerthagiri, A. Selvi, and J. Madhavan, ‘Synthesis and characterization of low-cost g-C 3 N 4 /TiO 2 composite with enhanced photocatalytic performance under visible-light irradiation’, *Optical Materials*, vol. 64, pp. 533–539, Feb. 2017, doi: 10.1016/j.optmat.2017.01.025.

[95] E. Jang *et al.*, ‘Atomic layer deposition with rotary reactor for uniform hetero-junction photocatalyst, g-C $_3$ N $_4$ @TiO $_2$ core–shell structures’, *RSC Adv.*, vol. 9, no. 57, pp. 33180–33186, 2019, doi: 10.1039/C9RA05958J.

[96] M. A. Alcudia-Ramos *et al.*, ‘Fabrication of g-C3N4/TiO2 heterojunction composite for enhanced photocatalytic hydrogen production’, *Ceramics International*, vol. 46, no. 1, pp. 38–45, Jan. 2020, doi: 10.1016/j.ceramint.2019.08.228.

[97] Y. Li, M. Zhou, B. Cheng, and Y. Shao, ‘Recent advances in g-C3N4-based heterojunction photocatalysts’, *Journal of Materials Science & Technology*, vol. 56, pp. 1–17, Nov. 2020, doi: 10.1016/j.jmst.2020.04.028.

[98] L. Chen, M. Chen, D. Jiang, and J. Xie, ‘A facile strategy for SnS2/g-C3N4 heterojunction composite and the mechanism in photocatalytic degradation of MO’, *Journal of Molecular Catalysis A: Chemical*, vol. 425, pp. 174–182, Dec. 2016, doi: 10.1016/j.molcata.2016.10.003.

[99] D. Monga, D. Ilager, N. P. Shetti, S. Basu, and T. M. Aminabhavi, ‘2D/2d heterojunction of MoS2/g-C3N4 nanoflowers for enhanced visible-light-driven photocatalytic and electrochemical degradation of organic pollutants’, *Journal of Environmental Management*, vol. 274, p. 111208, Nov. 2020, doi: 10.1016/j.jenvman.2020.111208.

[100] Z. Zheng, X. Zu, Y. Zhang, and W. Zhou, 'Rational design of type-II nano-heterojunctions for nanoscale optoelectronics', *Materials Today Physics*, vol. 15, p. 100262, Dec. 2020, doi: 10.1016/j.mtphys.2020.100262.

[101] J. Wang, P. Guo, Q. Guo, P. G. Jönsson, and Z. Zhao, 'Fabrication of novel g-C_3N_4/nanocage ZnS composites with enhanced photocatalytic activities under visible light irradiation', *CrystEngComm*, vol. 16, no. 21, pp. 4485–4492, 2014, doi: 10.1039/C4CE00107A.

[102] N. Güy, 'Directional transfer of photocarriers on CdS/g-C3N4 heterojunction modified with Pd as a cocatalyst for synergistically enhanced photocatalytic hydrogen production', *Applied Surface Science*, vol. 522, p. 146442, Aug. 2020, doi: 10.1016/j.apsusc.2020.146442.

[103] J. Zhang, M. Zhang, R.-Q. Sun, and X. Wang, 'A Facile Band Alignment of Polymeric Carbon Nitride Semiconductors to Construct Isotype Heterojunctions', *Angew. Chem. Int. Ed.*, vol. 51, no. 40, pp. 10145–10149, Oct. 2012, doi: 10.1002/anie.201205333.

[104] Q. Hao *et al.*, 'Accelerating the Hole Mobility of Graphitic Carbon Nitride for Photocatalytic Hydrogen Evolution via 2D/2D Heterojunction Structural Advantages and $Ni(OH)_2$ Characteristic', *Sol. RRL*, vol. 4, no. 8, p. 1900538, Aug. 2020, doi: 10.1002/solr.201900538.

[105] Q. Xu, L. Zhang, B. Cheng, J. Fan, and J. Yu, 'S-Scheme Heterojunction Photocatalyst', *Chem*, vol. 6, no. 7, pp. 1543–1559, Jul. 2020, doi: 10.1016/j.chempr.2020.06.010.

[106] J. Low, J. Yu, M. Jaroniec, S. Wageh, and A. A. Al-Ghamdi, 'Heterojunction Photocatalysts', *Adv. Mater.*, vol. 29, no. 20, p. 1601694, May 2017, doi: 10.1002/adma.201601694.

[107] J. Low, J. Yu, and C. Jiang, 'Design and fabrication of direct Z-scheme photocatalysts', in *Interface Science and Technology*, vol. 31, Elsevier, 2020, pp. 193–229. doi: 10.1016/B978-0-08-102890-2.00006-3.

[108] F. Wang, Q. Zeng, J. Tang, L. Peng, J. Shao, and S. Luo, 'Synthesis of g-C_3N_4/CuS Heterojunction with Enhanced Photocatalytic Activity Under Visible-Light', *j nanosci nanotechnol*, vol. 20, no. 9, pp. 5896–5905, Sep. 2020, doi: 10.1166/jnn.2020.18543.

[109] K. Liu *et al.*, 'Facile fabrication metal Cu-decorated g-C3N4 photocatalyst with Schottky barrier for efficient pollutant elimination', *Diamond and Related Materials*, p. 109116, May 2022, doi: 10.1016/j.diamond.2022.109116.

[110] D. Sun, T. Zhou, G. Che, and C. Liu, 'A synergism between Schottky junction and interfacial P-Ni bond for improving the hydrogen evolution of 2D/2D NiS/Phosphorus-doped g-C3N4 photocatalyst', *Applied Surface Science*, vol. 578, p. 152004, Mar. 2022, doi: 10.1016/j.apsusc.2021.152004.

[111] W. Chen, L. Chang, S.-B. Ren, Z.-C. He, G.-B. Huang, and X.-H. Liu, 'Direct Z-scheme 1D/2D WO2.72/ZnIn2S4 hybrid photocatalysts with highly-efficient visible-light-driven photodegradation towards tetracycline hydrochloride removal', *Journal of Hazardous Materials*, vol. 384, p. 121308, Feb. 2020, doi: 10.1016/j.jhazmat.2019.121308.

[112] J. Li, M. Zhang, Q. Li, and J. Yang, 'Enhanced visible light activity on direct contact Z-scheme g-C 3 N 4 -TiO 2 photocatalyst', *Applied Surface Science*, vol. 391, pp. 184–193, Jan. 2017, doi: 10.1016/j.apsusc.2016.06.145.

[113] L. Jiang *et al.*, 'In-situ synthesis of direct solid-state dual Z-scheme WO3/g-C3N4/Bi2O3 photocatalyst for the degradation of refractory pollutant', *Applied Catalysis B: Environmental*, vol. 227, pp. 376–385, Jul. 2018, doi: 10.1016/j.apcatb.2018.01.042.

[114] J.-T. Cao, Y.-X. Dong, Y. Ma, B. Wang, S.-H. Ma, and Y.-M. Liu, 'A ternary CdS@Au-g-C3N4 heterojunction-based photoelectrochemical immunosensor for prostate specific antigen detection using graphene oxide-CuS as tags for signal amplification', *Analytica Chimica Acta*, vol. 1106, pp. 183–190, Apr. 2020, doi: 10.1016/j.aca.2020.01.067.

[115] D. Zheng, G. zhang, and X. Wang, 'Integrating CdS quantum dots on hollow graphitic carbon nitride nanospheres for hydrogen evolution photocatalysis', *Applied Catalysis B: Environmental*, vol. 179, pp. 479–488, Dec. 2015, doi: 10.1016/j.apcatb.2015.05.060.

[116] Y. Li, M. Zhou, B. Cheng, and Y. Shao, 'Recent advances in g-C3N4-based heterojunction photocatalysts', *Journal of Materials Science & Technology*, vol. 56, pp. 1–17, Nov. 2020, doi: 10.1016/j.jmst.2020.04.028.

[117] P. Murugesan, J. A. Moses, and C. Anandharamakrishnan, 'Photocatalytic disinfection efficiency of 2D structure graphitic carbon nitride-based nanocomposites: a review', *J Mater Sci*, vol. 54, no. 19, pp. 12206–12235, Oct. 2019, doi: 10.1007/s10853-019-03695-2.

[118] Y. Ren, D. Zeng, and W.-J. Ong, 'Interfacial engineering of graphitic carbon nitride (g-C3N4)-based metal sulfide heterojunction photocatalysts for energy conversion: A review', *Chinese Journal of Catalysis*, vol. 40, no. 3, pp. 289–319, Mar. 2019, doi: 10.1016/S1872-2067(19)63293-6.

[119] B. He, M. Feng, X. Chen, D. Zhao, and J. Sun, 'One-pot construction of chitin-derived carbon/g-C3N4 heterojunction for the improvement of visible-light photocatalysis', *Applied Surface Science*, vol. 527, p. 146737, Oct. 2020, doi: 10.1016/j.apsusc.2020.146737.

[120] J. Deng, S. Zhu, J. Zheng, and L. Nie, 'Preparation of multi-dimensional (1D/2D/3D) carbon/g-C3N4 composite photocatalyst with enhanced visible-light catalytic performance', *Journal of Colloid and Interface Science*, vol. 569, pp. 320–331, Jun. 2020, doi: 10.1016/j.jcis.2020.02.100.

[121] Y. Shan *et al.*, 'Nanocellulose-derived carbon/g-C3N4 heterojunction with a hybrid electron transfer pathway for highly photocatalytic hydrogen peroxide production', *Journal of Colloid and Interface Science*, vol. 599, pp. 507–518, Oct. 2021, doi: 10.1016/j.jcis.2021.04.111.

[122] A. R. M. Shaheer, P. Karthik, G. Karthik, M. V. Shankar, and B. Neppolian, 'Dual role of a g-C_3N_4/carbon intra-Schottky junction in charge carrier generation and separation for efficient solar H_2 production', *Catal. Sci. Technol.*, vol. 9, no. 13, pp. 3493–3503, 2019, doi: 10.1039/C9CY00757A.

[123] N. Bao, X. Hu, Q. Zhang, X. Miao, X. Jie, and S. Zhou, 'Synthesis of porous carbon-doped g-C3N4 nanosheets with enhanced visible-light photocatalytic activity', *Applied Surface Science*, vol. 403, pp. 682–690, May 2017, doi: 10.1016/j.apsusc.2017.01.256.

[124] L. Meng *et al.*, 'Photocatalytic behavior of biochar-modified carbon nitride with enriched visible-light reactivity', *Chemosphere*, vol. 239, p. 124713, Jan. 2020, doi: 10.1016/j.chemosphere.2019.124713.

[125] Y. Wang *et al.*, 'Facile one-step synthesis of onion-like carbon modified ultrathin g-C3N4 2D nanosheets with enhanced visible-light photocatalytic performance', *Journal of Colloid and Interface Science*, vol. 533, pp. 47–58, Jan. 2019, doi: 10.1016/j.jcis.2018.08.039.

[126] Ferdi Schüth, ´Endo- and Exotemplating to Create High-Surface-Area Inorganic Materials´ *Angew Chem Int Ed* , 2003, 42, 3604 – 3622 - 2003, doi: 10.1002/anie.200300593.

[127] G. Dong, Y. Zhang, Q. Pan, and J. Qiu, 'A fantastic graphitic carbon nitride (g-C3N4) material: Electronic structure, photocatalytic and photoelectronic properties', *Journal of Photochemistry and Photobiology C: Photochemistry Reviews*, vol. 20, pp. 33–50, Sep. 2014, doi: 10.1016/j.jphotochemrev.2014.04.002.

[128] I. Papailias, T. Giannakopoulou, N. Todorova, D. Demotikali, T. Vaimakis, and C. Trapalis, 'Effect of processing temperature on structure and photocatalytic properties of g-C3N4', *Applied Surface Science*, vol. 358, pp. 278–286, Dec. 2015, doi: 10.1016/j.apsusc.2015.08.097.

[129] D. Han *et al.*, 'High-yield and low-cost method to synthesize large-area porous g-C3N4 nanosheets with improved photocatalytic activity for gaseous nitric oxide and 2-propanol photodegradation', *Applied Surface Science*, vol. 464, pp. 577–585, Jan. 2019, doi: 10.1016/j.apsusc.2018.09.108.

[130] S. C. Lee, H. O. Lintang, and L. Yuliati, 'A Urea Precursor to Synthesize Carbon Nitride with Mesoporosity for Enhanced Activity in the Photocatalytic Removal of Phenol', *Chem. Asian J.*, vol. 7, no. 9, pp. 2139–2144, Sep. 2012, doi: 10.1002/asia.201200383.

[131] Q. Li *et al.*, 'Facile synthesis of porous carbon nitride spheres with hierarchical three-dimensional mesostructures for CO2 capture', *Nano Res.*, vol. 3, no. 9, pp. 632–642, Sep. 2010, doi: 10.1007/s12274-010-0023-7.

[132] Y. Zheng *et al.*, 'Nanoporous Graphitic-C3N4@Carbon Metal-Free Electrocatalysts for Highly Efficient Oxygen Reduction', *Journal of the American Chemical Society*, p. 4, 2011.

[133] J. Zhang, F. Guo, and X. Wang, 'An Optimized and General Synthetic Strategy for Fabrication of Polymeric Carbon Nitride Nanoarchitectures', *Adv. Funct. Mater.*, vol. 23, no. 23, pp. 3008–3014, Jun. 2013, doi: 10.1002/adfm.201203287.

[134] J. Wang *et al.*, 'Environment-friendly preparation of porous graphite-phase polymeric carbon nitride using calcium carbonate as templates, and enhanced photoelectrochemical activity', *J. Mater. Chem. A*, vol. 3, no. 9, pp. 5126–5131, 2015, doi: 10.1039/C4TA06778A.

[135] Y. Cui, J. Huang, X. Fu, and X. Wang, 'Metal-free photocatalytic degradation of 4-chlorophenol in water by mesoporous carbon nitride semiconductors', *Catal. Sci. Technol.*, vol. 2, no. 7, p. 1396, 2012, doi: 10.1039/c2cy20036h.

[136] X.-H. Li *et al.*, 'Condensed Graphitic Carbon Nitride Nanorods by Nanoconfinement: Promotion of Crystallinity on Photocatalytic Conversion', *Chem. Mater.*, vol. 23, no. 19, pp. 4344–4348, Oct. 2011, doi: 10.1021/cm201688v.

[137] Y.-S. Jun, E. Z. Lee, X. Wang, W. H. Hong, G. D. Stucky, and A. Thomas, 'From Melamine-Cyanuric Acid Supramolecular Aggregates to Carbon Nitride Hollow Spheres', *Adv. Funct. Mater.*, vol. 23, no. 29, pp. 3661–3667, Aug. 2013, doi: 10.1002/adfm.201203732.

[138] Y. Chen *et al.*, 'Combined soft templating with thermal exfoliation toward synthesis of porous g-C3N4 nanosheets for improved photocatalytic hydrogen evolution', *Journal of Materials Research and Technology*, vol. 13, pp. 301–310, Jul. 2021, doi: 10.1016/j.jmrt.2021.04.056.

[139] L. Chen, Y. Man, Z. Chen, and Y. Zhang, 'Ag/g-C_3N_4 layered composites with enhanced visible light photocatalytic performance', *Mater. Res. Express*, vol. 3, no. 11, p. 115003, Nov. 2016, doi: 10.1088/2053-1591/3/11/115003.

[140] F. Li, D. Zhang, and Q. Xiang, 'Nanosheet-assembled hierarchical flower-like g-C_3N_4 for enhanced photocatalytic CO_2 reduction activity', *Chem. Commun.*, vol. 56, no. 16, pp. 2443–2446, 2020, doi: 10.1039/C9CC08793A.

[141] Y. Li, F. Gong, Q. Zhou, X. Feng, J. Fan, and Q. Xiang, 'Crystalline isotype heptazine-/triazine-based carbon nitride heterojunctions for an improved hydrogen evolution', *Applied Catalysis B: Environmental*, vol. 268, p. 118381, Jul. 2020, doi: 10.1016/j.apcatb.2019.118381.

[142] M. Liu *et al.*, 'Quenching induced hierarchical 3D porous g-C_3N_4 with enhanced photocatalytic CO_2 reduction activity', *Chem. Commun.*, vol. 55, no. 93, pp. 14023–14026, 2019, doi: 10.1039/C9CC07647F.

[143] P. Xia, B. Zhu, J. Yu, S. Cao, and M. Jaroniec, 'Ultra-thin nanosheet assemblies of graphitic carbon nitride for enhanced photocatalytic CO_2 reduction', *J. Mater. Chem. A*, vol. 5, no. 7, pp. 3230–3238, 2017, doi: 10.1039/C6TA08310B.

[144] X. Li, Z. Li, Q. Xia, H. Xi, and Z. Zhao, 'Effects of Textural Properties and Surface Oxygen Content of Activated Carbons on the Desorption Activation Energy of Water', *Adsorption Science & Technology*, vol. 24, no. 4, pp. 363–374, May 2006, doi: 10.1260/026361706779319625.

[145] X. Li, Z. Li, Q. Xia, and H. Xi, 'Effects of pore sizes of porous silica gels on desorption activation energy of water vapour', *Applied Thermal Engineering*, vol. 27, no. 5–6, pp. 869–876, Apr. 2007, doi: 10.1016/j.applthermaleng.2006.09.010.

[146] X. Li and Z. Li, 'Equilibrium and Do−Do Model Fitting of Water Adsorption on Four Commercial Activated Carbons with Different Surface Chemistry and Pore Structure', *J. Chem. Eng. Data*, vol. 55, no. 12, pp. 5729–5732, Dec. 2010, doi: 10.1021/je1006778.

[147] X. Li, H. Li, S. Huo, and Z. Li, 'Dynamics and isotherms of water vapor sorption on mesoporous silica gels modified by different salts', *Kinet Catal*, vol. 51, no. 5, pp. 754–761, Oct. 2010, doi: 10.1134/S0023158410050186.

[148] C. Shen, C. Chen, T. Wen, Z. Zhao, X. Wang, and A. Xu, 'Superior adsorption capacity of g-C3N4 for heavy metal ions from aqueous solutions', *Journal of Colloid and Interface Science*, vol. 456, pp. 7–14, Oct. 2015, doi: 10.1016/j.jcis.2015.06.004.

[149] A. Akbari Dehkharghani, 'Exfoliated Graphitic Carbon Nitride for the Fast Adsorption of Metal Ions from Acid Mine Drainage: A Case Study from the Sungun Copper Mine', *Mine Water Environ*, vol. 38, no. 2, pp. 335–341, Jun. 2019, doi: 10.1007/s10230-018-0561-x.

[150] X. Li, 'Preparation and Adsorption Properties of Biochar/g-C_3N_4 Composites for Methylene Blue in Aqueous Solution', *Journal of Nanomaterials*, vol. 2019, pp. 1–8, Jun. 2019, doi: 10.1155/2019/2394184.

[151] R. Agha Beygli, N. Mohaghegh, and E. Rahimi, 'Metal ion adsorption from wastewater by g-C3N4 modified with hydroxyapatite: a case study from Sarcheshmeh Acid Mine Drainage', *Res Chem Intermed*, vol. 45, no. 4, pp. 2255–2268, Apr. 2019, doi: 10.1007/s11164-018-03733-9.

[152] C. Shen, C. Chen, T. Wen, Z. Zhao, X. Wang, and A. Xu, 'Superior adsorption capacity of g-C3N4 for heavy metal ions from aqueous solutions', *Journal of Colloid and Interface Science*, vol. 456, pp. 7–14, Oct. 2015, doi: 10.1016/j.jcis.2015.06.004.

[153] W. K. Darkwah and Y. Ao, 'Mini Review on the Structure and Properties (Photocatalysis), and Preparation Techniques of Graphitic Carbon Nitride Nano-Based Particle, and Its Applications', *Nanoscale Res Lett*, vol. 13, no. 1, p. 388, Dec. 2018, doi: 10.1186/s11671-018-2702-3.

[154] Q. Gao, S. Sun, X. Li, X. Zhang, L. Duan, and W. Lü, 'Enhancing Performance of CdS Quantum Dot-Sensitized Solar Cells by Two-Dimensional g-C3N4 Modified TiO2 Nanorods', *Nanoscale Res Lett*, vol. 11, no. 1, p. 463, Dec. 2016, doi: 10.1186/s11671-016-1677-1.

[155] S. Styring, 'Artificial photosynthesis for solar fuels', *Faraday Discuss.*, vol. 155, pp. 357–376, 2012, doi: 10.1039/C1FD00113B.

[156] S. Kumar, S. Karthikeyan, and A. Lee, 'g-C3N4-Based Nanomaterials for Visible Light-Driven Photocatalysis', *Catalysts*, vol. 8, no. 2, p. 74, Feb. 2018, doi: 10.3390/catal8020074.

[157] Z. Li, C. Kong, and G. Lu, 'Visible Photocatalytic Water Splitting and Photocatalytic Two-Electron Oxygen Formation over Cu- and Fe-Doped g-C_3N_4', *J. Phys. Chem. C*, vol. 120, no. 1, pp. 56–63, Jan. 2016, doi: 10.1021/acs.jpcc.5b09469.

[158] S. Tonda, S. Kumar, S. Kandula, and V. Shanker, 'Fe-doped and -mediated graphitic carbon nitride nanosheets for enhanced photocatalytic performance under natural sunlight', *J. Mater. Chem. A*, vol. 2, no. 19, p. 6772, 2014, doi: 10.1039/c3ta15358d.

[159] S. C. Yan, Z. S. Li, and Z. G. Zou, 'Photodegradation of Rhodamine B and Methyl Orange over Boron-Doped g-C_3N_4 under Visible Light Irradiation', *Langmuir*, vol. 26, no. 6, pp. 3894–3901, Mar. 2010, doi: 10.1021/la904023j.

[160] S. Hu *et al.*, 'Enhanced visible light photocatalytic performance of g-C3N4 photocatalysts co-doped with iron and phosphorus', *Applied Surface Science*, vol. 311, pp. 164–171, Aug. 2014, doi: 10.1016/j.apsusc.2014.05.036.

[161] S. Wang and S. Zhou, 'Photodegradation of methyl orange by photocatalyst of CNTs/P-TiO2 under UV and visible-light irradiation', *Journal of Hazardous Materials*, vol. 185, no. 1, pp. 77–85, Jan. 2011, doi: 10.1016/j.jhazmat.2010.08.125.

[162] J. Xu, Y. Wang, and Y. Zhu, 'Nanoporous Graphitic Carbon Nitride with Enhanced Photocatalytic Performance', *Langmuir*, vol. 29, no. 33, pp. 10566–10572, Aug. 2013, doi: 10.1021/la402268u.

[163] Y. Yao *et al.*, 'Magnetic core–shell CuFe2O4@C3N4 hybrids for visible light photocatalysis of Orange II', *Journal of Hazardous Materials*, vol. 297, pp. 224–233, Oct. 2015, doi: 10.1016/j.jhazmat.2015.04.046.

[164] S.-H. Yoon and J. H. Lee, 'Oxidation Mechanism of As(III) in the UV/TiO $_2$ System: Evidence for a Direct Hole Oxidation Mechanism', *Environ. Sci. Technol.*, vol. 39, no. 24, pp. 9695–9701, Dec. 2005, doi: 10.1021/es051148r.

[165] X. Wang *et al.*, 'A metal-free polymeric photocatalyst for hydrogen production from water under visible light', *Nature Mater*, vol. 8, no. 1, pp. 76–80, Jan. 2009, doi: 10.1038/nmat2317.

[166] K. A. Davis, S. Yoo, E. W. Shuler, B. D. Sherman, S. Lee, and G. Leem, 'Photocatalytic hydrogen evolution from biomass conversion', *Nano Convergence*, vol. 8, no. 1, p. 6, Dec. 2021, doi: 10.1186/s40580-021-00256-9.

[167] D. I. Kondarides, V. M. Daskalaki, A. Patsoura, and X. E. Verykios, 'Hydrogen Production by Photo-Induced Reforming of Biomass Components and Derivatives at Ambient Conditions', *Catal Lett*, vol. 122, no. 1–2, pp. 26–32, Apr. 2008, doi: 10.1007/s10562-007-9330-3.

[168] C.-W. Huang, B.-S. Nguyen, J. C.-S. Wu, and V.-H. Nguyen, 'A current perspective for photocatalysis towards the hydrogen production from biomass-derived organic substances and water', *International Journal of Hydrogen Energy*, vol. 45, no. 36, pp. 18144–18159, Jul. 2020, doi: 10.1016/j.ijhydene.2019.08.121.

[169] Y. Zhan, Z. Liu, Q. Liu, and D. Huang, 'A facile and one-pot synthesis of fluorescent graphitic carbon nitride quantum dots for bio-imaging application', *New J. Chem.*, vol. 40, no. 1, pp. 101–106, 2016, doi: DOI: 10.1039/C7NJ00058H.

CHAPTER 2

Experimental work

2.1. Materials

Melamine (M) $C_3H_6N_6$, L (+) tartaric acid (TA) $C_4H_6O_6$, oxalic acid (OA) $C_2H_2O_4 \cdot 2H_2O$ and citric acid (CA) $C_6H_8O_7 \cdot H_2O$, with purity above 98 wt%, were purchased from MACH CHEMIKALIE (Czech Republic). All the reagents and materials were used as received without additional purification or treatment. Deionized water was used in the whole experiments.

2.2. Preparation of carbon nitrides materials

Melamine was placed in an alumina crucible with cover and then was put into a Muffle furnace for pyrolysis at 550 °C for 4h under the air with heating rate 5 °C min^{-1} and labelled CN (yellow g-C_3N_4). The yellow CN sample was further calcined under inert atmosphere at 620 °C for 2 h and labelled CNO (defective orange g-C_3N_4).

2.2.1. Synthesis of the adducts

Synthesis of adducts is based on the mixture of melamine and poly-carboxylic acids with M/A molar ratios of 1, 2, 3, 4, 5 and 6. This process was extended here to different polycarboxylic acids (A = TA, CA and OA), tartaric acid (TA), citric acid (CA) and oxalic acid (OA) mixed with melamine in different M/A molar ratios X (X= 1.5/1; 2.5/1; 3/1; 4/1 and 6/1). Typical, the synthesis of adducts follows these experimental steps: 2.52 g melamine was dissolved under vigorous stirring in 100 ml of distilled water heated up to 80 °C. Meanwhile, an appropriate mass of acid was dissolved in 20 ml distilled water. This solution was then added drop by drop into the melamine solution, which was kept warm and under stirring. A white precipitate appeared, then it was filtered and washed with distilled water before being dried at 80 °C for 4 h.

2.2.2. Preparation of C-rich-g-C_3N_4 materials

The white precipitate (adduct powder) was placed in a covered alumina crucible (3 x 5 cm) and then put into a tubular furnace for pyrolysis at 550 °C for 4h under inert atmosphere (N_2 flow 100 ml min^{-1}) at a heating rate of 5 °C min^{-1}. The series of adducts obtained were named according to the initial molar ratio X of melamine over poly-carboxylic acid A, following the formula MAX/1. For instance, melamine-(M), oxalic acid-(OA) adduct obtained with a ratio X of 3/1 was labelled MO3/1. Calcined materials at 550 °C were labelled with general name as MA/X-550. Depending on the type of acid and M/A ratio used, it occurred that the yield of the precipitate was too low, so the temperature of the solution was cooled down to 50 °C to recover enough solid, as summarized in Table 1. It is worth noting, as shown in the discussion part, that this cooling step could also lead to the precipitation of free reactants.

Table 1. Masses of melamine and carboxylic acids used as reactant in different molar ratios and masses of the obtained adducts after precipitation and drying. MR1 (molar ratio 1), MR2, MR3, MM (mass of melamine), MAMR 1 (mass of acids per molar ratio 1), MAD (mass after drying per composition).

Adducts	MR1	MR2	MR3	MM	MAMR 1	MAD
MT	2.5/1	4/1	6/1	2.52	1.26	3.5 1.5 1.6
MC	1.5/1	4/1	6/1	2.52	0.67	2.8 3.2 3.1
MO	3/1	4/1	6/1	2.52	0.62	3.4 2.5 4.1

2.2.3. Preparation of N-rich porous carbon materials

Synthesis of N-rich porous materials are continuation of C-rich-g-C_3N_4 samples. These samples were further calcined in the air on a muffle furnace with a cover crucible at 470 °C, 550 °C and 650 °C for 2 h, 1.5 h and 30 min, respectively, with heating rate 3 °C min^{-1}. Samples calcined further in air were labelled as follow MT-550-X (ox), MO-550-X (ox), MC-550-X (ox) with (X=470, 550, 650 °C temperature of calcination in presence of air).

2.2.4. Preparation of highly doped F-g-C_3N_4 materials

To perform the fluorination, firstly the samples were placed in a nickel boat and spread in the middle of the boat for good reactivity, then the boat was placed in the oven under N_2 atmosphere for 1.5 h at 20 °C. The fluorination process was carried out for 1.5 h with a maximum flow rate of 40 ml min^{-1} at 20 °C then annealed under N_2 for 5 h at 100 °C to avoid fluorine release species. Fluorination was followed and weight gains of 62, 47 and 73 % were observed for CN, CNO and CCN samples, respectively, in relation to the reactivity towards F_2. Hazardous and highly reactive (explosive) materials were obtained after fluorination. Samples were directly annealed after fluorination up to 50 °C in an inert atmosphere. After fluorination, the color of the samples changed. The CCN sample became white, while CN and CNO lighter yellow and orange, respectively, and looked like pasty samples with bad smells. After the fluorination, samples were labelled as follows : CN-F_2 _20, CNO-F_2 _20 and CCN-F_2 _20 (note: 20 °C on labelling is temperature of fluorination).

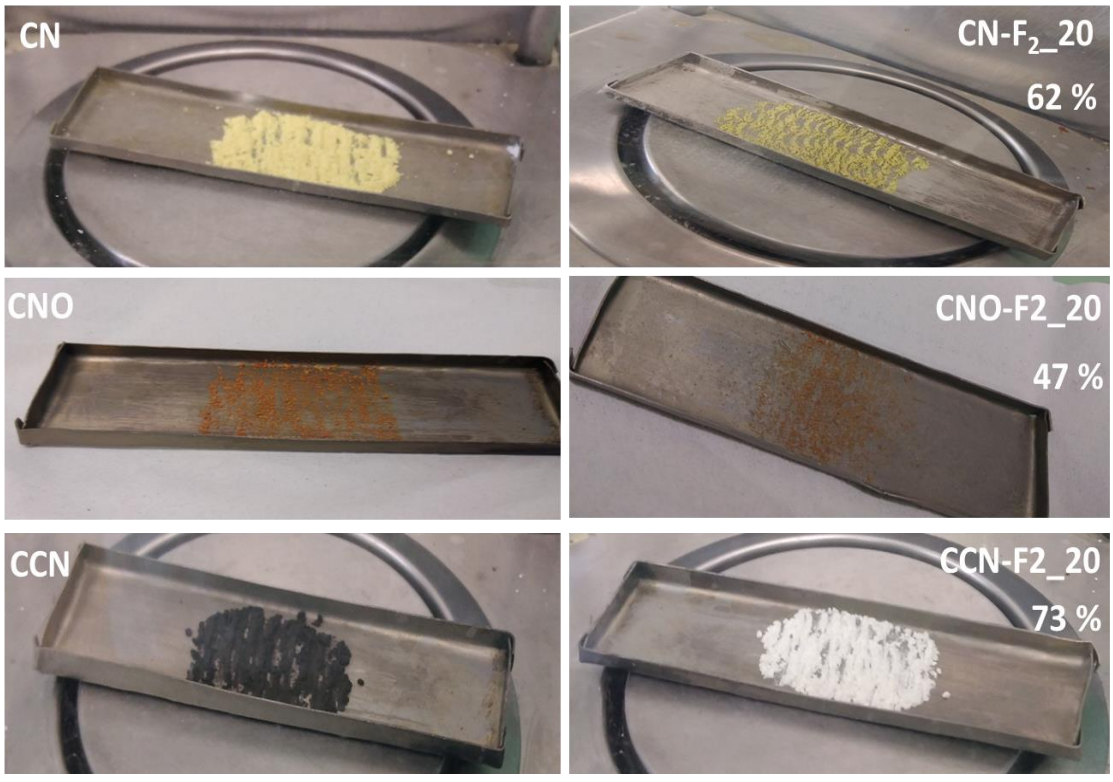

Figure 16. Materials before (left) and after (right) fluorination and their mass gain.

2.3. Characterization

The crystal structures of the samples were investigated by an X-ray diffractometer D8 ADVANCE A25 from Bruker using a Cu Kα radiation source (λ = 1.5406 Å). The morphology of the samples, previously gold-coated, was observed using a scanning electron microscopy (SEM) FEI Quanta 400 with a high-resolution low vacuum field emission gun (FEG). Elemental organic analysis (EOA) of the samples was performed using a Thermo Finnigan FLASH EA 1112 Series CHNS/O Analyzer (Thermo Fisher Scientific, USA). The nature of some chemical groups of the samples was identified by Diffusion Reflectance Infrared Fourier Transform (DRIFT) spectroscopy on a Thermo Scientific model iS50. Transmission electron microscope (TEM) micrographs were obtained on a Jeol apparatus (model ARM-200F) working at 200 kV. Raman spectra were recorded using a Horiba Jobin Yvon HR800 apparatus working with a laser at 488 and 532 nm. The I_D/I_G intensity ratio between the D and G bands was estimated using the Voigt function. X-ray photoelectron spectroscopy (XPS) was performed using a VG SCIENTA SES-2002 spectrometer equipped with a concentric hemispherical analyzer. The incident radiation used was generated by a monochromatic Al Kα x-ray source (1486.6 eV) operating at 420 W (14 kV; 30 mA). EPR was used to characterise the electron paramagnetic properties of the samples, performed on a Bruker EMX spectrometer. The thermogravimetric-Differential Scanning Calorimetric analysis (TG-DSC) was performed on a SETSYS-1750 CS analyzer with a heating rate of 10 °C min^{-1} . The nitrogen adsorption-desorption isotherms were measured at 77 K on Surface area and porosity analyzer Quantachrome Instrument.

2.4. Photodegradation experiments

Typically, 2.5 mg catalyst is added into a MO solution (~3 mL) with concentration $C_0 = 3.7 \cdot 10^{-5}$ mol dm^{-3}. The solution and photocatalyst were stirred magnetically in the dark for 1 h to ensure the adsorption-desorption equilibrium between the catalyst and the dye. Then, the cuvette (photocatalyst/MO solution) was irradiated by a Xenon lamp (1000 W) under stirring, and absorbance was measured every 20 min in the wavelength region of 200-800 nm. At the end, stirring is stopped, photocatalyst is removed (by centrifugation if needed) washed with water and

a new cycle can be tested with the same procedure. The concentration of the MO solution was analyzed by ultraviolet spectrophotometer. Complementary experiments were performed using fluoride solution to check their (F^-) photocatalytic influence.

2.5. Experiments of H_2 gas evolution

Photocatalytic tests were performed in a stainless steel photoreactor (348 mL) equipped with a quartz glass window. An aqueous solution of 100 mL, containing 50 % methanol and 0.1 g of photocatalyst, was placed in the reactor, purged by helium to remove air and irradiated by a Hg lamp (8 W Ultra-Violet Products Inc.maximum peak intensity at 254 nm). Sampling of the gaseous phase was performed every hour during 4 h intervals through a septum. The gas phase composition was analyzed by a gas chromatograph (Shimadzu Tracera GC-2010 Plus) equipped with BID (barrier discharge ionization detector). All the measurements were performed repeatedly.

2.6. Zeta Potential measurements

To a volume of 50 ml of distilled water was added 25 mg of g-C_3N_4. The flasks were placed in a tempered shake bath and shaken for 2 h, the temperature was 25 °C. An adequate portion was dispersed by ultrasonication, injected into the electrophoretic cell and Zeta potential values were recorded in the pH range from 2 to 14. The pH adjustments were made with solutions of 0.25 and 0.025 mol dm^{-3} HCl and 0.25 mol dm^{-3} NaOH. A sample was then taken to measure the Zeta potential. The zeta potential was measured using the Zetasizer Nano ZS (Malvern Instruments Ltd., GB). This machine uses laser Doppler velocity to determine the electrophoretic mobility. The zeta potential was obtained from the electrophoretic mobility using the Smoluchowski equation. The fixed measurement conditions were the following: temperature (25 °C), electric field (15 V), frequency (500 Hz), and the properties of the samples-viscosity (0.0089 kg m s^{-1}), refraction index (1.333), and dielectric constant (78.36). The zeta potential was measured three times for each pH and the isoelectric points (IEP, the pH values at which the zeta potential is equal to zero) were generated from the obtained electrophoretic mobility curves. The relative error of determination is ± 5 mV.

SUMMARY IN FRENCH

Les voies de synthèse et les caractérisations des échantillons préparés dans ce travail sont présentées dans ce chapitre.

1) Préparation des matériaux carbonitrures g-C_3N_4:

La mélamine a été placée dans un creuset d'alumine avec couvercle puis mise dans un four pour carbonisation à 550°C pendant 4h sous air avec une vitesse de chauffe de 50°C/min. L'échantillon a été noté CN. Il a une couleur jaune. Cet échantillon a également été calciné une second fois mais dans une atmosphère inerte à 620°C pendant 2 h. Il prend alors une couleur orange et a été noté CNO.

2) Préparation des matériaux g-C_3N_4 riches en C (g-C_3N_4 / C)

La mélamine a été dissoute sous agitation vigoureuse dans de l'eau chaude distillée. Pendant ce temps, une masse appropriée d'acide A (A = acide tartrique (TA), citrique (CA), oxalique (OA)) a été dissoute dans un autre bécher et ajoutée goutte à goutte dans la solution de mélamine qui a été maintenue chaude et sous agitation. Un précipité blanc est apparu qui a été filtré et lavé avec de l'eau distillée avant d'être séché. Le précipité blanc a été placé dans un creuset d'alumine couvert et ensuite mis dans un four tubulaire pour sa carbonisation à 550°C pendant 4h sous atmosphère inerte avec une vitesse de chauffage de 5 °C/min. Les séries de produits d'addition obtenus ont été nommées en fonction du rapport molaire initial X de la mélamine sur l'acide polycarboxylique A (X= 1,5/1 ; 2,5/1 ; 3/1 ; 4/1 et 6/1) selon la formule MAX/1. Par exemple, le produit d'addition mélamine-(M), acide oxalique-(OA) obtenu avec un rapport X de 3/1 a été étiqueté MO3/1. Les matériaux calcinés à 550°C ont été étiquetés comme suit : MAX/1-550.

3) Préparation des matériaux oxydés

Les matériaux g-C_3N_4 / C, en particulier les échantillons MTX-550 (X=2,5/1 et 6/1) ont été calcinés sous air (a) à 470°C ou 550°C ou 650°C de manière à subir une oxydation contrôlée. Les matériaux ont été notés respectivement MTX/1-550-470a, MTX/1-550-550a et MTX/1-550-650a.

4) Préparation des matériaux g-C_3N_4 et g-C_3N_4 / C modifiés par F_2

Pour réaliser la fluoration, les échantillons g-C_3N_4 (CN et CNO) et g-C_3N_4 / C (MT6 :1-550 noté CCN) ont été disposés dans un creuset en nickel et placés dans un four tubulaire. Après une

purge du four (N_2 - 1,5 h), un flux de F_2 pur est mis en contact avec les échantillons pendant 1h30 min à 20°C. Les échantillons fluorés obtenus ont ensuite été recuits sous N_2 pendant 5h à 100°C puis mis à l'air quelques jours afin de dégazer certaines espèces fluorés (ex : HF) et stabiliser les échantillons qui présentent un caractère explosif à la sortie du four. Les échantillons fluorés sont nommés comme suit : CN-F_2, CNO-F_2, CCN-F_2. Afin d'obtenir un aperçu des propriétés des matériaux fluorés, ces derniers ont été caractérisés avec différentes techniques telles que : la diffraction des rayons X (DRX), la spectroscopie RAMAN, la spectroscopie Infrarouge à transformée de Fourier (FTIR), la résonance paramagnétique électronique (RPE), la spectroscopie de photoélectron (XPS), la spectroscopie de réflectance diffuse UV-visible (DRS), la thermogravimétrie couplée spectroscopie de masse (TG-MS), la microscopie électronique à transmission (MET) ou à balayage (MEB) et l'analyse élémentaire. Leurs propriétés photocatalytiques ont également été étudiées en suivant la dégradation du colorant methyl-orange sous irradiation.

CHAPTER 3

Tuning the C/N ratio of C-rich graphitic carbon nitride (g-C_3N_4) materials by the melamine/carboxylic acid adduct route

3.1. Introduction

Graphitic carbon is formed of sp^2 carbon atoms arranged into condensed six-membered rings. Its π-orbitals are responsible for many properties, such as high electronic conductivity, which yield numerous applications, like electrode in Li-ion batteries [1]. It displays a high thermal stability in an inert atmosphere. In-between g-C and g-C_3N_4, a large range of compositions exist either as a doped phase (C-doped g-C_3N_4 and N-doped g-C) or as N-rich g-C or as C-rich-C_3N_4. The resulting compounds display modified properties compared to the pristine phases with interesting new functionalities and potential applications. For instance, doping of N into graphitic type carbon yields to new properties such as metal-free electrocatalysis [2] or enhanced performances in supercapacitor [3]. However, the addition of C into g-C_3N_4 structure improves the photocatalytic properties by either shifting the absorption range from UV to the visible range or by limiting the recombination of electron-hole pairs. It is proposed that carbon doping of g-C_3N_4 structure allows the formation of a large number of delocalized π-bonds with a change in the electronic structure [4]. The N content in the C-N system is strongly determined by the thermal stability of N-containing moieties with respect to carbon [5, 6]. Depending on the temperature and precursor used, the three main types of N-doping observed in g-C structure are pyrrolic-N, pyridinic-N and graphitic-N [7]. With the increase in the temperature, the nitrogen content is reduced and the first two groups tend to decompose in the profit of the most stable graphitic-N.

Interestingly, nanocomposites combining carbonitride and carbonaceous phase display a higher electronic conductivity, which enhances their performance compared to pristine g-C_3N_4 either in photocatalysis [8] through a longer exciton life-time, or in electrochemical energy storage (Na-ion storage batteries). Moreover, controlled gradient of composition between these two phases have shown to further improve the photocatalytic activity of the nanocomposite [9]. Those properties are strongly dependent on the interface between the two phases. Based on the potential applications of graphitic structure with C and N atoms and especially for those having a C-rich g-C_3N_4 composition, it appears interesting to control the C/N ratio of the graphitic phase over a large range of compositions and to evidence how the C atoms are distributed within the structure, especially when starting from homogeneous precursors having an atomic distribution of C and N atoms. For that purpose, different synthesis routes have been developed in the literature based on precursors containing C and N with different C/N ratios. CNx compounds with a high N-content are obtained

from the carbonization of N-rich precursors such as melamine, dicyanamide and urea [10]. The addition of C-precursors (e.g. glucose [11], polyaniline [12], cellulose, agricultural products etc.) to those N-rich precursors yields C-rich-g-C_3N_4 compounds. It was shown after the carbonization of the glucose and melamine mixture that the resulting g-C_3N_4 structure contains C-ring nanodomains with enhanced photocatalytic properties for water splitting compared to raw g-C_3N_4 [13]. However, these "physical mixture" processes lacked to finely tune the properties of these materials by controlling their precursors at the molecular level. Thus, nice and original synthesis for materials with optimized and tailored properties were developed *via* the formation of supramolecular self-assembled of C and N precursors. These products, also called adducts, are formed by the recognition and binding of complementary sub-units thanks to hydrogen bonds and non-covalent interactions (e.g. π interaction) [14]. Molecular crystals are then obtained. In this context, a wide variety of materials with different dimensionalities, ranging from 1D to 3D, were formed [15]. Melamine (M) is an interesting sub-unit as a g-C_3N_4 precursor since it has a strong ability to be involved in the formation of supramolecular self-assembled compounds through the recognition process. For instance, melamine associated with cyanuric acid [16], barbituric acid [17] has been largely investigated. More recently, adducts based on melamine and carboxylic acids have also been studied. With melamine and benzoic acid [18], or oxalic acid [19] , adducts were formed through hydrogen bonding (N-H . . . O and/or N-H . . . N), ionic interactions (according to the pH) and π-π interactions (if present) [20] as schematized in Fig.17.

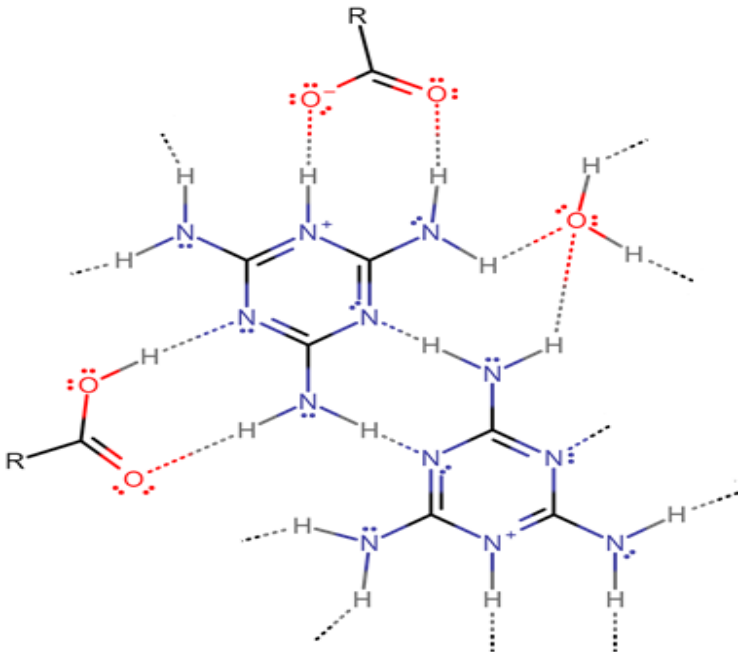

Figure 17. Schematic representation of attractive interactions in melamine-carboxylic acid self-assembled compounds.

Based on this self-assembled precursor type, Li *et al.* prepared for the first time g-C_3N_4 sticky nanotubes using melamine-ammonium oxalate complex [21]. This process leads to the formation of porous g-C_3N_4 nanotubes (PCN) within carbon in the structure. This process leads to the formation of porous g-C_3N_4 nanotubes (PCN) within the carbon in the structure. More recently, X. Fang *et al.* were also able to prepare co-crystals between teraphtalic acid (TPA) and melamine (M), via hydrogen-bonding functional groups -COOH from (TPA) and -NH_2 from (M), which led to the preparation of C-rich g-C_3N_4 [22]. This homogeneous distribution of C-rich (TPA) and N-rich molecules (M) within the crystalline adduct is supposed to lead to a homogeneous distribution of C and N species at the nanometric/atomic scale within the g-C_3N_4 structure.

Nevertheless, this adduct approach was never systematically investigated in the melamine-carboxylic acid system in order to tune the C/N ratio of carbonitride-type phase over a large range of compositions and with the potential formation of nanocomposite materials. We aimed to ´´build‘‘a bridge between g-C_3N_4 and C-rich materials and to construct nanocomposites, and to describe deeply the structuration of these materials in fundamental point of view. A possible explanation was proposed in photocatalytic point of view in relation with H_2 generation. For that purpose, different carboxylic acids, denoted A (for oxalic acid (OA), citric acid (CA) and tartaric acid (TA)), having different carbon chain lengths were used in the presence of melamine to yield different adducts labelled as MAX/1(z) with M for melamine, A for the acid, X/1 for the molar ratio M/A and z for the number given to the crystal phase (1 or 2). These phases were used as precursors of C-rich-C_3N_4 phases having different C/N ratios. This route, which does not require an organic solvent or hydrothermal step, appears as a simple way to tune the C/N ratio of the CNx carbonized materials by selecting either the nature of the carboxylic acid and/or the melamine/carboxylic acid ratio.

3.2. Evidence of adducts formation

3.2.1. Structure and morphology of adducts investigated by XRD and SEM

As shown in X-Ray diffraction (XRD) patterns (Fig. 18a-c), the mixture of M with the carboxylic acids leads to new crystalline phases called adducts. The latter depends on the nature of the carboxylic acid A and the ratio X/1. Interestingly, for each of the two ratios X/1 tested, a particular crystalline phase was obtained and denoted MAX/1(z) with z = 1 or 2. In some cases, due to the cooling step of the precipitation solution used to increase the yield of these adducts, the presence of M was detected. A list of the XRD peaks of these adducts and their positions are presented in Table 2.

Table 2. Peak positions 2θ degree of precursors and the new phases (adducts). Evidence formation of new peaks after the chemical reaction between starting materials.

Melamine	13.12	17.66	21.61	22.03	26.15	28.78	-
Oxalic acid	14.89	15.35	18.79	25.85	29.03	30.44	-
MO3/1	12.05	12.94	16.47	17.24	21.42	24.61	-
MO6/1	17.22	17.69	23.06	25.97	26.17	-	
Tartaric acid	11.64	18.82	20.73	23.38	25.08	29.73	32.01
MT2.5/1	14.12	20.79	29.96	30.97	33.36	34.34	-
MT6/1	12.54	15.95	16.88	17.68	23.90	26.94	32.24
Citric acid	15.19	16.95	18.16	22.28	23.04	26.01	-
MC1.5/1	13.23	18.94	27.72	30.51	-	-	-
MC6/1	13.29	19.69	21.94	25.86	26.18	27.02	-

Interestingly, peaks of MO3/1(1) and MO6/1(2) phases (samples with melamine-oxalic acid adduct obtained with 3/1 and 6/1 molar ratios) do not correspond to the phases reported by Han *et al*. [19]. These authors reported that the obtained phase displays the two most intense peaks at 2θ angle circa 18° and 27° for Cu Kα radiation. Since this is outside the scope of this study, the determination of the adduct crystal structures was not performed.

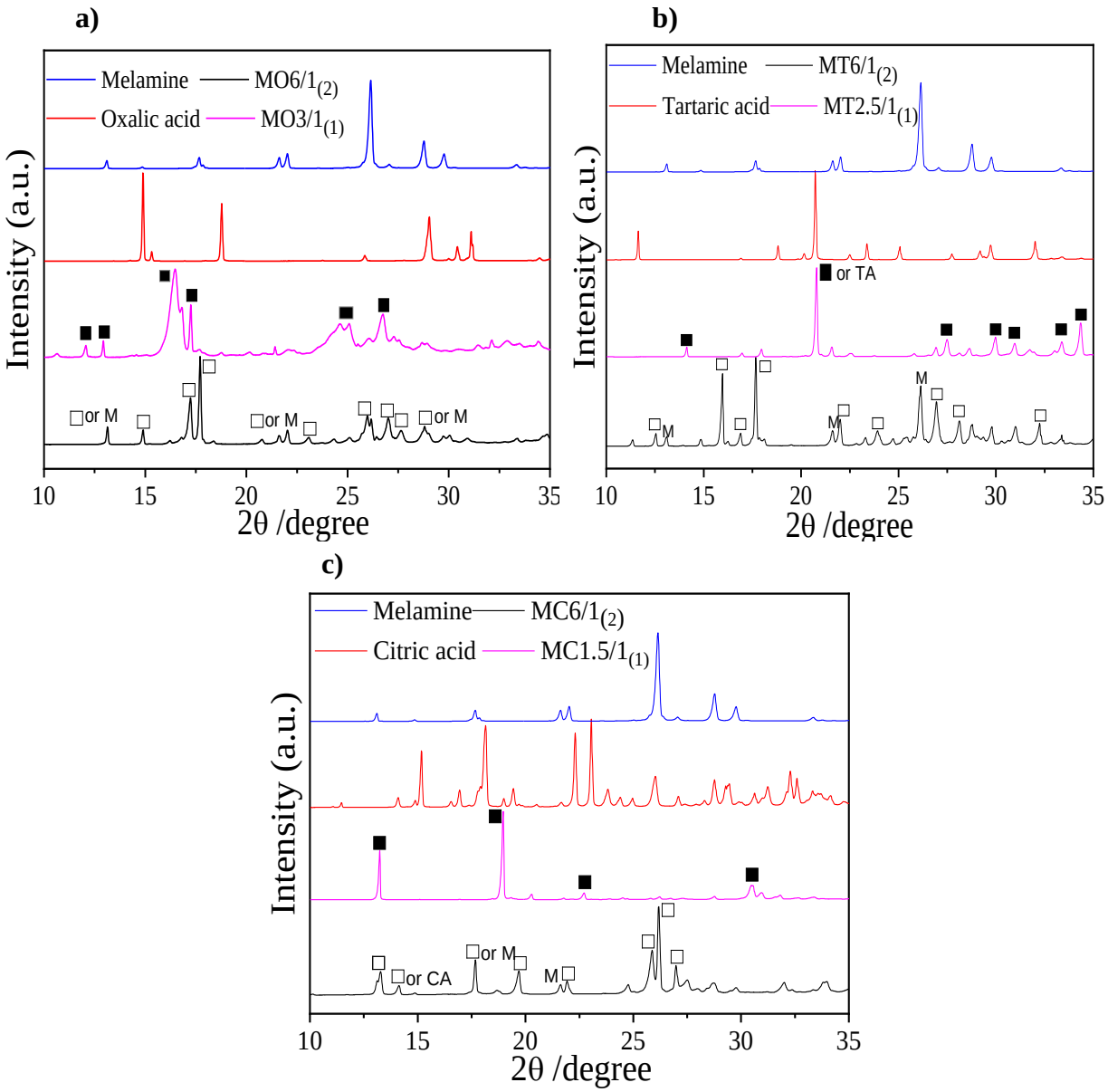

Figure 18. XRD patterns of the M and A precursors and their corresponding adducts obtained with two different M/A molar ratios: a) melamine, oxalic acid, MO3/1 $_{(1)}$, MO6/1 $_{(2)}$; b) melamine, tartaric acid, MT2.5/1 $_{(1)}$, MT6/1 $_{(2)}$; c) melamine, citric acid, MC1.5/1 $_{(1)}$, MC6/1 $_{(2)}$. The ■ and □ symbols indicate the main peaks of MA/X $_{(1)}$ and MA/X $_{(2)}$ adduct crystalline phases, respectively; M: melamine, O: oxalic acid; T: tartaric acid; C: citric acid.

Another evidence of adducts formation is their singular crystal shape compared to those of the M and A precursors as observed by SEM micrographs in Fig. 19a-g. The typical irregular granular shape of the precursors is not more encountered for the MA X/1 (z) samples, which display a typical regular needle-like shape for MT X/1 with X = 2.5 and X = 6.0 (Fig. 19d-e) and a lamellar-like shape for MC X/1 morphology for X = 1.5 and X = 6.0 (Fig. 19f-g). These different characterizations have evidenced the formation of adducts. Indeed, they all show that the phases obtained are not a physical mixture of M and A (even if impurities of M could be detected for some samples) since the adducts showed: a typical thermal degradation (Fig. 22), a particular XRD pattern (Fig. 18), single phase morphology evidenced by SEM observation in Fig. 19 and a peculiar infra-red (IR) spectrum compared to melamine (see the range 3000-3500 cm^{-1} in Fig. 20-21).

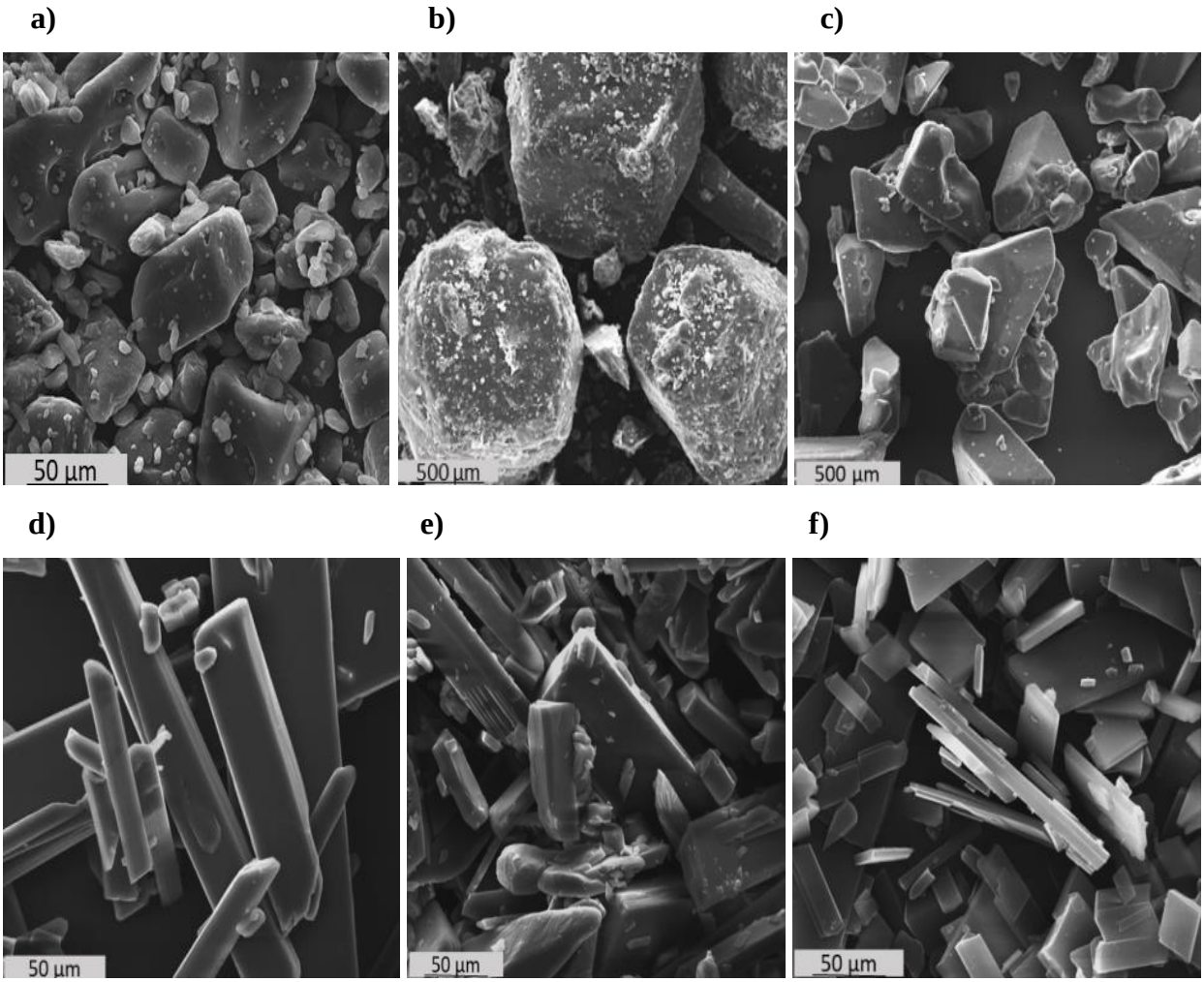

g)

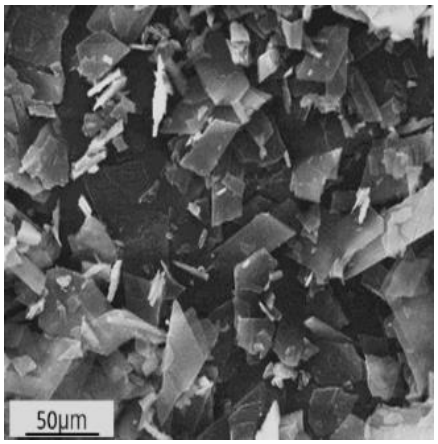

Figure 19. SEM micrographs of a) melamine, b) tartaric acid, c) citric acid and of the as synthesized adducts with two different molar ratios d) MT2.5/1 $_{(1)}$, e) MT6/1 $_{(2)}$, f) MC1.5/1 $_{(1)}$ and g) MC6/1 $_{(2)}$.

3.3. Composition of adducts

3.3.1. Elemental analysis

To determine the chemical composition of the adducts, elemental analysis was carried out and the results are reported in Table 3. Melamine and polycarboxylic acid compositions were compared with those of the adducts. For each acid considered, the as-synthesized adducts show nitrogen content following the molar ratios M/A of the starting precursors. As expected, the oxygen content follows the opposite trend due to the presence of carboxylic acid groups and hydroxyl (if any) possibly associated with water crystallization molecules. Based on these data, calculated M/A ratio of adducts could be determined considering that nitrogen is related to the melamine content and carbon arises from acid and melamine. These ratios may differ from the starting M/A ratios and are (close to) integer values, as expected for adducts. Discrepancy compared to integer values could be due to the impurities observed by XRD, therefore caution should be taken regarding these ratios, which could not always correspond to the real M/A ratios of the adducts.

Table 3. Elemental composition (CHNO analysis) of melamine, TA, CA and adducts for two molar ratios and corresponding calculated M/A ratio (based on C and N compositions).

Name of sample	C (wt%)	N (wt%)	O (wt%)	H (wt%)	M/A ratio
Melamine	28.5	66.63	-	4.80	-
TA	32.01	-	63.96	4.03	-
CA	37.51	-	58.29	4.19	-
MT2.5/1	27.5	39.09	28.77	4.64	2.1/1.0
MT6/1	28.03	53.27	14.12	4.55	5.9/1.0
MC1.5/1	31.56	37.65	26.48	4.28	2.1/1.0
MC4/1	30.45	42.57	22.26	4.62	3.0/1.0

3.3.2. Infrared spectroscopy

To further confirm the evidence of adducts formation, Diffuse reflectance infrared Fourier transform spectroscopy (DRIFT) was carried out on these new phases and compared with the pure precursors M and A shown in Fig. 20. For the M precursor, all the observed peaks are in agreement with the data of the literature. Two main broad peaks at 3122 cm^{-1} and 3326 cm^{-1}, related to NH_2 symmetrical vibration modes, appear. Two sharp bands at 3419 cm^{-1} and 3472 cm^{-1} show asymmetrical -NH_2 stretching, [23] while bands at 808 cm^{-1} and 1020 cm^{-1} correspond to triazine deformation modes [24]. The typical signatures of carboxylic acid groups were observed with the C=O stretching (1720 cm^{-1}) and C-O stretching (region 1105 cm^{-1} and 1200 cm^{-1}). Since the acid-base reaction is expected in the mixture of the precursors, partial protonation of amine and deprotonation of carboxylic acid groups may occur. This behaviour has been observed in the Melamine-Benzoic Acid system [25], where attractive interactions (ionic interaction, H-bond and Van der Waals forces) between reactants (melamine, melaminium, carboxylic and carboxylate) and together with water bridging molecules were encountered. Similar interactions may also be present within adducts. Indeed, the presence of two broad bands at 3102 cm^{-1} and 3335 cm^{-1} are shifted compared to that of melamine, which could correspond to the stretching of N-H···O bond of protonated melamine as observed in the melaminium chloride structure [26]. A small shift of this absorption band between the two M/A molar ratios can also be observed in agreement with the two different compositions of the adduct phases. The typical bands of carboxylic acids

expected in the range 1400-1600 cm^{-1} are almost no longer observed in the adducts. It indicates the formation of carboxylate groups. The band intensity region from 1377 to 1700 cm^{-1} is related to the C=N and C-N stretching vibrations of the melamine ring, that also appear in the adduct. Moreover, the peak associated to out of plane bending of triazine at 808 cm^{-1} for melamine disappeared in the adduct as observed for protonated melamine [27]. All spectra of the adducts are shown in Fig.21, exhibiting a similar trend with the other acids used.

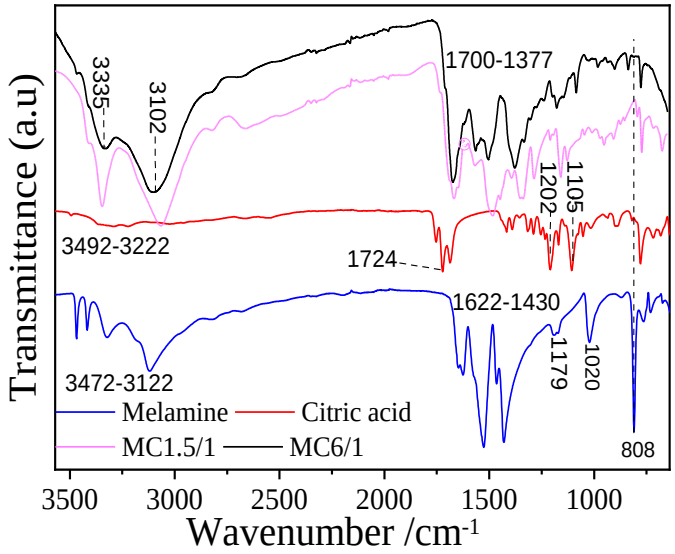

Figure 20. DRIFT spectra and characteristics vibrational peaks of melamine, citric acid and adducts (MC1.5/1 and MC6/1).

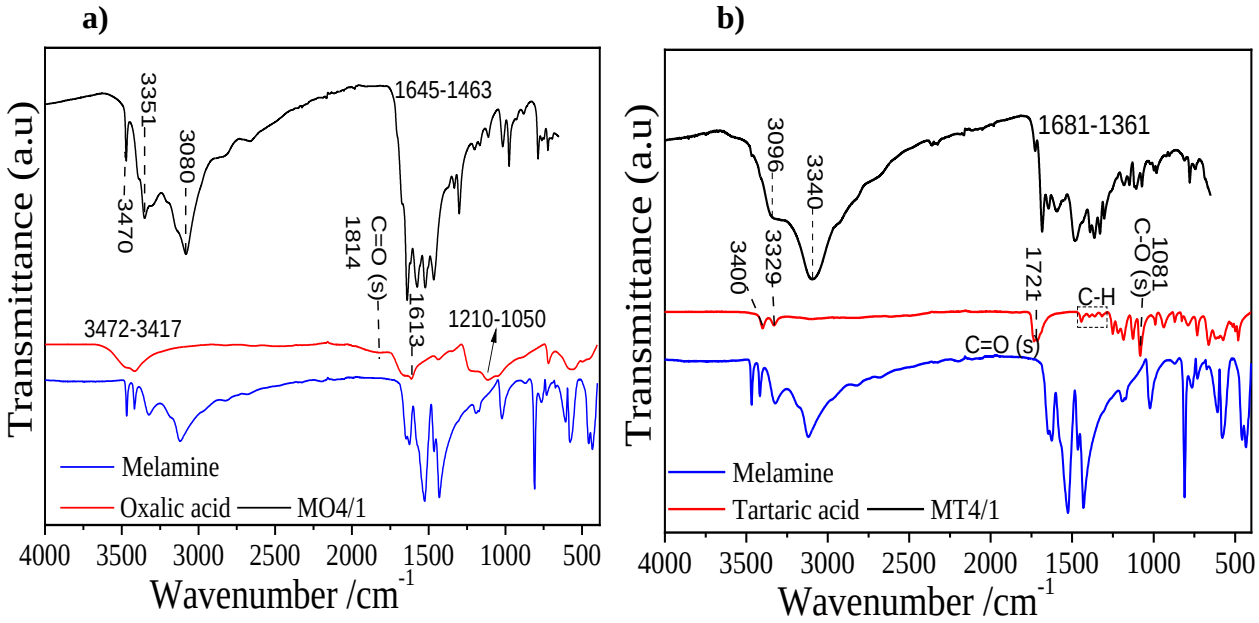

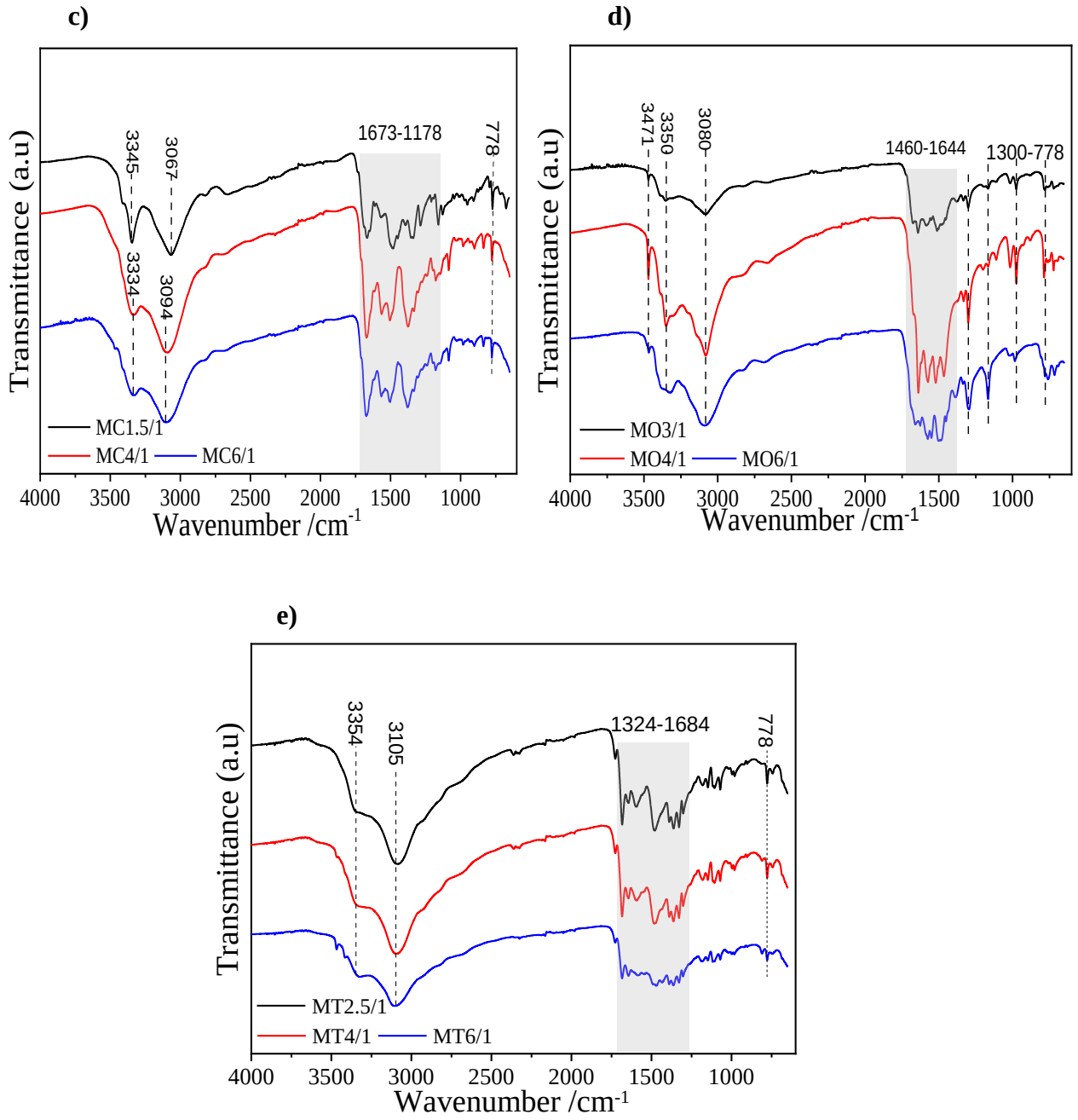

Figure 21. FTIR spectra of a) melamine, OA, MO4/1, b) melamine, TA, MT4/1, c) the adducts MC1.5/1, MC4/1, MC6/1; d) MO3/1, MO4/1, MO6/1 and e) MT2.5/1, MT4/1, MT6/1. The effect of the molar ratio on the shift of the vibrational peaks, evidenced in the region 1460-1644cm^{-1} (a) and 3000-3400 cm^{-1} (b).

3.4. Thermal behavior of adducts

To follow the thermal transformation of precursors and adducts during the heating process, thermogravimetric and differential thermal analysis (TG-DTA) were carried out in argon flow (Fig. 22a-e). For pure acids, thermal decompositions are endothermic (Fig. 22a) and occur in a single step or in two steps for the dehydrated oxalic acid owing to an additional dehydration step. In all cases, the decomposition is nearly complete between 200-285 °C, a small part of carbon (2 %) remaining at 1000 °C for only TA and CA acids. Melamine shows different thermal behaviour compared to the acids. Its endothermic decomposition temperature is observed starting at 295 °C up to 365 °C. The mass loss was more pronounced in this interval, and was followed by a sharp decomposition peak (Fig. 22b) due to deamination [28]. With the increase in the temperature, g-C_3N_4 is progressively formed in the range 400-500 °C and then completely decomposed at 750 °C. Adducts behave differently compared with their precursors, as displayed in Fig. 22c. To see more precisely adduct´s endothermic decomposition behaviour, DTA and DTG were plotted (Fig. 22c-d).

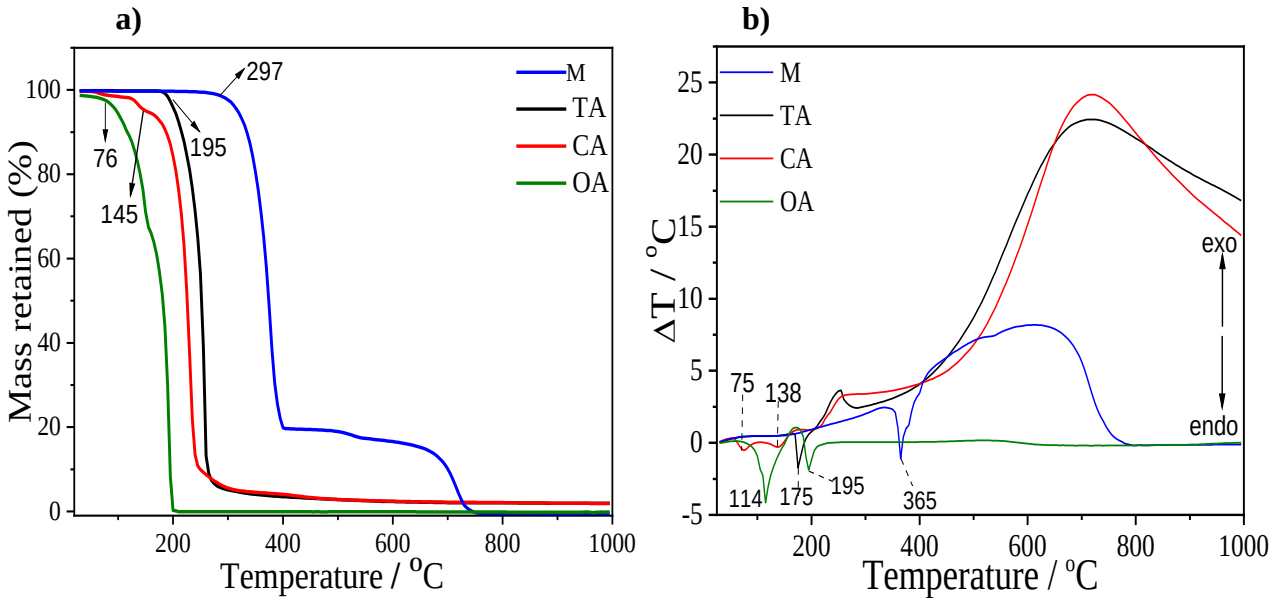

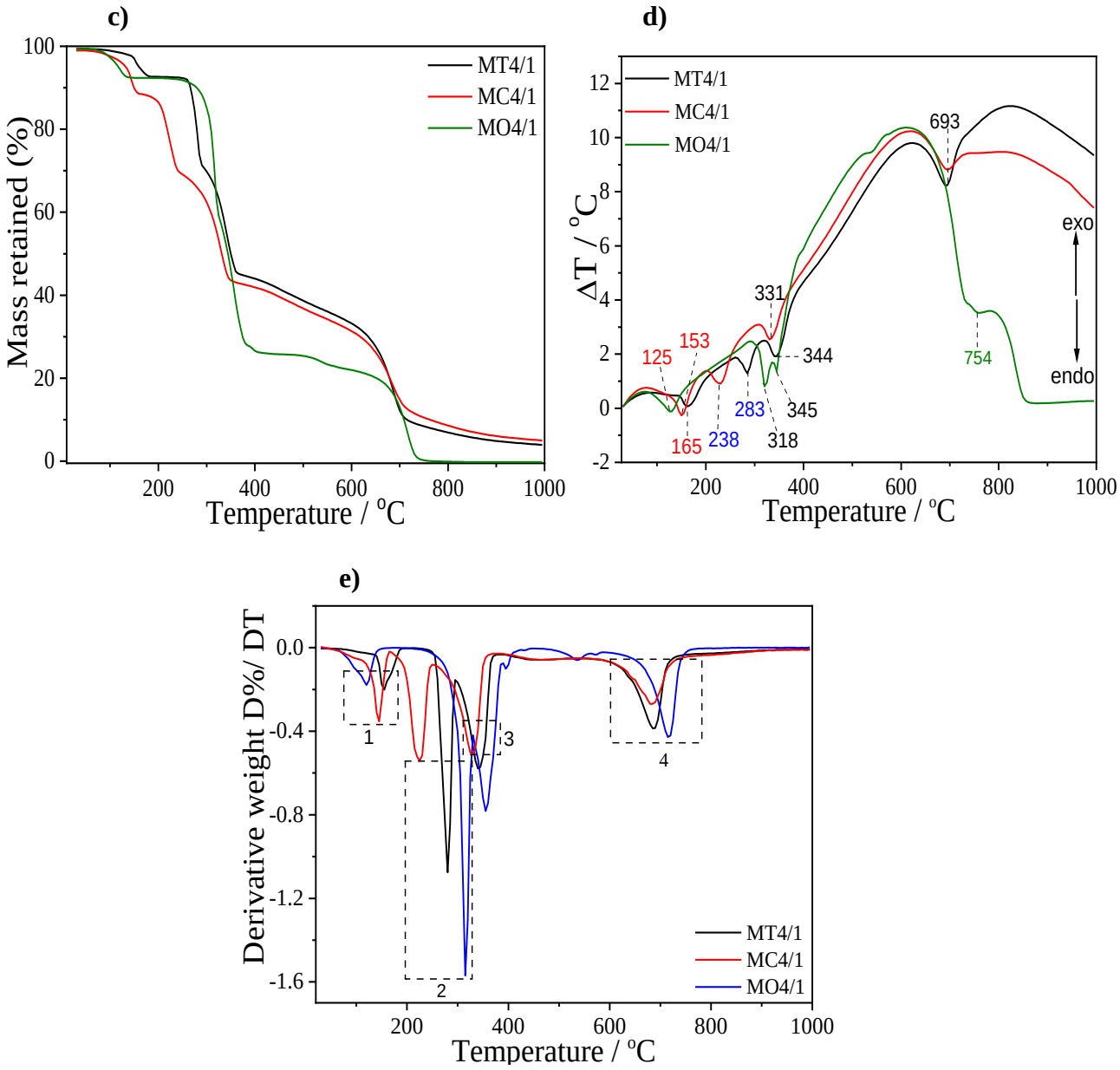

Figure 22. TG and DTA of precursors (a-b) and adducts (c-e) under nitrogen flow (heating rate 10 °C min^{-1}).

All adducts display four decomposition steps in the temperature ranges 110-155 °C, 225-314 °C, 322-357 °C and 683-715 °C (DTG data) in agreement with the four observed endothermic peaks. In the low temperature region (from 100 up to *circa* 350 °C), the steps are attributed, respectively, to the dehydration of the adduct and the acid decomposition, followed by the deamination of the melamine. The third step occurs at a lower temperature compared to pure melamine, giving another evidence of adducts the formation and rather than a physical mixture of the reactants. The last step

occurs in the high temperature region (above 650 °C) where thermal decomposition products are either completely decomposed (MO4/1 adduct) or partly decomposed with a carbon yield close to 5 % at 1000 °C (MT4/1 and MC4/1 adducts). This low thermal stability of MO4/1 at high temperature has already been observed for a similar adduct type made with melamine and oxalic acid and for pure melamine decomposition product. This suggests that the MO adducts decomposition product behaves almost like the g-C_3N_4 regarding melamine decomposition. Interestingly, another thermal behaviour is observed for the MT4/1 and MC4/1 adducts. This leads to a more stable decomposition products at high temperatures (yield close to 5 wt%).

3.5. Physico-chemical characterizations of C-rich-g-C_3N_4 materials

3.5.1. XPS, Elemental analysis and FTIR

The chemical composition of the calcined samples was investigated by elemental analysis (EA) and X-ray photoelectron spectroscopy (XPS). Since these techniques give an indication about respectively the bulk and the surface composition, discrepancy can be observed, but the evolution of the N/C ratios roughly follows the M/A ratio used to prepare the adducts (Table 4). Pure g-C_3N_4 is supposed to have theoretically 60.9 wt% of N and 39.1 wt% of C. The reference material g-C_3N_4 displays a slightly different composition since it was prepared in air (presence of oxygen), and at a temperature where its decomposition has started. The other samples, prepared at the same temperature but in an inert atmosphere, have lower nitrogen content and higher C content compared to the reference. Values ranging from 38 to 57 wt% were observed for the N content whereas carbon content lies between 38 to 49 wt%, meaning that the samples can be considered C-rich-C_3N_4 materials as confirmed later. Interestingly, relatively high oxygen content was detected with values ranging from 6 to 10 wt%. It has been proposed that oxygen arises from the carboxyl group of polycarboxylic acids.

Table 4. Chemical composition in (wt %) of the samples obtained from elemental (EA) and XPS analysis with carbonization yields (wt %). np, indicates not performed samples.

Name of sample	C		N		O		H	C/N atomic	Yield (%)
	EA	XPS	EA	XPS	EA	XPS	EA	EA	
g-C_3N_4-550(ox)	34.33	40.44	62.60	57.28	2.46	2.28	1.61	0.63	26
MO3/1- 550	34.4	n.p	56.99	n.p	6.67	n.p	1.94	0.70	40
MT2.5/1-550	46.26	50.40	41.88	45.04	10.13	4.56	1.22	1.29	26
MT6/1-550	42.29	41.33	46.18	57.53	10.43	1.13	1.37	1.07	35
MC1.5/1-550	49.23	55.96	38.12	40.28	11.14	3.76	1.48	1.50	29
MC4/1- 550	43.70	n.p	44.65	n.p	9.78	n.p	1.57	1.14	32
MC6/1-550	38.99	51.60	51.42	44.53	7.69	3.87	1.75	0.88	38

High-resolution XPS measurements of C-rich-g-C_3N_4 and g-C_3N_4 samples were also performed. For the g-C_3N_4 reference (Fig.23) two contributions are observed on the C1s high resolution spectra: 1) N-C=N at 288.4 eV typical of triazine and 2) C or H species bonded to C (C=C, C-C, and CHx) at 285.0 eV. The latter species, unexpected in g-C_3N_4, were attributed to "adventitious" carbon atoms which were gradually deposited on the surface of the material in the XPS chamber due to C-based gaseous pollutants [29].

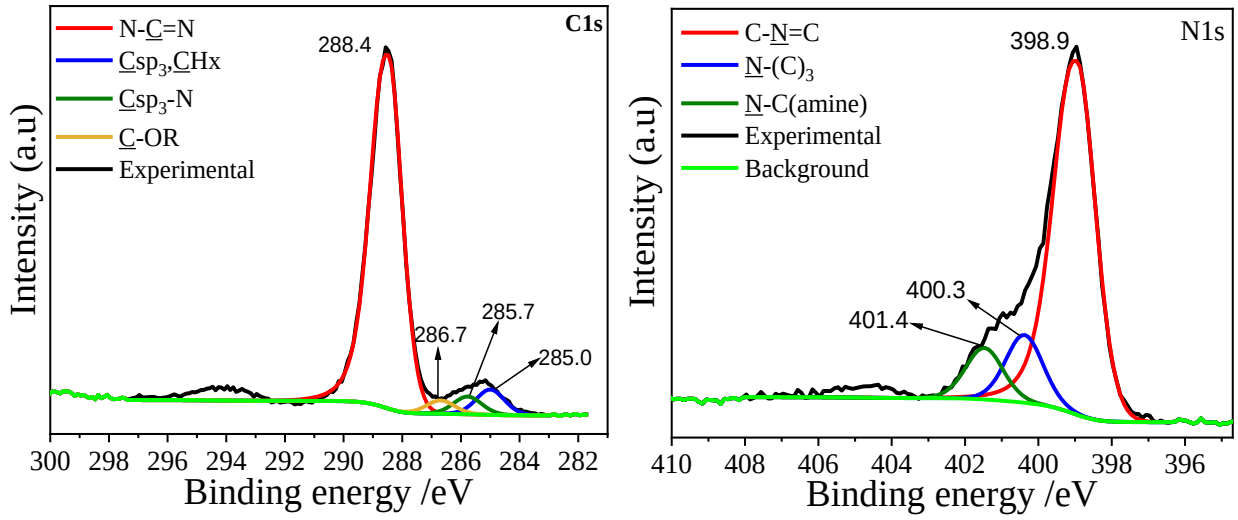

Figure 23. C1s and N1s high-resolution XPS spectra of g-C_3N_4-550 (ox).

For the C-rich-C_3N_4 samples, measurements were more difficult to record compared to the one of g-C_3N_4, owing probably to the presence of nested carbon-rich clusters or nanodomains with different electrical conductivities from their g-C_3N_4 environment. This required, for charge compensation, the use of an electron flood gun, which led to variable peak profiles and positions according to the voltage applied. As a result, the flood was adjusted for the C1s analysis, in order i) to obtain a profile of the C1s peak as fine as possible and ii) that the contribution of the lowest energy was attributed for each sample to C-C, C=C and CHx bonds at 285 eV (assuming that the sample contains similar species in different ratio). No quantitative analysis was extracted from these spectra. Thus, we have followed only the evolution of the main contributions for selected samples (Fig. 24). The signal at 285 eV was attributed to carbon-rich clusters or nanodomains originating from the carbonaceous skeleton of the adducts carboxylic groups. Its contribution clearly increases with the C content of the selected samples from 42 wt% for MT6/1-550 to 46 and 49 wt% for respectively MT2.5/1-500 and MC1.5/1-500 samples. Meanwhile, the contribution of N-C=N species decreases. From these findings, it is clear that beside the presence of g-C_3N_4 domains, a higher portion of carbon-carbon bonds is observed with a higher carbon content, presumably in the form of C=C bonds as suggested latter by Raman spectroscopy with the appearance of D and G bands characteristic of graphitic-type carbon.

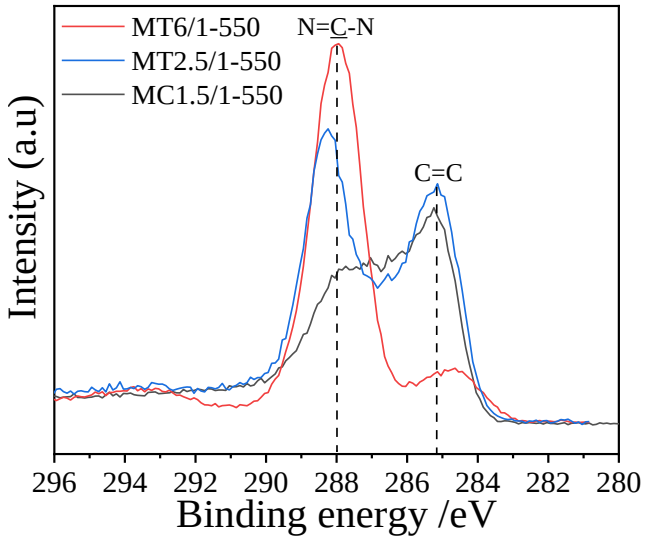

Figure 24. High resolution XPS C1s spectra of MT6/1-550, MT2.5/1-550 and MC1.5/1-550 samples showing the evolution of N-C=N and (C=C, C-C and C-H) contributions with variation of the carbon content.

The N1s spectra of MT6/1-550, MT2.5/1-550 and MC1.5/1-550 samples display three main contributions centered at the binding energy of 399.08 eV (corresponding to sp^2-hybridized pyridinic-N species in triazine rings (C-N=C), 400.6 eV (tertiary nitrogen N-$(C)_3$ groups) and 401.7 eV terminal amino groups (C-N-H) (Fig. 25). A clear evolution of these populations can be observed with the increasing carbon content; the C-N=C population decreases while the N-$(C)_3$ and N-C amine increases (Table 5).

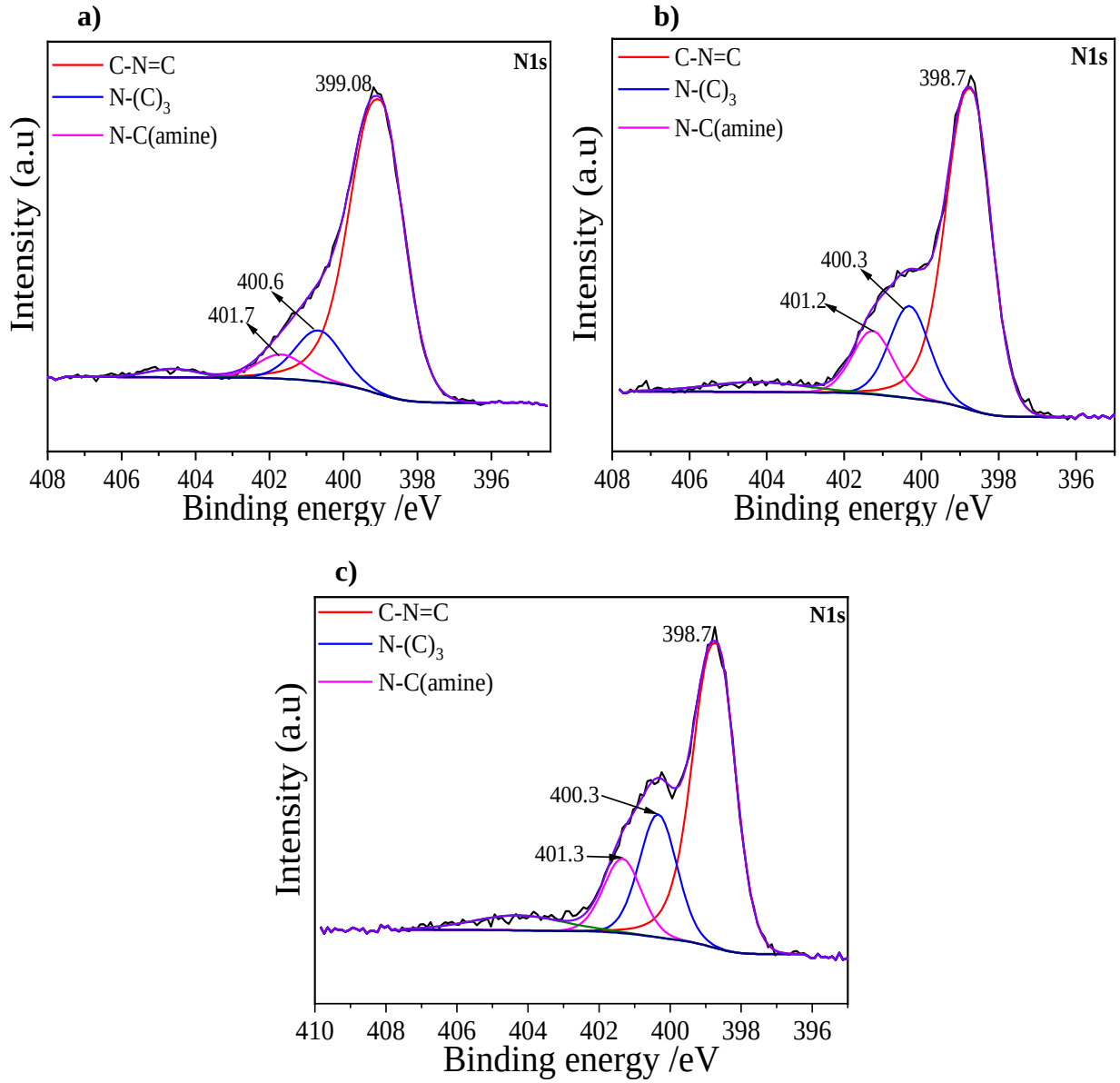

Figure 25. High resolution XPS N1s spectra of a) MT6/1-550, b) MT2.5/1-550, c) MC1.5/1-550 samples.

Table 5. Nitrogen bonding compositions and peak-ratio area of C-rich-C_3N_4 and g-C_3N_4 samples with variation on molar ratio.

Samples	N-$(C)_3$		C-N=C		N-C(amine)	
	Peak ratio %	Position/eV	Peak ratio %	Position/eV	Peak ratio %	Position /eV
g-C_3N_4-550 (ox)	12	400.3	73	398.9	10	401.4
MC1.5/1-550	21	400.3	60	398.7	13	401.3
MC6/1-550	12	400.5	74	398.8	10	401.5
MT2.5/1-550	17	400.3	67	398.7	11	401.2
MT6/1-550	12	400.6	80	399.0	6	401.6

The g-C_3N_4 and C-rich-C_3N_4 samples were analyzed by DRIFT spectroscopy, as shown in Fig. 26. The spectra of the g-C_3N_4 reference display typical and well-resolved absorption bands, as reported in the literature, at the opposite to those of C-rich-g-C_3N_4 samples (e.g. MT4/1-550 and MC4/1-550), which typically have poorly resolved bands as encounter usually for poorly ordered carbon-based materials. All selected samples displayed a band at 807 cm^{-1} which is attributed to the breathing mode of the triazine ring [30]. A similar trend is observed for the other peaks of the g-C_3N_4, 1319 cm^{-1} and 1562 cm^{-1} correspond to the C-N and C=N stretching mode of aromatics, whereas the peak at 1417 cm^{-1} corresponds to tertiary-N [31] also revealed by XPS. A broad absorption band around 3200 cm^{-1} presents in all spectra and a second band around 3600 cm^{-1} detected mainly for C-rich-C_3N_4 materials could be related to the stretching vibration mode of N-H and surface adsorbed water molecules O-H [32, 33] in g-C_3N_4 domains and/or C-rich clusters as evidenced latter by Raman spectroscopy. A small band at *about* 2177 cm^{-1} was detected for the C-rich materials; it could be attributed to the nitrile species [34]. It is presumed that these groups are yielded through the thermal decomposition process of amides, formed previously by a reaction between melamine amine groups and carboxylic acids. These amide groups could follow successive degradation steps and lead to nitrile species [35]. This hypothesis is strengthened by the fact that thermal degradation of nitriles yields HCN species, as observed by TG-MS (results unreported). The absorption band at 2363 cm^{-1} for the MO4/1-550 sample is related to the fluctuation in the CO_2 amount inside the spectrometer during measurements [36].

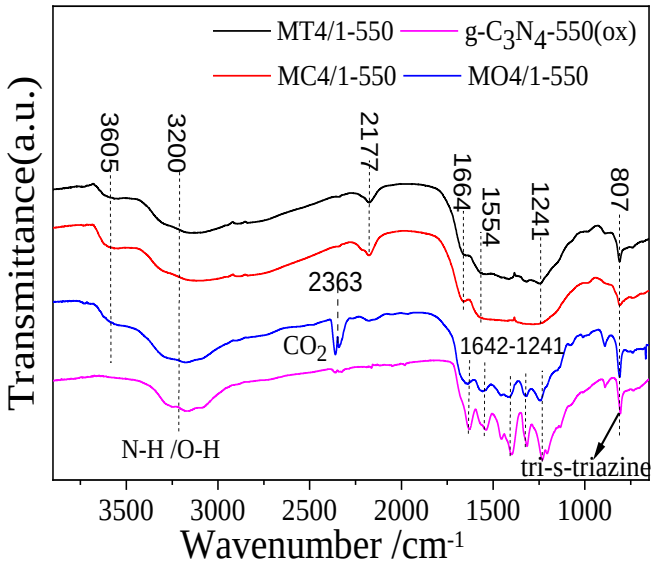

Figure 26. FTIR spectra of g-C_3N_4-550 (ox), MT4/1-550, MC4/1-550, MO4/1-550.

3.5.2. Structure investigation of C-rich-g-C_3N_4 materials

3.5.2.1. Raman Spectroscopy

Raman spectra of the samples MC1.5/1-550, MC6/1-550, MT2.5/1-550, MT6/1-550, MC4/1-550 (black) and MO4/1-550 (brownish color) are shown in Fig. 27a-b. The use of two different excitation wavelengths (488 and 532 nm) was necessary to overcome luminescence phenomena, which yielded poorly resolved spectra for some samples. In some cases, this problem could not be overcome and therefore, spectra of g-C_3N_4 (reference), MO4/1-550 and MT6/1-550 (beige color) samples were then not presented for all wavelengths. For an excitation wavelength of 488 nm Fig. 27a, only the black samples display the two typical D and G bands of graphitic-type carbon at respectively 1371 cm^{-1} and 1566 cm^{-1}. Even if caution should be taken due to a luminescence phenomenon, the intensity ratio of D and G bands (R= ID/IG) follows a clear decrease with the carbon content, as shown by the sequence: R (MC1.5/1-550) = 3.6 > R (MT2.5/1-550) = 3.3 > R (MC6/1-550) = 1.5 for respectively 49, 46 and 38 wt% of C (Table 4). This feature fits well with I_D/I_G ratio evolution observed for disordered carbon having for instance very low coherence length (La) in the in-plane graphitic structure, typically below 2 nm. In that size range, the intensity ratio

is proportional to La^2 (i.e. the carbon cluster area) and follows the degree of ordering of the carbon structure. Indeed, in this case, the D mode intensity is related to the probability of finding a sixfold C ring and this probability decreases with the loss of ordering (and the La size) owing to the formation of C chains, sp^3 species, or other types of rings. At the opposite, the intensity of the G mode, related to the motion of C sp^2 atoms, is considered as relatively constant in this range whatever the disorder [37]. Hence, in this study, with the decrease of the carbon content in the carbonitride samples, lower probability to form sixfold C rings is expected, resulting in a decrease of I_D/I_G ratio. This trend is supported by the absence of second order bands such as the 2D bands observed usually around 2750 cm^{-1} and which is replaced by a bump for highly disordered carbon in the range 2400-3100 cm^{-1}. Usually a decrease in the G band position with the amorphization of the graphitic structure from 1580 (graphite) down to 1510 cm^{-1} (amorphous carbon) is expected for carbon materials. This feature is not encountered in the study samples. Indeed, values ranging from 1580 to 1602 cm^{-1} were observed at different wavelengths for the G band. This suggests a high presence of sp^2 carbon atoms arranged in six-membered rings, probably as clusters within the g-C_3N_4 structure. Fig. 27b shows the Raman spectra of the MC4/1-550, MO4/1-550 and MT6/1-550 samples recorded with an excitation wavelength of 532 nm. A clear difference could be observed between the MO4/1-550 sample, having a composition close to g-C_3N_4, and the two other samples, which are more carbon rich. The former did not display any strong absorbance bands, as expected for disordered g-C_3N_4 prepared in air. For the latter samples, beside the typical D and G bands, a hump in the region between 2600-3000 cm^{-1} is observed as for very disordered carbon materials [38].

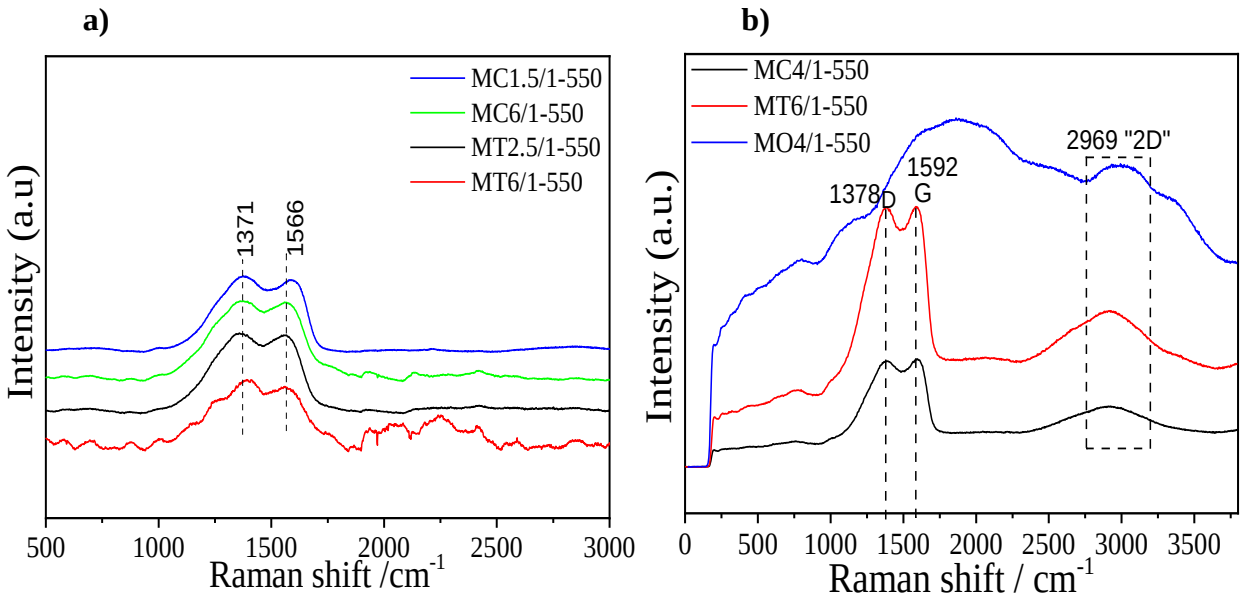

Figure 27. Raman spectra of carbonized samples recorded with an excitation wavelength at 488 nm (a) and 532 nm (b)

A hypothetical representation of the C-rich-g-C_3N_4 nanostructure is reported in Fig.28 with sixfold carbon ring nanometric domains, where the carbon domain are indicated in black color, whereas blue and black balls in hexagons represent N and C atoms, respectively .

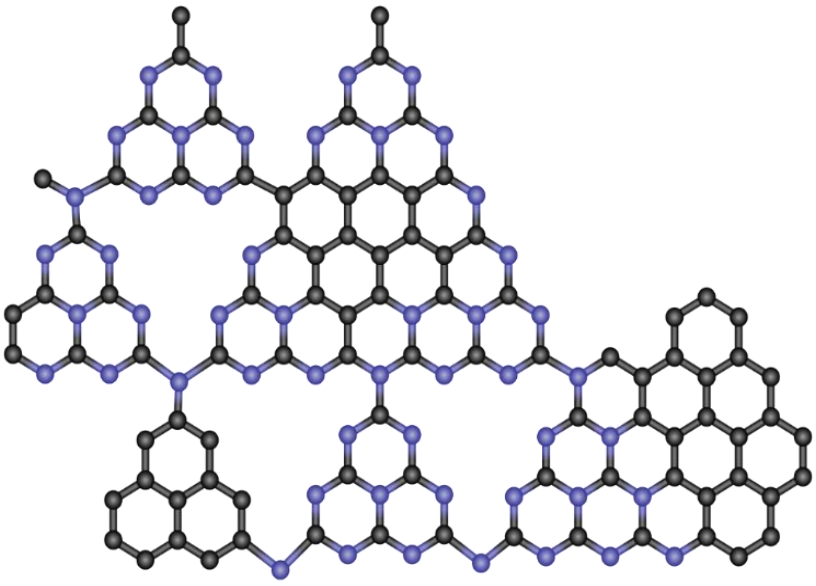

Figure 28. Hypothetical representation of the C-rich-C_3N_4 heterostructure with presence of sixfold-carbon ring nanometric domains embedded within g-C_3N_4 structure.

3.5.2.2. X-ray diffraction (XRD)

The g-C_3N_4 and C-rich-g-C_3N_4 materials were investigated by XRD. The XRD difractograms show large diffraction peaks, typical of highly disordered crystalline materials with a hump at 13.10° (for g-C_3N_4 and MO3/1-550 samples only), and a peak in a large range 26.9-27.4° (Fig. 29). The hump corresponds to the (100) interplanar distance of g-C_3N_4 and is typical of the in-plane structural packing motif of heptazine units, as described in the literature [39].

The peak around 27° is attributed to (002) planes present in both crystalline graphitic carbonitride (g-C_3N_4) and graphite C structures and corresponds to interlayer stacking distances. Compared to perfect crystalline structures of g-C_3N_4 with d_{002} = 0.3246 nm and graphite C d_{002} = 0.336 nm [40], the observed d_{002} values lie in this range. Moreover, these values are higher when disorder is present in the lamellar structure [41], (e.g. treatment above the decomposition temperature of g-C_3N_4 in oxidation or inert atmosphere, presence of heteroatoms and activation of graphitic carbon). Among the two samples exhibiting the heptazine structure, the MO4/1-550 sample shows the lowest d_{002} value (d = 0.3252 nm) slightly above the value of perfect g-C_3N_4 followed by the reference g-C_3N_4 sample prepared in air (d_{002} = 0.3265 nm). It indicates that both samples, having a yellow-beige color and prepared at the same temperature, have a slightly disorder structure, close to perfect g-C_3N_4, but with more defects when heat-treatment was performed in air. For the other samples, the d_{002} spacing follows the sequence MO3/1-550 < g-C_3N_4-550(air) < MT6/1-550 < MC6/1-550 < MT2.5/1-550 < MC1.5/1-550, which is nicely correlated with the carbon content of the sample (Table 4). This trend indicates that the increase in the carbon content in the lamellar structure significantly increases the interlayer distance. The highest d_{002} value (0.331 nm) observed for MC1.5/1-550 sample having the highest carbon content is below the interlayer distance of graphite [42], suggesting that all materials prepared have compositions ranging between crystalline g-C_3N_4 and graphite, so they can be considered C-rich carbonitride phases. Thus, the absence of peak at around 13° for these samples could be attributed to the introduction of C as a heteroatom within the lamellar structure of g-C_3N_4 with a breakdown of the long- range periodicity of the in-plane heptazine units. As the carbon content increases, a nanocomposite of g-C_3N_4 with carbon nanodomains could appear.

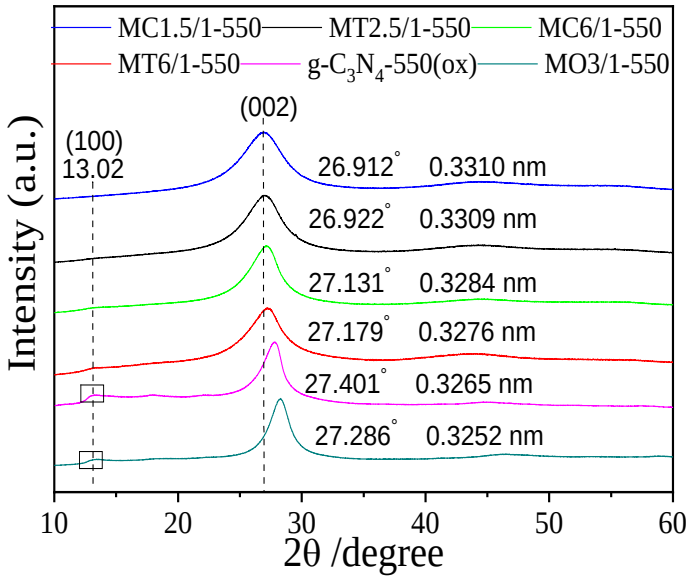

Figure 29. XRD patterns of MC1.5/1-550, MT2.5/1-550, MC6/1-550, MT6/1-550, g-C_3N_4-550 (ox), MC4/1-550, MO3/1-550.

3.5.3. Morphology and structuration

3.5.3.1. Transmission Electron microscopy (TEM) and Energy Dispersive X-ray analysis (EDX)

The nanostructuration of the samples was analyzed by TEM (Fig. 30a-d). Materials like g-C_3N_4 and MO3/1-550, which have both a low thermal behaviour, display a nanoporous structure with holes with a few tens of nm (Fig. 30a-b). This nanostructure is not so evident for C-rich samples having higher thermal stability (MC1.5/1-550 and MT2.5/1-550), as shown in Fig. 30 c-d. High-resolution TEM was difficult to perform owing to the decomposition of the samples under the beam. The structuration of the materials does not lead to porous materials as evidence by the low surface area (13-26 $m^2\ g^{-1}$ from BET model) revealed by N_2 adsorption at 77 K. EDX analysis coupled with STEM experiments have showed a homogenous distribution of C and N at the sub-micrometric scale (Fig. 31a-c).

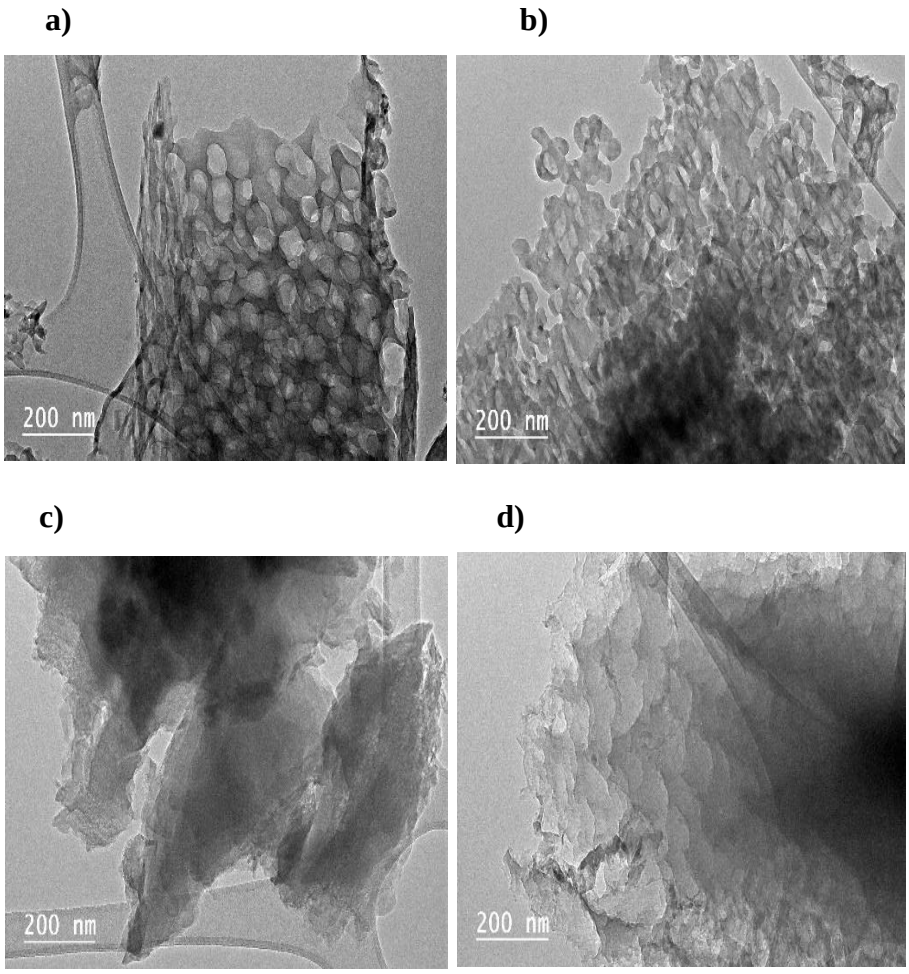

Figure 30. TEM images of a) g-C_3N_4-550 (ox), b) MO3/1-550, c) MC1.5/1-550 and d) MT2.5/1-550 samples.

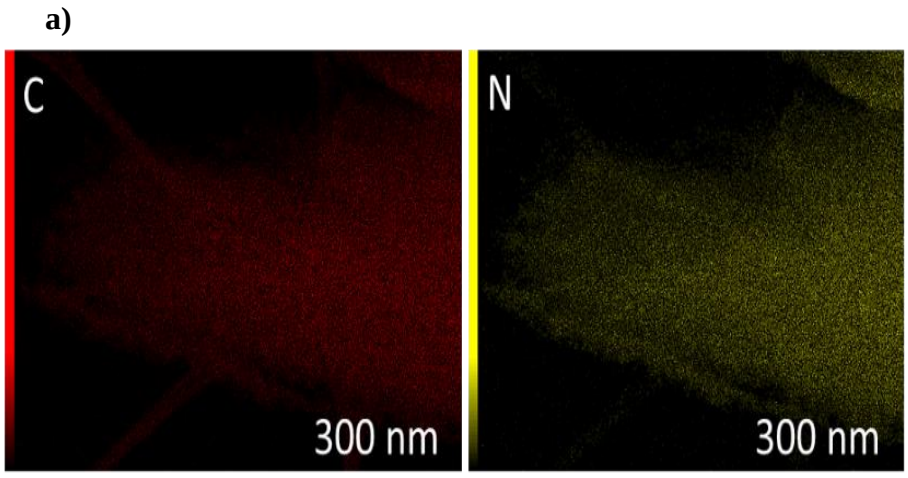

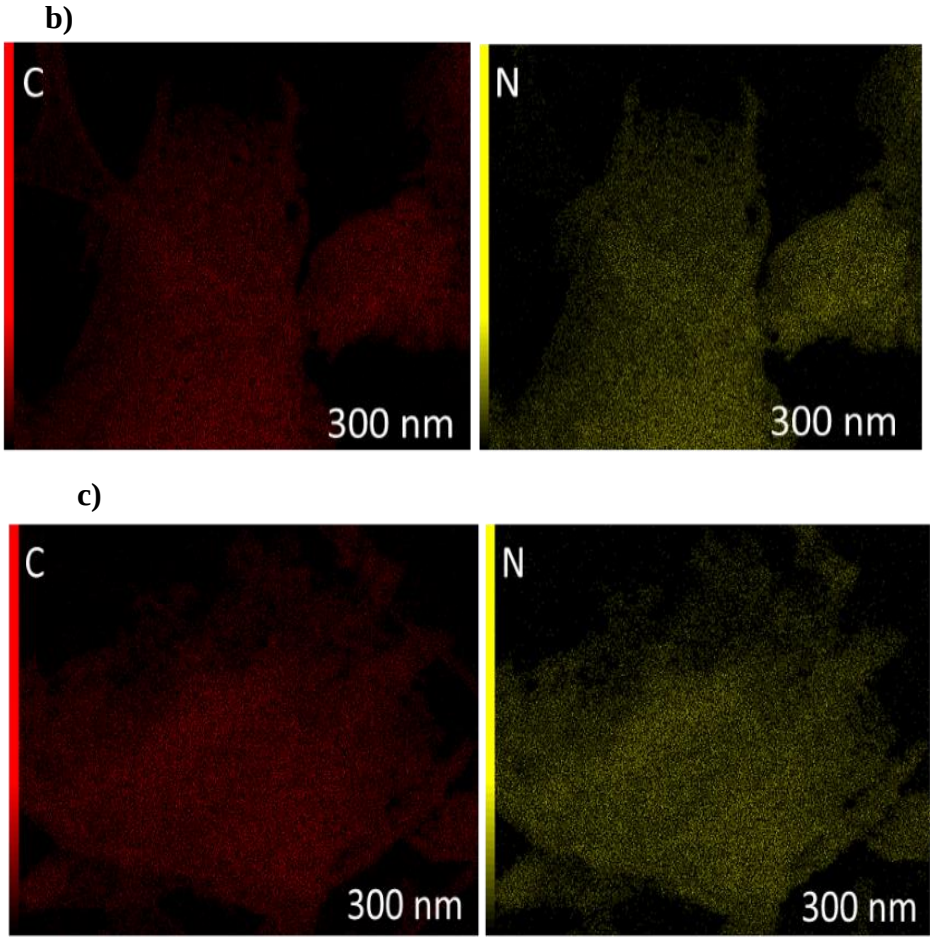

Figure 31. STEM-EDX elemental mapping and uniform distributions of C and N in nanometric scale of a) MT2.5/1-550, b) g-C_3N_4-550 (ox), c) MO3/1-550.

3.5.4. Thermal stability of C-rich-g-C_3N_4 materials

3.5.4.1. Thermogravimetric analysis (TGA) and Differential Scaning Calorimetry (DSC)

To investigate the thermal properties of the calcined samples, TG-DSC analysis under an argon atmosphere was carried out. In agreement with the literature, the thermal stability of g-C_3N_4 in inert atmosphere was limited with a decomposition onset at *circa* 630 °C and complete decomposition at 780 °C (Fig. 32a). For C-rich-g-C_3N_4 samples, interestingly, the temperature-

decomposition onset occurs at lower temperatures than the g-C_3N_4 reference, around 534 °C and 630 °C for respectively MT4/1-550 and MC4/1-550 (Fig.32b). Surprisingly, this behaviour is associated with good high-temperature stability since these materials are still present with a yield of around 20 wt% at 1000 °C. The MO4/1-550 sample lies in-between C-rich samples and g-C_3N_4 regarding nitrogen content as its temperature decomposition onset of 650 °C. It appears that the introduction of extra carbon (and oxygen) atoms within the heptazine structure leads to its destabilization and to a lowered decomposition temperature. The resulting structure, probably enriched with carbon, is then more stable at high temperature. All materials exhibit an endothermic behavior during these decomposition steps (Fig. 32c).

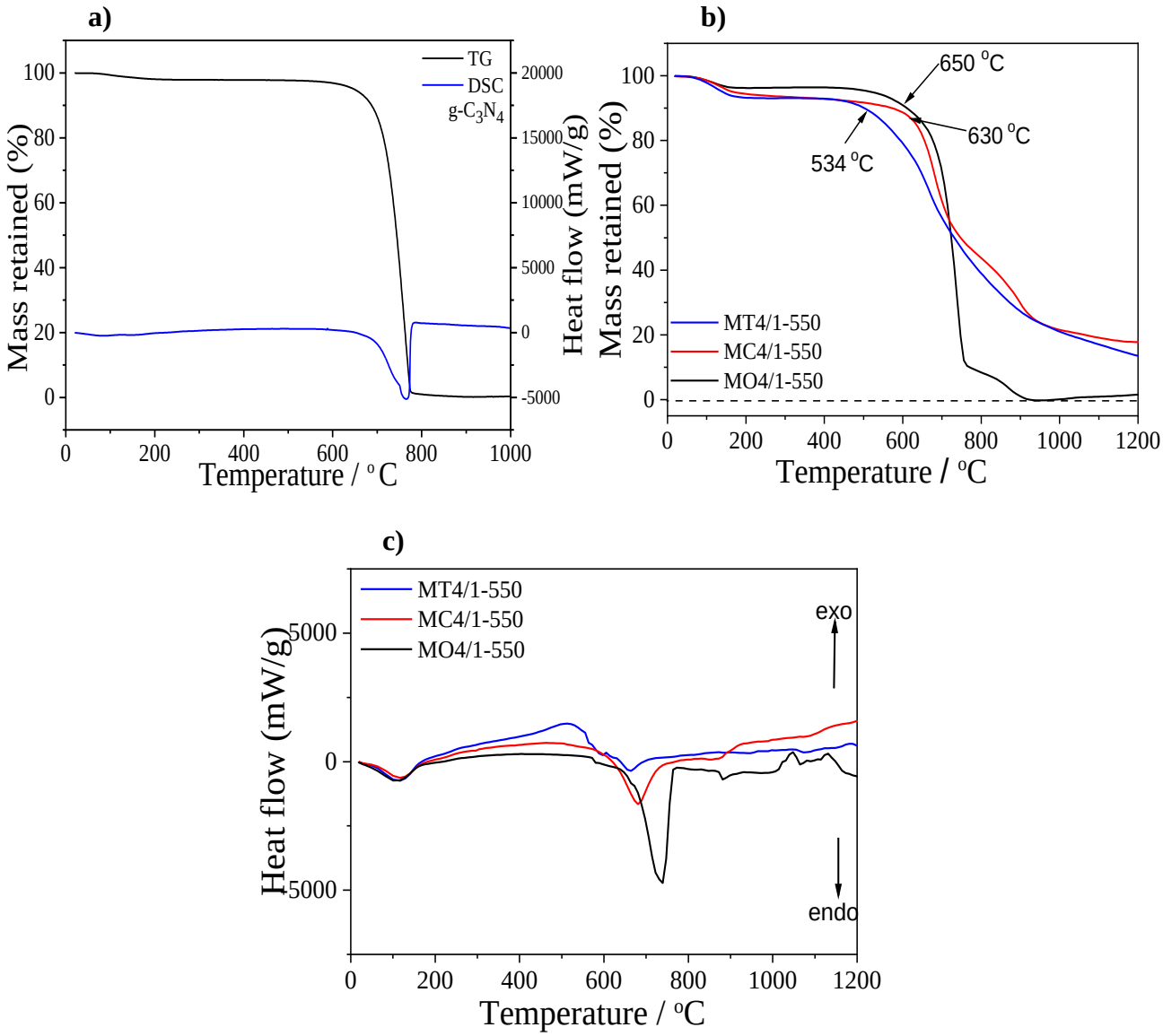

Figure 32. TG-DSC thermograms of g-C_3N_4-550 (ox) (a), TG thermograms (b) and DSC thermograms (c) of MT4/1-550, MC4/1-550, and MO4/1-550 samples under nitrogen flow.

3.5.5. Optical properties of C-rich-g-C_3N_4 materials

3.5.5.1. Diffuse reflectance spectroscopy (DRS)

A large panel of colored samples were obtained, ranging from yellow (g-C_3N_4 -550 (air)) to black (C-rich-C_3N_4 materials), via a brownish (MO3/1-550) and beige (MT6/1-550) color for materials containing a limited amount of extra carbon compared to g-C_3N_4. DRS spectra of g-C_3N_4-550 (ox), MO4/1-550, MT6/1-550 and MC1.5/1-550 samples are reported in Fig.33a. Reflection band edges of around 450 nm and 520 nm were observed for respectively g-C_3N_4-550 (ox) and MO4/1-550. This shift is related to the higher carbon content of the latter sample, which also shows a lower reflectance than the reference in the whole visible range. For even higher carbon content (MC1.5/1-550), the reflectance values are the lowest in the visible region, whereas no significant differences were observed in the UV region. It was impossible to calculate the band gap energy Eg from the Kubelka-Munk theory [43] for the MT1.5/1-550 material. Indeed, if we consider that the material structure is composed of C-rich domains nested within a disordered g-C_3N_4 structure, this structure could lead to ill-defined conductive and valence bands for each phase and therefore, difficulties in isolating their individual contributions by the Kubelka-Munk theory. Therefore, the calculation of the band gap was not performed as recommended in reference [43]. The possible band gap estimation was performed only for g-C_3N_4-550 (ox) and MO4/1-550 (Fig. 33b). The band gap of the photocatalyst was determined using Tauc plot, where $(F(R)\cdot h\nu)^{½}$) was plotted against photon energy (hυ) according to Kubelka-Munck function. The band gap for g-C_3N_4-550 (ox) and MO4/1-550 photocatalysts was obtained from x-intercept by drawing a tangent line of each curve. While the estimation band gap of MC1.5/1-550 was difficult to carry out, due to the black color and higher amount of carbon, and not optimized method for these kinds of samples.

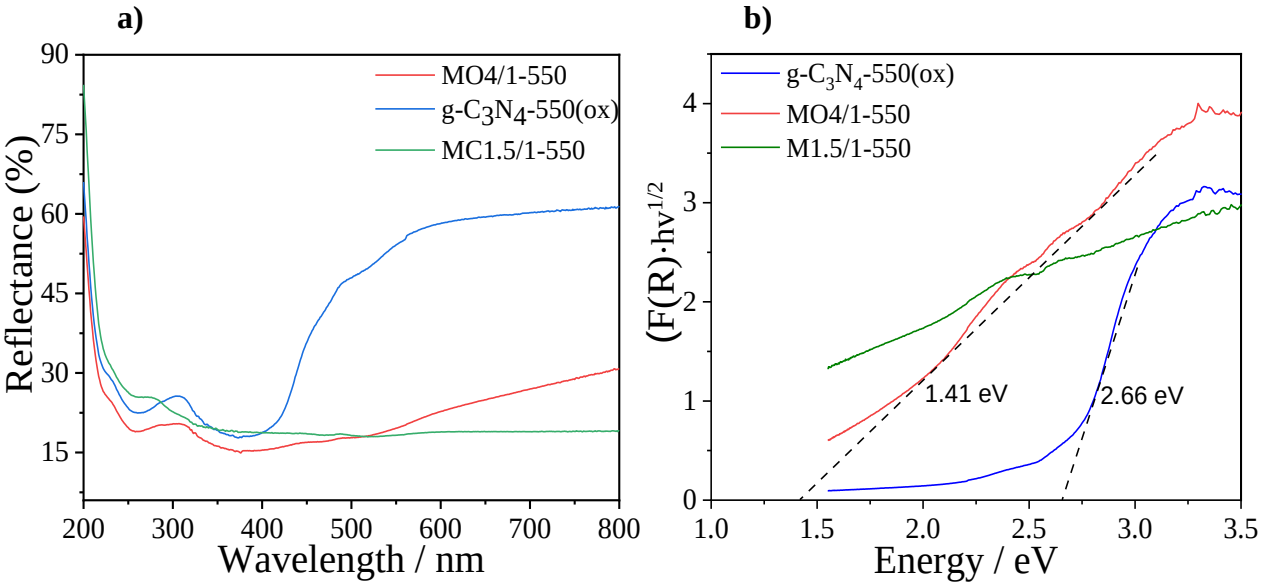

Figure 33. Reflectance spectra (a) and energy band gap (b) of g-C_3N_4-550 (ox), MO4/1-550 and MC1.5/1-550.

3.6. Photocatalytic properties of materials

3.6.1. Hydrogen evolution

The potential photocatalytic properties of those raw C-rich-g-C_3N_4 materials were investigated briefly with the water splitting reaction. Previous studies, based on g-C_3N_4/C composites obtained from a carbonized mixture of carbon black [44] or graphene oxide [45] with melamine, have shown enhanced photocatalytic performances compared to g-C_3N_4 on H_2 production. This was related to the improved photogenerated electron-hole pairs separation owing to the increased electrical conductivity of the carbon part. In our case, the nanostructure of adduct-derived materials is presumably different since the carbon is introduced with the melamine as a precursor (acid) and not as a carbon-based material. The photocatalytic properties of the adduct-derived carbonitride samples were explored by the decomposition of methanol in aqueous media under deep UV irradiation. Hydrogen appears as the main product detected in the photocatalytic decomposition products. Its amount evolved after 4 h of irradiation, is reported in Fig.34 with the results obtained for TiO_2 (P25 Evonik) and g-C_3N_4 for comparison. Although the performance of the C-rich-g-

C_3N_4 material (MT6/1-550 sample) is lower than those of the well-known and optimized references. A photocatalytic behavior is evidenced and appears encouraging since there is probably room to enhance their properties for this application. It is also possible that the carbon content is too high and limits the light absorption of the carbonitride part compared to previous studies [51,52] where the N/C atomic ratio (determined by XPS) is in the range 1.19-1.35 whereas it is 0.93 and 1.61 for the studied samples.

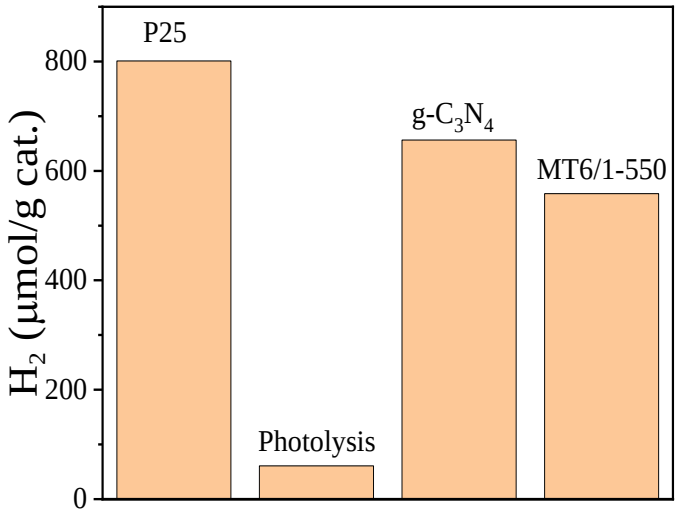

Figure 34. Amounts of H_2 evolve after 4h of photocatalytic decomposition of methanol in the presence of different photocatalysts at 254 nm (pen-ray lamp). Photolysis is reported for comparison.

3.6.2. Colloidal properties of materials

3.6.2.1. Zeta Potential

The zeta potential of g-C_3N_4-550 (ox), MO3/1-550, MT2.5/1-550 and MC4/1-550 samples was investigated versus pH (Fig. 35). It shows a typical shape, i.e., increasing pH, the Zeta potential values become more and more negative. The isoelectric point value for samples MO3/1-550 and MT2.5/1-550 is around pH = 2, as well as for sample g-C_3N_4-550 (ox). An exception is the sample MC4/1-550 of which isoelectric point has the value at pH = 4. It is essential for applications that in the neutral range and more especially in the basic pH range, the Zeta potential values are very

low. In other words, in this pH ranges, the surface of the materials is strongly negatively charged, which gives a good precondition for the adsorption of positively charged particles, such as heavy metal ions or some organic substances.

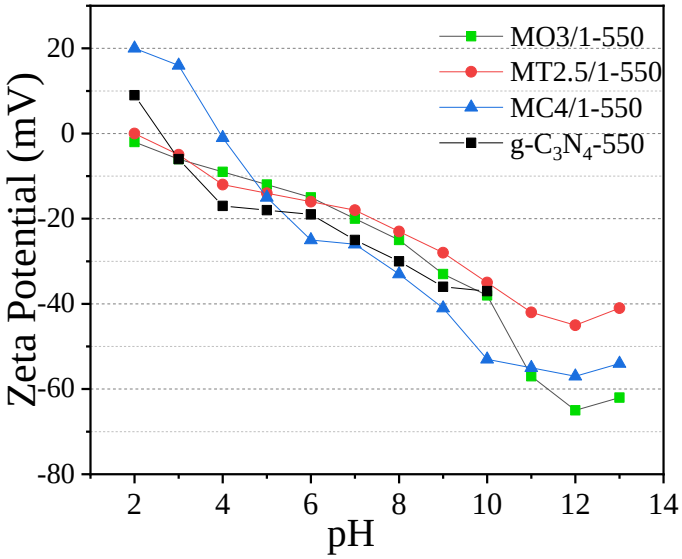

Figure 35. Dependence of Zeta potential with pH.

3.7. Conclusions

We have shown that the adduct route is a versatile synthesis route since according to the starting melamine/acid ratio and the nature of the acid, a large panel of supramolecular-self assembled and crystalline phases could be obtained easily. It results after carbonization at moderate temperature (550 °C) to compounds with composition ranging from graphitic carbonitride to C-rich graphitic carbonitride CN_x ($0.66 < x < 1.4$). It appears, although C and N species are distributed at the molecular level in the precursor (adduct), that a segregation occurs during the carbonization with the appearance of bigger C-rich (sub) nanometric phase (clusters) within the layered structure when the carbon content increase. This feature is also indirectly evidenced by the disappearance of the long-range ordering of heptazine units and a decrease in N-C=N bond portion in the profit of C=C bonds as the carbon content increases. A progressive evolution of the properties between the two end compositions, such as thermal stability, can then be easily tuned by this process. It also introduced a higher portion of oxygen within the structure compared to standard g-C_3N_4, probably due to the presence of carboxylic groups within the adducts. The optical properties are strongly modified even with a limited amount of extra carbon within the g-C_3N_4 structure.

SUMMARY IN FRENCH

Grâce à la voie des adduits mélamine/acide carboxylique, des matériaux à base de g-C_3N_4 enrichis avec du carbone ont été préparés dans une large gamme de composition CN_x ($0.66<x<1.4$). Ce procédé est basé sur la décomposition de produits d'addition mélamine/acide polycarboxylique. Après avoir valider la formation des adduits par DRX et MEB en montrant que la forme cristalline du produit d'addition mélamine/acide est différente de celles de la mélamine et des acides utilisés, nous avons montré que cette approche par le procédé des adduits est efficace pour contrôler la teneur en C et N tout en assurant une grande homogénéité à l'échelle atomique des espèces C et N. La nanostructure du matériau carbonisé a été étudiée à l'aide de différentes techniques (DRX, Spectroscopie RAMAN, MET). La stabilité thermique de ces matériaux CN_x a été comparée à celle du g-C_3N_4 pur. Les matériaux sélectionnés ont aussi été testés pour la photodégradation du méthylorange et la production de H_2 à partir d'un mélange méthanol/eau.

L'évolution des différents types de liaison N-C=N et C=C en fonction de la teneur en C des adduits carbonisés a été suivie par XPS. Le signal à 285 eV a été attribué à des clusters riches en carbone ou à des nanodomaines graphitiques issu probablement du squelette carboné des adduits de l'acide carboxylique. Sa contribution augmente clairement avec la teneur en C des échantillons sélectionnés, de 42 % en masse (MT6/1-550) à 46 % (MT2.5/1-500) et 49 % (MC1.5/1-500). Cette évolution s'accompagne d'une diminution de la contribution des espèces N-C=N. La montre la stabilité thermique sous argon des échantillons de C_3N_4 riche en C. Le début de la décomposition thermique se produit à des températures plus basses que la référence g-C_3N_4. Il est proposé que la substitution du C dans la structure g-C_3N_4 déstabilise thermiquement la structure. Cependant, une meilleure stabilité à haute température des échantillons de C_3N_4 riches en carbone est observée par rapport au carbonitrure de référence. En effet, pour le matériau C_3N_4 riche en C, il reste encore 20 % de sa masse initiale à 1000 °C alors que la décomposition est totale dès 900°C pour le carbonitrure de référence. Il est proposé que cette stabilité soit liée à la présence d'une partie riche en C stable thermiquement. Les matériaux pourraient donc être décrits comme des nanocomposites de type carbonitrure dopé en N/ phase carbonée (riche en N) notés de manière simplifiée g-C_3N_4 /C.

Les activités de photodégradation du méthyl-orange (MO) et la photolyse de l'eau (en présence de l'agent sacrificiel CH_3OH). On constate une amélioration des performances des composites C_3N_4/C dans la dégradation du MO par rapport aux matériaux de type g-C_3N_4. Cette amélioration peut être liée à la présence de nanodomaines riches en C dont les orbitales π-conjuguées, par la possibilité de délocalisation des électrons qu'elles offrent, permettent de séparer les électrons des trous générés dans la phase g-C_3N_4 ; ceci limite ainsi leur recombinaison. Un autre comportement est observé pour la photolyse de l'eau. Les performances du matériau C_3N_4 /C (échantillon MT6/1-550) sont dans ce cas inférieures à celles des références bien connues (TiO_2 P25 et g-C_3N_4). Il est possible que la teneur en carbone soit trop élevée et que sa trop forte absorption limite l'intensité du rayonnement accessible à la partie photocatalytique du carbonitrure. Ces études préliminaires semblent encourageantes car il est probablement possible d'améliorer les propriétés photocatalytiques de ces matériaux nanocomposites carbonitrures /C pour cette dernière application.

References

[1] N. M. R. Peres, 'Graphene, new physics in two dimensions', *Europhysics News*, vol. 40, no. 3, pp. 17–20, May 2009, doi: 10.1051/epn/2009501.

[2] J. Zhang *et al.*, 'Graphitic N in nitrogen-Doped carbon promotes hydrogen peroxide synthesis from electrocatalytic oxygen reduction', *Carbon*, vol. 163, pp. 154–161, Aug. 2020, doi: 10.1016/j.carbon.2020.02.084.

[3] Y. Hu, H. Liu, Q. Ke, and J. Wang, 'Effects of nitrogen doping on supercapacitor performance of a mesoporous carbon electrode produced by a hydrothermal soft-templating process', *J. Mater. Chem. A*, vol. 2, no. 30, p. 11753, Jun. 2014, doi: 10.1039/C4TA01269K.

[4] J. Fang, H. Fan, M. Li, and C. Long, 'Nitrogen self-doped graphitic carbon nitride as efficient visible light photocatalyst for hydrogen evolution', *J. Mater. Chem. A*, vol. 3, no. 26, pp. 13819–13826, 2015, doi: 10.1039/C5TA02257F.

[5] S. Zhang, S. Tsuzuki, K. Ueno, K. Dokko, and M. Watanabe, 'Upper Limit of Nitrogen Content in Carbon Materials', *Angew. Chem. Int. Ed.*, vol. 54, no. 4, pp. 1302–1306, Jan. 2015, doi: 10.1002/anie.201410234.

[6] J. P. Paraknowitsch, J. Zhang, D. Su, A. Thomas, and M. Antonietti, 'Ionic Liquids as Precursors for Nitrogen-Doped Graphitic Carbon', *Adv. Mater.*, vol. 22, no. 1, pp. 87–92, Jan. 2010, doi: 10.1002/adma.200900965.

[7] T. Katoh, G. Imamura, S. Obata, and K. Saiki, 'Growth of N-doped graphene from nitrogen containing aromatic compounds: the effect of precursors on the doped site', *RSC Adv.*, vol. 6, no. 16, pp. 13392–13398, 2016, doi: 10.1039/C5RA22664C.

[8] Y. Wang *et al.*, 'Facile One-Step Synthesis of Hybrid Graphitic Carbon Nitride and Carbon Composites as High-Performance Catalysts for CO_2 Photocatalytic Conversion', *ACS Appl. Mater. Interfaces*, vol. 8, no. 27, pp. 17212–17219, Jul. 2016, doi: 10.1021/acsami.6b03472.

[9] Z. Chen *et al.*, 'A gradual carbon doping graphitic carbon nitride towards the metal-free visible light photocatalytic hydrogen evolution', *J. Mater. Chem. A*, vol. 1–3, no. 1, pp. 15310–15319, 2018, doi: DOI: 10.1039/C8TA03303J.

[10] H. Dong, X. Guo, C. Yang, and Z. Ouyang, 'Synthesis of g-C3N4 by different precursors under burning explosion effect and its photocatalytic degradation for tylosin', *Applied Catalysis B: Environmental*, vol. 230, pp. 65–76, Aug. 2018, doi: 10.1016/j.apcatb.2018.02.044.

[11] K. Wang, X. Wang, H. Pan, Y. Liu, S. Xu, and S. Cao, 'In situ fabrication of CDs/g-C3N4 hybrids with enhanced interface connection via calcination of the precursors for photocatalytic H2 evolution', *International Journal of Hydrogen Energy*, vol. 43, no. 1, pp. 91–99, Jan. 2018, doi: 10.1016/j.ijhydene.2017.11.003.

[12] R. Kumar, 'Oxidized g-C3N4/polyaniline nanofiber composite for the selective removal of hexavalent chromium', *Scientific Reports*, p. 11.

[13] W. Che *et al.*, 'Fast Photoelectron Transfer in (Cring)–C3N4 Plane Heterostructural Nanosheets for Overall Water Splitting', *J. Am. Chem. Soc.*, vol. 139, no. 8, pp. 3021–3026, Mar. 2017, doi: 10.1021/jacs.6b11878.

[14] Y.-S. Jun, E. Z. Lee, X. Wang, W. H. Hong, G. D. Stucky, and A. Thomas, 'From Melamine-Cyanuric Acid Supramolecular Aggregates to Carbon Nitride Hollow Spheres', *Adv. Funct. Mater.*, vol. 23, no. 29, pp. 3661–3667, Aug. 2013, doi: 10.1002/adfm.201203732.

[15] S. Dolai, J. Barrio, G. Peng, A. Grafmüller, and M. Shalom, 'Tailoring carbon nitride properties and photoactivity by interfacial engineering of hydrogen-bonded frameworks', *Nanoscale*, vol. 11, no. 12, pp. 5564–5570, 2019, doi: 10.1039/C9NR00711C.

[16] N. Vu, C. Nguyen, S. Kaliaguine, and T. Do, 'Synthesis of g-C_3N_4 Nanosheets by Using a Highly Condensed Lamellar Crystalline Melamine–Cyanuric Acid Supramolecular Complex for Enhanced Solar Hydrogen Generation', *ChemSusChem*, vol. 12, no. 1, pp. 291–302, Jan. 2019, doi: 10.1002/cssc.201802394.

[17] Z. Zhou, Y. Zhang, Y. Shen, S. Liu, and Y. Zhang, 'Molecular engineering of polymeric carbon nitride: advancing applications from photocatalysis to biosensing and more', *Chem. Soc. Rev.*, vol. 47, no. 7, pp. 2298–2321, 2018, doi: 10.1039/C7CS00840F.

[18] X. Zhang, 'Synthesis and Crystal Structure of a Complex of Melamine with Benzoic Acid', *Chemical Research in Chinese Universities*, vol. 24, no. 4, pp. 396–400, Jul. 2008, doi: 10.1016/S1005-9040(08)60084-7.

[19] X. Han *et al.*, 'Facile transformation of low cost melamine–oxalic acid into porous graphitic carbon nitride nanosheets with high visible-light photocatalytic performance', *RSC Adv.*, vol. 7, no. 24, pp. 14372–14381, 2017, doi: 10.1039/C7RA01205E.

[20] G. J. Perpétuo and J. Janczak, 'Supramolecular architectures in crystals of melamine and aromatic carboxylic acids', *Journal of Molecular Structure*, vol. 891, no. 1–3, pp. 429–436, Nov. 2008, doi: 10.1016/j.molstruc.2008.04.032.

[21] C. Zhou *et al.*, 'Highly porous carbon nitride by supramolecular preassembly of monomers for photocatalytic removal of sulfamethazine under visible light driven', *Applied Catalysis B: Environmental*, vol. 220, pp. 202–210, Jan. 2018, doi: 10.1016/j.apcatb.2017.08.055.

[22] X. Fang, R. Gao, Y. Yang, and D. Yan, 'A Cocrystal Precursor Strategy for Carbon-Rich Graphitic Carbon Nitride toward High-Efficiency Photocatalytic Overall Water Splitting', *iScience*, vol. 16, pp. 22–30, Jun. 2019, doi: 10.1016/j.isci.2019.05.015.

[23] X. Yuan, K. Luo, K. Zhang, J. He, Y. Zhao, and D. Yu, 'Combinatorial Vibration-Mode Assignment for the FTIR Spectrum of Crystalline Melamine: A Strategic Approach toward Theoretical IR Vibrational Calculations of Triazine-Based Compounds', *J. Phys. Chem. A*, vol. 120, no. 38, pp. 7427–7433, Sep. 2016, doi: 10.1021/acs.jpca.6b06015.

[24] S. Sarkar, S. Dutta, C. Ray, B. Dutta, J. Chowdhury, and T. Pal, 'A two-component hydrogelator from citrazinic acid and melamine: synthesis, intriguing role of reaction parameters and iodine adsorption study', *CrystEngComm*, vol. 17, no. 42, pp. 8119–8129, 2015, doi: 10.1039/C5CE01001B.

[25] X.-I. Zhang, 'Synthesis and Crystal Structure of a Complex of Melamine with Benzoic Acid', vol. 24, no. 4, pp. 396–400, 2008, doi: doi.org/10.1016/S1005-9040(08)60084-7.

[26] X.-L. Zhang and X.-M. Chen, ‘Supramolecular Architectures and Helical Water Chains in Cocrystals of Melamine and Aromatic Carboxylic Acids’, *Crystal Growth & Design*, vol. 5, no. 2, pp. 617–622, Mar. 2005, doi: 10.1021/cg0498251.

[27] P. J. Larkin, M. P. Makowski, and N. B. Colthup, ‘The form of the normal modes of s-triazine: infrared and Raman spectral analysis and ab initio force field calculations’, *Spectrochimica Acta Part A: Molecular and Biomolecular Spectroscopy*, vol. 55, no. 5, pp. 1011–1020, May 1999, doi: 10.1016/S1386-1425(98)00244-3.

[28] S. C. Yan, Z. S. Li, and Z. G. Zou, ‘Photodegradation Performance of g-C $_3$ N $_4$ Fabricated by Directly Heating Melamine’, *Langmuir*, vol. 25, no. 17, pp. 10397–10401, Sep. 2009, doi: 10.1021/la900923z.

[29] D. J. Miller, M. C. Biesinger, and N. S. McIntyre, ‘Interactions of CO2 and CO at fractional atmosphere pressures with iron and iron oxide surfaces: one possible mechanism for surface contamination’, *Surf. Interface Anal.*, p. 7, 2002.

[30] H.-J. Li, B.-W. Sun, L. Sui, D.-J. Qian, and M. Chen, ‘Preparation of water-dispersible porous g-C $_3$ N $_4$ with improved photocatalytic activity by chemical oxidation’, *Phys. Chem. Chem. Phys.*, vol. 17, no. 5, pp. 3309–3315, 2015, doi: 10.1039/C4CP05020G.

[31] N. D. Shcherban *et al.*, ‘Melamine-derived graphitic carbon nitride as a new effective metal-free catalyst for Knoevenagel condensation of benzaldehyde with ethylcyanoacetate’, *Catal. Sci. Technol.*, vol. 6, no. 1, pp. 73–80, 2016, doi: DOI: 10.1039/x0xx00000x.

[32] W. Zhang, L. Zhou, and H. Deng, ‘Ag modified g-C3N4 composites with enhanced visible-light photocatalytic activity for diclofenac degradation’, *Journal of Molecular Catalysis A: Chemical*, vol. 423, pp. 270–276, Nov. 2016, doi: 10.1016/j.molcata.2016.07.021.

[33] T. Ramanathan, F. T. Fisher, R. S. Ruoff, and L. C. Brinson, ‘Amino-Functionalized Carbon Nanotubes for Binding to Polymers and Biological Systems’, *Chem. Mater.*, vol. 17, no. 6, pp. 1290–1295, Mar. 2005, doi: 10.1021/cm048357f.

[34] G. Camino, L. Operti, and L. Trossarelli, ‘Mechanism of thermal degradation of urea-formaldehyde polycondensates’, *Polymer Degradation and Stability*, vol. 5, no. 3, pp. 161–172, May 1983, doi: 10.1016/0141-3910(83)90007-1.

[35] L. J. Broadbelt, A. Chu, and M. T. Klein, ‘Thermal stability and degradation of aromatic polyamides. Part 2. Structure-reactivity relationships in the pyrolysis and hydrolysis of benzamides’, *Polymer Degradation and Stability*, vol. 45, no. 1, pp. 57–70, Jan. 1994, doi: 10.1016/0141-3910(94)90178-3.

[36] P. F. Britt, ‘Pyrolysis and Combustion of Acetonitrile (CH3CN)’, OAK RIDGE NATIONAL LABORATORY, 2002. [Online].Available: https://info.ornl.gov/sites/publications/Files/Pub57226.pdf

[37] A. C. Ferrari, S. E. Rodil, and J. Robertson, ‘Interpretation of infrared and Raman spectra of amorphous carbon nitrides’, *Phys. Rev. B*, vol. 67, no. 15, p. 155306, Apr. 2003, doi: 10.1103/PhysRevB.67.155306.

[38] A. Merlen, J. Buijnsters, and C. Pardanaud, ‘A Guide to and Review of the Use of Multiwavelength Raman Spectroscopy for Characterizing Defective Aromatic Carbon

Solids: from Graphene to Amorphous Carbons', *Coatings*, vol. 7, no. 10, p. 153, Sep. 2017, doi: 10.3390/coatings7100153.

[39] G. R. Dillip, T. V. M. Sreekanth, and S. W. Joo, 'Tailoring the bandgap of N-rich graphitic carbon nitride for enhanced photocatalytic activity', *Ceramics International*, vol. 43, no. 8, pp. 6437–6445, Jun. 2017, doi: 10.1016/j.ceramint.2017.02.057.

[40] J. Liu, Y. Zhang, L. Zhang, F. Xie, A. Vasileff, and S. Qiao, 'Graphitic Carbon Nitride (g-C_3N_4)-Derived N-Rich Graphene with Tuneable Interlayer Distance as a High-Rate Anode for Sodium-Ion Batteries', *Adv. Mater.*, p. 1901261, Apr. 2019, doi: 10.1002/adma.201901261.

[41] Z. Yang *et al.*, 'Facile synthesis of highly crystalline g-C3N4 nanosheets with remarkable visible light photocatalytic activity for antibiotics removal', *Chemosphere*, vol. 271, p. 129503, May 2021, doi: 10.1016/j.chemosphere.2020.129503.

[42] J. Y. Howe, C. J. Rawn, L. E. Jones, and H. Ow, 'Improved crystallographic data for graphite', *Powder Diffr.*, vol. 18, no. 2, pp. 150–154, Jun. 2003, doi: 10.1154/1.1536926.

[43] G. D. Gesesse, A. Gomis-Berenguer, M.-F. Barthe, and C. O. Ania, 'On the analysis of diffuse reflectance measurements to estimate the optical properties of amorphous porous carbons and semiconductor/carbon catalysts', *Journal of Photochemistry and Photobiology A: Chemistry*, vol. 398, p. 112622, Jul. 2020, doi: 10.1016/j.jphotochem.2020.112622.

[44] Z. Wu, H. Gao, S. Yan, and Z. Zou, 'Synthesis of carbon black/carbon nitride intercalation compound composite for efficient hydrogen production', *Dalton Trans.*, vol. 43, no. 31, pp. 12013–12017, 2014, doi: 10.1039/C4DT00256C.

[45] R. Wang, X. Wang, X. Li, L. Pei, X. Gu, and Z. Zheng, 'Facile one-step synthesis of porous graphene-like g-C3N4 rich in nitrogen vacancies for enhanced H2 production from photocatalytic aqueous-phase reforming of methanol', *International Journal of Hydrogen Energy*, vol. 46, no. 1, pp. 197–208, Jan. 2021, doi: 10.1016/j.ijhydene.2020.09.156.

CHAPTER 4

Selective thermal oxidation of C-rich-g-C_3N_4 materials for the preparation of N-rich porous carbon material

4.1. Introduction

Carbon materials with sp^2 hybridization possess a combination of essential properties, such as high electrical conductivity. These materials have a wide range of applications in the fields of energy, environment, catalysis, adsorption process, etc. Their structure could be tailored by changing the atomic framework construction and adjusting its properties. By replacing the 6-rings graphene with any possible defects on the sites, could lead to the structure distortion. The rearrangement of the structure of C-based materials could lead to changes of textural properties, which endow a porous framework [1]. Moreover, C-based materials could also be tailored in terms of electronic and surface atomic structure by different approaches as heteroatom-doping, atmosphere oxidation, etc. Plenty of studies have been carried out on the incorporation of nitrogen into the carbon framework, which form N-doped carbons, or carbon nitride, having different stoichiometry. The incorporation of N atoms into carbons could be done using in situ doping method, from nitrogen-containing precursors, etc. This enables to homogeneously incorporate the N via controlled chemistry [2]. There are two ways to incorporate N into the C framework, either directly during synthesis or by post-treatment of carbons. The latter one deals with the treatment by nitrogen-containing atmosphere, like NH_3 [3, 4, 5, 6], high thermal, chemical stability, low price, and easily tailorable structure. Another promising way of incorporation N in carbon framework is to use g-C_3N_4 as a source of high nitrogen content, and take advantage of some physico-chemical properties of g-C_3N_4 [7]. In the previous chapter was investigated the route to tailor the C/N ratio starting from molecular level to calcined samples under inert atmosphere, and emphasized the role of carbon and nitrogen in surface chemistry, thermal properties and structural modification. Materials prepared in the previous chapter were investigated with regarding to their thermal stability and reactivity towards the oxygen. Benefiting from C-rich-g-C_3N_4 composite, we aimed to produce N-rich porous carbon, while controlling the temperature of oxidation. Then a structural model based on C-rich g-C_3N_4/N-rich carbonaceous phase nanocomposites is proposed, and the validity of this structural model will be described in relation with oxidizing atmosphere conditions. The contents of O, C and N could have an impact on the thermal and structural properties of materials.

4.2. Physico-chemical characterization of N-rich porous carbon materials

4.2.1. Thermal evolution of g-C_3N_4–based materials in air and inert atmosphere

The thermal degradation of g-C_3N_4 and C-rich-g-C_3N_4 materials was monitored under inert and in air atmosphere in order to investigate their reactivity towards O_2. It appears that the temperature-decomposition onset is strongly dependent on the atmosphere and to a lower extend of the C-content. Under inert atmosphere, four different behaviours were observed by TGA in Fig. 36a. Carbonitride as a reference material exhibits a decomposition onset at around 688 °C followed by MO4/1-550 that is close to carbonitride in chemical composition point of view with the onset of decomposition at 674 °C. While on the other hand for C-rich MC1.5/1-550 and MT6/1-550 samples, the temperature-decomposition onset start earlier compared to g-C_3N_4 which was explained in chapter 3, and was attributed to the high-temperature stability, which still yields a mass of around 28 wt% at 1000 °C. A complete decomposition of g-C_3N_4 and MO4/1-550 was observed opposed to other samples, which led to C stable residue. Moreover, the thermal behaviour of the samples was investigated under air atmosphere (Fig. 36b). Carbon less-containing samples g-C_3N_4 and MO4/1-550 exhibit higher thermal stability in air compare to C-rich samples, with no mas residue above temperature 750 °C. Thermal stability and reactivity of the samples were also investigated in relation with the influence of chemical composition. Three different behaviours were observed for g-C_3N_4, MO4/1-550 and those of C-rich samples, following the C content variation (see Table 4, Chapter 3). A proposed mechanism based on the C content could be given. A clear evolution of thermal stability with respect to carbon content could be observed (Fig. 36a) as followed: g-C_3N_4 and MO4/1-550 samples contain similar amount of C, but different O and N content. The high and low presence of O and N, respectively, of the MO4/1-550 sample make this material more thermally stable opposed to g-C_3N_4. Moreover, its thermal stability towards the inert atmosphere and air is almost similar. But MO4/1-550 seems to be more stable towards oxygen then g-C_3N_4. Unlike from abovementioned samples, the C-rich MT6/1-550 and MC1.5/1-550 samples which, which contain higher amount of carbon and oxygen, are more predisposed towards the oxidation. They exhibit a huge exothermic peak (discussed below) with rapid mass loss and without mass residue at high temperature. Whereas, under

an inert atmosphere, the MC1.5/1-550 sample with the highest C content 49.2 % exhibits still mass residue up to 28 % even at 1000 °C. This behavior may be attributed to the carbon nano-domains, which could enhance the thermal stability, compared to MT6/1-550 having 42.2 % carbon content, with mass residue of around 2.9 % (Fig. 36a). C-rich-g-C_3N_4 samples enriched with defects on their structure, containing C-rich domains, could increase the reactivity and decrease the onset of decomposition. Hence, a possible explanation could be attributed to a lower kinetic of oxidation by C-rich domains.

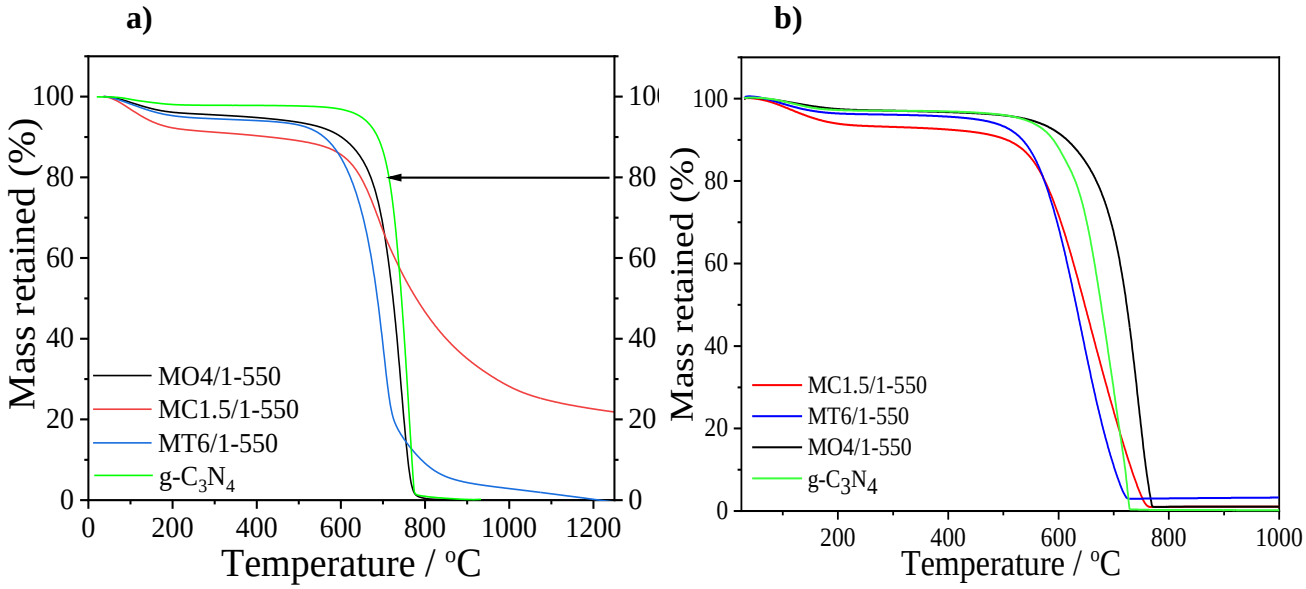

Figure 36. Thermogravimetric analysis of non-oxidized samples performed under inert atmosphere N_2 (a) and under air (b) at 10 °C min^{-1}.

In Fig. 37a-d were displayed the TG-DSC results of the same samples compared under inert and air atmosphere, but shown individually in four different separated graphs from Fig. 36. When heating was performed under inert atmosphere endothermic behaviors were evidenced for all samples. Reference g-C_3N_4 (Fig. 37a) exhibits a small endothermic peak compared to others, presuming for a slowly mass loss, while under air, two exothermic events could be observed, a small and big sharp peak, for the last one showing a higher mass loss. On the other hand, MO4/1-550 sample (Fig. 37b) exhibits a big and sharp endothermic peak under inert atmosphere. But what is surprisingly that under the air atmosphere, two thermal events were evidenced for this sample, the first endothermic

behavior accompanied by a small peak and then other small exothermic sharp peak. Maybe this phenomena could be related that in first step the g-C_3N_4 structure was oxidized, which was followed by burning the carbon nano-domains in the second step. The C-rich MT6/1-550 and MC1.5/1-550 samples (Fig. 37c-d), when heated under an inert atmosphere, were accompanied by thermal endothermic behavior characterized by a small peak, different from the MO4/1-550 which possesses a huge endo-peak. Maybe this phenomena could be attributed that MO4/1-550 sample possess chemical groups which are reactive towards the N_2.

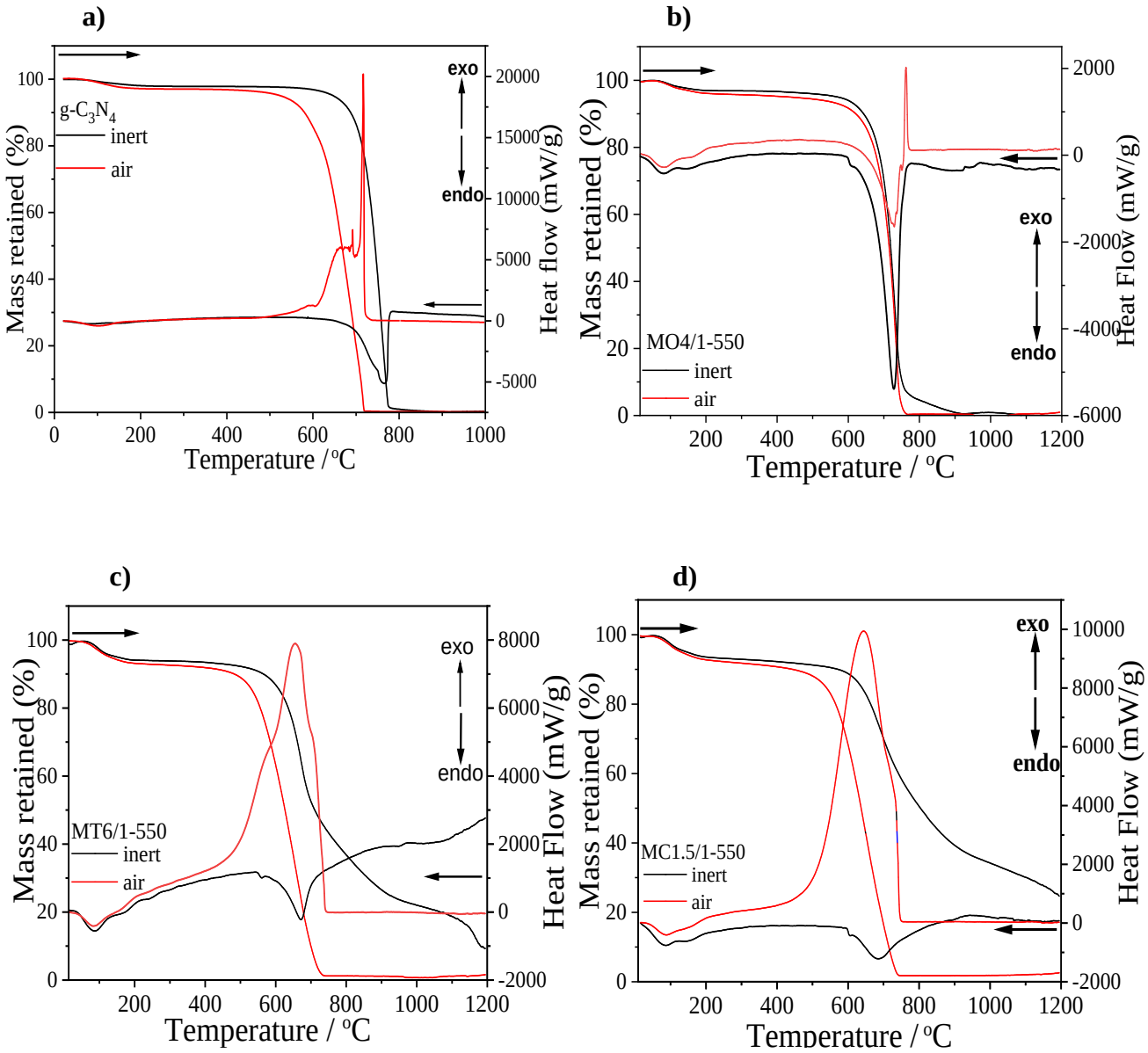

Figure 37. TG-DSC analysis of non-oxidized samples performed under inert and air atmosphere at 10 °C min^{-1}.

In Table 6 is summarized the onset of decomposition and complete mass loss of oxidized and non-oxidized samples. Clearly can be seen that, thermal stability under air is limited for all kinds of samples compared.

Table 6. Onset and mass loss of non-oxidized and oxidized samples under air and inert atmosphere.

Samples	**Onset of Decomposition under inert atm. (°C)**	**Temperature of complete mass loss under inert atm. (°C)**	**Onset of Decomposition under air (°C)**	**Temperature of complete mass loss under air (°C)**
g-C_3N_4-550 (ox)	688	760	611	687
MO4/1-550	674	735	654	739
MC4/1-550	608	860	571	668
MT6/1-550	625	705	535	661
MC1.5/1-550	605	970	556	685
MT2.5/1-550-650 (ox)	585	1040	529	629
MT6/1-550-650 (ox)	560	860	525	629
MC4/1-550-470 (ox)	620	893	540	606
MT4/1-550-470 (ox)	538	852	522	589
MO4/1-550-470 (ox)	663	738	617	703

4.2.2. Composition of N-rich porous C materials

4.2.2.1. Elemental analysis

Based on elemental analysis, g-C_3N_4 as a reference material with C/N at. ratio 0.63 differs in chemical composition point of view compared to the other samples, which exhibit higher C/N ratio. The MO3/1-550 sample is similar to g-C_3N_4 with a higher amount of O and N. Both abovementioned samples exhibit high thermal stability in the air with close composition whatever the oxidation temperature. Whereas the MT and MC samples are more reactive in an oxidative atmosphere, with a more variation in their chemical composition. According to the EA, the carbon content slightly increases with the oxidation temperature for each couple of samples. Opposite and more pronounced trend is observed

for nitrogen, as evidenced with the evolution of the C/N ratio (Table 7). We can deduce that O_2 possesses higher reactivity on nitrogen centers than on carbon one. This preferential reactivity could promote the release of N-containing gaseous species compared to carbon. We notice also an increase in the O content (up to 17 wt%) with the increase in the oxidation temperature. Similar trends were observed by XPS analysis but with discrepancies related to their particular surface composition determination (a few nanometer) compared to the bulk. It appears on the MT2.5/1 group of samples that the surface composition is higher in C, lower in O compared to the bulk, determined by EA, whereas nitrogen showed similar composition for both analysis. It could be proposed that oxidation has started from the outside surface of the sample, is still in progress for the MT2.5/1-550-T (ox) samples (T = 470, 550, 650 °C). Thus, the analyzed external surface is more carbon rich than the bulk. Surprisingly, the oxygen content of the surface is lower than that of the bulk (6 instead of 17 wt%). This feature could be due to the existence of oxygenated species stable in the bulk of the sample, where O_2 pressure is due to its consumption by the material oxidation at a surface rich in oxygen. These groups are oxidized further and yield gaseous species, leaving only the most stable carbonaceous species. As a matter of fact, after the treatment in oxidation atmosphere, the skeleton of g-C_3N_4 is lost, and remains only carbonaceous local domains, also evidenced by FTIR and Raman. We also noted that the samples contain H as well, implying the existence of uncondensed amino groups which are bound to the edges of a graphene-like C-N sheet in the form of C-NH_2 bonds [1], evidenced also by XPS, while another source of hydrogen could be due to the poly-carboxylic acids.

Table 7. Elemental composition of the samples (wt. %) obtained from EA and XPS analysis.

Name of sample	C		N		O		H	C/N atomic ratio
	EA	XPS	EA	XPS	EA	XPS	EA	EA
g-C_3N_4-550 (ox)	34.33	40.44	62.60	57.28	2.46	2.28	1.61	0.63
MO4/1-550	34.4	-	56.99	-	6.67	-	1.94	0.70
MO4/1-550-470 (ox)	33.86	-	57.73	-	6.51	-	2.09	0.68
MO3/1-550-650 (ox)	34.15	-	56.95	-	6.85	-	1.88	0.70
MT6/1-550	42.29	41.33	46.18	57.53	10.43	1.13	1.37	1.06
MT6/1-550-470 (ox)	47.42	-	37.04	-	13.98	-	1.30	1.49
MT2.5/1-550	46.26	50.40	41.88	45.04	10.13	4.56	1.22	1.29
MT2.5/1-550-470 (ox)	48.19	-	34.90	-	15.82	-	1.15	1.61
MT2.5/1-550-550 (ox)	-	60.4	-	35.04	-	4.49	-	-
MT2.5/1-550-650 (ox)	49.78	62.2	29.85	31.5	17.12	6.2	1.69	1.94
MC4/1-550	43.70		44.65		9.78		1.57	1.14
MC4/1-550-470 (ox)	45.16		38.52		13.77		2.01	1.36
MC1.5/1-550	49.2		38.1		11.4		1.48	1.50

4.2.3. Controlled oxidation of g-C_3N_4 based samples followed by TGA (static mode)

Based on the data obtained in the previous section, controlled oxidation in air of g-C_3N_4 based materials was performed at different temperatures (470 to 625 °C) for 4 h. The mass evolution was followed by TGA and is reported in Fig. 38 on two selected samples, based on higher carbon containing sample MT2.5/1-550, and MO4/1-550 with less amount of carbon and reactivity towards the oxygen atmosphere. Two completely different behaviours were observed for these two samples, as described below.

As stated in section (4.2.1) the MT2.5/1-550 sample in an inert atmosphere exhibits high thermal stability of its carbon-rich part (as confirmed latter). This part remains in contact with a C-doped carbonitride and destabilizes it by the presence of C. With the increase in the controlled oxidation temperature-dwell (Fig. 38a), both parts are oxidized but with a higher speed for the C-doped carbon nitride leading to a higher portion of the C part (N-rich) in the material. As the latter shows, the gasification of the C-doped g-C_3N_4 part promotes the formation of pores, and the amount of

the C part remains.Thus promoting a more complete oxidation at a lower temperature compared to pure g-C_3N_4. High thermal stability under the air atmosphere of MO4/1-550 sample (Fig. 38b) is indication that this material has a composition close to g-C_3N_4 with a stable chemical structure and limited decomposition, and number of gaseous species released during the pyrolysis in the air as seen by mass loss. As shown later, this small amount gaseous species released is related to a material with limited specific surface area (See N_2 adsorption isotherm latter).

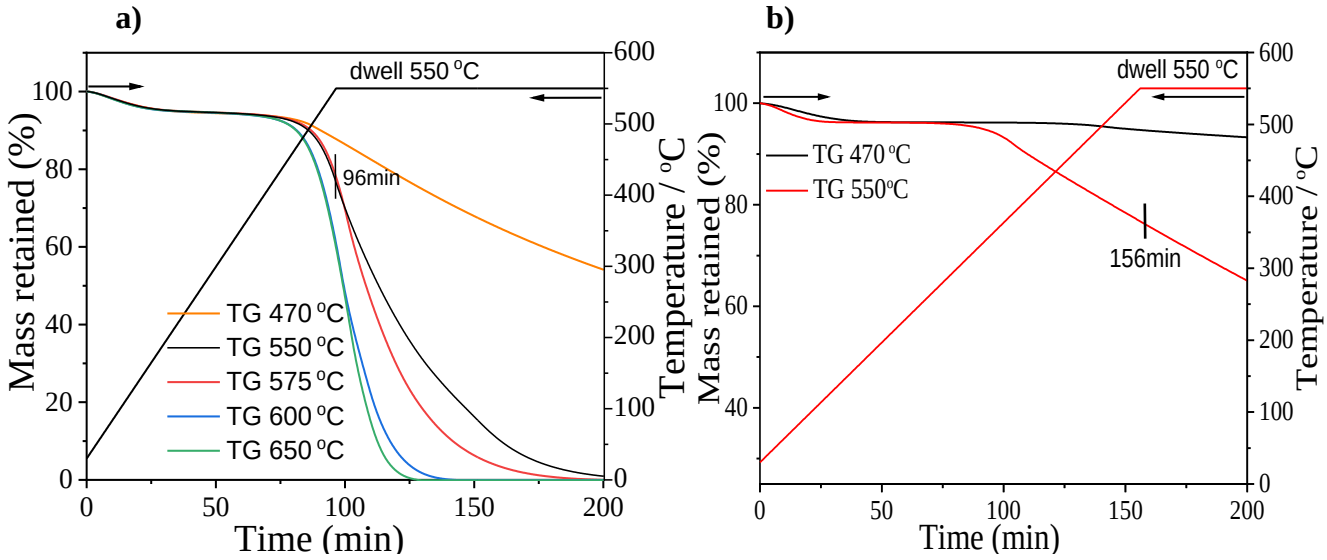

Figure 38. TGA of controlled oxidation in air with different dwell temperatures (470-625 °C) of, a) MT2.5/1-550 and b) MO4/1-550 samples. Temperature profile corresponds the sample oxidized in static mode at 550 °C.

4.2.4. Structure investigation

4.2.4.1. XRD and Raman Spectroscopy

From the previous chapter, was stated that increasing the carbon content in the lamellar structure significantly increases the interlayer distance. Thus, interlayer distance (*d*) is a function of disorder and C content. In the previous chapter, we have indicated the *d* spacing of the perfect crystalline structure of g-C_3N_4 with the value of (d_{002} = 0.3246 nm) and graphite C with (d_{002} = 0.336 nm),

which lies in values of this range. As a reminder, the non-oxidized samples have exhibited the values of (d_{002}) within this range, higher than reference g-C_3N_4 (ox). As a continue of the previous chapter, here is investigated the effect of oxidation and C content on structural features like, peak position, *d* spacing and peak broadness of materials structure. All the samples have shown the same very broad XRD peak around 27° theta angle. This peak is presented for both g-C_3N_4 and graphite C structure, corresponding to the interlayer stacking reflections denoted as the (002) plane. The peak position evolution of the (002) plane is detected over a large angle interval circa 26.9-27.9° theta angle (Fig. 39). Compare to non-oxidized materials calcined only at 550 °C and oxidized at (470-650 °C), no clear evolution was observed for the peak position with increasing the O or C content. Compare to different oxidation temperatures, *d* spacing evolution was also investigated. The mass loss of these oxidized samples MT6/1 and MT2.5/1 at 650 °C and MO4/1 at 470 °C (Fig.38) under inert atmosphere is around 88 and 79 % respectively. While for MO4/1 a complete decomposition occured before reaching 1200 °C. This behaviour strengthens the fact that structural disorder is limited (see d_{002} = 0.325 nm from previous chapter) for MO4/1 due to the early decomposition step. A slight increase of interlayer distance value (*d*) is observed with increasing the temperature of oxidation. Thus, disorder is increased and associated to higher O (Oxygenated functional group) and C portion with maximal O content 17.1 % and 49.7 % of C (see Table 7). For MT2.5/1-550-650 (ox) sample with the highest d = 0.3312 nm, calcined also under the highest oxidization temperature, similar to MT6/1-550-650 (ox) with d = 0.3301 nm. The determined parameters (C content, temperature of oxidation, O content and N content) do not always follow the trend, and discrepancy could be observed. When oxidation occurs, is accompanied by loss of g-C_3N_4 part mainly, remaining the C part with possible close composition (N-rich) and disorder, yielding to similar *d* value. The broadness of the (002) diffraction peak is another feature that was investigated. As the temperature oxidation rises, the broadness of peak is increased e.g. two cases of MT2.5/1-550-650 (ox) and MT6/1-550-650 samples characterized with the most broadness of peak. This evolution is attributed to the decrease of the long range ordering in the (002) direction, associated with reduction of the thickness of crystallite and enlarge the interlayer spacing. The FWHM values of the (002) peak broadness was estimated. These values increased as temperature of oxidation and C content raised, following the trend from: MT2.5/1-550-650 (ox) > MT6/1-550-650 (ox) > MT2.5/1-550-550 (ox) > MT2.5/1-550 > MT6/1-550-550 (ox) > MT6/1-550 > g-C_3N_4 (Table 8). For the feature of the (100) plane, the presence of hump at

13° is described in previous chapter. Although here is explained the effect of oxidation on the disappearance of this hump. The appearance of (100) is observed only for g-C_3N_4 reference and slightly for MT6/1-550, while for oxidized samples is completely disappeared. The disappearance of the hump at 13° on oxidized samples is justified that in-plane heptazine units are destroyed, confirmed also by FTIR. Presuming that these materials do not form an extended planar structure. The carbon matrix was the most of disordered part, and partially composed of a graphite structure, which inhibit the growth of g-C_3N_4 framework [8, 9, 10, 11].

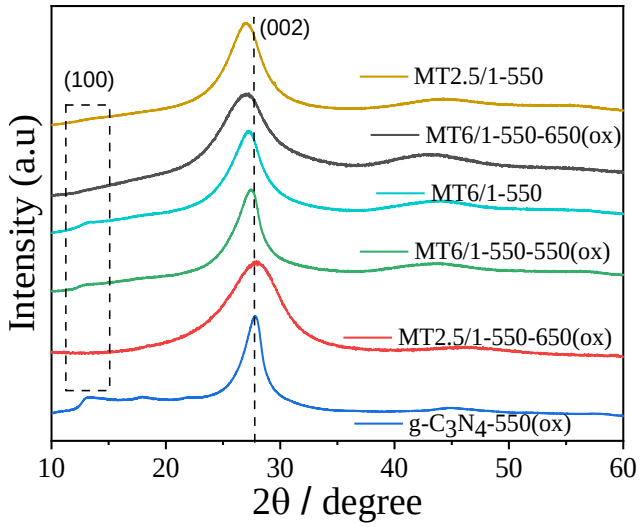

Figure 39. XRD patterns of MT2.5/1-550, MT2.5/1-550-550 (ox), MT2.5/1-550-650 (ox), MT6/1-550, MT6/1-550-550 (ox), MT6/1-550-650 (ox), g-C_3N_4-550 (ox).

Table 8. *d* (spacing), FWHM, and position of (002) plane for selected sample in different temperature and atmosphere.

Samples	2θ angle	d (spacing) nm	Peak broadness (FWHM in °)
g-C_3N_4-550(ox)	27.72	0.3265	1.68
MT2.5/1-550	26.92	0.3309	2.95
MT2.5/1-550-550(ox)	26.9	0.3310	3.21
MT2.5/1-550-650(ox)	27.76	0.3312	4.50
MT6/1-550	27.23	0.3276	2.60
MT6/1-550-550(ox)	27.41	0.326	2.80
MT6/1-550-650(ox)	26.97	0.330	4.10

The Raman spectra of the samples were recorded with an excitation wavelength at the 488 nm shown in Fig.40. Two distinct characteristic peaks of the carbon nanostructure part, the D and G bands, appear, respectively, at 1358 cm^{-1} and 1567 cm^{-1} with no significant shift according to the oxidation temperature. But a small shift for MT6/1-550 sample, which could arise due to fluorescence phenomena (Fig. 40a). The disorder is correlated with the D band intensity, while the graphitic part is evidenced by the G band. With the oxidation and its temperature increase, the I_D/I_G ratio did not change significantly for both MT2.5/1-550 and MT6/1-550 type samples (Table 9). Based on the Raman discussion in the previous chapter, since coherent graphitic domains are even smaller after oxidation (see enlargement of the XRD (002) peaks in Table 8 after oxidation. It is believed that graphitic domains are not significantly modified during the controlled oxidation, and that it is mainly the carbonitride part which is oxidized. The remaining carbon part, probably undergoes some slight rearrangements, (e.g. a slight increase of I_D/I_G consistent with an increase of the coherence length). Observed also with the decrease of the d_{002} spacing for MT2.5/1-550-650 (ox), compared to the pristine materials, attributed to an increase in the carbon content in the material rather than to a more disordered structure.

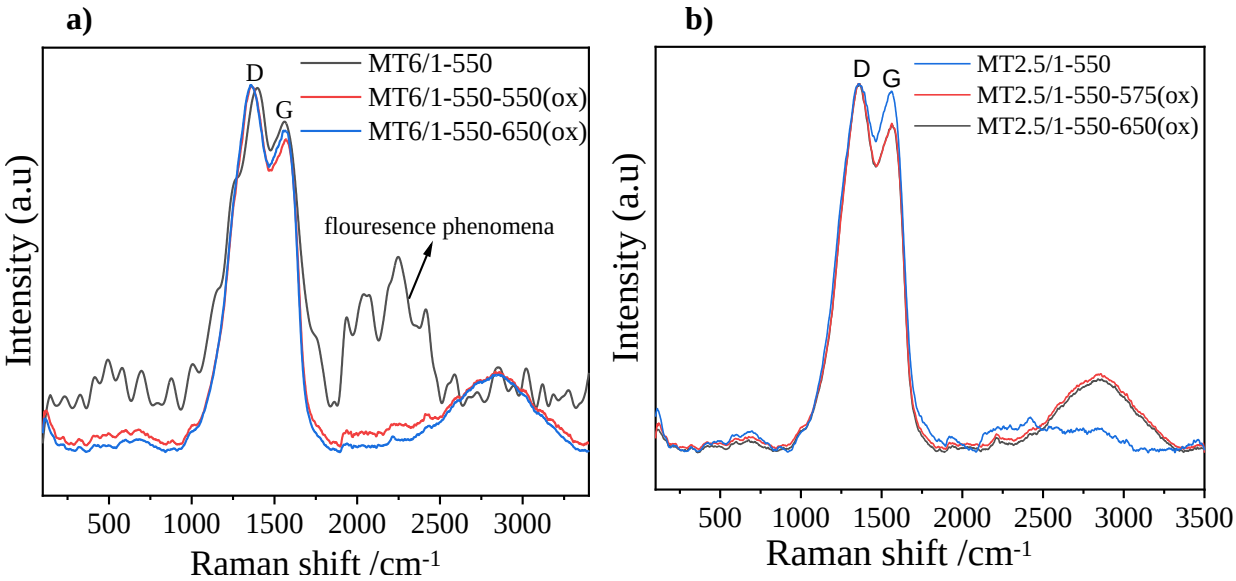

Figure 40. Raman spectrum of MT2.5/1-550, MT2.5/1-550-550 (ox), MT2.5/1-550-650 (ox), MT6/1-550, MT6/1-550-550 (ox), MT6/1-550-650 (ox), g-C_3N_4-550 (ox).

Table 9. I_D/I_G ratio of non-oxidized and oxidized selected samples.

Samples	D position /cm^{-1}	G position/cm^{-1}	I_D/I_G ratio
MT2.5/1-550	1358	1560	3.3
MT2.5/1-550-575(ox)	1358	1565	3.5
MT2.5/1-550-650(ox)	1358	1565	3.6
MT6/1-550	1394	1559	1.5
MT6/1-550-550(ox)	1358	1567	3.1
MT6/1-550-650(ox)	1358	1567	3.2

4.2.4.2. Infrared spectroscopy

DRIFT-FTIR spectrum of MT2.5/1-550 and MT2.5/1-550-650 (ox) samples are shown in Fig. 41. The IR spectrum of non-oxidized MT2.5/1-550 sample has already been described in the previous chapter. It displays four absorption bands: i) a broad peak in the 3000-3550 cm^{-1} range attributed to the stretching vibration of uncondensed N-H and adsorbed O-H groups, ii) peaks in the range 1246-1552 cm^{-1} which correspond to the C-N and C=N stretching mode of aromatics with also related to tertiary N at 1417 cm^{-1}, iii) the typical band at 810 cm^{-1} is attributed to the breathing mode of the triazine ring, and iv) a band at 2179 cm^{-1} which may arise due to the presence of nitrile C≡N species [12] or isonitrile -N≡C [13, 14]. The mechanism of formation was described in previous chapter. The stretching bands of nitriles most likely fall between 2300 and 2200 cm^{-1}, compared to isonitriles, which produce bands between 2180 and 2140 cm^{-1} [15].

After oxidization MT2.5/1-550-650 (ox) sample exhibits a different IR spectrum with poorly resolved bands typical of carbonaceous materials. The band at 810 cm^{-1} is not more detected, revealing the disappearance of the triazine rings, presumably through an oxidation process. Moreover, C-N and C=N functionalities typical for g-C_3N_4-based material are faded and replaced by typical C-C or C=C bonds, characterized by two broad peaks arising from the carbon skeleton and disordered structure confirmed also by XPS. Interestingly after oxidation the small band at

2225 cm^{-1} is observed and possible explanation could be related to incorporation of O and oxidation of tri-s-triazine hexagon and formation of N-oxide nitrile ($C{\equiv}N^{+}O^{-}$) species.

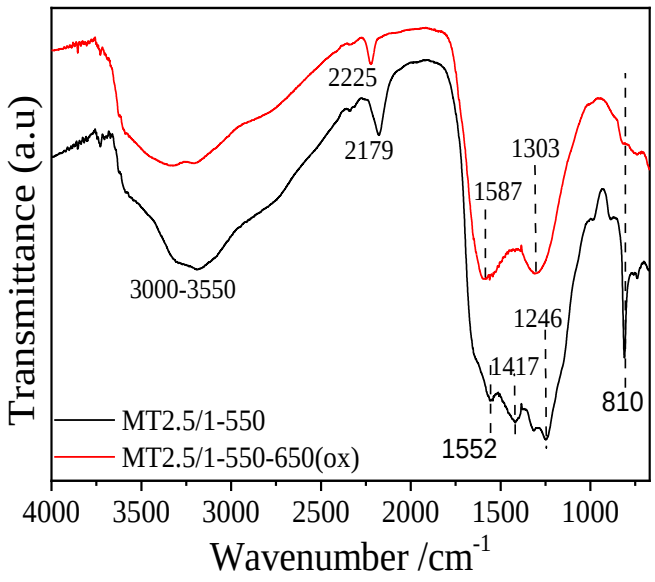

Figure 41. FTIR spectra of MT2.5/1-550 and MT2.5/1-550-650 (ox).

4.2.4.3. XPS (X-ray photoelectron spextroscopy)

The chemical composition of porous g-C_3N_4/N-rich carbon samples was modified, when further calcined under air atmosphere. Thus, the high resolution XPS C1s and N1s spectra showed a difference in the portion of C1s (N-C=N, C-OR, Csp^3-N and N1s (C-N=C, N-(C)$_3$, N-C (amine) with the addition of C, O, or N in the structure. The C1s peak-area ratio of N=C-N on C-rich samples shows an obvious decrease with respect to g-C_3N_4 reference and C-rich-g-C_3N_4 samples. Suggesting the lost portion of heptazine rings occurred during the treatment in air atmosphere. On the other hand C-C sp^3 or C=C sp^2 peak contribution at 285.0 eV is significantly increased, meaning that the carbon is incorporated as C=C form in a higher portion compared to C-rich-g-C_3N_4 samples, also strenghthened from Raman spectra by the presence of G peak. Since the material was calcined in air, it also contains an amount of oxygen, which is represented via C-OR contribution at 286.7 eV (Fig. 42a). The presence of this contribution could support the idea, that the C part of the structure is oxidized.

Regarding to N1s spectra, the meaning of each contributions in chemical point of view was explained in previous chapter. Variations in N1s resolved peaks were obtained with increasing and decreasing C and N content, respectively. The peak area ratio of C-N=C contribution at 398.5 eV for oxidize sample decreases from 67 to 51 %, compare to non-oxidized one. It reveals that the hexagons of heptazine units are losing their features due to oxidation. The bridging nitrogen N-$(C)_3$, which bonds three units of heptazine is no more encountered, due to the addition of C and it could be converted to the nitrile C≡N functional group. This nitrile group exhibits binding energy at 400.0 eV, this fact is strengthened by literature with the given value of 400.1 eV [16]. Moreover, the presence of N-H peak at 401.1 eV is observed due to uncondensed amine groups (NH_2, N-H) , which is consistent with the FTIR analysis [17].

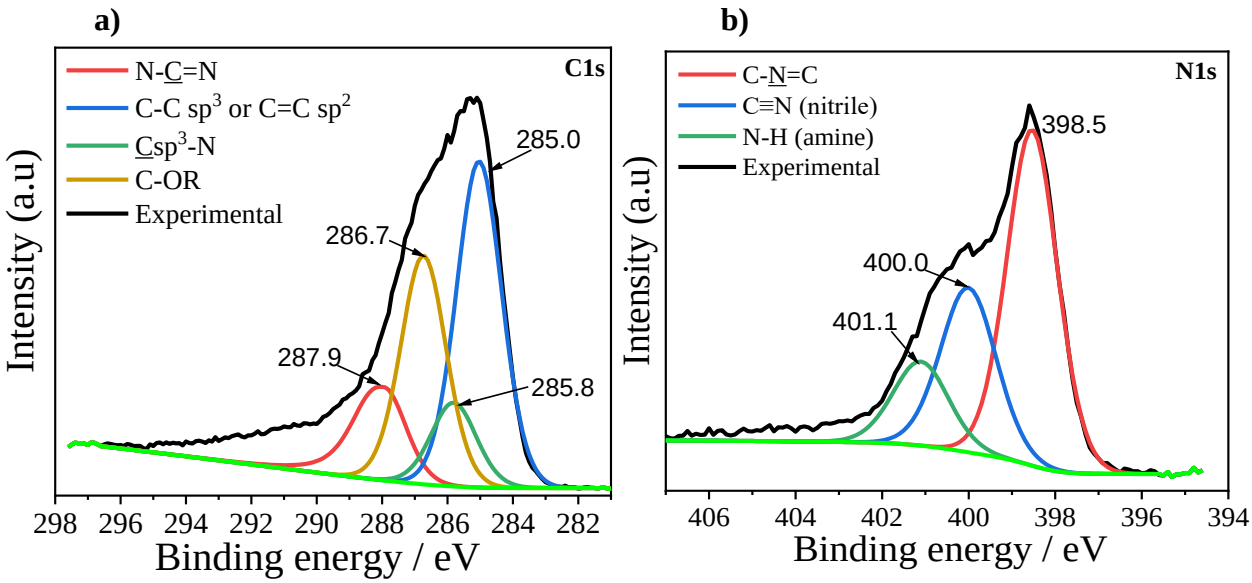

Figure 42. C1s (a) and N1s (b) XPS high resolution spectra of MT2.5/1-550-650 (ox).

4.3. Evolution of morphology

Evolution of morphology is shown from the adduct, to the oxidized samples via its carbonized step (Fig. 43). Surprisingly, the needle-like shape of the adduct MT2.5/1 is maintained, with a slight distortion, even after oxidation at 470 and 650 °C. Due to the high weight loss related to this oxidation step (80 % from the carbonized sample and 44 % starting from the adduct), a morphology loss could have been expected.

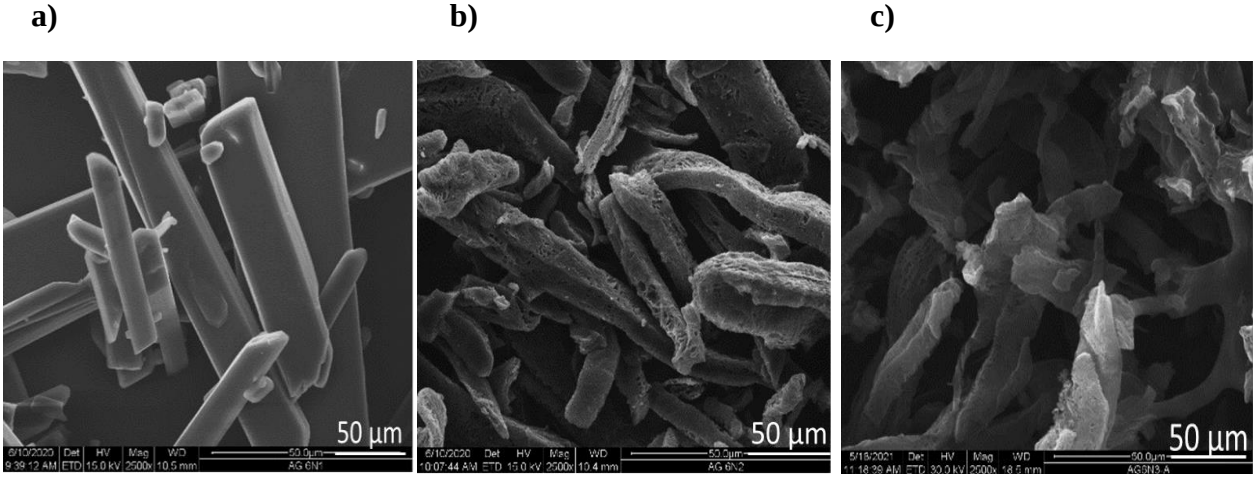

Figure 43. SEM micrographs of a) MT2.5/1 adduct, b) MT2.5/1-550-470 (ox), and c) MT2.5/1-550-650 (ox). Evolution of morphology from adduct to oxidized sample at 470 and 650 °C.

To investigate the detailed nanostructure of the prepared samples, TEM nano-graphs of g-C_3N_4, non-oxidized and oxidized samples are shown in Fig. 44a-d. Moreover, it could be seen that the bulk g-C_3N_4 presents a dense nanostructure, which could be related to crumpled and stacked nanosheets (Fig. 44a). The MT6/1-550 sample, which was calcined under inert atmosphere Fig. 44b exhibits a dense structure in agreement with its non-porous character revealed in the previous chapter. After treatment in air at 650 °C (Fig. 44c), a complete different nanostructure is exhibited, which could be described as composed of filaments. It is proposed that, based on the low stability in air of this material (see TGA), a selective thermal etching (oxidation) occurs with a high weight loss, yielding only a small amount of the remaining stable carbonaceous part, with plenty of cracking due to thermal oxidation etching. As show latter, this nanostructure will display porosity and a fairly high surface area. After oxidation at 650 °C (Fig. 44d), a nanostructure different from

that of MT6/1-550-650 (ox) is observed. In that case, the sample is richer in carbon than MT6/1-550 and more resistence to oxidative thermal etching. Hence, it results in a limited etching of the material and a structure similar to its non-oxidized counterpart.

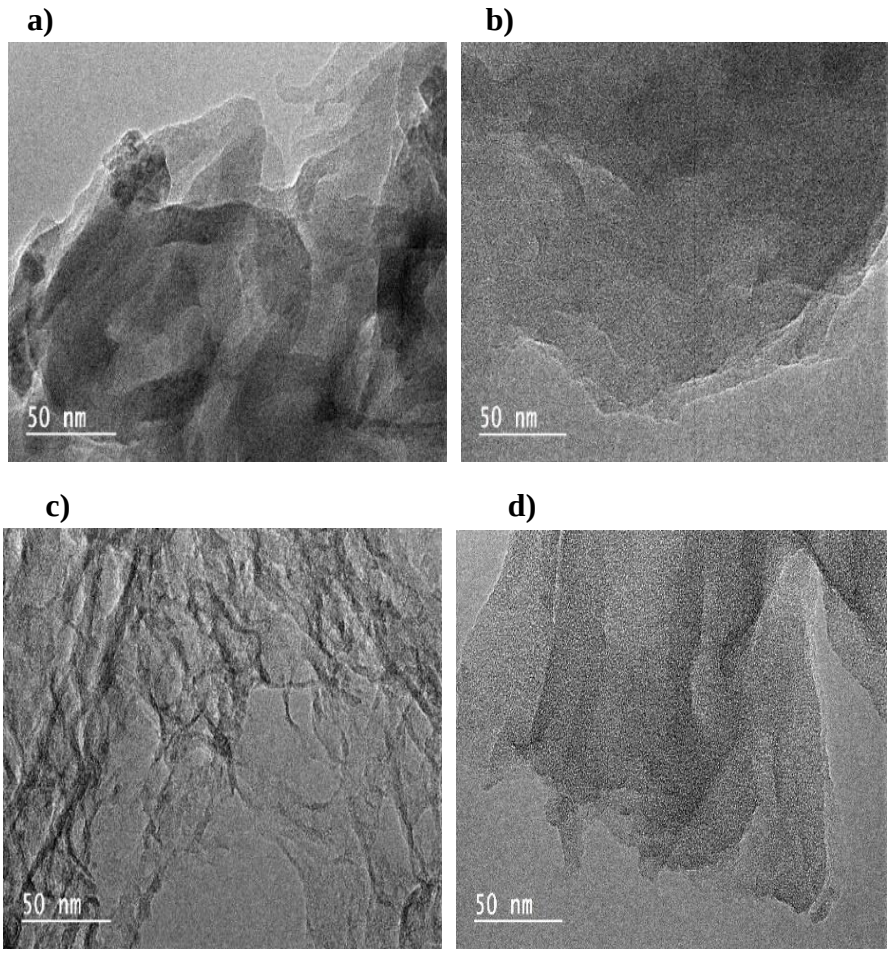

Figure 44. TEM images of a) g-C_3N_4-550 (ox), b) MT6/1-550, c) MT6/1-550-650 (ox), d) MT2.5/1-550-650 (ox).

Further, to understand the distribution of the chemical composition in the samples, investigations were performed using TEM-EDX. The element mapping images of the MT6/1 sample before and after oxidation are shown in Fig. 45. The mapping images show a high uniform distribution of C, N and O. But if we refer to the oxidized sample (Fig. 45b), plenty of void were observed in the structure in relation to its high-oxidative thermal etching.

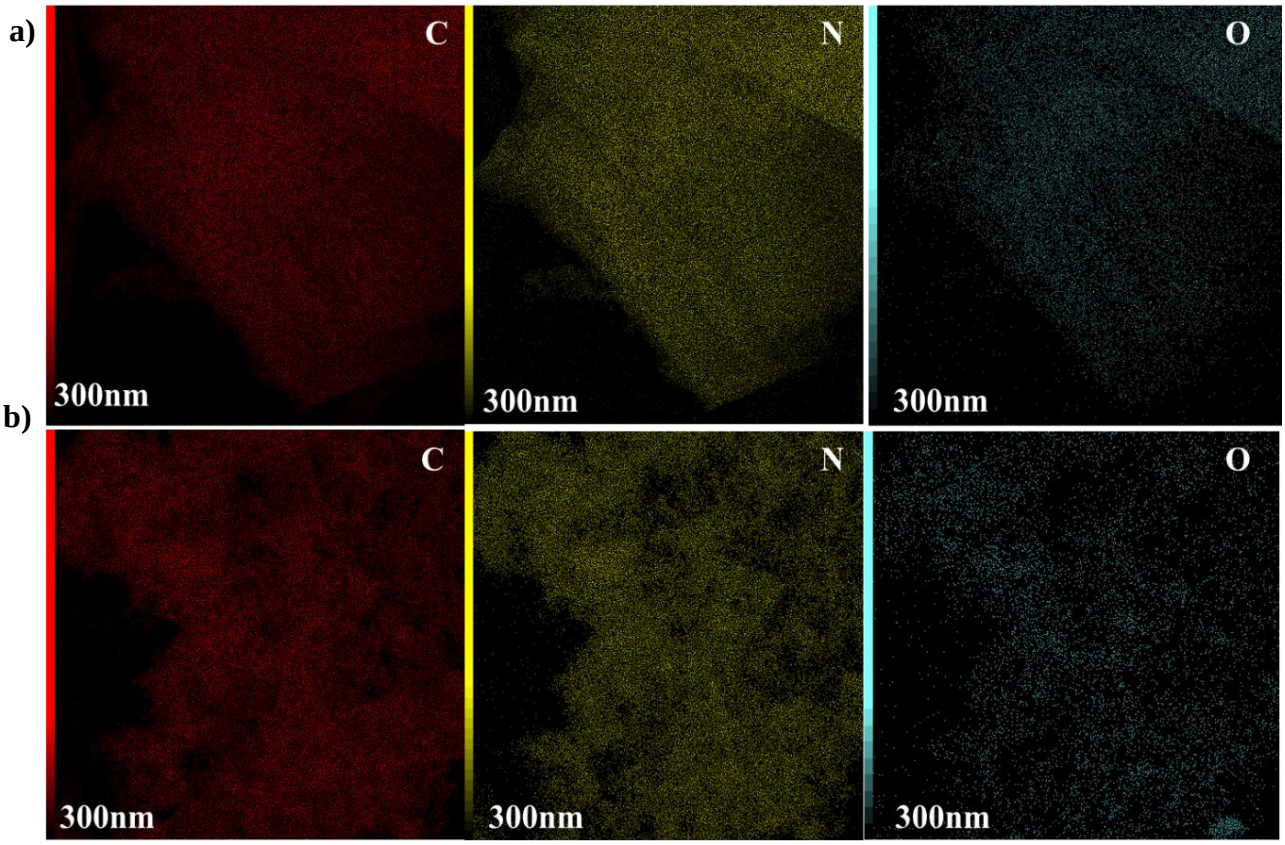

Figure 45. STEM-EDX elemental mapping of a) MT6/1-550, b) MT6/1-550-650 (ox)

4.4. Textural properties

4.4.1. Nitrogen and CO_2 adsorption

Nitrogen and CO_2 gas adsorption-desorption isotherms of the samples are shown in Fig. 46-47. The nitrogen gas adsorption-desorption isotherm graph was demonstrated by Type I isotherm given by microporous non-porous solids, having relatively small external surfaces as shown in Fig. 46a for MT2.5/1-550 black and MC1.5/1-550-470 (ox) blue curve samples. The limiting uptake is governed by the accessible micropore volume rather than by the internal surface area. Based on the BET equation used for calculation, when $P/P_0 < 1$ and $C > 1$, as a consequence it leads the adsorption at the initial part and monolayer formation represented by Type I isotherm. A combination of Type I and Type IV isotherm characterize the MT2.5/1-550-650 (ox) red, MC1.5/1-550-650 (ox) pink and MT6/1-550-650 (ox) green samples, typically adsorption on

mesoporous solids followed by multilayer adsorption and capillary condensation, resulting in Type IV [18, 19]. The corresponding textural properties of all samples are listed in Table 10. Compared with g-C_3N_4 and MO type sample having high thermal stability, C-rich carbonitride/N-rich porous C samples display a higher specific surface area and pore volume. Both values increased with the oxidation temperature (from 470 to 650 °C). Regarding the carbon content, it appears that too much carbon content is detrimental to the formation of porosity, as evidenced from the carbon content of MT6/1-550 and MT2.5/1-550 samples oxidized at 650 °C with respectively 48.01 and 49.7 wt% C. The effect of carbon is not the only main contributor to increasing the porosity in the gas phase, but also there are contributions from the N and O sides. It is due to the reduced portion of C-rich carbon nitride part, acting as a sacrificial porogen agent and leaving behind (after decomposition) a lower portion of pores. All samples exhibit a relatively narrow distribution in pore size (DFT model) centered at around 1 nm related to micropores and 3-7 nm pores. The MT6/1-550-650 (ox) sample possesses a good carbon content compromise regarding porosity since it displays the highest surface area and pore volume among the prepared samples.

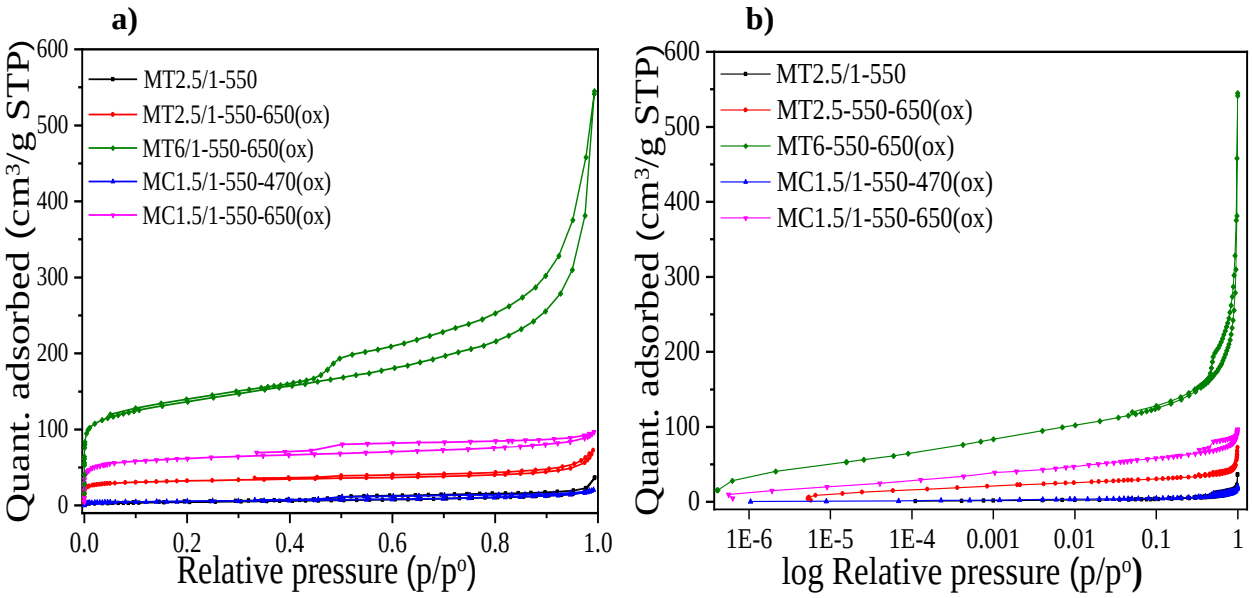

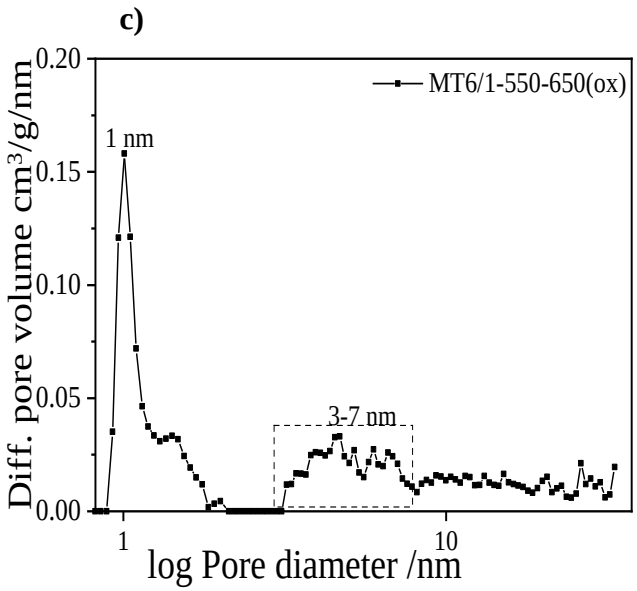

Figure 46. Nitrogen Adsorption-desorption isotherm at 77 K of selected non-oxidized and oxidized samples, on normal (a) and logarithm scale (b). PSD in logarithm scale using DFT model for MT6/1-550-650 (ox) sample obtained from N_2 adsorption isotherm (DFT pore shape model) (c).

The CO_2 adsorption at 273 K and sub-atmospheric pressure was also performed on some selected samples having high porous features in order to investigate their ultra-microporous character and the possible reactivity of CO_2 with the surface (with carbamate formation) (Fig. 47). It appears that ultra-porosity is rather limited and that no chemisorption is present at 273 K, as shown by the reversible adsorption and desorption isotherms. The latter point could be due to the low amine content of the sample remaining after oxidation compared to N-graphitic one (14 % peak ratio of N-H from XPS). In Fig. 48 is displayed the possible hypothetic formation of the mechanism of N-rich porous C material (oxidized material) by an oxidation process, which facilitates the formation of a porous structure, which endowed with a higher portion of C-domains, richer in nitrogen.

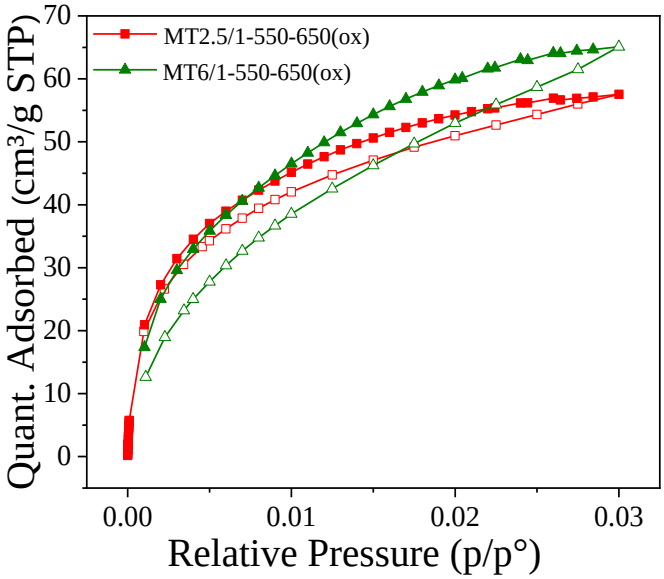

Figure 47. CO_2 adsorption-desorption isotherm at 273 K of MT2.5/1-550-650 (ox) and MT6/1-550-550 (ox).

Table 10. Textural properties of g-C_3N_4 based samples, derived from N_2 and CO_2 adsorption-desorption isotherm and calculated according to DFT model. Variation of carbon content on textural properties of the samples.

	N_2/77K				**CO_2/273K**	
	V_{micro}(cm^3g^{-1})	**V_{meso}(cm^3g^{-1})**	**S(m^2g^{-1}) DFT**	**C content wt%**	**V_{micro}(cm^3g^{-1})**	**S(m^2g^{-1}) DFT**
MO3/1-550-650(ox)	0.0	0.0	13	34.1	0.0	8
g-C_3N_4 (ox)	0.0	0.06	16	34.3	0.0	11
MT4/1-550-470 (ox)	0.001	0.0	35	-	0.0	15
MT2.5/1-550-470 (ox)	0.008	0.0	50	48.1	0.0	28
MC1.5/1-550-600 (ox)	0.06	0.0	234	-	-	-
MT2.5/1-550-650 (ox)	0.07	0.25	276	49.7	0.038	283
MT6/1-550-650 (ox)	0.13	0.40	600	48.01	0.031	430

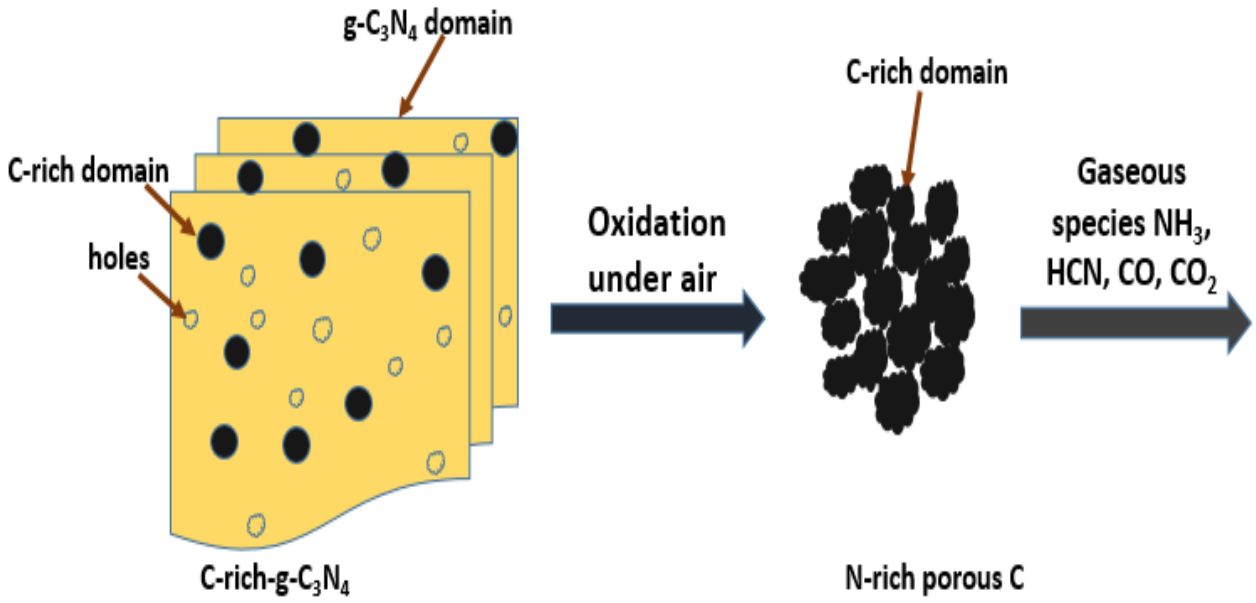

Figure 48. Schematic ilustration of N-rich porous C material formation with the aid of thermal oxidation etching and C-rich-g-C_3N_4 as a sacrifical compound.

4.5. Conclusions

A simple way to obtain Nitrogen-rich porous materials has been developed through the oxidation process of C-rich-g-C_3N_4 materials. A moderate oxidation temperature was applied to preserve the yield. This process ensures selective thermal oxidation of the g-C_3N_4 domains within the C-rich structure, which leads to the improvement of porosity and specific surface area. Structural analysis showed that the (002) peak after the oxidation process undergoes the increase of broadness and interlayer distance, with increasing the temperature of oxidation and C content. Moreover, results from Raman strengthen this fact, with the increase in the D peak confirming the disordered structure. At high oxidation temperature, surprisingly needle-like shape morphology was kept, from adducts to oxidized samples with the shrinkage of the shape, which was expected due the high mass loss. The thermal stability of materials depends on the atmosphere of calcination (air and inert) and carbon content.

SUMMARY IN FRENCH

Dans ce chapitre, nous avons étudié la réactivité de g-C_3N_4 et des nanocomposites g-C_3N_4 /C avec l'oxygène de l'air. L'oxydation a été réalisée à différentes températures (470, 550 et 650 °C) tout en suivant l'évolution de leur composition. En tirant profit de la différence de stabilité thermique et de réactivité à l'oxygène entre la phase C_3N_4 et la phase carbonée, de nouveaux matériaux carbonés riches en N (env. 30% en masse) et à haute porosité (jusqu'à 600 m^2/g) ont été préparés. En effet, avec l'augmentation de la température de calcination sous air, on observe une décomposition préférentielle de la phase carbonitrure associée à un enrichissement relatif en carbone. Ces matériaux oxydés, riches en carbone présentent alors une plus forte réactivité à l'oxygène que les matériaux à base de carbonitrure (non oxydés) comme le montre les thermogrammes avec un début de la perte de masse des échantillons oxydés se produisant à plus basse température que pour les échantillons non oxydés.

Les surfaces spécifiques ont été estimées avec le modèle DFT à partir des isothermes d'adsorption d'azote à 77K. Il y a une augmentation significative des surfaces, jusqu'à 600 $m^2\ g^{-1}$ pour les matériaux oxydés alors que les matériaux non oxydés présentent qu'une surface de quelques dizaines de $m^2\ g^{-1}$. En effet, la décomposition préférentielle de la phase C_3N_4 dans le nanocomposite C_3N_4/C durant l'oxydation pourrait conduire à la formation de micropores et de mésopores. Ce procédé semble être une façon originale de produire du carbone poreux en utilisant le carbonitrure comme un nouvel agent porogène.

References

[1] R. Walczak *et al.*, 'Template- and Metal-Free Synthesis of Nitrogen-Rich Nanoporous "Noble" Carbon Materials by Direct Pyrolysis of a Preorganized Hexaazatriphenylene Precursor', *Angew. Chem. Int. Ed.*, vol. 57, no. 33, pp. 10765–10770, Aug. 2018, doi: 10.1002/anie.201804359.

[2] J. P. Paraknowitsch, J. Zhang, D. Su, A. Thomas, and M. Antonietti, 'Ionic Liquids as Precursors for Nitrogen-Doped Graphitic Carbon', *Adv. Mater.*, vol. 22, no. 1, pp. 87–92, Jan. 2010, doi: 10.1002/adma.200900965.

[3] S.C.Roy, A.W.Harding, A.E.Russell and K.M.Thomas "Northern Carbon Research Laboratories (NCRL) and Department of Chemistry,University of Newcastle, Newcastle-upon-Tyne NE1 7RU, England

[4] R. A. Sidik, A. B. Anderson, N. P. Subramanian, S. P. Kumaraguru, and B. N. Popov, 'O_2 Reduction on Graphite and Nitrogen-Doped Graphite: Experiment and Theory', *J. Phys. Chem. B*, vol. 110, no. 4, pp. 1787–1793, Feb. 2006, doi: 10.1021/jp055150g.

[5] L. Jiang and L. Gao, 'Modified carbon nanotubes: an effective way to selective attachment of gold nanoparticles', *Carbon*, vol. 41, no. 15, pp. 2923–2929, 2003, doi: 10.1016/S0008-6223(03)00339-7.

[6] F. Jaouen, M. Lefèvre, J.-P. Dodelet, and M. Cai, 'Heat-Treated Fe/N/C Catalysts for O_2 Electroreduction: Are Active Sites Hosted in Micropores?', *J. Phys. Chem. B*, vol. 110, no. 11, pp. 5553–5558, Mar. 2006, doi: 10.1021/jp057135h.

[7] J. Ren, X. Liu, L. Zhang, Q. Liu, R. Gao, and W.-L. Dai, 'Thermal oxidative etching method derived graphitic C_3N_4: highly efficient metal-free catalyst in the selective epoxidation of styrene', *RSC Adv.*, vol. 7, no. 9, pp. 5340–5348, 2017, doi: 10.1039/C6RA26137J.

[8] J. Liu, Y. Zhang, L. Zhang, F. Xie, A. Vasileff, and S. Qiao, 'Graphitic Carbon Nitride ($g\text{-}C_3N_4$)-Derived N-Rich Graphene with Tuneable Interlayer Distance as a High-Rate Anode for Sodium-Ion Batteries', *Adv. Mater.*, p. 1901261, Apr. 2019, doi: 10.1002/adma.201901261.

[9] Y. C. Zhao, D. L. Yu, H. W. Zhou, Y. J. Tian, and O. Yanagisawa, 'Turbostratic carbon nitride prepared by pyrolysis of melamine', *J Mater Sci*, vol. 40, no. 9–10, pp. 2645–2647, May 2005, doi: 10.1007/s10853-005-2096-3.

[10] Y. Li, R. Zhang, L. Du, Q. Zhang, and W. Wang, 'Constructing of fragmentary g-C3N4 framework with rich nitrogen defects as highly efficient metal-free catalyst for acetylene hydrochlorination', *Catal. Sci. Technol.*, vol. 6, no. 1, pp. 73–80, 2016, doi: 10.1039/C5CY00777A.

[11] T. Komatsu and T. Nakamura, 'Polycondensation/pyrolysis of tris-s-triazine derivatives leading to graphite-like carbon nitrides', *J. Mater. Chem.*, vol. 11, no. 2, pp. 474–478, 2001, doi: 10.1039/b005982j.

[12] G. Camino, L. Operti, and L. Trossarelli, ‘Mechanism of thermal degradation of urea-formaldehyde polycondensates’, *Polymer Degradation and Stability*, vol. 5, no. 3, pp. 161–172, May 1983, doi: 10.1016/0141-3910(83)90007-1.

[13] L. J. Broadbelt, A. Chu, and M. T. Klein, ‘Thermal stability and degradation of aromatic polyamides. Part 2. Structure-reactivity relationships in the pyrolysis and hydrolysis of benzamides’, *Polymer Degradation and Stability*, vol. 45, no. 1, pp. 57–70, Jan. 1994, doi: 10.1016/0141-3910(94)90178-3.

[14] A. Majumdar, G. Scholz, Rainer Hippler, ´Structural characterization of amorphous hydrogenated-carbon nitride (aH-CNx) film deposited by CH4/N2 dielectric barrier discharge plasma: 13C, 1 H solid state NMR, FTIR and elemental analysis´, *Surface & Coatings Technology, vol* 203 (2009) pp. 2013–2016, Feb.2009, doi:10.1016/j.surfcoat.2009.01.038

[15] Max P. Bernstein, Scott A. Sanford, and Louis J. Allamandola, Astrophysics Branch, NASA-Ames Research Center, Mail Stop 245-6, Moffett Field, CA 94035-1000 Received 1996 May 31 ; accepted 1996 September 6 303651.’.

[16] R. J. J. Jansen and H. van Bekkum, ‘XPS of nitrogen-containing functional groups on activated carbon’, *Carbon*, vol. 33, no. 8, pp. 1021–1027, Jan. 1995, doi: 10.1016/0008-6223(95)00030-H.

[17] J. Cao, H. Fan, C. Wang, J. Ma, G. Dong, and M. Zhang, ‘Facile synthesis of carbon self-doped g-C3N4 for enhanced photocatalytic hydrogen evolution’, *Ceramics International*, vol. 46, no. 6, pp. 7888–7895, Apr. 2020, doi: 10.1016/j.ceramint.2019.12.008.

[18] Sagar M Gawande, Niharika S Belwalkar, Anuja A Mane, ´ Adsorption and its Isotherm – Theory´, *International Journal of Engineering Research*, Volume No.6, Issue No.6, pp : 312-316, doi : 10.5958/2319-6890.2017.00026.5

[19] T. Narkbuakaew and P. Sujaridworakun, ‘Synthesis of Tri-S-Triazine Based g-C3N4 Photocatalyst for Cationic Rhodamine B Degradation under Visible Light’, *Top Catal*, vol. 63, no. 11–14, pp. 1086–1096, Oct. 2020, doi: 10.1007/s11244-020-01375-z.

CHAPTER 5

Synthesis and characterization of highly fluorinated g-C_3N_4 and C-rich-C_3N_4 via pure F_2 gas

5.1. Introduction

As a potential photocatalyst, due to suitable properties described in the previous chapter, g-C_3N_4 can be used for remediation, such as organics degradation, water splitting under visible light irradiation [1] and degradation of gaseous species [2, 3, 4, 5, 6]. Several techniques and methods have been developed to improve its photocatalytic activity [7]. Among these methods, doping with halogen elements has recently gained interest [8] and when associated with disordered structure and defects, which arises from the incomplete g-C_3N_4 de-amination of precursors during the pyrolysis. Thus, different halogenation mechanisms could be encountered. Doping with Br and Cl occurs with halogen sources such as NH_4Br [9] and NH_4Cl [10]. Few studies in the literature deal with F-doped g-C_3N_4, and they have been presented in the bibliographic part. These materials possess interesting properties, to their low doped-flourine content, including good chemical stability, tunable band gap, good thermal conductivity, and hydrophobicity due to their C-F bond [11]. They have also evidenced potential in terms of photo-degradation of pollutants and photogeneration of H_2 by water-splitting, e.g by the HF hydrothermal method, with an atomic concentration of F incorporation around 0.31 % [12]. The functionalization, associated with the exfoliation of g-C_3N_4 nanosheets, by a hydrothermal method in the presence of NH_4F was reported [13]. This method ensures up to 9 % atomic concentration of F incorporated on the structure. The advantages of this method include, one-step process, high yield, mild reaction conditions and low cost [14]. The reaction of the nucleophilic substitution of F on the carbon as a positively charged centre, is considered the main mechanism of incorporation of F into the structure of g-C_3N_4, with the formation of C-F bonds. However, this route not only suffers from low level of F-doping but also has some limitations in photocatalytic properties. Therefore, other F-doping approaches were investigated in order to improve those properties.

For the gas phase method, fluorination process involves the reaction of fluorine (F_2) with carbon atoms, resulting in the formation of C-F bonds. However, this process also depends on the temperature applied; the lower the fluorination temperature, the lower the C-F bond energy [15]. Since g-C_3N_4 material possesses a packed layered structure similar to the one of graphite, it could be possible to incorporate F atoms in the g-C_3N_4 structure at a high level, similar as in graphite, *via* the use of F_2 gas reaction [16]. The utilisation of F_2 gas diluted with N_2 at high temperature (150 °C), was reported. The maximum F doping reached within g-C_3N_4 structure was around 10

at. %. We believed thatbelieve that higher fluorine content could be reached using pure F_2 gas and that the properties of highly fluorinated g-C_3N_4 materials deserve to be investigated through physico-chemical characterisations and photocatalytic tests. Moreover, F_2 appeared as an interesting probe to further investigate the structural and complex nature of defective g-C_3N_4 and C-rich g-C_3N_4 materials since the specific reactivity was expected for structural defects, C-doping and C-rich nanodomains.

Hence, our work dealt with the preparation of highly fluorinated carbonitride *via* pure F_2 gas at room temperature, starting with three types of g-C_3N_4-based samples prepared according to the procedure described in the Chapter 2 of the experimental part; two g-C_3N_4 with different defects and a C-rich-g-C_3N_4. Here is a brief reminder of the characteristics of the pristine materials used for fluorination. The F_2 gas method is extremely convenient and leads to drastic distortion of the g-C_3N_4 layer structure due to the transformation of sp^2 hybridization of C atoms to sp^3 ones, and enrichment with nitrogen defects (vacancies) [17].

The yellow carbonitride sample, denoted CN, is considered to have mainly structural defects related to the presence of NH and/or NH_2 groups left by the incomplete deamination of the melamine precursor during pyrolysis in air [18]. The second material, the orange CNO sample display more defects, which could be attributed to the structural and chemical changes, since the additional pyrolysis step in an inert atmosphere compared to CN may cause the deformation of planar CN domains and the partial removal of NH or NH_2 groups [19]. Even if the chemical composition of CN is quite similar to that one CNO (it differs only by a slight increase and decrease in the content of N and O respectively (see Chapter 3) with some structural variation evidenced by XRD. The shift of the (002) peak, to a lower theta angle corresponds to an increase in the interlayer distance between CN and CNO samples due to the higher disorder of the latter material. It is also associated with a lower long-range ordering of heptazine units, evidenced by the disappearance of the (100) peak around 13° as also reported in reference [20].

Our study was extended to the analysis of the C-rich-g-C_3N_4 material (CCN) which can be considered a C/g-C_3N_4 composite, where N-rich carbon parts are homogeneously distributed within the C-doped g-C_3N_4 counterpart. A completely different reactivity may arise between F_2 and these two phases. Knowing that F_2 usually reacts with graphite at high temperatures (> 350 °C) but also for disorder or activated carbons at room temperature [21, 22].

5.2. Physico-chemical characterization of F-doped g-C_3N_4 materials

5.2.1. XRD analysis

The XRD patterns of fluorinated and non-fluorinated samples are shown in Fig. 49. Different features of the diffractogram like, *d* interspacing of (002) planes, (002) peak broadness and, the presence or absence of the (100) peak were carefully investigated. All non-fluorinated samples exhibit two representative diffraction peaks, the (100) at about 13° and the (002) at 27°, which were both described in the previous chapter.

The evolution of the (002) peak position around 27.6° from CN to CN-F_2_20 sample (see Fig. 49a) does not appear significant since the corresponding *d* spacing is determined at 0.322 nm for CN and 0.321 nm for CN-F_2_20. Meanwhile, the intensity of this peak is drastically decreased after fluorination. It is proposed that both features ((002) peak position and intensity) are related to a remaining carbonitride part not being fluorinated; it appears then at the same peak position with a lower intensity. The fluorinated part, at the opposite, may be present as probably exfoliated and disordered layers without long-range periodicity [14]. The diffraction peak at 13.1° for CN-F_2_20 is nearly vanished, indicating the overwhelmingly reduced in-plane ordering of tri-s-triazine units caused by the reactivity with F_2 [3, 23].

A similar trend was observed for the CNO and CNO-F_2_20 samples (Fig. 49b) regarding the (002) plane, which appears at 27.76° [24]. There is also a slight decrease in the interlayer distance after fluorination, from d = 0.320 nm for CNO to d = 0.319 nm for CNO-F_2_20 sample, which could be related to a higher portion, after fluorination, of more ordered g-C_3N_4. This material, having a slightly lower interlayer spacing than the disordered one is supposed to be less reactive and therefore is presented in a higher portion after fluorination. As opposed from the abovementioned samples, the low-angle (100) hump shows a down-shift from 13.01° for the CNO down to 12.01° for the CNO-F_2_20. This surprising behaviour could reveal a larger distance of the in-planar structure packing order, as already observed for hydrothermal post-treated carbonitride [25, 26].

A different behaviour was observed for the CCN and CCN-F_2_20 samples (Fig. 49c). As stated in Table 11 for the EA composition, the CCN sample contains a high portion of carbon content (46.2wt %) of a broad (002) peak at 27°, is expected for such samples since its more disorder due to high

presence of carbon within heptazine unit and as aromatic “clusters”. Surprisingly, a large down-shift of this peak, corresponding to the inter-layer *d* stacking, was observed after fluorination, from 27.46° (*d* = 0.323 nm) for the CCN sample down to 21.28° (*d* = 0.417 nm) for the CCN-F_2_20. Due to the composite part of that sample containing layered carbon-rich nanodomains, it is possible that such domains yield to fluorinated nanographite-like material (or stacked fluorinated nanographene) with an expansion of the inter-layer distance. Indeed, such compounds, derived from graphite or graphene, display a significant shift compared to their parent materials with a peak position down to 12.5° (*d* = 7.24 nm) [27, 28].

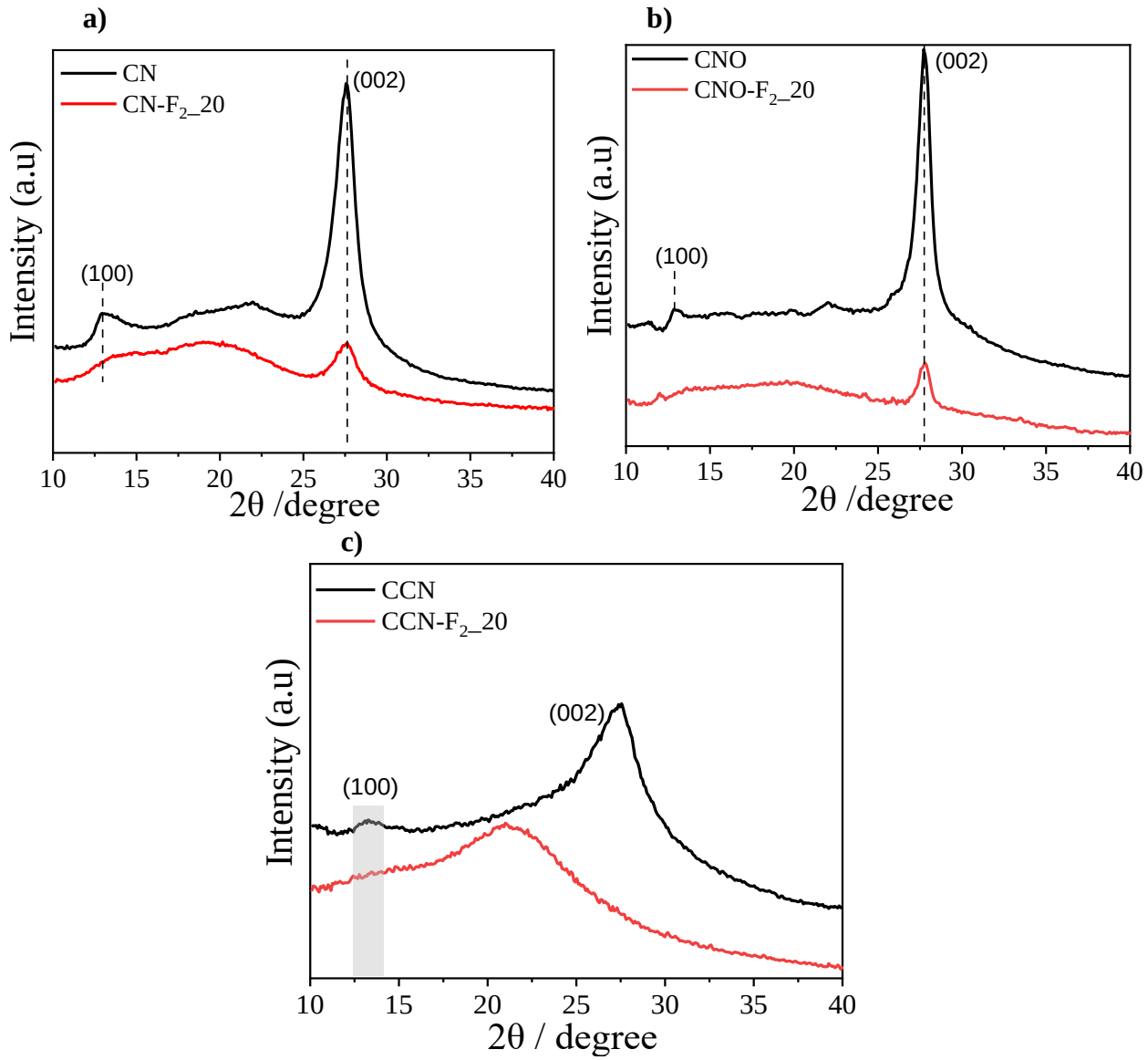

Figure 49. XRD patterns before and after fluorination starting for the pristine materials (a) CN, (b) CNO and (c) CCN samples.

5.2.2. FTIR analysis

The chemical structures of fluorinated and non-fluorinated samples were confirmed using Fourier-transform infra-red spectroscopy. As shown in Fig. 50, the spectra display typical and sometimes well-resolved absorption bands. Well-known g-C_3N_4 (Fig. 50a) shows the common absorption bands of N-H or OH bonds between 3300-2950 cm^{-1}, while triazine derivatives are located in the range of 1626-909 cm^{-1} , which represent C-N and C=N bonds of stretching vibrations of heterocycles [29]. The breathing mode of the triazine ring lies at approximately 801 cm^{-1}. After fluorination, the CN-F_2 _20 sample displayed some discrepancies compared to the pristine materials at the difference in F_2 fluorinated carbonitride described in the literature and having lower F content [30].

First, it is worth say that some peaks are the same between pristine CN and fluorinated. CN-F_2 _20 samples, probably due to the unreacted carbonitride part present in CN-F_2 _20 sample as revealed by XRD (e.g evidence of the breathing mode of the heptazine at 800 cm^{-1}). Otherwise, the peak in the region 2180 cm^{-1} is not more observed after fluorination, as already reported in [31], suggesting that the cyano groups (C≡N) have disappeared in the presence of F_2. Due to the overlap of the CN aromatic vibration modes and the C-F ones, it is difficult to ambiguously identify the C-F vibration modes [6]. Nevertheless, some clear shift or appearance of new vibration modes can be observed at 909, 1130 and 1694 cm^{-1}. However, the defectous CNO sample roughly exhibits the similar bands (grey part) Fig. 50a-b. But these bands become more dominant and intense compared to CN. Maybe they could be attributed to an increase in C-NH-C bridges, due to heptazine units which are linearly linked with each other [32]. These units could create defects in the g-C_3N_4 structure. Whereas, the CNO-F_2_20 sample looks really similar to the CN-F_2_20. The spectra of the CCN and CCN-F_2_20 samples (Fig. 50c) exhibit broader bands in relation to the more disordered structure of the pristine material. Three peaks, in the same range as those detected for CN-F_2 _20, are evidenced at 923, 1144 and 1694 cm^{-1}. The typical breathing mode of the heptazine unit was completely vanished in accordance with the XRD data.

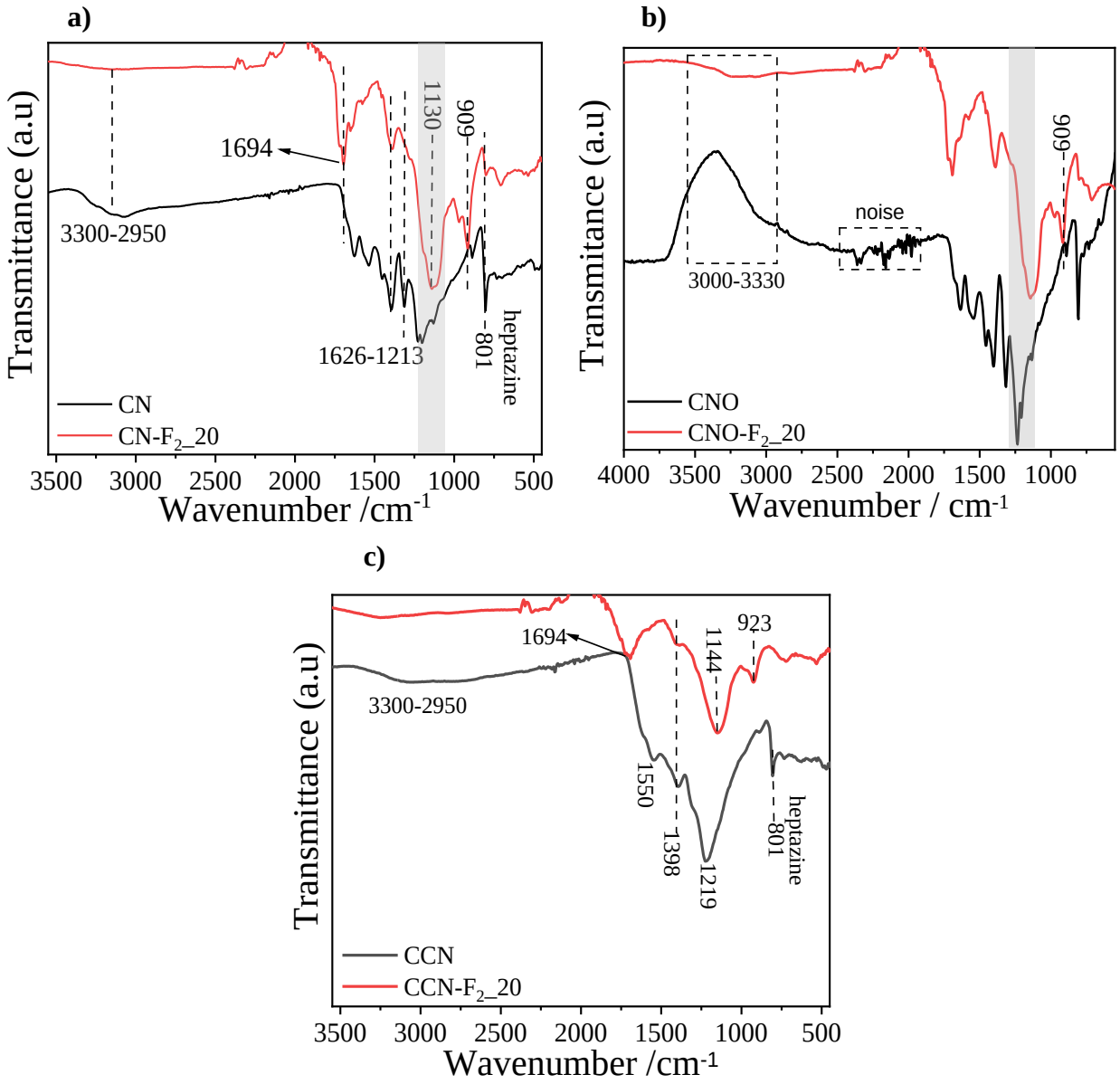

Figure 50. The FTIR spectra of CN, CN-F_2_20 (a), CNO, CNO-F_2_20 (b), and CCN, CCN-F_2_20 (c).

5.2.3. TEM analysis

TEM images of non-fluorinated and fluorinated samples are shown in Fig. 51a-g. The first ones are constructed of solid agglomerates of a few hundred nanometres, with a dense nanostructure (Fig. 51a-b), while the CCN sample displays a more apparent and nano-layered structure (Fig. 51c). On the other hand, fluorinated samples (Fig. 51d-f) have a completely different aspect with

a sponge-like morphology composed of numerous pores and denser nanoparticles. This morphology change is attributed to the reactivity of CN with F_2 with possible partial exfoliation of its lamellar structure associated with the formation of volatile species (e.g fluorocarbon-type compounds, HF or O…) and leading to more transparent domains. The remaining non-fluorinated domains appears then as the dense nanoparticles with a size between 20 and 40 nm (Fig. 51g). Estimation of the specific surface area (SSA) and pore size could not be performed due to the pasty form and limited mass of materials.

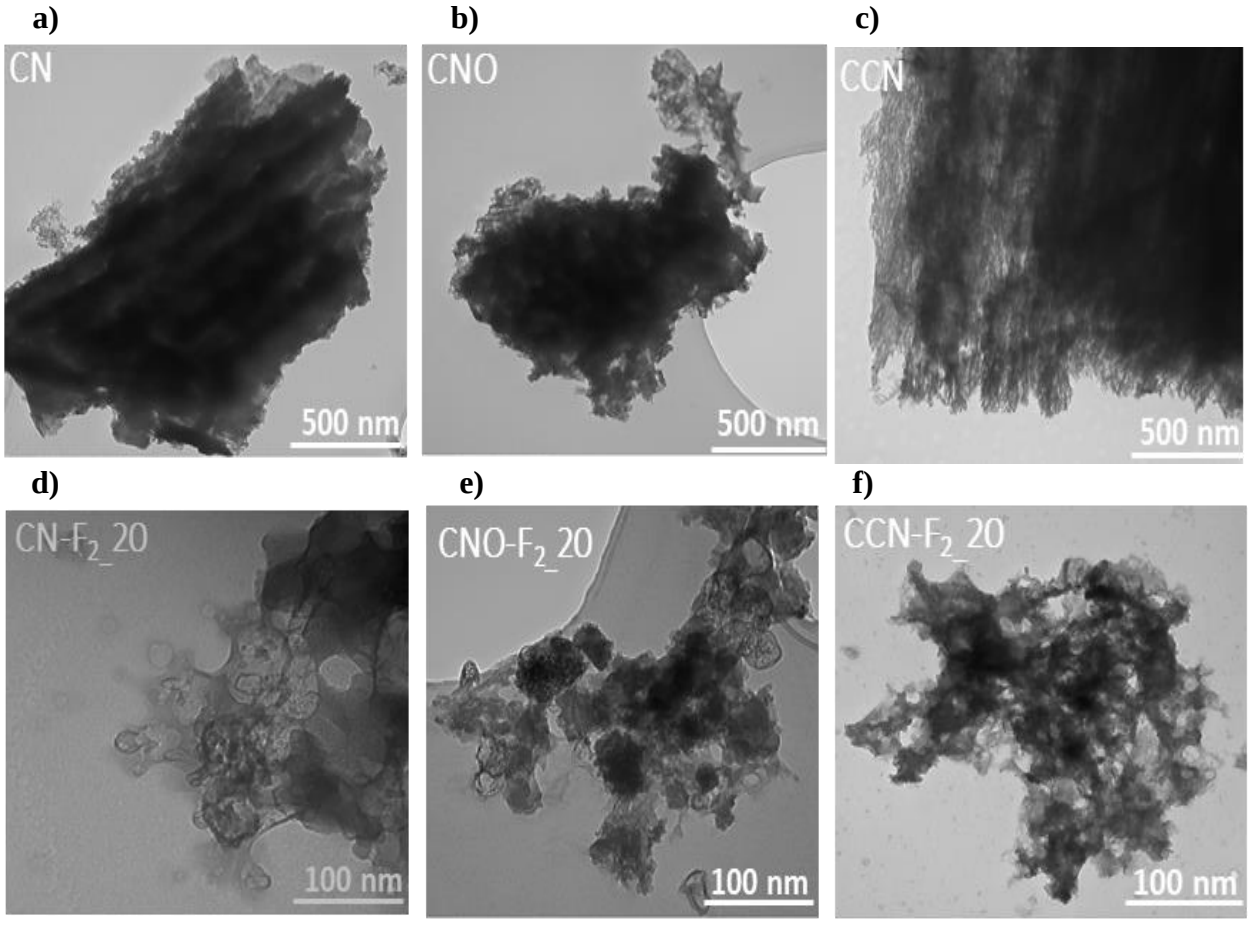

g)

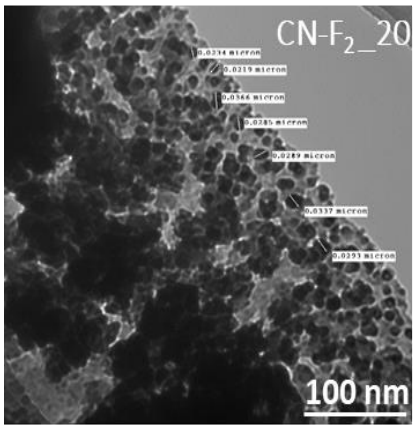

Figure 51. TEM images of CN, CNO, CCN (a, b, c) and CN-F_2_20, CNO-F_2_20 and CCN-F_2_20 (d, e, f, g).

5.2.4. XPS analysis

The global composition of the samples consist of C, N, F and O, therefore content of elements was given in Table 11. High fluorination content up to 26 at. % was observed for CN-F_2_20 sample. This seems to be dependent on the type of CN, followed by CNO-F_2_20 with 20 at. % and down to 9 at. % for CCN-F_2_20 sample, respectively. Between the CN and CNO samples, the decrease of F content is associated to a decrease of the weight gain of the remaining solid phase during fluorination for the samples CCN 73 %, CN 62 %, and CNO 47 %. Since CNO is supposed to be more reactive than CN, then it is expected that the latter yield more fluorine-based volatile species and subsequently to a lower weight gain than for CN. Moreover, the CCN sample containing C-rich domains is presumed to be less reactive, thus, more weight gain is associated with this sample [22]. The C/N ratio decreases systematically after fluorination for CN and CNO samples at the opposite of CCN, which increases. This indicates that a higher portion of carbon than nitrogen is released in the gas phase during fluorination of carbonitrides. This feature seems to confirm the higher reactivity with F_2 in the heptazine units of C compared to N. The peculiar behaviour of CCN with the lowest F content while having the highest weight gain and the highest O content could be explained by two phenomena; firstly the enhanced reactivity of some N groups with F_2 (compared to C groups) yielding to gaseous species, and explaining the increase of C/N ratio during fluorination, and second explanation the reactivity of fluorinated samples with water, when

they are exposed in air after fluorination. Formation of oxygenated compounds could then occurs with an associated weight gain and an increase of the O content as observed by XPS. The carbon-rich part of the CCN sample could be less reactive toward F_2 than CN, yielding to less volatile compounds and limited C-F groups in the solid state. On the other hand, the decrease of F/C and F/N ratios from CN-F_2_20 to CCN-F_2_20 samples could be explained from two prespectives; -firstly the F/C ratio is higher than F/N ratio for each sample except the CCN-F_2_20. This revealed the higher portion of C-F bond formed reather than N-F bond. This directs the explanation to the lower electronegativity of C compare to N, while the higher F/N ratio of CCN-F_2_20 is explained by the fact that N-groups are less released in gas phase an remain in solid phase which increase this ratio; -the second prespective is, that F/C ratio is the lowest for CCN sample, meaning that C-rich domain are less reactive toward the F_2, due to the local ordering of of some C units which is limited on the formation of long range extended structure, which also limit the incorporation of F.

Table 11. XPS composition (at. %) and F/C, F/N and C/N atomic ratio of the samples before and after fluorination. The global compositions determined by elemental analysis is given in bracket for comparison.

Names	**C**	**N**	**O**	**F**	**F/C atomic ratio**	**F/N atomic ratio**	**C/N atomic ratio**
CN	42 (34.3)	54(61.5)	4	0			0.78
CN-F_2-20	27	41	6	26	0.963	0.634	0.66
CNO	43 (33.8)	51(57.1)	6	0			0.84
CNO-F_2_20	31	43	6	20	0.645	0.465	0.721
CCN	41 (46.2)	55(41.8)	4	0			0.745
CCN-F_2_20	44	34	12	9	0.204	0.264	1.129

To further analyse the chemical bonds, the high-resolution XPS measurements of the C1s, N1s and F1s spectra were performed for all samples, but the explanation focused only on the fluorinated samples (Fig. 52a-e). The C1s spectrum of the carbonitrides and C-rich-g-C3N4 samples before fluorination has already been described in chapter 3.

The C1s spectra of the CN-F2_20, CNO-F_2_20 and CCN-F_2_20 samples (Fig. 52a-c) show new contributions added to those of the g-C_3N_4 samples. In fact, three contributions with higher binding energy are detected: C-F bonds at 289.7 eV with sp3 hybridisation already observed by two peaks due to a higher degree of fluorination: F-C-N-H at 291.5 eV and N-C-F_2 at 292.7 eV. The lower C-N=C fraction at 288.3 eV of the CN-F_2_20 sample compared to the CNO-F_2_20 sample means that a higher F content was introduced into the structure and a higher fraction reacted with F, leading to a decrease in the intensity of the peak and the formation of new F-containing species. This provides evidence that the CN sample again has a particular reactive structure compared to CNO, while the F-C-N-H peak at 291.5 eV is increased for CN-F_2_20 and lower for CNO-F_2_20, which is consistent. In detail, the presence of the N-C=N peak at 288.3 eV shows that the sp2-C atoms are bound to N within the hexagonal structure. Moreover, the peak area ratio of the N-C-F contribution follows this trend: 34.1, 27.8 and 14.0 for CN-F_2_20, CNO-F_2_20 and CCN-F_2_20, respectively. This could be due to the fact that the CN sample has a higher chemical reactivity towards F_2 compared to CNO and CCN. The possibility of forming a covalent C-F bond is higher because F atoms with high electronegativity tend to bond with C atoms with lower electronegativity than N. This leads to a partial conversion of sp2 hybridisation to sp3. In addition, a weak peak at 281.9 eV is registered for this sample, which is due to the not yet completed coverage of the carbon by the CCN, which does not have the same surface charges. For all fluorinated samples, a small number of graphitic C=C/C bonds were detected at 284.8 eV, but with a higher fraction for CCN-F2_20, which is consistent with its composition [33].

In summary, many C=N bonds were fluorinated in the bulk of g-C3N4, depending on the chemical nature of the sample, and additional bonds appeared, such as F-C-N-H and N-C-F2, but the latter is not present in CCN-F2_20, perhaps due to the limited fluorination of this sample. Moreover, the peak at 289.7 eV, which represents the C-F bond, shows a weak intensity in the CCN-F2_20 sample, implying that less C is associated with F, while the peak is quite intense in the other samples.

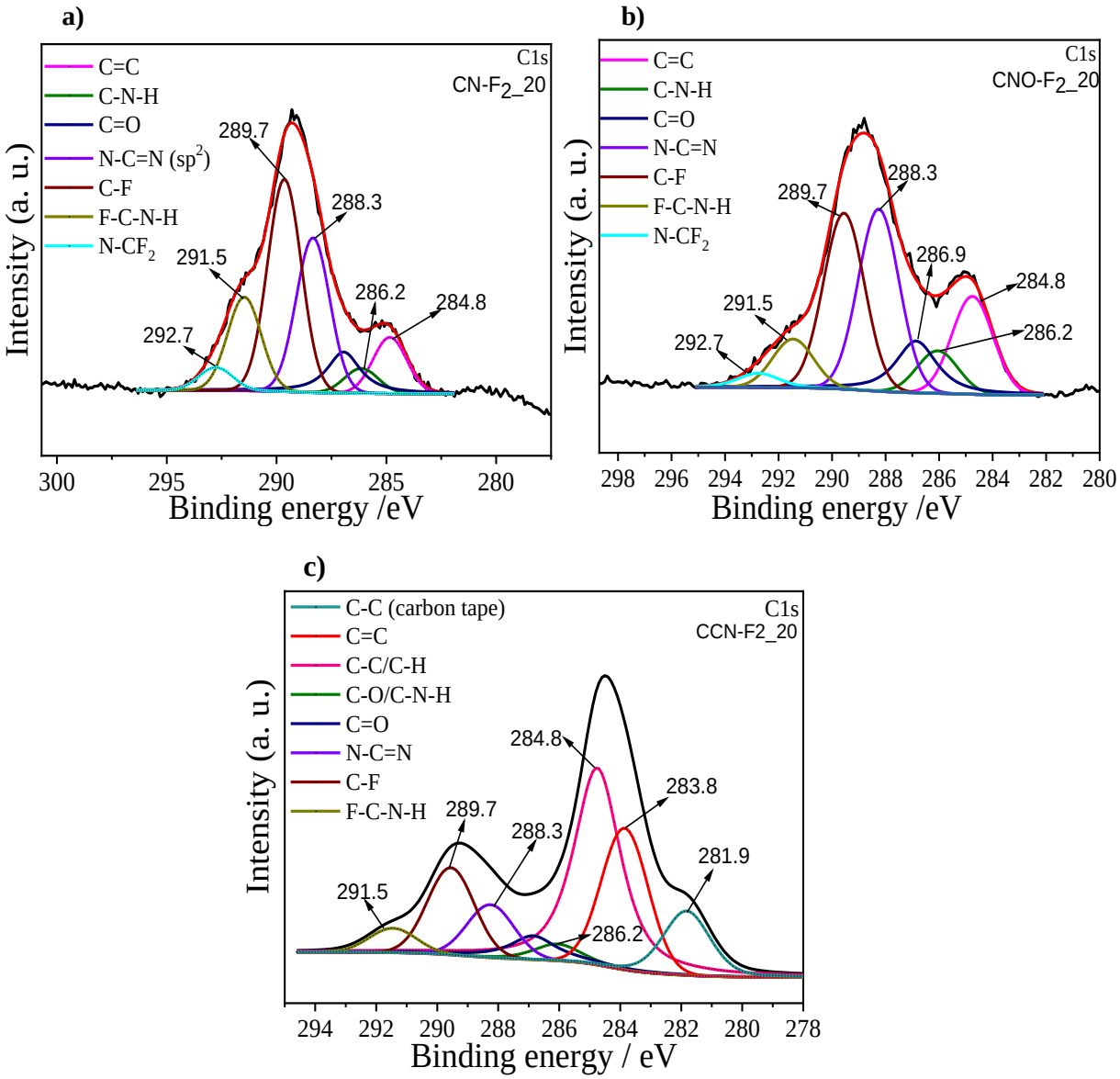

Figure 52. High resolution XPS C1s spectra of (a) CN-F_2_20, (b) CNO-F_2_20 and (c) CCN-F_2_20.

The high-resolution N1s spectra of the samples (Fig. 53d-f) show an additional peak at 400.8 eV, 401.8 eV and 402.4 eV for CN-F_2_20, CNO-F_2_20 and CCN-F_2_20, respectively. This peak represents the C-N-F contribution due to the high F content in the samples and was not observed in the low-fluorine studies. The peak area ratio of the corresponding peak follows the trend 19.4 % for CN-F_2_20, with a decrease of 6.6 % for CNO-F_2_20, while the CCN-F_2_20 sample shows the highest value by 22.5 %. This was explained at the very beginning of the XPS interpretation and is due to the lower portion of N released in the gas phase compared to C for this sample. The

other peaks are related to the (C-N=C)-sp^2 hybridization N, the (N-C_3)-sp^3 hybridization N and the amino functional groups (C-N-H), respectively [34, 35].

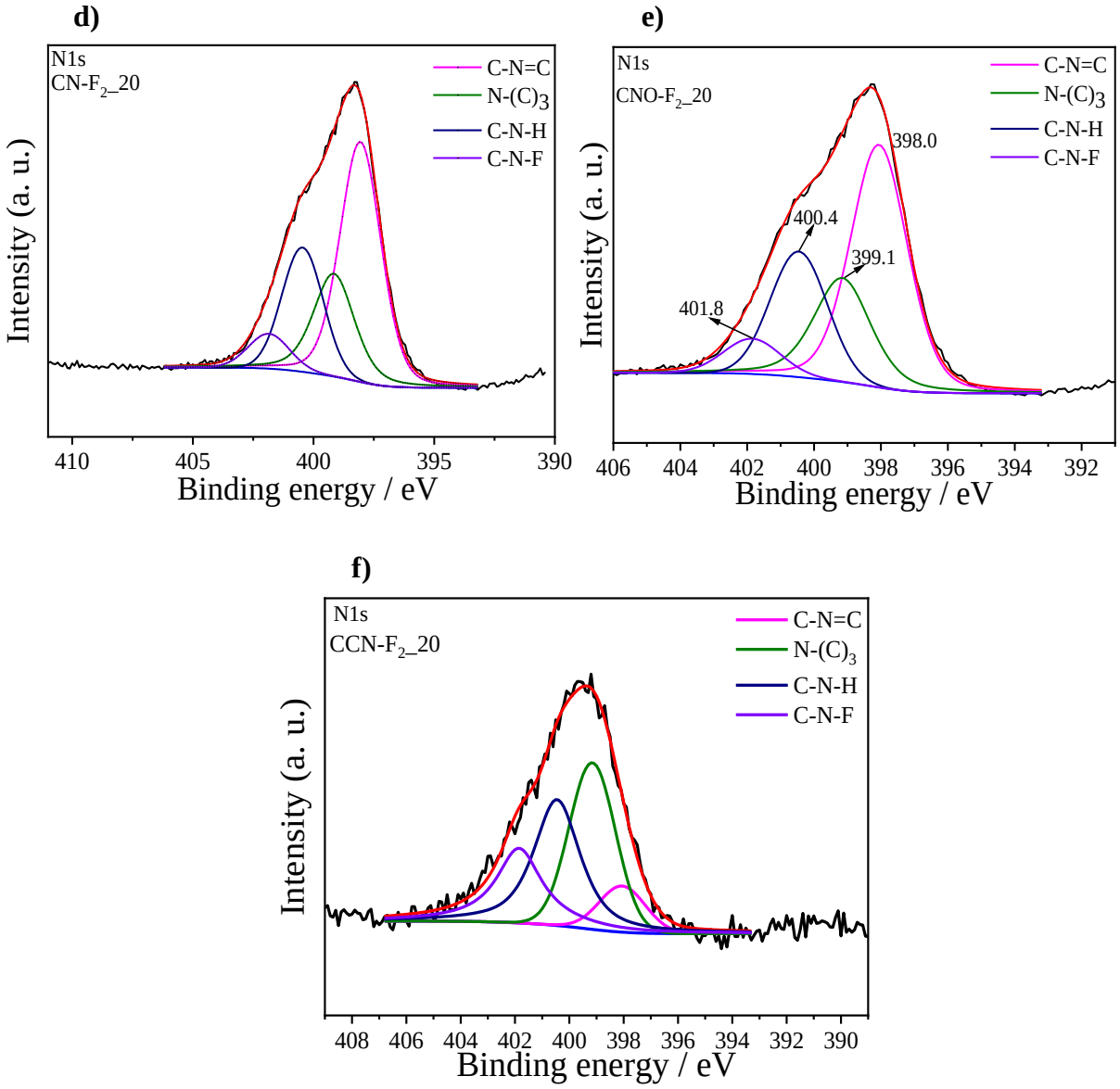

Figure 53. High resolution XPS N1s spectra of (d) CN-F_2_20, (e) CNO-F_2_20 and (f) CCN-F_2_20.

This interpretation is supported by the F1s spectrum, which is decomposed into two contributions in the fluorinated samples (Fig. 54g-h). Indeed, a high peak around 684.5 eV is detected, corresponding to the covalent C-F bond, and a weaker peak around 683.0 eV attributed to a higher fluorination of the carbon, the C-F_2 bonds. On the other hand, the CCN-F_2_20 sample shows a less

intense peak at 683.0 eV, implying that less fluorine is bound with C atoms on the hexagons of the g-C_3N_4 network, but part of the fluorine is directed towards the lone C-rich nanodomain away from the carbonitride structure, leading to a decrease in this peak [36, 37].

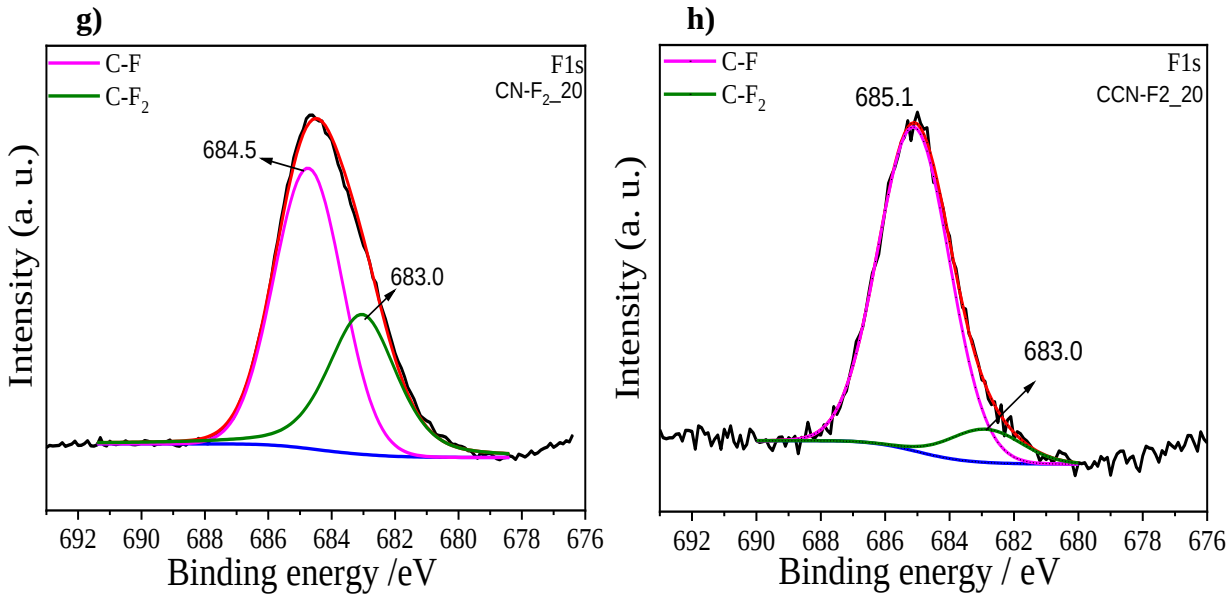

Figure 54. High resolution XPS F1s spectra of CN-F_2_20 (g) and CCN-F_2_20 (h).

Table 12. Peak area ratio (%) of each contribution.

Samples	**C1s**								**N1s**				**F1s**	
	C=C	**C-C/C-H**	**C-O/C-N-H**	**C=O**	**C-N_3**	**N-C-F**	**N-C-F_2**	**N-C-F**	**N=C**	**N-C_3**	**C-N-H**	**C-N-F**	**C-F**	**C-F_2**
CN	4.2	37.4	4.3	4.1	50.1	-	-	-	79.4	11.5	9.2	-	-	-
CNO	8.9	43.0	4.3	2.0	41.7	-	-	-	75.6	14.8	9.7	-	-	-
CCN	2.6	42.4	7.1	11.6	36.3	-	-	-	71.9	16.5	11.6	-	-	-
CN-F_2_20	0.0	9.0	4.0	9.4	24.8	34.1	15.0	3.7	30.2	24.7	25.7	19.4	62.8	37.2
CNO-F_2_20	0.0	15.5	6.7	11.1	28.8	27.8	7.7	2.5	48.3	22.4	22.7	6.6	54.2	45.8
CCN-F_2_20	22.8	41.9	3.2	5.6	8.6	14.0	3.9	-	9.4	34.1	34.1	22.5	90.7	9.3

5.3. Optical , electronic and photocatalytic properties

5.3.1. Difussion reflectance spectroscopy (DRS)

The optical properties and electronic structure of non-fluorinated and fluorinated materials were investigated using DRS. The reflectance spectra are shown in Fig. 55a. All fluorinated samples show a blue-shifted absorption in the visible range compared to g-C_3N_4, which is accompanied by a decrease in their band gap energy (Eg). The Eg was determined by the well-known Kubelka-Munk equation [26]. This equation is given as function of $(F(R) \cdot hv)^{1/2}$ versus Eg (energy).

As shown in Fig. 55b, the calculated values for CN and CN-F2_20 were between 2.66 and 2.57 eV. This could be due to the fact that the presence of F causes an additional electronic state with a partial conversion of C sp^2 hybridization to C sp^3 in the structural units. The large π-conjugated system of g-C_3N_4 benefits from the lone pair electrons located at the F atoms, and the incorporation of F into the C/N framework may provide the addition of a π-π conjugation system that increases the electron density at the HOMO [38]. This is easy to understand because in a conjugated π-system the electrons are able to capture the photons from the radiation, and so the electrons resonate along the distance of the π-orbitals and the photons with higher wavelength are captured by the higher conjugated π-system [39].

Consequently, it tunes the position of the conduction band (CB) and the valence band (VB), which significantly reduces the band gap. In the case of the CNO and CNO-F_2_20 samples, the band gap values are between 1.87 and 1.63 eV. The lower band gap value for this sample could be attributed to the higher structural defects compared to the CN or CN-F_2_20 samples. As already known, defects can promote new electronic states in the structure [20]. The band gap estimation for CCN and CCN-F_2_20 was calculated in the same way. Unlike the other samples, the CCN sample has a black colour and can therefore absorb more light, so it was difficult to calculate the band gap accurately. However, CCN-F_2_20 shows a decrease in the band gap from 1.55 to 1.27 eV, which is even lower compared to the other samples. The reason for this could be the higher C content (Fig. 55c), which could provide for a more delocalised π-structure [40].

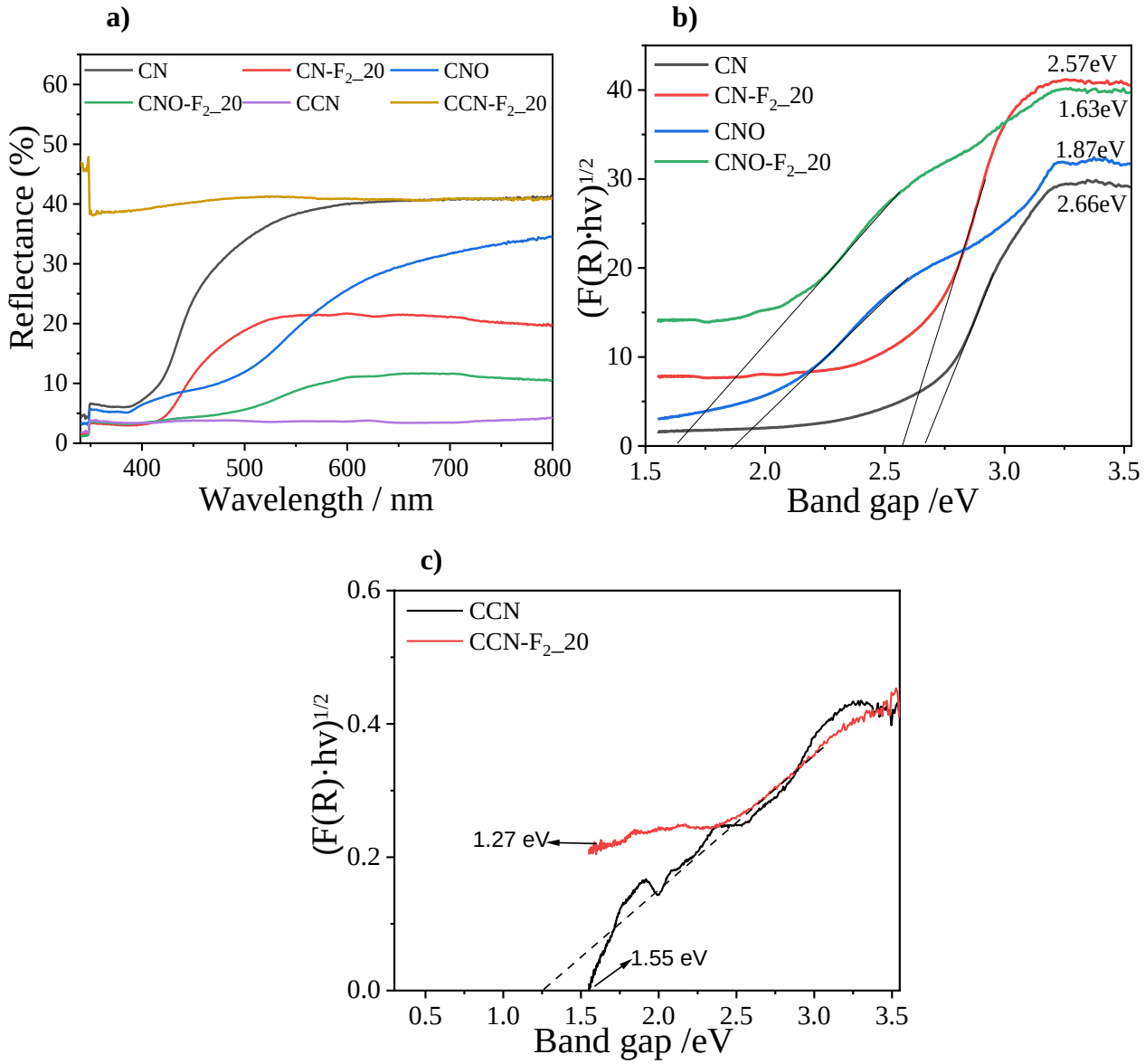

Figure 55. DRS absorption spectra (a), Kubelka-Munk function curves of CN, CN-F_2_20, CNO, CNO-F_2_20 (b) and CCN, CCN-F_2_20(c).

5.3.2. Electron paramagnetic resonance (EPR) under dark and light

In addition, information on the optical and electronic properties was obtained by using the solid-state EPR technique at room temperature (Fig. 56a-f). This technique was used to identify the presence of paramagnetic species under three different conditions: without light, under irradiation

and after irradiation (without light). The idea was to study the effect of visible light on the separation and transport efficiency of charge carriers, which is an important feature for photocatalytic purposes.

The CN sample shown in Fig. 56a shows a signal peak centred at g = 2.00407, indicating that the sample contains only one paramagnetic species within the π-conjugated aromatic rings of g-C_3N_4. These paramagnetic species could originate from unpaired electrons in the localized π-conjugated structure, and not from the electron pairs in σ-bonds. The reason is that these electron pairs have the opposite magnetic spin moment and therefore cannot produce the paramagnetic resonance absorption [41, 42].

After irradiation, the same peak is observed, but with a higher intensity, which means that the recombination of charge carrier pairs is hindered [43]. It could be hypothesised that electrons could be transferred from the σ-bonds to the π-conjugated structure under irradiation, so that electrons migrated from the VB of g-C_3N_4 to the CB and photoelectrons were generated. The CN-F_2_20 and two other fluorinated samples show an altered EPR line shape and variation in g-factor position compared to non-fluorinated samples [44]. The reason for this is probably the presence of more defects in the structure of these samples and the formation of new electronic states. The intensity of the EPR signal increased significantly when CN-F_2_20 was exposed to irradiation, but the g-factor remained similar. This is due to the fact that their localised π-conjugated structure harbours new paramagnetic species under irradiation, which might be the photoelectrons [45, 46]. Moreover, the increase of the signal under and after irradiation indicates that the concentration of photoelectrons in the localised π-conjugated structure is higher after fluorination.

Similar behaviour is observed in CNO and CNO-F_2_20 (Fig. 56c-d). However, the difference is observed in the CNO sample, which shows a shift of the g-factor to a lower value. The shift of the g-factor can be explained by the local order and the local magnetic field around the atom. If minor changes occur in the structure of the material, such as the number of defects or the strain/crystallinity, the g-factor may shift [47]. The CCN sample, which has a higher carbon content, does not show significant changes in the EPR signal after exposure, but only a shift in the g-factor, as described previously.

A different trend is observed for the CCN-F_2_20 sample (Fig. 56f). It shows several types of free electrons and different g-values. Possibly, other radicals are present, which could be due to higher defects, distortions and bond breaking in this type of sample after fluorination. In addition, the

EPR signal intensity of the CCN-F_2_20 sample did not show a significant increase after exposure to light compared to dark. Presumably, the high carbon content is detrimental as it hinders the formation of new paramagnetic species (photoelectrons) and their concentration in the localised π-conjugated structure [48].

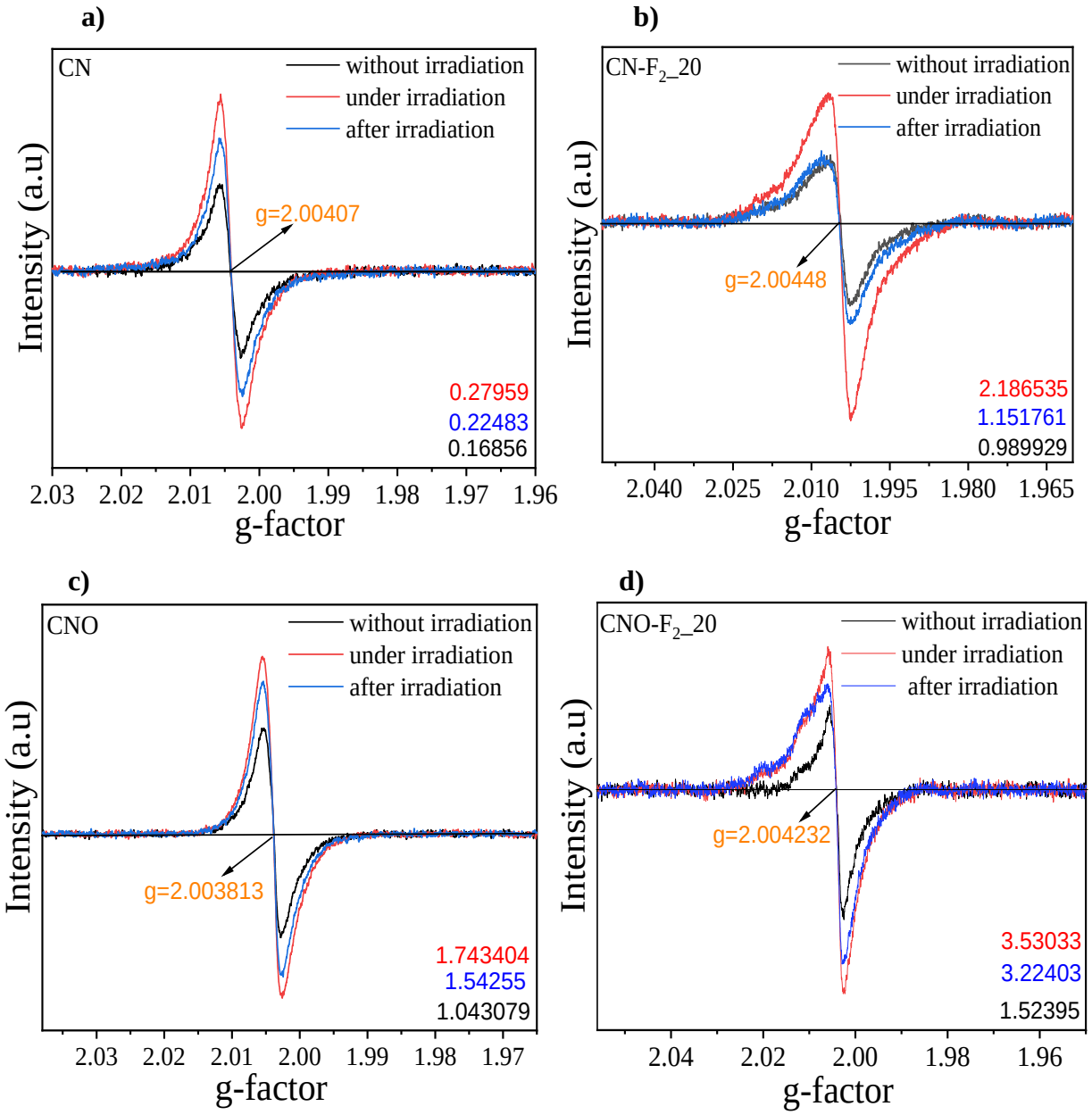

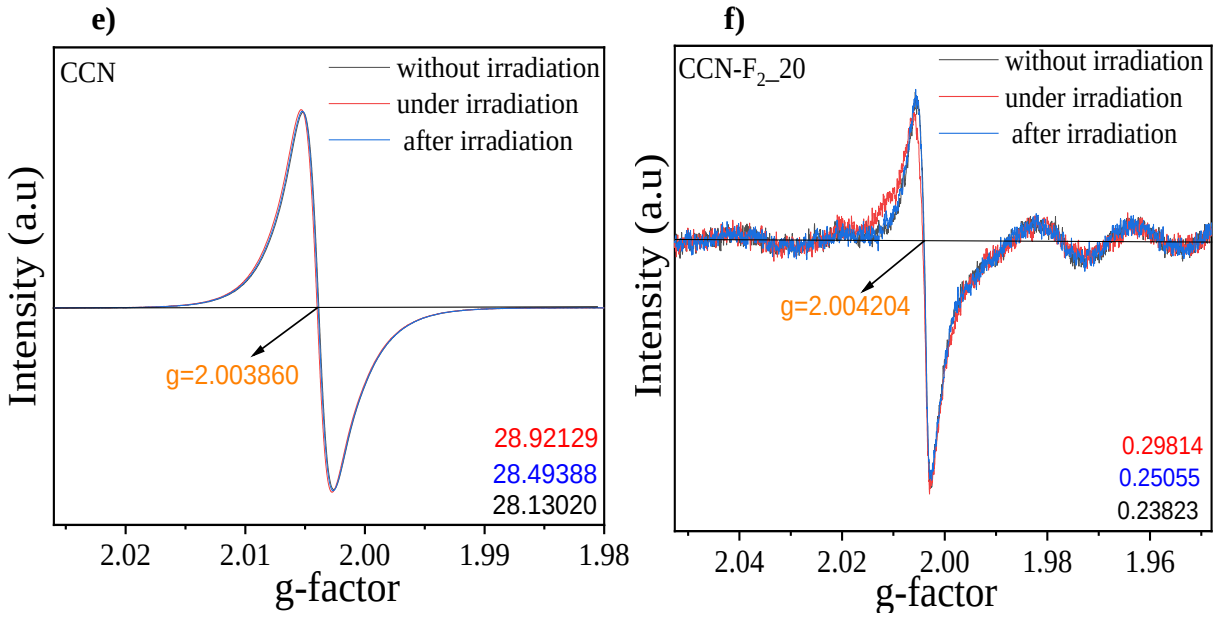

Figure 56. EPR spectra of a) CN, b) CN-F_2_20, c) CNO , d) CNO-F_2_20, e) CCN and f) CCN-F_2_20 samples in the dark, under irradiation and after irradiation (Xenon Mercury lamp $\lambda \geq$ 200-800 nm).

5.4. Photocatalytic activity of materials before and after fluorination

The photocatalytic performances of carbonitride-based materials were carried out by studying the photochemical degradation of methyl orange (MO) under visible light irradiation. For this purpose, in a first step, all samples (fluorinated or not) were put in contact with MO for one hour in the dark to study the adsorption phenomena of MO on the surface of the material. The spectra of the solution were analysed every 20 minutes and shown in Fig. 57a-f.

No evolution of the absorption peak position was observed for the CN, CNO and CCN samples (λmax = 464 nm), whereas clear near spectra related to the appearance of the acidic form of MO (λmax = 502 nm) were measured for CN-F_2_20, CNO-F_2_20 and CCN-F_2_20 samples (Fig. 57b, d, f) [49]. This feature is a clear indication of the acidification of the solution of fluorinated carbonitride when it comes into contact with water. A possible reaction of the fluorinated material with water could occur with formation of HF for instance. Therefore, for these samples, the evolution of the MO absorption intensity during photocatalysis was recorded at 502 nm (acidic form) than to its initial acidic form.

Since the pristine materials have a rather low specific surface area, it is assumed that the adsorption is negligible and that the evolution of the absorption intensity is rather related to a change in the pH of the solution. The surface area of the fluorinated samples could not be measured due to their pasty state. Therefore, to better substantiate the photocatalytic behaviour, we decided to plot the normalised absorbance (A/A°) as a function of the irradiation time, where A° is the absorbance at the initial irradiation (t = 0) of MO, measured at either the wavelength of the basic or acidic form, assuming that no strong pH changes occur during irradiation and decomposition of MO. The data are shown in Fig. 58-59.

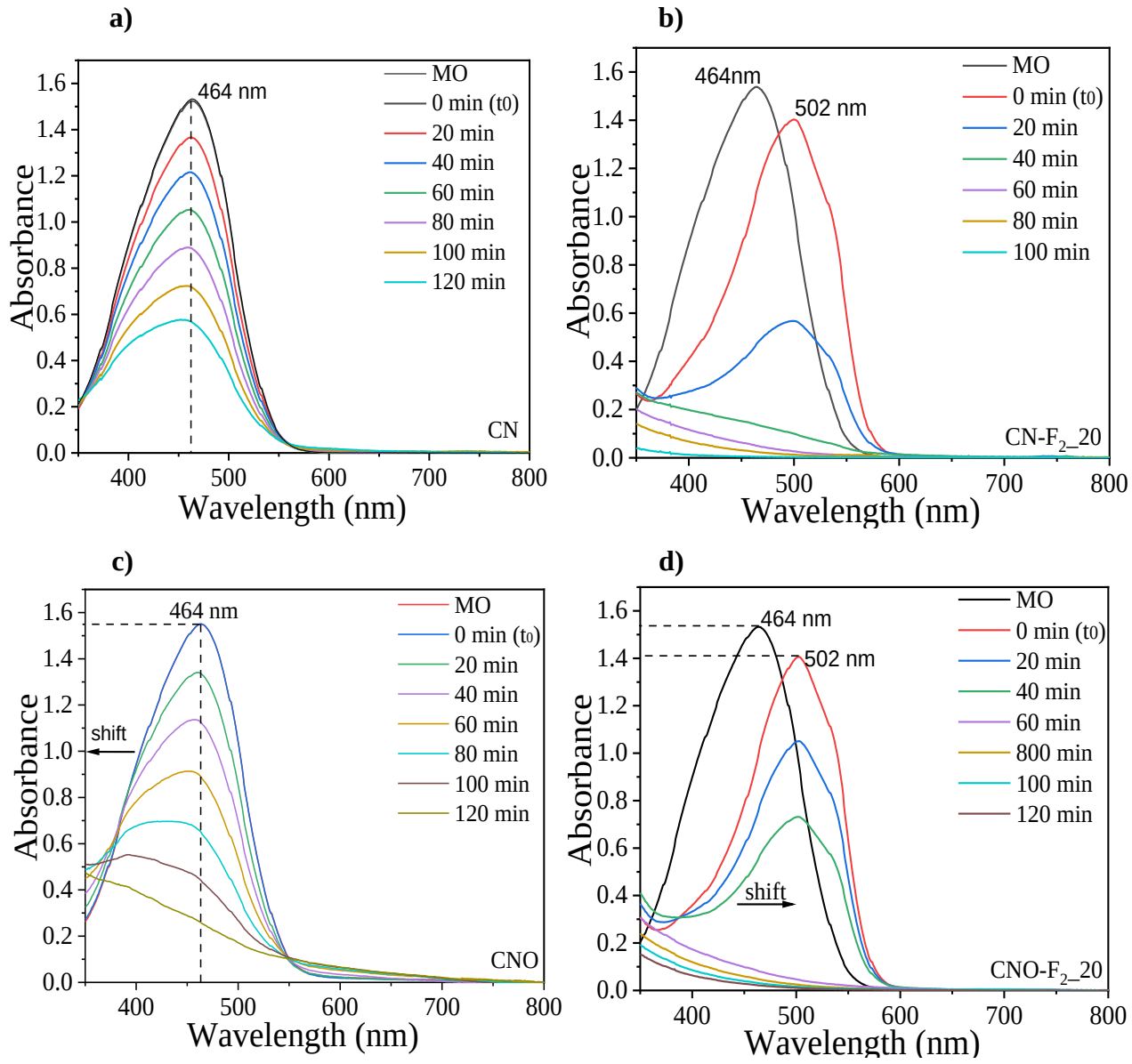

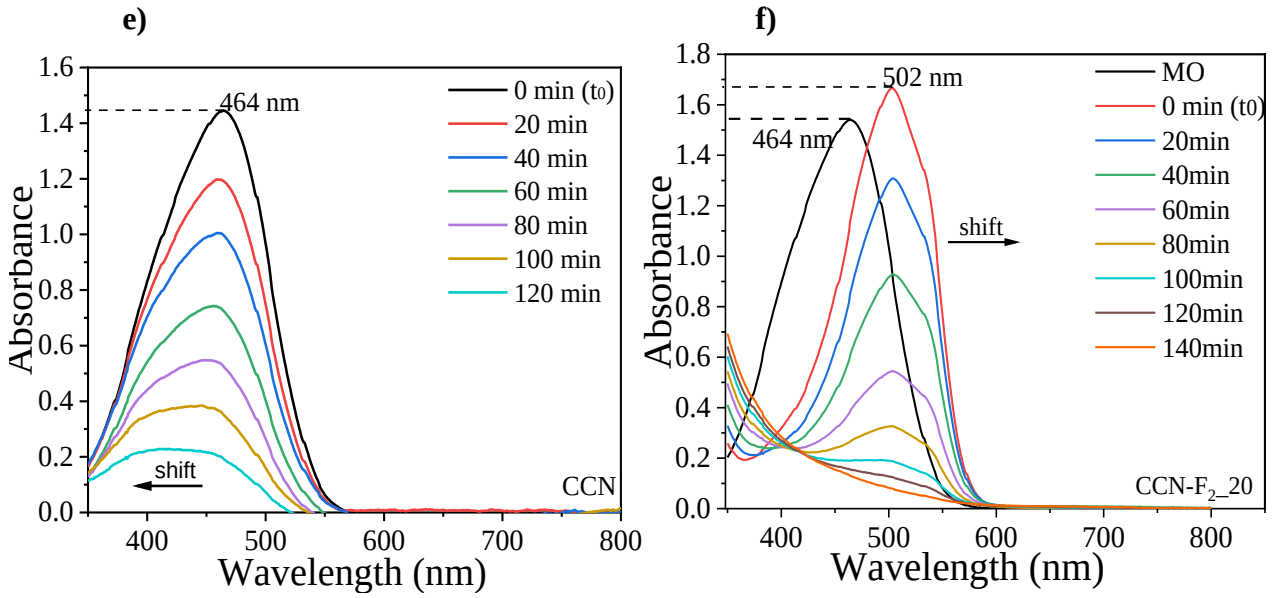

Figure 57. Absorption spectra of MO degradation under irradiation, for fluorinated and non-fluorinated carbonitride-based materials, analysed every 20 min.

Since the non-fluorinated samples have different characteristics, different photodegradation efficiencies are also observed (Fig. 58a-d). After contacting MO with the carbonitride-based material and after 120 min of irradiation, 62.15% of MO is degraded by the CN sample, while CNO and CCN (C-rich sample) show better performance. The reason could be that these materials contain more defects and more C respectively. These defects could behave like a separation centre for electron-hole pairs, and carbon is considered a good electron acceptor material due to its two-dimensional π-conjugation structure, which effectively prevents the recombination of electron-hole pairs [50, 51]. The carbon sites in the structure of the material are considered to be electron-poor, which in the absence of MO could be complexed with the adsorbed water via C···O-H, while in the presence of MO the C sites tend to be complexed with the more electron-rich methyl orange sites via C···O-C bonds. Furthermore, if the structure has N vacancies or defects, this would increase the longevity of the reaction sites [52, 53].

On the other hand all the fluorinated samples exhibit higher decomposition efficiency compared to CN, CNO and CCN. The photocatalytic experiment showed that around 99.76 % of MO is degraded after 100 min by CN-F_2_20 sample with a degradation rate 0.022646 min^{-1} which was 3.96 times higher than that of CN. Good performance was also exhibited by CNO-F_2_20 and CCN-

F_2_20 samples. After 120 min exposure to the light, around 98.55 and 99.95 % respectively of MO was degraded, with their corresponding degradation rates 0.018688 min^{-1} and 0.025641 min^{-1}. For CNO-F_2_20, 2.29 times higher than that of CNO, while for CCN-F_2_20; 2.18 times higher than CCN sample.

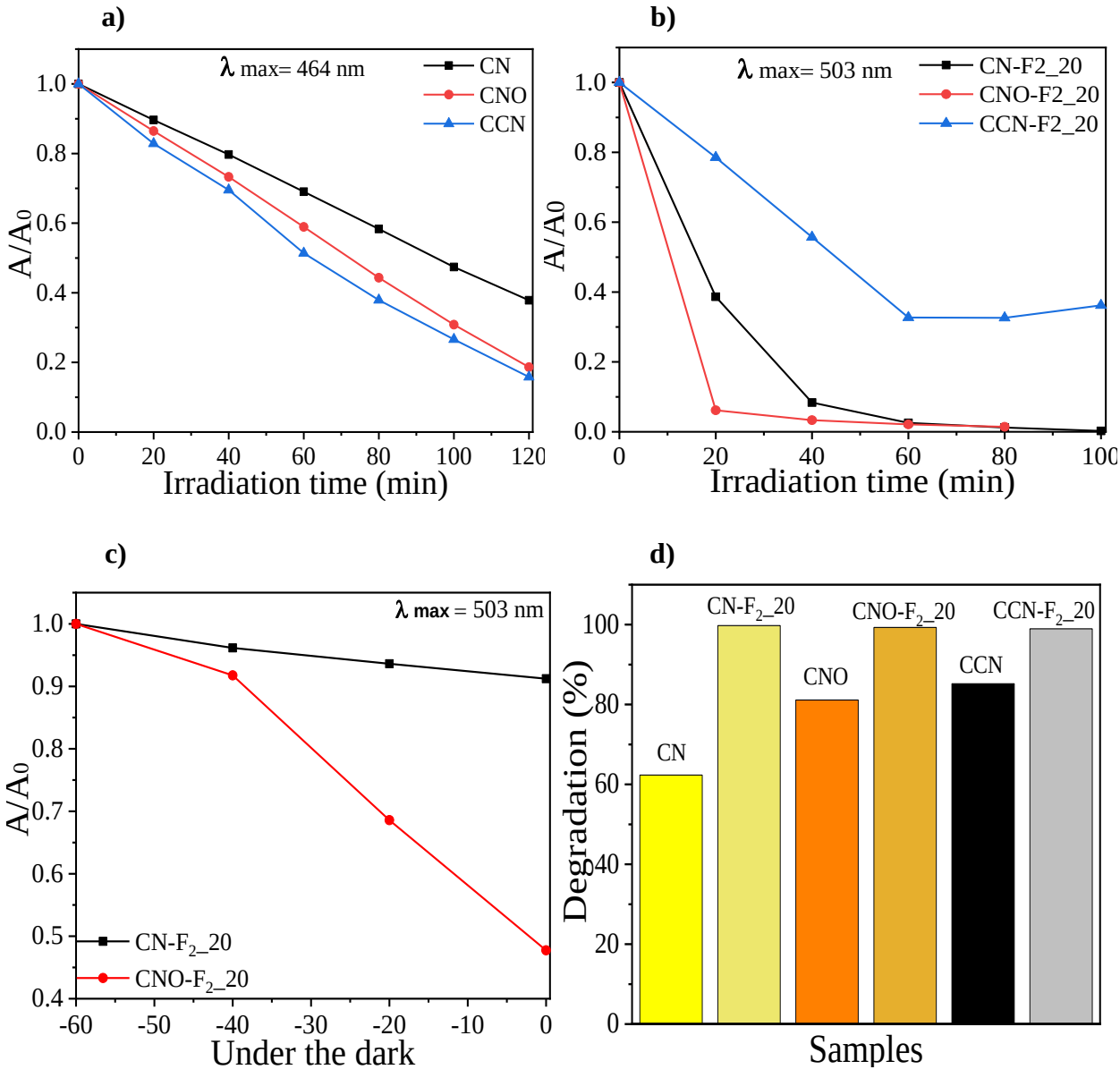

Figure 58. Photodegradation spectra of MO. A/A0 is determined by two wavelengths centered at 464 nm for non-fluorinated samples and 503 nm for fluorinated samples. Maximal absorbance determined at certain wavelength was used as initial absorbance (A0), at t = 0, while A is absorbance after each 20 min, for (a) non-fluorinated samples, (b) fluorinated samples, (c) fluorinated samples in the dark, (d) comparison of degradation performance of the samples.

The photodegradation is carried out repeatedly for the sample CN-F_2_20 with an amount of 7 mg (Fig. 59). After 40 minutes of light exposure, about 99% of MO is degraded, and the same amount is degraded in the second and third cycles. After each cycle, almost all of the photocatalyst was recovered, demonstrating the good reusability of the catalyst.

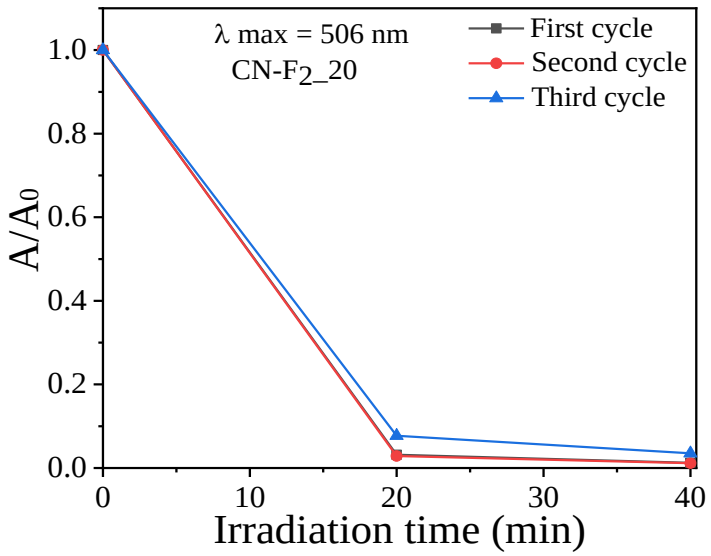

Figure 59. Photodegradation spectra of MO by CN-F_2_20 sample, with three cycles.

Table 13. Degradation rate and degradation efficiency of fluorinated and non-fluorinated samples.

Names	**Rate constant k min^{-1}**	**Degradation efficiency (%)**
CN	0.0057166	62.1
CN-F_2-20	0.022646	99.76
CNO	0.008152	81.14
CNO-F_2_20	0.018688	98.91
CCN	0.011747	85.20
CCN-F_2_20	0.025641	99.95

5.5. Conclusions

In summary, we have shown that gas phase method is with a high influence to produce highly F-doped g-C_3N_4 based material at room temperature. It results to compounds with high content of F ranging from (9, 20 and 26 at.%) for CCN-F_2_20 (C-rich-g-C_3N_4), CNO-F_2_20 (defective orange g-C_3N_4) and CN-F_2_20 (yellow g-C_3N_4). Drastical changes in morphology and exfoliation of lamellar structure is observed for fluorinated materials. Incorporation of F leads to a large number of pores. The structural defects were occurred by formation of C-F and surprisingly by N-F bond. Electronic and optical properties were significantly improved, by reducing band gap, and hinder the charge separation. Compared with pristine materials, fluorinated samples have shown significant improvement of photocatalytic activity of methyl orange degradation. These investigations and results are optimistic to understand the impact of high amounts of F on the structure of materials and improving the properties of photocatalysts. This approach with pure F_2 could lead to a more effective solution in engineering of photocatalysts.

SUMMARY IN FRENCH

La réactivité de g-C_3N_4 et de g-C_3N_4/C vis-à-vis du F_2 gazeux pur à température a été étudiée dans ce chapitre. Cette voie permet l'incorporation d'une teneur en fluor élevée par rapport aux autres méthodes de fluoration (synthèse hydrothermale, F_2 dilué) ce qui modifie significativement de nombreuses propriétés. Les matériaux fluorés ont subit une stabilisation à 100°C (N_2) puis à l'air (température ambiante) afin de limiter leur caractère explosif à la sortie de l'enceinte réactionnelle. Trois types de carbonitrure ont été étudiés : g-C_3N_4 (jaune), g-C_3N_4 (orange avec plus de défauts) et g-C_3N_4/C. Ces matériaux après fluoration ont été caractérisés par différentes techniques (EPR, DRS, XRD, TEM, TG-MS, XPS) pour comprendre les modifications physicochimiques apportées par la fluoration et évaluer les propriétés photocatalytiques. La représentation de Kubelka-Munk pour la détermination des bandes interdites (Eg) des échantillons est présentées. Les matériaux fluorés ont été testés sur la photodégradation du méthyl-orange (MO) sous lumière UV-visible. Tous les échantillons fluorés ont montré de meilleures performances envers la dégradation du MO sous illumination.

References

[1] L. Ge, C. Han, and J. Liu, 'Novel visible light-induced g-C3N4/Bi2WO6 composite photocatalysts for efficient degradation of methyl orange', *Applied Catalysis B: Environmental*, vol. 108–109, pp. 100–107, Oct. 2011, doi: 10.1016/j.apcatb.2011.08.014.

[2] K. Kočí *et al.*, 'Photocatalytic hydrogen production from methanol over Nd/TiO2', *Journal of Photochemistry and Photobiology A: Chemistry*, vol. 366, pp. 55–64, Nov. 2018, doi: 10.1016/j.jphotochem.2018.03.007.

[3] H. Wang *et al.*, 'Structural distortion in graphitic-C_3N_4 realizing an efficient photoreactivity', *Nanoscale*, vol. 7, no. 12, pp. 5152–5156, 2015, doi: 10.1039/C4NR07645A.

[4] S. Wang and S. Zhou, 'Photodegradation of methyl orange by photocatalyst of CNTs/P-TiO2 under UV and visible-light irradiation', *Journal of Hazardous Materials*, vol. 185, no. 1, pp. 77–85, Jan. 2011, doi: 10.1016/j.jhazmat.2010.08.125.

[5] Y. Liu, J. Wang, C. Yin, H. Duan, S. Kang, and L. Cui, 'Facile synthesis of highly active fluorinated ultrathin graphitic carbon nitride for photocatalytic H_2 evolution using a novel NaF etching strategy', *RSC Adv.*, vol. 8, no. 48, pp. 27021–27026, 2018, doi: 10.1039/C8RA04691C.

[6] M. Xu, B. Chai, J. Yan, H. Wang, Z. Ren, and K.-W. Paik, 'Facile Synthesis of Fluorine Doped Graphitic Carbon Nitride with Enhanced Visible Light Photocatalytic Activity', *NANO*, vol. 11, no. 12, p. 1650137, Dec. 2016, doi: 10.1142/S179329201650137X.

[7] H. Wang, C. Yang, M. Li, F. Chen, and Y. Cui, 'Enhanced photocatalytic hydrogen production of restructured B/F codoped g-C3N4 via post-thermal treatment', *Materials Letters*, vol. 212, pp. 319–322, Feb. 2018, doi: 10.1016/j.matlet.2017.10.112.

[8] B. Zhu, J. Zhang, C. Jiang, B. Cheng, and J. Yu, 'First principle investigation of halogen-doped monolayer g-C3N4 photocatalyst', *Applied Catalysis B: Environmental*, vol. 207, pp. 27–34, Jun. 2017, doi: 10.1016/j.apcatb.2017.02.020.

[9] Z.A. Lan, G. Zhang, and X. Wang, 'A facile synthesis of Br-modified g-C3N4 semiconductors for photoredox water splitting', *Applied Catalysis B: Environmental*, vol. 192, pp. 116–125, Sep. 2016, doi: 10.1016/j.apcatb.2016.03.062.

[10] C. Liu *et al.*, 'Chlorine intercalation in graphitic carbon nitride for efficient photocatalysis', *Applied Catalysis B: Environmental*, vol. 203, pp. 465–474, Apr. 2017, doi: 10.1016/j.apcatb.2016.10.002.

[11] Y. Liu *et al.*, 'A brief review for fluorinated carbon: synthesis, properties and applications', *Nanotechnology Reviews*, vol. 8, no. 1, pp. 573–586, Dec. 2019, doi: 10.1515/ntrev-2019-0051.

[12] L. Zeng *et al.*, 'Enhancement of photocatalytic hydrogen evolution activity of g-C3N4 induced by structural distortion via post-fluorination treatment', *Applied Catalysis B: Environmental*, vol. 227, pp. 276–284, Jul. 2018, doi: 10.1016/j.apcatb.2018.01.040.

[13] Y. Wang, Y. Di, M. Antonietti, H. Li, X. Chen, and X. Wang, 'Excellent Visible-Light Photocatalysis of Fluorinated Polymeric Carbon Nitride Solids', *Chem. Mater.*, vol. 22, no. 18, pp. 5119–5121, Sep. 2010, doi: 10.1021/cm1019102.

[14] F. Ma, C. Sun, Y. Shao, Y. Wu, B. Huang, and X. Hao, 'One-step exfoliation and fluorination of g-C $_3$ N $_4$ nanosheets with enhanced photocatalytic activities', *New J. Chem.*, vol. 41, no. 8, pp. 3061–3067, 2017, doi: 10.1039/C7NJ00035A.

[15] K. Guérin, M. Dubois, A. Houdayer, and A. Hamwi, 'Applicative performances of fluorinated carbons through fluorination routes: A review', *Journal of Fluorine Chemistry*, vol. 134, pp. 11–17, Feb. 2012, doi: 10.1016/j.jfluchem.2011.06.013.

[16] Y. Zhao, L. Yang, C. Ma, and G. Han, 'One-Step Fabrication of Fluorine-Doped Graphite Derived from a Low-Grade Microcrystalline Graphite Ore for Potassium-Ion Batteries', *Energy Fuels*, vol. 34, no. 7, pp. 8993–9001, Jul. 2020, doi: 10.1021/acs.energyfuels.0c01608.

[17] L. Sun, Y. Li, and W. Feng, 'Gas-Phase Fluorination of g-C3N4 for Enhanced Photocatalytic Hydrogen Evolution', *Nanomaterials*, vol. 12, no. 1, p. 37, Dec. 2021, doi: 10.3390/nano12010037.

[18] X. Jiang *et al.*, 'The photocatalytic performance of g-C3N4 from melamine hydrochloride for dyes degradation with peroxymonosulfate', *Journal of Photochemistry and Photobiology A: Chemistry*, vol. 336, pp. 54–62, Mar. 2017, doi: 10.1016/j.jphotochem.2016.12.018.

[19] G. Xin and Y. Meng, 'Pyrolysis Synthesized g-C $_3$ N $_4$ for Photocatalytic Degradation of Methylene Blue', *Journal of Chemistry*, vol. 2013, pp. 1–5, 2013, doi: 10.1155/2013/187912.

[20] J. Chen *et al.*, 'Porous g-C3N4 with defects for the efficient dye photodegradation under visible light', *Water Science and Technology*, vol. 84, no. 6, pp. 1354–1365, Sep. 2021, doi: 10.2166/wst.2021.313.

[21] J.-C. Agopian, O. Téraube, K. Charlet, and M. Dubois, 'A review about the fluorination and oxyfluorination of carbon fibres', *Journal of Fluorine Chemistry*, vol. 251, p. 109887, Nov. 2021, doi: 10.1016/j.jfluchem.2021.109887.

[22] J. Parmentier, S. Schlienger, M. Dubois, E. Disa, F. Masin, and T. A. Centeno, 'Structural/textural properties and water reactivity of fluorinated activated carbons', *Carbon*, vol. 50, no. 14, pp. 5135–5147, Nov. 2012, doi: 10.1016/j.carbon.2012.06.054.

[23] S. Tang, Z. Fu, Y. Li, and Y. Li, 'Study on boron and fluorine-doped C3N4 as a solid activator for cyclohexane oxidation with H2O2 catalyzed by 8-quinolinolato ironIII

complexes under visible light irradiation', *Applied Catalysis A: General*, vol. 590, p. 117342, Jan. 2020, doi: 10.1016/j.apcata.2019.117342.

[24] A. Mirzaei, Z. Chen, F. Haghighat, and L. Yerushalmi, 'Magnetic fluorinated mesoporous g-C3N4 for photocatalytic degradation of amoxicillin: Transformation mechanism and toxicity assessment', *Applied Catalysis B: Environmental*, vol. 242, pp. 337–348, Mar. 2019, doi: 10.1016/j.apcatb.2018.10.009.

[25] Q. Han *et al.*, 'Atomically Thin Mesoporous Nanomesh of Graphitic C $_3$ N $_4$ for High-Efficiency Photocatalytic Hydrogen Evolution', *ACS Nano*, vol. 10, no. 2, pp. 2745–2751, Feb. 2016, doi: 10.1021/acsnano.5b07831.

[26] A. Mirzaei, Z. Chen, F. Haghighat, and L. Yerushalmi, 'Magnetic fluorinated mesoporous g-C3N4 for photocatalytic degradation of amoxicillin: Transformation mechanism and toxicity assessment', *Applied Catalysis B: Environmental*, vol. 242, pp. 337–348, Mar. 2019, doi: 10.1016/j.apcatb.2018.10.009.

[27] B. Shen, J. Chen, X. Yan, and Q. Xue, 'Synthesis of fluorine-doped multi-layered graphene sheets by arc-discharge', *RSC Adv.*, vol. 2, no. 17, p. 6761, 2012, doi: 10.1039/c2ra20593a.

[28] W. Kang and S. Li, 'Preparation of fluorinated graphene to study its gas sensitivity', *RSC Adv.*, vol. 8, no. 41, pp. 23459–23467, 2018, doi: 10.1039/C8RA03451F.

[29] P. J. Larkin, 'General Outline for IR and Raman Spectral Interpretation', in *Infrared and Raman Spectroscopy*, Elsevier, 2018, pp. 135–151. doi: 10.1016/B978-0-12-804162-8.00007-0.

[30] L. Sun, Y. Li, and W. Feng, 'Gas-Phase Fluorination of g-C3N4 for Enhanced Photocatalytic Hydrogen Evolution', *Nanomaterials*, vol. 12, no. 1, p. 37, Dec. 2021, doi: 10.3390/nano12010037.

[31] Y. Jiang, Z. Sun, C. Tang, Y. Zhou, L. Zeng, and L. Huang, 'Enhancement of photocatalytic hydrogen evolution activity of porous oxygen doped g-C3N4 with nitrogen defects induced by changing electron transition', *Applied Catalysis B: Environmental*, vol. 240, pp. 30–38, Jan. 2019, doi: 10.1016/j.apcatb.2018.08.059.

[32] P. Wu, J. Wang, J. Zhao, L. Guo, and F. E. Osterloh, 'Structure defects in g-C $_3$ N $_4$ limit visible light driven hydrogen evolution and photovoltage', *J. Mater. Chem. A*, vol. 2, no. 47, pp. 20338–20344, 2014, doi: 10.1039/C4TA04100C.

[33] V. Mazánek *et al.*, 'Tuning of fluorine content in graphene: towards large-scale production of stoichiometric fluorographene', *Nanoscale*, vol. 7, no. 32, pp. 13646–13655, 2015, doi: 10.1039/C5NR03243A.

[34] X. She *et al.*, 'Oxygenated monolayer carbon nitride for excellent photocatalytic hydrogen evolution and external quantum efficiency', *Nano Energy*, vol. 27, pp. 138–146, Sep. 2016, doi: 10.1016/j.nanoen.2016.06.042.

[35] H. Yu *et al.*, 'Alkali-Assisted Synthesis of Nitrogen Deficient Graphitic Carbon Nitride with Tunable Band Structures for Efficient Visible-Light-Driven Hydrogen Evolution', *Adv. Mater.*, vol. 29, no. 16, p. 1605148, Apr. 2017, doi: 10.1002/adma.201605148.

[36] A. Jablonski and C. J. Powell, 'Effective Attenuation Lengths for Different Quantitative Applications of X-ray Photoelectron Spectroscopy', *Journal of Physical and Chemical Reference Data*, vol. 49, no. 3, p. 033102, Sep. 2020, doi: 10.1063/5.0008576.

[37] M. A. Mahjoub, G. Monier, C. Robert-Goumet, L. Bideux, and B. Gruzza, 'New method for the determination of the correction function of a hemisperical electron analyser based on elastic electron images', *Journal of Electron Spectroscopy and Related Phenomena*, vol. 197, pp. 80–87, Dec. 2014, doi: 10.1016/j.elspec.2014.09.010.

[38] N. Wang, H. Fan, J. Sun, Z. Han, J. Dong, and S. Ai, 'Fluorine-doped carbon nitride quantum dots: Ethylene glycol-assisted synthesis, fluorescent properties, and their application for bacterial imaging', *Carbon*, vol. 109, pp. 141–148, Nov. 2016, doi: 10.1016/j.carbon.2016.08.004.

[39] J. Thiele, 'Zur Kenntniss der ungesättigten Verbindungen. Theorie der ungesättigten und aromatischen Verbindungen', *Justus Liebigs Ann. Chem.*, vol. 306, no. 1–2, pp. 87–142, 1899, doi: 10.1002/jlac.18993060107.

[40] S. Patnaik, S. Martha, S. Acharya, and K. M. Parida, 'An overview of the modification of g-C_3N_4 with high carbon containing materials for photocatalytic applications', *Inorg. Chem. Front.*, vol. 3, no. 3, pp. 336–347, 2016, doi: 10.1039/C5QI00255A.

[41] J. Zhang, M. Zhang, R.-Q. Sun, and X. Wang, 'A Facile Band Alignment of Polymeric Carbon Nitride Semiconductors to Construct Isotype Heterojunctions', *Angew. Chem. Int. Ed.*, vol. 51, no. 40, pp. 10145–10149, Oct. 2012, doi: 10.1002/anie.201205333.

[42] Zhang et *al*', Co-Monomer Control of Carbon Nitride Semiconductors to Optimize Hydrogen Evolution with visible light', *Angew. Chem. Int. Ed.* 2012, no. 51, pp. 3183 – 3187, doi: 10.1002/anie.201106656

[43] W. Lin *et al.*, 'Defects remodeling of g-C3N4 nanosheets by fluorine-containing solvothermal treatment to enhance their photocatalytic activities', *Applied Surface Science*, vol. 474, pp. 194–202, Apr. 2019, doi: 10.1016/j.apsusc.2018.03.140.

[44] A. Alessi, S. Agnello, F. M. Gelardi, G. Messina, and M. Carpanese, 'Influence of Ge doping level on the EPR signal of Ge(1), Ge(2) and E'Ge defects in Ge-doped silica', *Journal of Non-Crystalline Solids*, vol. 357, no. 8–9, pp. 1900–1903, Apr. 2011, doi: 10.1016/j.jnoncrysol.2010.11.108.

[45] W. Ho *et al.*, 'Copolymerization with 2,4,6-Triaminopyrimidine for the Rolling-up the Layer Structure, Tunable Electronic Properties, and Photocatalysis of g-C_3N_4', *ACS Appl. Mater. Interfaces*, vol. 7, no. 9, pp. 5497–5505, Mar. 2015, doi: 10.1021/am509213x.

[46] Li *et al.*, Macroscopic Foam-Like Holey Ultrathin g-C3N4 Nanosheets for Drastic Improvement of Visible-Light Photocatalytic Activity', *Advanced Energy Materials*, 2016, no. 6, pp. 1601273', doi: 10.1002/aenm.201601273.

[47] A. Krupska, W. Jurga, L. Piekara-Sady, P. Szroeder, and F. Rozpłoch, 'Effect of lattice compression on -factor in graphite', *Solid State Communications*, vol. 148, no. 3–4, pp. 148–150, Oct. 2008, doi: 10.1016/j.ssc.2008.07.035.

[48] R. C. Barklie, M. Collins, J. Cunniffe, and S. R. P. Silva, 'An EPR study of defects in hydrogenated amorphous carbon thin films', *Diamond and Related Materials*, vol. 7, no. 6, pp. 864–868, Jun. 1998, doi: 10.1016/S0925-9635(97)00315-4.

[49] W. Xin, D. Zhu, G. Liu, Y. Hua, and W. Zhou, 'Synthesis and Characterization of Mn–C–Codoped TiO 2 Nanoparticles and Photocatalytic Degradation of Methyl Orange Dye under Sunlight Irradiation', *International Journal of Photoenergy*, vol. 2012, pp. 1–7, 2012, doi: 10.1155/2012/767905.

[50] Li *et al*, 'Synthesis of carbon-doped g-C3N4 composites with enhanced visible-light photocatalytic activity', *Materials Letters*, p. 4, pp. 281–284, Sep. 2014, doi.org/10.1016/j.matlet.2014.08.142.

[51] N. V. Phuc *et al.*, 'Synthesis and Photocatalytic Activity of Fluorine DOPED-g-C_3N_4', *AMM*, vol. 889, pp. 24–32, Mar. 2019, doi: 10.4028/www.scientific.net/AMM.889.24.

[52] L. Lyu, G. Yu, L. Zhang, C. Hu, and Y. Sun, '4-Phenoxyphenol-Functionalized Reduced Graphene Oxide Nanosheets: A Metal-Free Fenton-Like Catalyst for Pollutant Destruction', *Environ. Sci. Technol.*, vol. 52, no. 2, pp. 747–756, Jan. 2018, doi: 10.1021/acs.est.7b04865.

[53] L. J. Fang *et al.*, 'One-step fabrication of porous oxygen-doped g-C_3N_4 with feeble nitrogen vacancies for enhanced photocatalytic performance', *Chem. Commun.*, vol. 52, no. 100, pp. 14408–14411, 2016, doi: 10.1039/C6CC08187H.

CONCLUSIONS

In this thesis were prepared three different composite based g-C_3N_4 materials; C-rich-g-C_3N_4, N-rich porous carbon and F-doped-g-C_3N_4.

The results have shown that it is possible to achieve homogeneity at the molecular level between precursors. By changing the molar ratio of the initial precursors, diferent range of compositions of adducts were prepared. Adducts have exhibited different thermal behaviour, morphology and crystal structure in comparision of pure precursors. These results have proven that adducts are formed by high distribution in atomic scale of C and N within the precursors (are not as a physical mixture). The derived C-rich-g-C_3N_4 materials display tailored C/N ratio and variation in structure compare to g-C_3N_4. Despite the high carbon content, g-C_3N_4 features were preserved within the composite. Prepared C-rich-g-C_3N_4 materials can be potential photocatalyst for H_2 production, but still required an optimization of carbon content, to avoid obstacles for utilisation of visible light.

Furthermore, the reactivity of C-rich-g-C_3N_4 was investigated in presence of oxygen (air). Due to diferent thermal stability/reactivity of g-C_3N_4 part compare to C-rich part, new materials with high porosity were obtained. Increasing the temperature of oxidation, materials become more disorder. The process, based on the use of g-C_3N_4 (with lower thermal stability), appears as a new way to produce N-rich porous carbon materials.

High level of doping with fluorine was incorporated on g-C_3N_4 structure, using F_2 as gas phase. All F-doped-g-C_3N_4 samples have shown enormous changes in the structure, in comparision with pristine materials. Diferent morphology with exfoliated layers were obtained after fluorination compared to g-C_3N_4. The inclusion of fluorine has caused changes in the optical and electronic properties, in favour of photocatalytic activity. This gas phase approach is powerful tool to open new avenue to prepare g-C_3N_4 composites, over conventional multi-step hydrothermal methods.

SUMMARY IN FRENCH

Dans le cadre de cette thèse, trois types de matériaux à base de g-C_3N_4 ont été préparés : g-C_3N_4/C avec des teneurs différentes en C, un carbone poreux riche en azote et un matériau fluoré dérivé de g-C_3N_4.

La synthèse de g-C_3N_4/C par la voie des adduits permet d'obtenir une homogénéité des précurseurs au niveau moléculaire tout en contrôlant le rapport C/N après carbonisation par l'ajustement du rapport molaire des précurseurs et leur nature chimique. Les adduits ont montré un comportement thermique, une morphologie et une structure cristalline différents de ceux des précurseurs purs. Les matériaux g-C_3N_4/C sont photocatalytiquement actifs pour la production de H_2, mais ils nécessitent encore une optimisation, en particulier en ce qui concerne leur teneur en carbone.

La réactivité de g-C_3N_4/C à l'oxygène a été étudiée. En raison de la stabilité/réactivité thermique différente de la partie g-C_3N_4 et de la partie carbonée, de nouveaux matériaux carbonés à grande surface spécifique et riche en carbone ont été obtenus. Le procédé, basé sur l'utilisation de g-C_3N_4 comme agent porogène apparaît comme une nouvelle façon de produire des matériaux en carbone poreux riches en azote.

Un niveau élevé de dopage au fluor a été incorporé au composé g-C_3N_4 en utilisant F_2 pur. Tous les échantillons fluorés obtenus ont montré des changements notables dans leur structure et leurs propriétés optiques et électroniques en comparaison avec les matériaux de départ. Cette modification chimique s'accompagne d'une amélioration de l'activité photocatalytique de la dégradation du colorant en phase aqueuse. La fluoration en phase gazeuse est un procédé très prometteur dans la préparation de composés fluorés ex-g-C_3N_4 par rapport aux méthodes hydrothermales conventionnelles.

APPENDIX 1: A list of original publications

- Arianit Gashi, Julien Parmentier, Philippe Fioux, Roman Marsalek, *'Tuning the C/N Ratio of C-rich Graphitic Carbon Nitride (g-C_3N_4) Materials by the Melamine/Carboxylic Acid Adduct Route'* doi.org/10.1002/chem.202103605, Chemistry-A European Journal, February 2022

APPENDIX 2: A LIST OF PRESENTATIONS

- **Preparation and characterization of g-C_3N_4**

  Arianit Gashi, Roman Marsalek (ICASS 3rd International Conference on Applied Surface Science Pisa, Italy 17-20 June 2019)

- **Adsorption of heavy metal ions onto g-C_3N_4**

  Roman Marsalek, Arianit Gashi (Presentation 3rd International Conference on Applied Surface Science Pisa, Italy 17-20 June 2019)

- **Synthesis and Characerization of C-rich-g-C_3N_4 materials from the melamine/carboxylic acid adduct route**

  Arianit Gashi (Conference YSD Journée des jeunes scientifiques UHA, Mulhouse, France)

APPENDIX 3: ORIGINAL PUBLICATIONS TITLE

´´Tuning the C/N Ratio of C-rich Graphitic Carbon Nitride (g-C_3N_4) Materials by the Melamine/Carboxylic Acid Adduct Route´´

Chemistry–A European Journal
Research Article
doi.org/10.1002/chem.202103605
Chemistry Europe
European Chemical Societies Publishing
www.chemeurj.org

Tuning the C/N Ratio of C-Rich Graphitic Carbon Nitride (g-C_3N_4) Materials by the Melamine/Carboxylic Acid Adduct Route

Arianit Gashi,[a, b] Julien Parmentier,*[b] Philippe Fioux,[b] and Roman Marsalek*[a]

Abstract: C-rich graphitic carbonitride materials (CN_x) with a large range of compositions have been prepared thanks to the self-assembly, in different ratios, of melamine (M) and a panel of polycarboxylic acids (A) such as oxalic, tartaric and citric acid. The thermal conversion of the formed adducts (MA_y), led to CN_x phases, with x ranging from 0.66 to 1.4 (x = 1.33 for g-C_3N_4 for comparison). The properties of these materials were examined by different techniques (XRD, Raman spectroscopy, TEM, TGA, XPS and DRIFT). It appears that the increase in the C content is associated with the disappearance of the long-range order of heptazine units and an increase in the sub-nanometer carbon-rich cluster size within the graphitic g-C_3N_4 structure. This trend is followed by a significant increase in the interlayer spacing and a lower proportion of N=C–N bonds compared to C=C bonds. The thermal stability under an inert atmosphere of these phases and their UV-Visible absorbance properties were also investigated.

Introduction

Layered materials in the N/C composition range from graphitic carbon (g-C) to graphitic carbonitride (g-C_3N_4). Although both composition ends are denoted as "graphitic", they display different structures and properties.[1] Briefly, g-C_3N_4 is composed of condensed π-conjugated six-membered rings of triazine or tri-s-triazine (s-heptazine, C_6N_7) units bonded together with the so-called nitrogen bridges which give a two-dimensional structure with planar layers like in graphite.[2] This compound is a yellow semiconductor materials with promising applications as metal-free photocatalyst[3] (although it suffers from high recombination of holes and electrons[4] in the latter case) and as part of Na-ion batteries electrode materials.[5] It is the most stable allotrope among C_3N_4 phases at standard conditions[6] but it has a low thermal stability, even in inert atmosphere (500–700 °C), compared to carbon. Graphitic carbon is formed of sp^2 carbon atoms arranged to condensed six-membered rings. Its π-orbitals are responsible for many properties[7] such as a high electronic conductivity which yield numerous applications such as electrode in Li-ion batteries. It displays a high thermal stability in inert atmosphere. In-between g-C and g-C_3N_4, a large range of composition exist either as a doped phase (C-doped g-C_3N_4 and N-doped g-C) or as N-rich g-C and as C-rich C_3N_4. The resulting compounds display modified properties compared to the pristine phases with interesting new functionalities and potential applications. For instance, doping of N into graphitic type carbon yields to new properties such as metal-free electrocatalysis[8] or enhanced performances in supercapacitor.[9] On the other hand, addition of C into g-C_3N_4 structure has shown to improve the photocatalytic properties by either shifting the absorption range from UV to the visible range and by limiting the recombination of electron-hole pairs. It is proposed that carbon doping of g-C_3N_4 structure allows the formation of a large number of delocalized π bonds with a change of the electronic structure and an increase in visible light absorption.[10] The N content in the C–N system is strongly determined by the thermal stability of N-containing moieties in respect to carbon.[11,12] Depending on the temperature and the precursor used, the three main type of N doping observed in g-C structure are pyrrolic N, pyridinic N and graphitic N.[13] With the increase of the temperature, the nitrogen content is reduced and the first two groups tend to decompose in profit of the most stable graphic N.

Interestingly, nanocomposites combining carbonitride and carbonaceous phase display a higher electronic conductivity which enhance the performance compared to pristine g-C_3N_4 either in photocatalysis[14] through a longer exciton life-time, or in electrochemical energy storage (Na-ion storage batteries). Moreover, controlled gradient of composition between these two phases have shown to improved further the photocatalytic activity of the nanocomposite.[15] Those properties are strongly dependent on the interface between those two phases.

Based on the potential applications of graphitic structure with C and N atoms and especially for those having a C-rich g-C_3N_4 composition, it appears interesting to control the C/N ratio of the graphitic phase over a large range of composition and to evidence how the C atoms are distributed within the structure

[a] A. Gashi, Dr. R. Marsalek
Department of Chemistry
University of Ostrava
30. Dubna 22, Ostrava, 701 03 (Czech Republic)
E-mail: roman.marsalek@osu.cz

[b] A. Gashi, Dr. J. Parmentier, Dr. P. Fioux
Institut de Science des Matériaux de Mulhouse (IS2 M),
Université de Strasbourg, Université de Haute-Alsace
15 rue Jean Starcky, BP 2488, 68057 Mulhouse Cedex (France)
E-mail: julien.parmentier@uha.fr

Supporting information for this article is available on the WWW under https://doi.org/10.1002/chem.202103605

especially when starting from homogeneous precursors having an atomic distribution of C and N atoms. For that purpose, different synthesis routes have been developed in the literature based on precursors containing C and N with different C/N ratio. CN_x compounds with high N content are obtained by the carbonization of N-rich precursors such as melamine, dicyanamide and urea.[16] Addition of C precursors (e.g., glucose,[17] polyaniline,[18] cellulose, agricultural products, etc.) to those N-rich precursors yield to C-rich g-C_3N_4 compounds. It was shown after carbonization of glucose and melamine mixture that the resulting C_3N_4 structure contains C-ring nanodomains with enhanced photocatalytic properties for water splitting compared to raw g-C_3N_4.[19] However, these "physical mixture" processes lacked to finely tune the properties of these materials by controlling their precursors at the molecular level. Thus, good and original synthesis for materials with optimized and tailored properties were developed through the formation of supramolecular self-assembled of C and N precursors. These products, also called adducts, are formed by the recognition and binding of complementary subunits thanks to hydrogen bonds and noncovalent interactions (e.g., π interaction).[20] Molecular crystals are then obtained. In this context, a wide variety of materials with different dimensionalities, ranging from 1D to 3D, were formed.[21] Melamine (M) is an interesting subunit as a g-C_3N_4 precursor since it has a strong ability to be involve to the formation of supramolecular self-assembled compound through recognition process. For instance, melamine associated with cyanuric acid,[22] barbituric acid[23] have been largely investigated. More recently, adducts based on melamine and carboxylic acids have also been studied. With melamine and benzoic acid,[24] or oxalic acid,[25] adducts were formed through hydrogen bonding (N–H···O and/or N–H···N), ionic interactions (according to the pH) and π–π interactions (if present)[26] as schematized in Figure 1.

Based on this self-assembled precursor type, Li et al. prepared for the first time g-C_3N_4 sticky nanotubes using melamine-ammonium oxalate complex.[27] This process leads to the formation of porous g-C_3N_4 nanotubes (PCN) within carbon

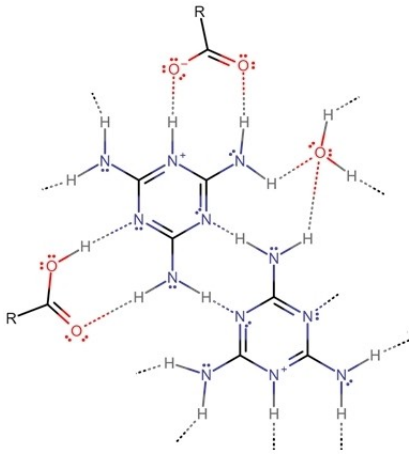

Figure 1. Schematic representation of attractive interactions in melamine-carboxylic acid self-assembled compounds

in the structure. More recently, X. Fang et al. were also able to prepare co-crystals between terephthalic acid (TPA) and melamine (M), through hydrogen-bonding functional groups –COOH from (TPA) and $-NH_2$ from (M) which led the preparation of C-rich g-C_3N_4.[28] This homogeneous distribution of C-rich (TPA) and N-rich molecules (M) within the crystalline adduct is supposed to lead to a homogeneous distribution of C and N species at the nanometer/atomic scale within the g-C_3N_4 structure. Nevertheless, this adduct approach was never systematically investigated in the melamine—carboxylic acid system in order to tune the C/N ratio of carbonitride—type phase over a large range of composition and with potential formation of nanocomposite materials. For that purpose, different carboxylic acids, denoted A (for oxalic acid (OA), citric acid (CA) and tartaric acid (TA)), having different carbon chain lengths were used in presence of melamine to yield different adducts labeled as MAX/1(z) with M for melamine, A for the acid, X/1 for the molar ratio M/A and z for the number given to the crystal phase (1 or 2). These phases where used as precursors of C-rich C_3N_4 phases having different C/N ratios. This route, which does not require organic solvent or hydrothermal step, appears as a simple way to tune the C/N ratio of the CN_x carbonized materials by selecting either the nature of the carboxylic acid and/or the melamine/carboxylic acid ratio.

Results and Discussion

Evidence of adducts formation

As shown on X-ray diffraction (XRD) patterns (Figure 2), the mixture of M with the carboxylic acids leads to new crystalline phases called adducts. The latter depend on the nature of the carboxylic acid A and the ratio X/1. Interestingly, for each of the two ratios X/1 tested, a particular crystalline phase was obtained and denoted MAX/1(z) with $z=1$ or 2. In some cases, due to the cooling step of the precipitation solution used to increase the yield of these adducts, presence of M was detected. A list of the XRD peaks of these adducts and their position are reported in (Table S2 in the Supporting Information). Interestingly, peaks of $MO3/1_{(1)}$ and $MO6/1_{(2)}$ phases (samples with melamine-oxalic acid adduct obtained with 3/1 and 6/1 molar ratios) do not corresponds to the phases reported by Han et al.[25] These authors reported that the obtained phase displays the two most intense peaks at 2θ circa 18° and 27° for $Cu_{K\alpha}$ radiation. As it is outside the scope of this study, the crystal structure of the adduct was not determined.

Another evidence of adducts formation is their singular crystal shape compared those of the M and A precursors as observed by SEM micrographs (Figure 3). The typical irregular granular shape of the precursors is not more encountered for the MAX/1(z) samples which display a typical regular needle-like shape for MTX/1 with $X=2.5$ and 6.0 (Figure 3d and e) and a lamellar-like shape for MCX/1 morphology for $X=1.5$ and 6.0 (Figure 3f and g).

These different characterizations have evidenced the formation of adducts. Indeed, they all shown that the phases

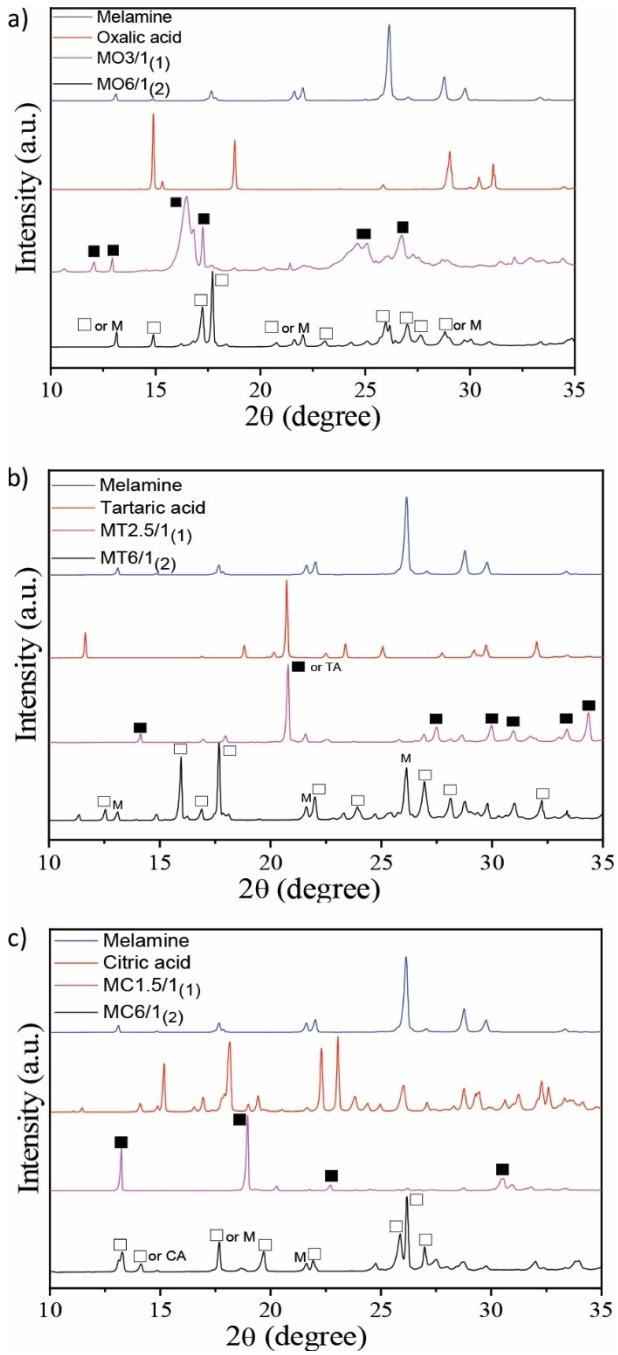

Figure 2. XRD patterns of the M and A precursors and their corresponding adducts obtained with two different M/A molar ratios: a) melamine, oxalic acid, $MO3/1_{(1)}$, $MO6/1_{(2)}$; b) melamine, tartaric acid, $MT2.5/1_{(1)}$, $MT6/1_{(2)}$; c) melamine, citric acid, $MC1.5/1_{(1)}$, $MC6/1_{(2)}$. The ■ and □ indicate the main peaks of $MA/X_{(1)}$ and $MA/X_{(2)}$ adduct crystalline phases, respectively; M: melamine, O: oxalic acid; T: tartaric acid; C: citric acid.

obtained are not a physical mixture of M and A (even if impurities of M could be detected for some samples) since adducts showed:, a particular XRD pattern (Figure 2), a single phase morphology (SEM observation in Figure 3), a peculiar infra-red (IR) spectrum compared to melamine (see the range 3000–3500 cm^{-1} in Figure 4) and a typical thermal degradation (Figure 5, below).

To determine the chemical composition of adducts, elemental analysis was carried out and results are reported in Table 1. Melamine and polycarboxylic acid compositions were compared with those of adducts. For each acid considered, the as-synthesized adducts show a nitrogen content following the molar ratios M/A of the starting precursors. As expected, the oxygen content follows the opposite trend due to the presence of carboxylic acid groups and hydroxyl (if any) possibly associated with water crystallization molecules. Based on these data, calculated M/A ratio of adducts could be determined considering that nitrogen is related to the melamine content and carbon arises from acid and melamine. These ratios may differ from the starting M/A ratios and are (close to) integer values as expected for adducts. Discrepancy compared to integer values could be due to the impurities observed by XRD therefore caution should be taken regarding these ratios which could not always correspond to the real M/A ratios of the adducts.

To confirm further the evidence of adducts formation, diffuse-reflectance infrared Fourier transform spectroscopy (DRIFT) was carried out on these new phases and compared to the pure precursors M and A (Figure 4). For the M precursor, all the observed peaks are in agreement with the data of the literature. Two main broad peaks at 3122 and 3326 cm^{-1}, related with NH_2 symmetrical vibration modes, appear. Two sharp bands at 3419 and 3472 cm^{-1} show asymmetrical –NH_2 stretching,[29] while bands at 808 and 1020 cm^{-1} corresponds to triazine deformation modes.[30] The typical signatures of carboxylic acid groups were observed with the C=O stretching (1720 cm^{-1}) and C–O stretching (region 1105 and 1200 cm^{-1}). Since acid–base reaction is expected in the mixture of the precursors, partial protonation of amine and deprotonation of carboxylic acid groups may occur. This behavior has been observed in the melamine–benzoic acid system[24] where attractive interactions (ionic interaction, H-bond and van der Waals) between reactants (melamine, melaminium, carboxylic and carboxylate) and together with water bridging molecules were encountered. Similar interactions may be present within adducts. Indeed, the presence of two broad bands at 3102 and 3335 cm^{-1}, shifted compared to melamine, could correspond to the stretching of N–H···O bond of protonated melamine as observed in the melaminium chloride structure.[31] A small shift

Table 1. Elemental composition (CHNO analysis) of melamine, TA, CA and adducts for two molar ratios and corresponding calculated M/A ratio (based on C and N compositions).

Name of sample	C [wt %]	N [wt %]	O [wt %]	H [wt %]	Calcd M/A ratio of the sample
Melamine	28.5	66.63	–	4.80	–
TA	32.01	–	63.96	4.03	–
CA	37.51	–	58.29	4.19	–
MT2.5/1	27.5	39.09	28.77	4.64	2.1/1.0
MT6/1	28.03	53.27	14.12	4.55	5.9/1.0
MC1.5/1	31.56	37.65	26.48	4.28	2.1/1.0
MC4/1	30.45	42.57	22.26	4.62	3.0/1.0

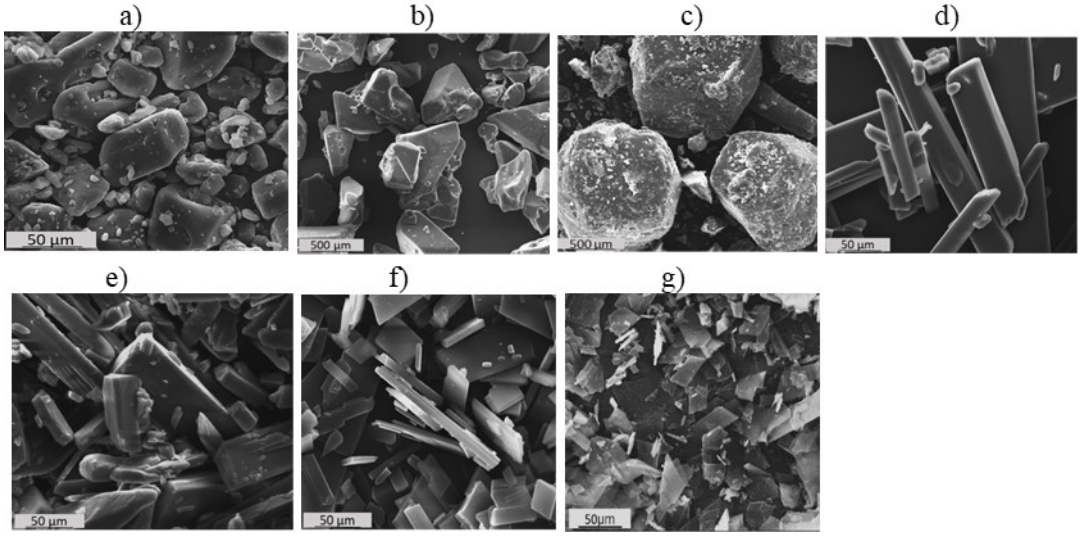

Figure 3. SEM micrographs of a) melamine, b) tartaric acid, c) citric acid and the as-synthesized adducts with two different molar ratios d) MT2.5/1$_{(1)}$, e) MT6/1$_{(2)}$, f) MC1.5/1$_{(1)}$ and g) MC6/1$_{(2)}$.

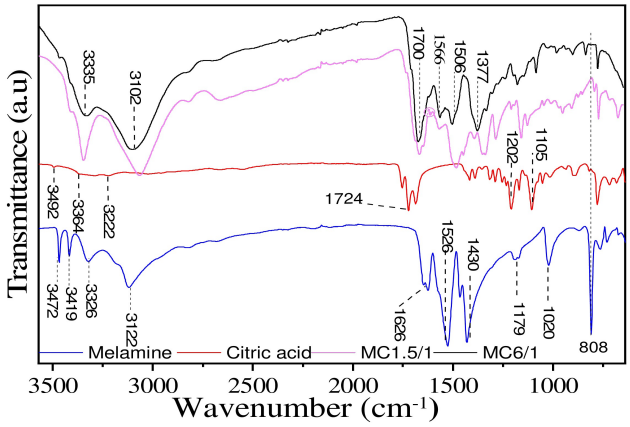

Figure 4. DRIFT spectra and characteristics vibrational peaks of melamine, citric acid and adducts (MC1.5/1 and MC6/1)

of this absorption bands between the two M/A molar ratio can also be observed in agreement with the two different composition of the adduct phases. The typical bands of carboxylic acids expected in the range 1400–1600 cm^{-1} are almost no more observed in the adducts. It indicates the formation of carboxylate groups. Band intensities region from 1377 to 1700 cm^{-1} are related with C=N and C–N stretching vibration of melamine ring; they appear also in the adduct. Moreover, the peak associated with out-of-plane bending of triazine at 808 cm^{-1} for melamine, has disappeared in the adduct as observed for protonated melamine.[32] All adducts DRIFT spectra are shown in (Figure S2), showing a similar trend with the other acids used.

To follow the thermal transformation of precursors and adducts during the heating process, thermogravimetric and differential thermal analysis (TG-DTA) were carried out in argon flow (Figure 5). For pure acids, thermal decompositions are endothermic (Figure 5a) and occur in a single step or in two steps for the dihydrated oxalic acid owing to an additional dehydration step. In all cases, the decomposition is nearly complete between 200–285 °C, a small part of carbon (2%) remaining at 1000 °C for only TA and CA acids. Melamine shows different thermal behavior compared to the acids. Its endothermic decomposition temperature is observed starting at 295 °C up to 365 °C. The mass loss is more pronounced in this interval and is followed by a sharp decomposition peak (Figure 5b) due to deamination.[33] With the increase of the temperature, g-C_3N_4 is progressively formed in the range 400–500 °C and it is then completely decomposed at 750 °C. Adducts behave differently compared to their precursors (Figure 5c). To see more precisely adduct's endothermic behavior of decomposition, DTA (Figure 5d) and DTG were plotted (Figure S3). All adducts display four decomposition steps in the temperature range 110–155, 225–314, 322–357 and 683–715 °C (DTG data) in agreement with the four observed endothermic peaks. In the low temperature region (from 100 up to ca. 350 °C), the steps are attributed respectively to the dehydration of the adduct and the acid decomposition followed by the deamination of the melamine. The third step occurs at a lower temperature compared to pure melamine giving another evidence of the formation of adducts and that the analyzed products are not just a physical mixture of the reactants. The last step occurs in the high temperature region (>650 °C) where thermal decomposition products are either completely decomposed (MO4/1 adduct) or partly decomposed with a carbon yield close to 5% at 1000 °C (MT4/1 and MC4/1 adducts). This low thermal stability of MO4/1 at high temperature was already observed for a similar adduct type made with melamine and oxalic acid and for pure melamine decomposition product. It suggests that the MO adducts decomposition product behaves almost like the g-C_3N_4 regarding melamine decomposition. Interestingly, another thermal behavior is observed for the MT4/1 and MC4/1 adducts. They

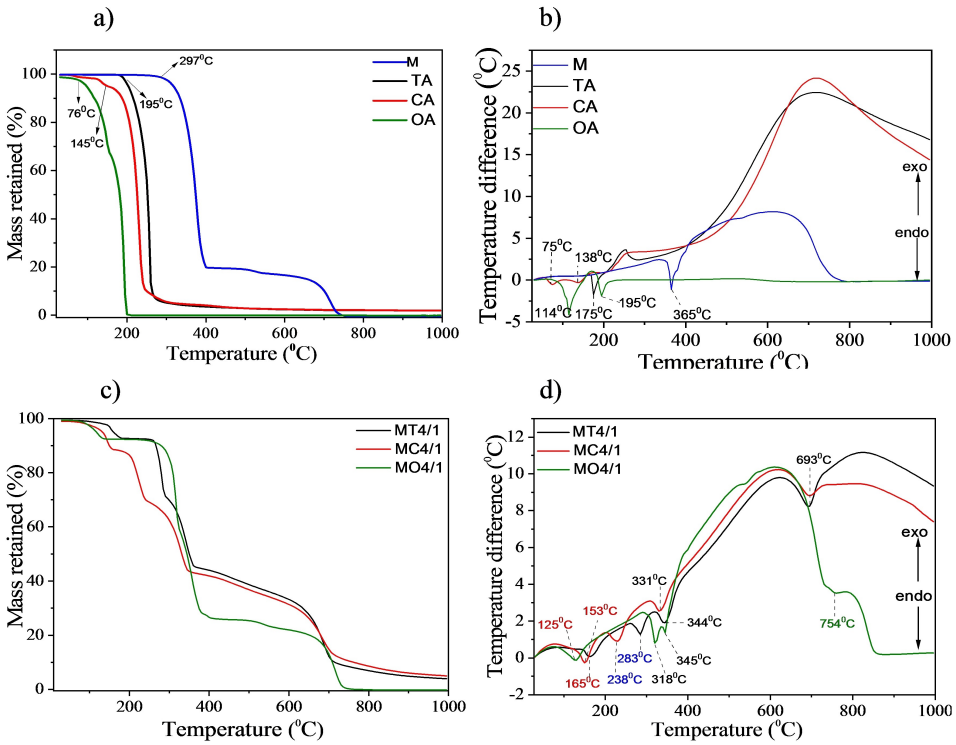

Figure 5. TG and DTA of precursors (top) and of the adducts (bottom) under nitrogen flow (heating rate 10 °C min^{-1}).

lead to more stable decomposition products at high temperature (yield close to 5 wt.%).

Physicochemical characterizations of C-rich C_3N_4

Chemical analyses of the calcined samples were investigated by elemental analysis (EA) and X-ray photoelectron spectroscopy (XPS). As these techniques give indication about respectively the bulk and the surface composition, any discrepancy can be observed but the evolution of the N/C ratios follows roughly the M/A ratio used to prepare the adducts (Table 2). Pure g-C_3N_4 is supposed to have theoretically 60.9 wt.% of N and 39.1 wt.% of C. The reference material g-C_3N_4, displays a slightly different composition since it was prepared in air (presence of oxygen) and at a temperature where its decomposition has started. The other samples, prepared at the same temperature but in an inert atmosphere have lower nitrogen content and a higher C content compared to the reference. Values ranging from 38 to 57 wt.% were observed for the N content whereas carbon content lies between 38 to 49 wt.% meaning that the samples can be considered as C-rich C_3N_4 materials as confirmed later. Interestingly, relatively high oxygen content is detected with values ranging from 6 to 10 wt. %. It is proposed that this oxygen arises from the acids carboxyl and hydroxy groups of the adduct precursors.

High-resolution XPS measurements of C-rich C_3N_4 and g-C_3N_4 samples were also performed. For the g-C_3N_4 reference (see XPS spectra in Figure S4), two contributions are observed on the C1s high resolution spectra: 1) N–C=N at 288.4 eV typical of triazine and; 2) C or H species bonded to C (C=C, C–C, and CH_x) at 285.0 eV. The latter species, not expected in g-C_3N_4, were attributed to "adventitious" carbon atoms which were gradually deposited on the surface of the material in the XPS

Table 2. Chemical composition [wt.%] of the samples obtained from elemental (EA) and XPS analysis with carbonization yields [wt.%].

Name of sample	C EA	C XPS	N EA	N XPS	O EA	O XPS	H EA	N/C XPS	Yield [%]
g-C_3N_4-550(air)	34.33	40.44	62.60	57.28	2.46	2.28	1.61	1.61	26
MO3/1- 550	34.82	n.p.	56.99	n.p.	6.67	n.p.	1.94	1.42	40
MC1.5/1-550	49.23	55.96	38.12	40.28	11.14	3.76	1.48	0.66	29
MT2.5/1-550	46.26	50.40	41.88	45.04	10.13	4.56	1.22	0.77	26
MT6/1-550	42.29	41.33	46.18	57.53	10.43	1.13	1.37	0.93	35
MC4/1-550	43.70	n.p.	44.65	n.p.	9.78	n.p.	1.57	0.87	32
MC6/1-550	38.99	51.60	51.42	44.53	7.69	3.87	1.75	1.13	38

n.p.: not performed.

chamber due to C-based gaseous pollutants.[34] For the C-rich C_3N_4 samples, measurements were more difficult to record compared to the one of g-C_3N_4, owing probably to the presence of nested carbon-rich clusters or nanodomains having different electrical conductivity from their g-C_3N_4 environment. It required, for charge compensation, the use of an electron flood gun which led to variable peak profiles and positions according to the voltage applied. As a result, the flood was adjusted for the C1s analysis, in order i) to obtain a profile of the C1s peak as fine as possible and ii) that the contribution of the lowest energy was attributed for each sample to C–C, C=C and CH_x bonds at 285 eV (assuming that the sample contains similar species in different ratio). No quantitative analysis was extracted from these spectra. Thus, we have followed only the evolution of the main contributions for selected samples (Figure 6). The signal at 285 eV was attributed to carbon-rich clusters or nanodomains originating from the carbonaceous skeleton of the adducts carboxylic groups. Its contribution clearly increases with the C content of the selected samples from 42 wt.% for MT6/1-550 to 46 and 49 wt.% for respectively MT2.5/1-500 and MC1.5/1-500 samples. Meanwhile, the contribution of N–N=N species decreases. From these findings, it is clear that beside the presence of g-C_3N_4 domains, a higher portion of carbon–carbon bonds is observed with a higher carbon content, presumably in the form of C=C bonds as suggested latter by Raman spectroscopy with the appearance of D and G bands characteristic of graphitic-type carbon.

N1s spectra of MT6/1-550, MT2.5/1-550 and MC1.5/1-550 samples display three main contributions, centered at the binding energy of 399.08 eV (corresponding to sp^2-hybridized pyridinic-N species in triazine rings (C–N=C), 400.6 eV (tertiary nitrogen N-$(C)_3$ groups) and 401.7 eV (terminal amino groups (C–N–H; Figure 7). A clear evolution of these populations can be observed with the increasing carbon content: the C–N=C population decreases while the N–$(C)_3$ and N–C amine increase (Table 3).

The g-C_3N_4 and C-rich C_3N_4 samples were analyzed by DRIFT spectroscopy as shown in (Figure 8). The spectra of the g-C_3N_4 reference displays typical and well-resolved absorption bands,

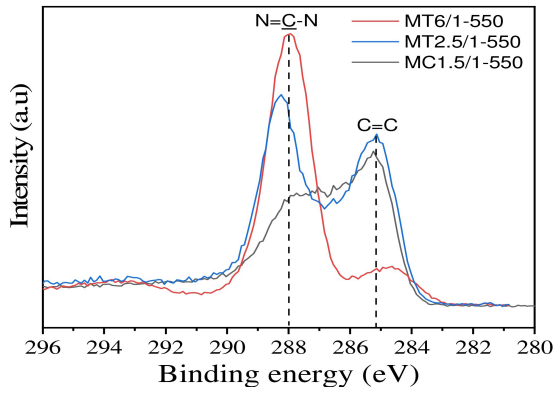

Figure 6. High-resolution XPS C1s spectra of MT6/1-550, MT2.5/1-550 and MC1.5/1-550 samples showing the evolution of N–C=N and (C=C, C–C and C–H) contributions with variation of the carbon content

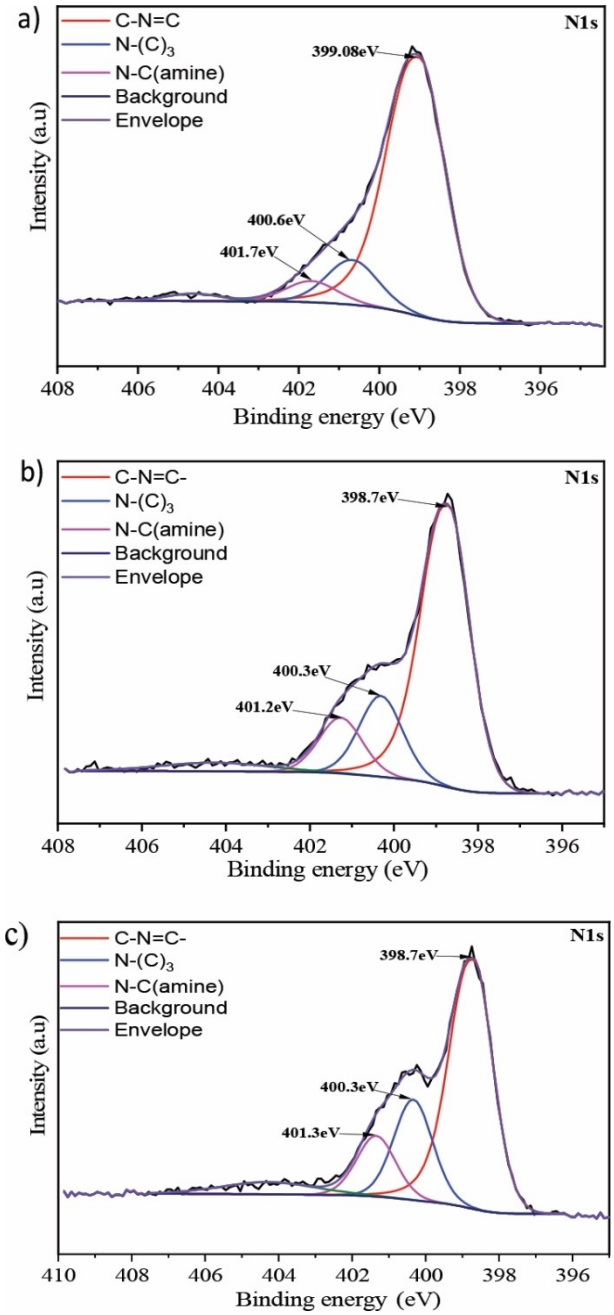

Figure 7. High-resolution XPS N1s spectra of a) MT6/1-550, b) MT2.5/1, and c) MC1.5/1-550 samples.

as reported in the literature, at the opposite of those of C-rich g-C_3N_4 samples (e.g., MT4/1-550 and MC4/1-550) which have poorly resolved bands as encounter usually for poorly ordered carbon-based materials. All selected samples displays a band at 807 cm^{-1} which is attributed to the breathing mode of the triazine ring.[35] A similar trend is observed for the other peaks of the g-C_3N_4, 1319 cm^{-1} and 1562 cm^{-1} correspond to the C–N and C=N stretching mode of aromatics, whereas the peak at 1417 cm^{-1} corresponds to tertiary N[36] also revealed by XPS. A broad absorption band around 3200 cm^{-1} presents in all spectra and a second band around 3600 cm^{-1} detected mainly for C-

Table 3. Nitrogen bonding compositions and peak-ratio area of C-rich C_3N_4 and g-C_3N_4 samples with variation in molar ratio.

Sample	N–$(C)_3$ Peak ratio [%]	Position [eV]	C–N=C Peak ratio [%]	Position [eV]	N–C(amine) Peak ratio [%]	Position [eV]
g-C_3N_4-550(air)	12	400.3	73	398.9	10	401.4
MC1.5/1-550	21	400.3	60	398.7	13	401.3
MC6/1-550	12	400.5	74	398.8	10	401.5
MT2.5/1-550	17	400.3	67	398.7	11	401.2
MT6/1-550	12	400.6	80	399.0	6	401.6

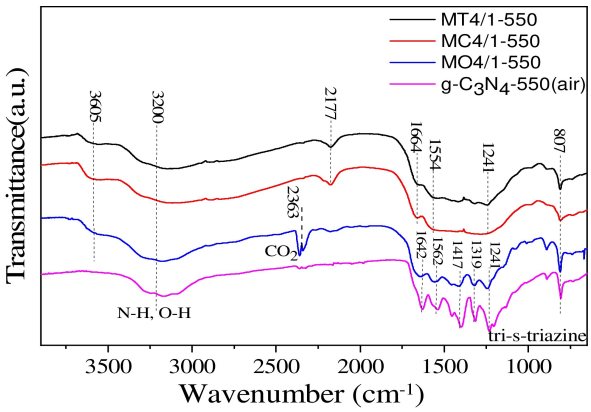

Figure 8. FTIR spectra of g-C_3N_4-550(air), MT4/1-550, MC4/1-550, MO4/1-550.

rich C_3N_4 materials could be related to the stretching vibration mode of N–H and surface-adsorbed water molecules O–H[37,38] in g-C_3N_4 domains and/or C-rich clusters as evidenced latter by Raman spectroscopy.

A small band at around 2177 cm^{-1} is detected for the C-rich materials; it could be attributed to nitrile species.[39] It is presumed that these groups are yielded through the thermal decomposition process of amides, formed previously by reaction between melamine amine groups and carboxylic acids. These amide groups could follow successive degradation steps. and lead to nitrile species.[40] This hypothesis is strengthened by the fact that thermal degradation of nitriles yields HCN species,[41] as observed by TG-MS (results not reported). Absorption band at 2363 cm^{-1} for the MO4/1-550 sample is related to fluctuation of the CO_2 amount inside the spectrometer during measurements.[41]

Raman spectra of the samples MC1.5/1-550, MC6/1-550, MT2.5/1-550, MT6/1-550, MC4/1-550 (black color) and MO4/1-550 (brownish color) are shown in (Figure 9a and b). The use of two different excitation wavelengths (488 and 532 nm) was necessary to overcome luminescence phenomena which yield poorly resolved spectra for some samples. In some cases, this problem could not be overcome and therefore spectra of g-C_3N_4 (reference), MO4/1-550 and MT6/1-550 (beige color) samples were then not presented for all wavelengths. For an excitation wavelength of 488 nm (Figure 9a), only the black samples display the two typical D and G bands of graphitic-type carbon at respectively 1371 and 1566 cm^{-1}. Even if caution should be taken due to a luminescence phenomena, the intensity ratio of D and G bands ($R = I_D/I_G$) follows a clear decrease with the carbon content as shown by the sequence: R (MC1.5/1-550) = 3.6 > R (MT2.5/1-550) = 3.3 > R (MC6/1-550) = 1.5 for respectively 49, 46 and 38 wt. % of C (Table 2). This feature fits well with I_D/I_G ratio evolution observed for disordered carbon having for instance very low coherence length (L_a) in the in-plane graphitic structure, typically below 2 nm. In that size range, the intensity ratio is proportional to L_a^2 (i.e., the carbon cluster area) and follows the degree of ordering of the carbon structure. Indeed, in this case, the D mode intensity is related to the probability of finding a sixfold C ring and this probability decreases with the loss of ordering (and the L_a size) owing to the formation of C chains, sp^3 species or other type of rings. At the opposite, the intensity of the G mode, related to the motion of C sp^2 atoms, is considered as relatively constant in this range whatever the disorder.[42] Hence, in our case, with the decrease of the carbon content in the carbonitride samples, a lower probability to form sixfold C rings is expected, resulting in a decrease of I_D/I_G ratio. This trend is

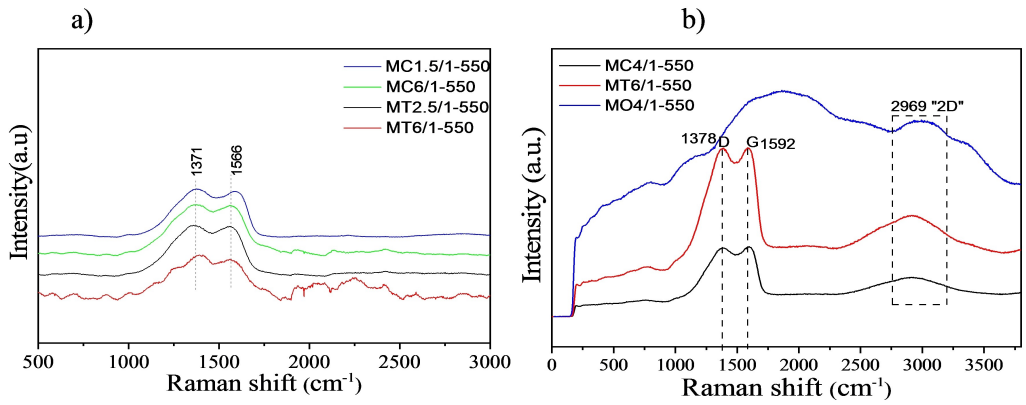

Figure 9. Raman spectra of carbonized samples recorded with an excitation at a) 488 and b) 532 nm.

supported by the absence of second order bands such as the 2D bands observed usually around 2750 cm^{-1} and which is replaced by a bump for highly disordered carbon in the range 2400–3100 cm^{-1}.

Usually a decrease in the G band position with amorphization of the graphitic structure from 1580 (graphite) down to 1510 cm^{-1} (amorphous carbon) is expected for carbon materials. This feature is not encountered for the studied samples. Indeed, values ranging from 1580 to 1602 cm^{-1} were observed at different wavelengths for the G band. It suggests a high presence of sp^2 carbon atoms arranged in six-membered rings, probably as clusters within the g-C_3N_4 structure. In Figure 9b is shown the Raman spectrum of MC4/1-550, MO4/1-550 and MT6/1-550 samples recorded with an excitation wavelength of 532 nm. A clear difference could be observed between the MO4/1-550 sample, having a composition close to g-C_3N_4, and the two other samples which are more carbon rich. The former did not display any strong absorbance bands as expected for disordered g-C_3N_4-550 prepared in air. For the latter samples, beside the typical D and G bands, a hump in the region between 2600–3000 cm^{-1} is observed as for very disordered carbon materials.[43]

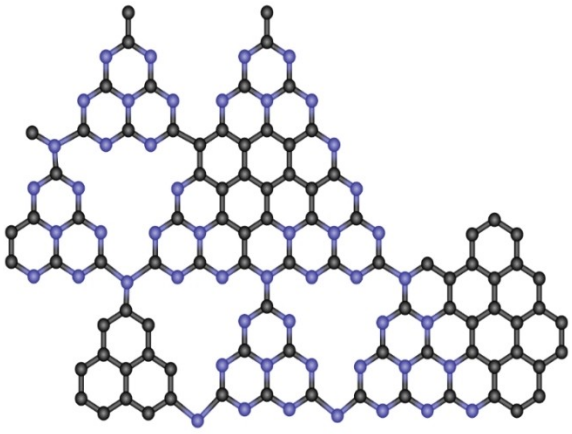

Figure 10. Hypothetical representation of the C-rich C_3N_4 heterostructure with six-carbon-ring nanometer domains embedded within a g-C_3N_4 structure.

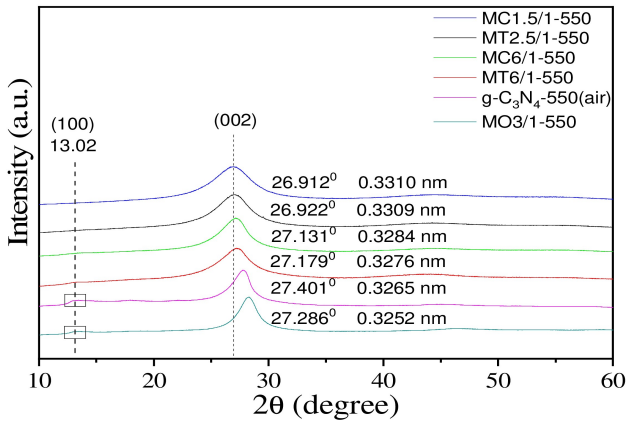

Figure 11. XRD patterns of MC1.5/1-550, MT2.5/1-550, MC6/1-550, MT6/1-550, g-C_3N_4-550(air), MC4/1-550, MO3/1-550

A hypothetical representation of the C-rich C_3N_4 nanostructure is reported in (Figure 10) with sixfold carbon ring nanometer domains, where the carbon domain are indicated in black.

The g-C_3N_4 and C-rich C_3N_4 materials were investigated by X-ray diffraction (XRD). XRD shows large diffraction peaks, typical of highly disordered crystalline materials with a hump at 13.10° (for g-C_3N_4 and MO3/1-550 samples only), and a peak in a large range 26.9–27.4° (Figure 11). The hump corresponds to the (100) interplanar distance of g-C_3N_4 and is typical of the in-plane structural packing motif of heptazine units as described in the literature.[44] The peak around 27° is attributed to (002) planes present in both crystalline graphitic carbonitride (g-C_3N_4) and graphite C structures and corresponds to interlayer stacking distances. Compared to perfect crystalline structures of g-C_3N_4 with d_{002} = 0.3246 nm and graphite C d_{002} = 0.336 nm,[45] the observed d_{002} values lie in this range. Moreover, it is well known that these values are higher when disorder is present in the lamellar structure,[46] (e.g., treatment above the decomposition temperature of g-C_3N_4 in oxidation or inert atmosphere, presence of heteroatoms and activation of graphitic carbon). Among the two samples exhibiting the heptazine structure, the MO3/1-550 sample shows the lowest d_{002} value (d_{002} = 0.3252 nm) slightly above to the value of perfect g-C_3N_4 followed by the reference g-C_3N_4 sample prepared in air (d_{002} = 0.3265 nm). It indicates that both samples, having yellow-beige color and prepared at the same temperature, have a slightly disorder structure, close to perfect g-C_3N_4, but with more defects when heat-treatment was performed in air. For the other samples, the d_{002} spacing follows the sequence MO3/1-550 < g-C_3N_4-550air < MT6/1-550 < MC6/1-550 < MT2.5/1-550 < MC1.5/1-550, which is nicely correlated to the carbon content of the sample (Table. 2). This trend indicates that the increase of the carbon content in the lamellar structure significantly increases the interlayer distance. The highest d_{002} value (0.331 nm) observed for MC1.5/1-550 sample having the highest carbon content is below the interlayer distance of graphite,[47] suggesting that all materials prepared have compositions ranging between crystalline g-C_3N_4 and graphite, so they can be considered as C-rich carbonitride phases. Thus, the absence of peak at around 13° for these samples could be attributed to the introduction of C as a heteroatom within the lamellar structure of g-C_3N_4 with a breakdown of the long-range periodicity of the in-plane heptazine units. As the carbon content increases, a nanocomposite of g-C_3N_4 with carbon nanodomains could appear.

The nanostructure of the samples was analyzed by TEM. Materials like g-C_3N_4 and MO3/1-550, which have both a low thermal behavior, display a nanoporous structure with holes of a few tens of nm (Figure 12a and b). This nanostructure is not so evident for C-rich samples with a higher thermal stability (MC1.5/1-550 and MT2.5/1-550; Figure 12 c and d). High-resolution TEM was difficult to perform owing to the decomposition of the samples under the beam. The structuration of the materials does not lead to porous materials as evidence by

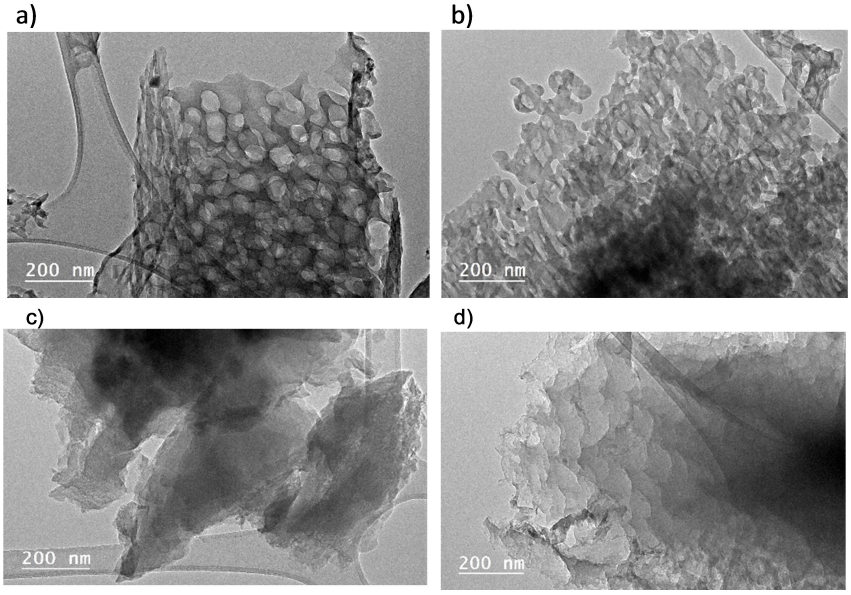

Figure 12. TEM images of a) g-C_3N_4-550(air), b) MO3/1-550, c) MC1.5/1-550, and d) MT2.5/1-550 samples.

the low surface area (13–26 m^2/g, BET model) revealed by N_2 adsorption at 77 K. EDX analysis coupled with STEM experiments showed a homogenous distribution of C and N at the sub-micrometer scale (Figure S5).

To investigate the thermal properties of the calcined samples, TG-DSC analysis under argon atmosphere was carried out. In agreement with the literature, the thermal stability of g-C_3N_4 in an inert atmosphere was limited with a decomposition onset at *circa* 630 °C and complete decomposition at 780 °C (Figure 13a). For C-rich C_3N_4 samples, interestingly, the temperature-decomposition onset occurs at lower temperatures than the g-C_3N_4 reference, around 534 °C and 630 °C for respectively MT4/1-550 and MC4/1-550 (Figure 13b). Surprisingly this behavior is associated with good high-temperature stability since these materials are still present with a yield of around 20 wt. % at 1000 °C. The MO4/1-550 sample lies in-between C-rich samples and g-C_3N_4 regarding nitrogen content (Cf Table 2) as its temperature decomposition onset of 650 °C. It appears that the introduction of extra carbon (and oxygen) atoms within the heptazine structure leads to its destabilization and to a lowered decomposition temperature. The resulting structure, probably enriched with carbon, is then more stable at high temperature. All materials exhibit an endothermic behavior during these decomposition steps (Figure 13c).

A large panel of colored samples were obtained, ranging from yellow (g-C_3N_4 -550 (air)) to black (C-rich C_3N_4 materials), via a brownish (MO3/1-550) and beige (MT6/1-550) color for materials containing a limited amount of extra carbon compared to g-C_3N_4.The diffusion reflectance (DRS) spectra of g-C_3N_4-550(a), MO4/1-550, MT6/1-550 and MC1.5/1-550 samples are reported in (Figure 14). The reflection band edge around 450 and 520 nm was observed for respectively g-C_3N_4-550(air) and MO4/1-550. This shift is related to the higher carbon content of the later sample which also shows a lower reflectance than the reference in the whole visible range. For even higher carbon content (MC1.5/1-550), the reflectance values are the lowest in the visible region whereas no significant differences were observed in the UV region. It was not possible to calculate the band gap energy E_g by the Kubelka–Munk theory[48] for the MT1.5/1-550 material. Indeed, if we consider that the material structure is composed of C-rich domains nested within disordered g-C_3N_4 structure, this structure could lead to ill-defined conductive and valence bands for each phase and therefore difficulties to isolate their individual contributions by the Kubelka–Munk theory. Therefore, calculation of the band gap was not performed as recommended in ref. [48]. While the possible band gap estimation was performed only for g-C_3N_4-550(a) and MO4/1-550 (Figure S6).

The potential photocatalytic properties of those raw C-rich C_3N_4 materials were investigated briefly with the water splitting reaction.

Previous studies, based on C_3N_4/C composites obtained by a carbonized mixture of carbon black[49] or graphene oxide[50] with melamine, have shown enhanced photocatalytic performances compared to g-C_3N_4, on H_2 production. It was related to the improved photogenerated electron–hole pairs separation owing to the increased electrical conductivity of the carbon part. In our case, the nanostructure of adduct-derived materials is presumably different since the carbon is introduced with the melamine as a precursor (acid) and not as a carbon-based material. The photocatalytic properties of the adduct-derived carbonitride samples were explored by the decomposition of methanol in aqueous media under deep UV irradiation. Hydrogen appears as the main product detected from the photocatalytic decomposition products. Its amount, evolved after 4 h of irradiation, is reported in (Figure 15) with results obtained for TiO_2 (P25 Evonik) and g-C_3N_4 for comparison. Although perform-

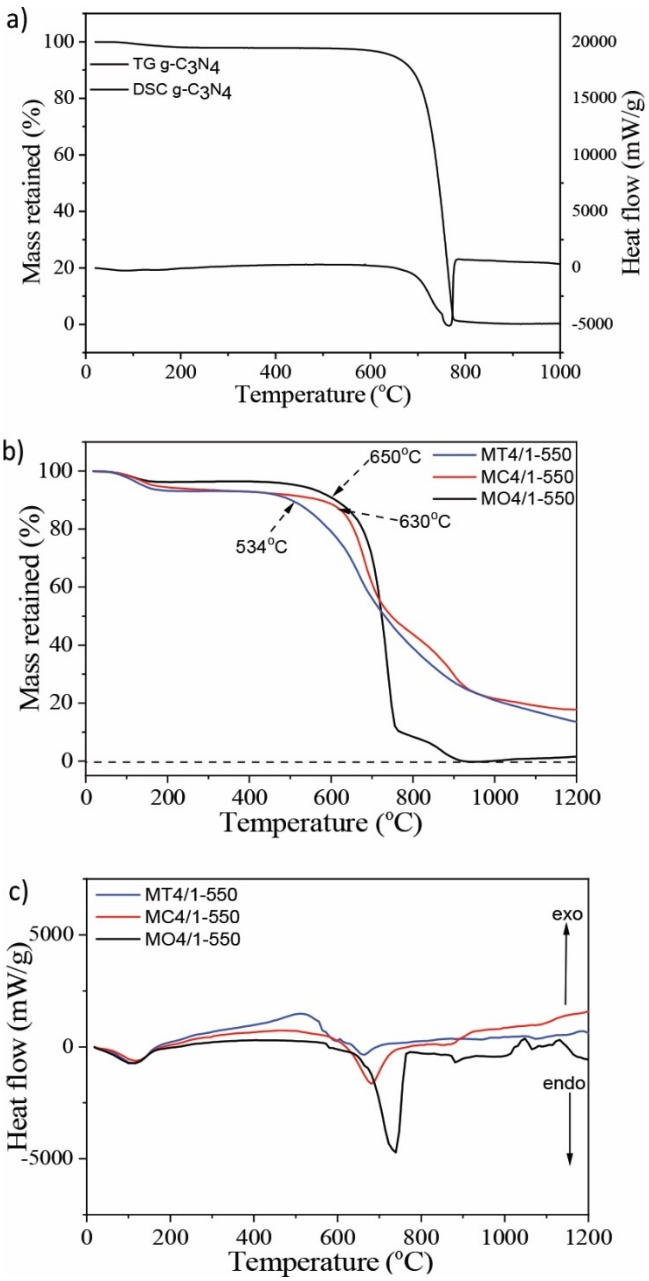

Figure 13. TG-DSC thermograms of a) g-C_3N_4-550(air) and b) TG thermograms, as well as c) DSC thermograms of MT4/1-550, MC4/1-550, and MO4/1-550 samples under nitrogen flow.

ance of the C-rich C_3N_4 material (MT6/1-550 sample) is lower than those of the well-known and optimized references, a photocatalytic behavior is evidenced and appears encouraging since there is probably room to enhance their properties for this application. It is also possible that the carbon content is too high and limits the light absorption of the carbonitride part compared to previous studies[50,51] where the N/C atomic ratio (determined by XPS) is in the range 1.19–1.35 whereas it is 0.93 and 1.61 for the studied samples.

The zeta potential of g-C_3N_4-550, MO3/1-550 MT2.5/1-550 and MC4/1-550 samples has been investigated versus pH

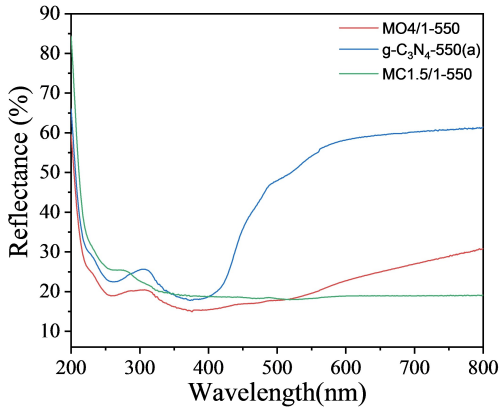

Figure 14. Reflectance spectra of g-C_3N_4-550(a), MO4/1-550, MC1.5/1-550 samples.

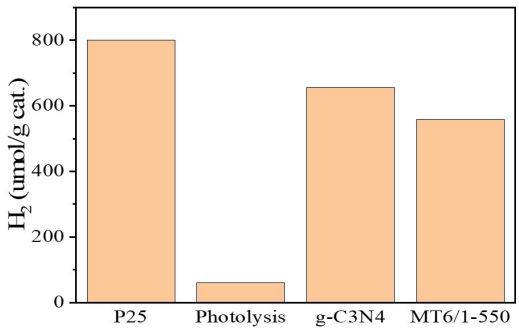

Figure 15. Amounts of H_2 to evolve after 4 h of photocatalytic decomposition of methanol in the presence of different photocatalysts at 254 nm (pen-ray lamp). Photolysis reported for comparison.

(Figure 16). It shows a typical shape, that is, increasing pH, the zeta potential values become more and more negative. The isoelectric point value for samples MO3/1-550 and MT2.5/1-550 is around pH 2, as well as for sample g-C_3N_4-550. An exception is the sample MC4/1-550 of which isoelectric point has the value 4. It is very important for applications that in the neutral range and more especially in the basic pH range, the zeta

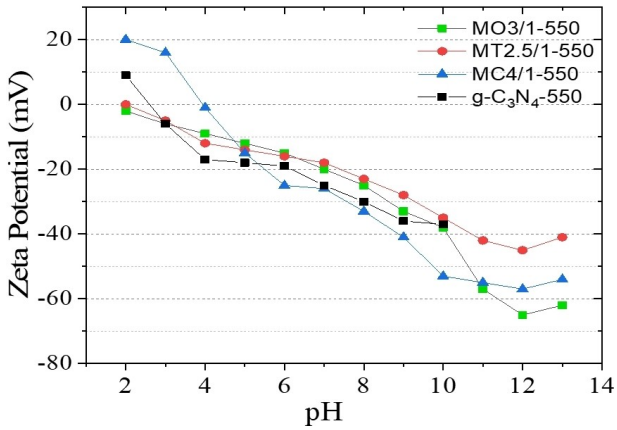

Figure 16. Dependence of the zeta potential on pH.

potential values are very low. In other words, in these pH ranges, the surface of the materials is strongly negatively charged, which gives a good precondition for the adsorption of positively charged particles, such as heavy metal ions or some organic substances.

Conclusions

We have shown that the adduct route is a versatile synthesis route as, depending on the starting melamine/acid ratio and the nature of the acid, a large panel of supramolecular-self assembled and crystalline phases could easily be obtained. After carbonization at moderate temperature (550 °C), it results in compounds with compositions ranging from graphitic carbonitride to C-rich graphitic carbonitride CN_x ($0.66 < x < 1.4$). It appears that, although C and N species are distributed at the molecular level in the precursor (adduct), segregation occurs during the carbonization with the appearance of a bigger C-rich (sub)nanometer phase (clusters) within the layered structure when the carbon content increases. This feature is also indirectly evidenced by the disappeared of the long-range ordering of heptazine units and a decrease in the number of N–C=N bonds in favor of C=C bonds as the carbon content increases. A progressive evolution of the properties between the two end compositions, such as thermal stability, can then easily be tuned by this process. It also introduced a higher portion of oxygen within the structure compared to standard g-C_3N_4, probably due to the presence of carboxylic group within adducts. The optical properties are strongly modified even with a limited amount of extra carbon within the g-C_3N_4 structure.

Experimental Section

Materials: Melamine (M) $C_3H_6N_6$, L-(+)-tartaric acid (TA) $C_4H_6O_6$, oxalic acid (OA) $C_2H_2O_4 \cdot 2H_2O$ and citric acid (CA) $C_6H_8O_7 \cdot H_2O$, with purity above 98 wt.%, were purchased from MACH CHEMIKALIE (Czech Republic). All the reagents and materials were used as received without additional purification or treatment. Deionized water was used in the whole experiment. Developed formulas of the reactants are given in Figure S1.

Synthesis of adducts: Synthesis of adducts was inspired from the procedure described by Han et al.[25] which is based on the mixture of melamine and oxalic acid with M/A molar ratios of 1, 2, 3, 4, 5 and 6. This process was extended here to different polycarboxylic acids (A=TA, CA, OA) mixed with melamine in different M/A molar ratios X ($X = 1.5/1$; 2.5/1; 3/1; 4/1 and 6/1). Typical synthesis is as follows: 2.52 g of melamine was dissolved under vigorous stirring in 100 mL of distilled water heated up to 80 °C. Meanwhile, an appropriate mass of acid was dissolved in 20 mL distilled water. This solution was then added drop by drop into the melamine solution which was kept warm and under stirring. A white precipitate appeared which was filtered and washed with distilled water before being dried at 80 °C for 4 h. The white precipitate was placed in a covered alumina crucible (3×5 cm) and then put into a tubular furnace for pyrolysis at 550 °C for 4 h under an inert atmosphere (N_2 flow 100 mL/min) and with a heating rate of 5 °C min^{-1}. The series of adducts obtained were named according to the initial molar ratio X of melamine over poly-carboxylic acid A following the formula MAX/1. For instance, melamine-(M), oxalic acid-(OA) adduct obtained with a ratio *X* of 3/1 was labeled MO3/1. Calcined materials at 550 °C were labeled as follows MA/X-550. Depending on the type of acid and M/A ratio used, it occurred that yield of the precipitate was too low, so the temperature of the solution was cooled down to 50 °C to recover enough solid, as summarized in (Table S1). It is worth noting, as shown in the discussion part, that this cooling step could also lead to the precipitation of free reactants.

Characterizations: The crystal structures of the samples were investigated by an X-ray diffractometer D8 ADVANCE A25 from Bruker using $Cu_{K\alpha}$ radiation source ($\lambda = 1.5406$ Å). The morphology of samples, previously gold-coated, was observed with the scanning electron microscopy (SEM) FEI Quanta 400 with a high-resolution low vacuum field emission gun (FEG). Elemental organic analysis (EOA) of the samples was performed with Thermo Finnigan FLASH EA 1112 Series CHNS/O Analyzer (Thermo Fisher Scientific, USA). The nature of some chemical groups of the samples was identified by diffusion reflectance infrared Fourier transform (DRIFT) spectroscopy on Thermo Scientific model iS50. Transmission electron microscope (TEM) micrographs were obtained on a Jeol apparatus (model ARM-200F) working at 200 kV. Raman spectra were recorded using a Horiba Jobin Yvon HR800 apparatus working with a laser at 488 and 532 nm. I_D/I_G intensity ratio between D and G bands was estimated using Voigt function.[51] X-ray photoelectron spectroscopy (XPS) was performed with a VG SCIENTA SES-2002 spectrometer equipped with a concentric hemispherical analyzer. The incident radiation used was generated by a monochromatic $Al_{K\alpha}$ X-ray source (1486.6 eV) operating at 420 W (14 kV; 30 mA). Thermogravimetric–differential scanning calorimetric analysis (TG-DSC) was performed on SETSYS-1750 CS analyzer with a heating rate of 10 °C min^{-1}. The nitrogen adsorption–desorption isotherms were measured at 77 K on Surface area and porosity analyzer Quantachrome Instrument. Photocatalytic tests were performed in a stainless steel photoreactor (348 mL) equipped with a quartz glass window. An aqueous solution (100 mL) containing 50% methanol and 0.1 g of photocatalyst, was placed in the reactor, purged by helium (to remove air) and irradiated by a Hg lamp (8 W Ultra-Violet Products Inc.-maximum peak intensity at 254 nm). Sampling of the gaseous phase was performed every hour during 4 h interval through a septum. The gas phase composition was analyzed by a gas chromatograph (Shimadzu Tracera GC-2010Plus) equipped with BID (barrier discharge ionization detector). All of the measurements were performed repeatedly.

Acknowledgements

This work was funded through Support for science and research in the Moravian–Silesian Region 2019 code RRC/10/2019, within the framework of the project "Support for talented doctoral students at the University of Ostrava III. This work was also supported by project SGS09/PrF/2021–Advanced porous materials 2–synthesis, characterization and applications. We thank Jean-Marc Le Meins, Gautier Schrod, Simon Gree and Cyril Vaulot, for XRD, TG, vibrational spectroscopy and N_2 adsorption analyses performed on IS2M Mulhouse technical platforms. The authors gratefully acknowledge Dr. Vaclav Slovak, Tomas Zelenka, Joseph Dentzer and Benedicte Rety for fruitful discussions, experiments and complementary measurements. We would like to acknowledge Prof. Kamila Koci and Martin Reli from the Technical University of Ostrava for discussions on

photocatalysis and allowing us to use their equipment to perform photocatalytic measurements.

Conflict of Interest

The authors declare no conflict of interest.

Keywords: adducts · carbonitrides · carbon-rich g-C_3N_4 · doping · supramolecular chemistry

[1] M. Inagaki, T. Tsumura, T. Kinumoto, M. Toyoda, *Carbon* **2019**, *141*, 580–607.
[2] P. Kumar, E. Vahidzadeh, U. K. Thakur, P. Kar, K. M. Alam, A. Goswami, N. Mahdi, K. Cui, G. M. Bernard, V. K. Michaelis, K. Shankar, *J. Am. Chem. Soc.* **2019**, *141*, 5415–5436.
[3] L. Peng, R. Zheng, D. Feng, H. Yu, X. Dong, *Arab. J. Chem.* **2020**, *13*, 4275–4285.
[4] Y. Wang, X. Wang, M. Antonietti, *Angew. Chem. Int. Ed.* **2012**, *51*, 68–89; *Angew. Chem.* **2012**, *124*, 70–92.
[5] G.-M. Weng, Y. Xie, H. Wang, C. Karpovich, J. Lipton, J. Zhu, J. Kong, L. D. Pfefferle, A. D. Taylor, *Angew. Chem. Int. Ed.* **2019**, *58*, 13727–13733; *Angew. Chem.* **2019**, *131*, 13865–13871.
[6] A. Thomas, A. Fischer, F. Goettmann, M. Antonietti, J.-O. Müller, R. Schlögl, J. M. Carlsson, *J. Mater. Chem.* **2008**, *18*, 4893–4908.
[7] N. M. R. Peres, *Europhys. News* **2009**, *40*, 17–20.
[8] J. Zhang, G. Zhang, S. Jin, Y. Zhou, Q. Ji, H. Lan, H. Liu, J. Qu, *Carbon* **2020**, *163*, 154–161.
[9] Y. Hu, H. Liu, Q. Ke, J. Wang, *J. Mater. Chem. A* **2014**, *2*, 11753–11758.
[10] J. Fang, H. Fan, M. Li, C. Long, *J. Mater. Chem. A* **2015**, *3*, 13819–13826.
[11] S. Zhang, S. Tsuzuki, K. Ueno, K. Dokko, M. Watanabe, *Angew. Chem. Int. Ed.* **2015**, *54*, 1302–1306; *Angew. Chem.* **2015**, *127*, 1318–1322.
[12] J. P. Paraknowitsch, J. Zhang, D. Su, A. Thomas, M. Antonietti, *Adv. Mater.* **2010**, *22*, 87–92.
[13] T. Katoh, G. Imamura, S. Obata, K. Saiki, *RSC Adv.* **2016**, *6*, 13392–13398.
[14] Y. Wang, X. Bai, H. Qin, F. Wang, Y. Li, X. Li, S. Kang, Y. Zuo, L. Cui, *ACS Appl. Mater. Interfaces* **2016**, *8*, 17212–17219.
[15] Z. Chen, T. Fan, J. Zhao, X. Yu, Q.-L. Wu, Q.-H. Zhu, L.-Z. Zhang, *J. Mater. Chem. A* **2018**, *1–3*, 15310–15319.
[16] H. Dong, X. Guo, C. Yang, Z. Ouyang, *Appl. Catal. B* **2018**, *230*, 65–76.
[17] K. Wang, X. Wang, H. Pan, Y. Liu, S. Xu, S. Cao, *Int. J. Hydrogen Energy* **2018**, *43*, 91–99.
[18] R. Kumar, M. A. Barakat, F. A. Alseroury, *Sci. Rep.* **2017**, *7*,12850.
[19] W. Che, W. Cheng, T. Yao, F. Tang, W. Liu, H. Su, Y. Huang, Q. Liu, J. Liu, F. Hu, Z. Pan, Z. Sun, S. Wei, *J. Am. Chem. Soc.* **2017**, *139*, 3021–3026.
[20] Y.-S. Jun, E. Z. Lee, X. Wang, W. H. Hong, G. D. Stucky, A. Thomas, *Adv. Funct. Mater.* **2013**, *23*, 3661–3667.
[21] S. Dolai, J. Barrio, G. Peng, A. Grafmüller, M. Shalom, *Nanoscale* **2019**, *11*, 5564–5570.
[22] N. Vu, C. Nguyen, S. Kaliaguine, T. Do, *ChemSusChem* **2019**, *12*, 291–302.
[23] Z. Zhou, Y. Zhang, Y. Shen, S. Liu, Y. Zhang, *Chem. Soc. Rev.* **2018**, *47*, 2298–2321.
[24] X. Zhang, *Chem. Res. Chin. Univ.* **2008**, *24*, 396–400.
[25] X. Han, L. Tian, H. Jiang, L. Kong, J. Lv, J. Shan, J. Wang, X. Fan, *RSC Adv.* **2017**, *7*, 14372–14381.
[26] G. J. Perpétuo, J. Janczak, *J. Mol. Struct.* **2008**, *891*, 429–436.
[27] C. Zhou, C. Lai, D. Huang, G. Zeng, C. Zhang, M. Cheng, L. Hu, J. Wan, W. Xiong, M. Wen, X. Wen, L. Qin, *Appl. Catal. B* **2018**, *220*, 202–210.
[28] X. Fang, R. Gao, Y. Yang, D. Yan, *iScience* **2019**, *16*, 22–30.
[29] X. Yuan, K. Luo, K. Zhang, J. He, Y. Zhao, D. Yu, *J. Phys. Chem. A* **2016**, *120*, 7427–7433.
[30] S. Sarkar, S. Dutta, C. Ray, B. Dutta, J. Chowdhury, T. Pal, *CrystEngComm* **2015**, *17*, 8119–8129.
[31] X.-L. Zhang, X.-M. Chen, *Cryst. Growth Des.* **2005**, *5*, 617–622.
[32] P. J. Larkin, M. P. Makowski, N. B. Colthup, *Spectrochim. Acta Part A* **1999**, *55*, 1011–1020.
[33] S. C. Yan, Z. S. Li, Z. G. Zou, *Langmuir* **2009**, *25*, 10397–10401.
[34] D. J. Miller, M. C. Biesinger, N. S. McIntyre, *Surf. Interface Anal.* **2002**, *33*, 299–305.
[35] H.-J. Li, B.-W. Sun, L. Sui, D.-J. Qian, M. Chen, *Phys. Chem. Chem. Phys.* **2015**, *17*, 3309–3315.
[36] N. D. Shcherban, P. Maki-Arvela, A. Aho, S. A. Sergiienko, P. S. Yaremov, K. Eranen, D. Yu, Murzin, *Catal. Sci. Technol.* **2016**, *6*, 73–80.
[37] W. Zhang, L. Zhou, H. Deng, *Mol. Catal. A: Chem.* **2016**, *423*, 270–276.
[38] T. Ramanathan, F. T. Fisher, R. S. Ruoff, L. C. Brinson, *Chem. Mater.* **2005**, *17*, 1290–1295.
[39] G. Camino, L. Operti, L. Trossarelli, *Polym. Degrad. Stab.* **1983**, *5*, 161–172.
[40] L. J. Broadbelt, A. Chu, M. T. Klein, *Polym. Degrad. Stab.* **1994**, *45*, 57–70.
[41] P. F. Britt, *Pyrolysis and Combustion of Acetonitrile (CH_3CN)*, can be found under https://info.ornl.gov/sites/publications/Files/Pub57226.pdf, **2002**..
[42] A. C. Ferrari, S. E. Rodil, J. Robertson, *Phys. Rev. B* **2003**, *67*, 155306.
[43] A. Merlen, J. Buijnsters, C. Pardanaud, *Coating* **2017**, *7*, 153.
[44] G. R. Dillip, T. V. M. Sreekanth, S. W. Joo, *Ceram. Int.* **2017**, *43*, 6437–6445.
[45] J. Liu, Y. Zhang, L. Zhang, F. Xie, A. Vasileff, S. Qiao, *Adv. Mater.* **2019**, *31*, 1901261.
[46] Z. Yang, L. Li, H. Yu, M. Liu, Y. Chi, J. Sha, S. Xu, *Chemosphere* **2021**, *271*, 1295033.
[47] J. Y. Howe, C. J. Rawn, L. E. Jones, H. Ow, *Powder Diffr.* **2003**, *18*, 150–154.
[48] G. D. Gesesse, A. Gomis-Berenguer, M.-F. Barthe, C. O. Ania, *J. Photochem. Photobiol. A* **2020**, *398*, 112622.
[49] Z. Wu, H. Gao, S. Yan, Z. Zou, *Dalton Trans.* **2014**, *43*, 12013–12017.
[50] R. Wang, X. Wang, X. Li, L. Pei, X. Gu, Z. Zheng, *Int. J. Hydrogen Energy* **2021**, *46*, 197–208.
[51] M. A. AL-Jalali, I. F. Aljghami, Y. M. Mahzia, *Spectrochim. Acta Part A* **2016**, *157*, 34–40.

Manuscript received: October 5, 2021
Accepted manuscript online: February 2, 2022
Version of record online: February 19, 2022